UNIVERSITY OF NAPLES "FEDERICO II"

POLYTECHNIC AND BASIC SCIENCES SCHOOL

DEPARTMENT OF CHEMICAL SCIENCES

PH.D. IN CHEMICAL SCIENCES

Structural Characterization of Olefin-based Multiblock Copolymers by Chain Shuttling Technology

Gaia Urciuoli*

Advisors

*Prof. Finizia Auriemma**

*Prof. Claudio De Rosa**

Examiner

*Prof. Roberta Cipullo**

XXXIV CYCLE 2018/2021

**DPI, P.O. Box 902, 5600 AX-Eindhoven, the Netherlands*

DPI
The Polymer Research Platform

Abstract

Aim of this Ph.D. project was to understand the complex and elusive molecular structure of olefin-based multiblock copolymers (OBCs), obtained via chain shuttling technology (CST). The CST is a process in which reversible trans-alkylation reactions take place between two organometallic catalysts through the mediation of a chain shuttling agent (i.e., diethyl-zinc). Since the two organometallic catalysts differ in their comonomer incorporation ability, the repeated exchanges of the growing polymeryl chains between the catalytic metal centers lead to OBC constituted by alternating blocks of different comonomer content. Furthermore, as a result of the stochastic shuttling process that involves homo- and hetero-shuttling events, the resultant OBCs feature a statistical distribution of block lengths and of number of blocks/chain. In particular, ethylene-based multiblock copolymers represent the latest breakthrough in polyolefins and are characterized by alternating hard and soft blocks. The crystallizable hard blocks are constituted by HDPE with very low comonomer content (1-octene, 1-hexene, or another α-olefin), whereas the soft amorphous blocks are constituted by random ethylene/1-alkene copolymers with high comonomer content.

To address the complexity of these systems, research activities were first focused on the systematic characterization of paradigmatic Infuse™ commercial samples, which are the first example of OBCs synthetized in chain shuttling conditions. The commercial grades were selected as benchmarks, since they are available in large quantity, and used to test the different experimental and semi-empirical methods aimed at assessing the non-uniform polydisperse microstructure, the average molecular mass of the blocks, the

average number of blocks/chain, and the distribution of methylene sequence length in the hard blocks. Analysis of the inter- and intrachain heterogenous microstructure and of the segmental mobility of the hard and soft blocks have been reported in Chapters 3 and 5.

In a second step, in order to grasp what is the effect of different operating parameters in the chain shuttling copolymerization on the microstructure, phase separation, and on the final properties, OBCs were synthetized ad hoc in a Parallel Pressure Reactor system (PPR), since the high-throughput synthetic approach allows to explore the entire set of variables. A thorough analysis, reported in Chapter 4, of microstructure and morphology was then carried out to understand the role of variables such as weight fraction of hard and soft blocks, different comonomers and differences in comonomer contents between the blocks, different values of segregation strength (χN values), and differences in the distribution of block size.

By closing the disambiguation loop, it has been possible to determine OBCs microstructure and architecture and correlate them univocally to material structure and morphology.

Index

Acknowledgement

This research forms part of the DPI research program, project #817.

1. Introduction

1.1. Block Copolymers

Block copolymers are polymeric materials constituted by two or more distinct repeating units linked together by a chemical bond and forming linear architectures (di-, tri-, or multi-block copolymers) or non-linear architectures (star block, graft, or mixed arm copolymers, see Figure 1).[1-4]

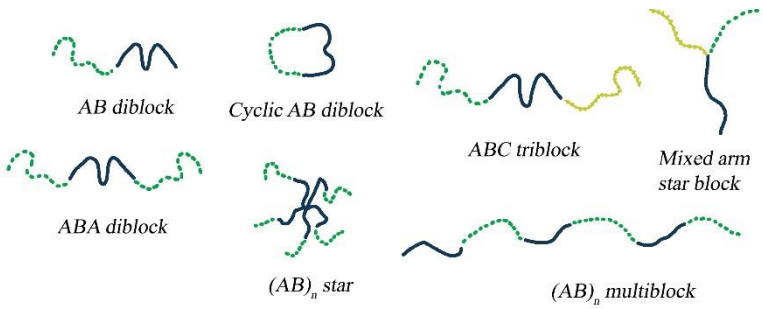

Figure 1. Common architectures of block copolymers.

Chemical incompatibility between the constituting blocks leads to phase segregation of the different blocks in micro- or nanodomains with periodical order, a phenomenon known as "self-assembly". As a matter of fact, because of the competition between chemical incompatibility and chemical connectivity, the building blocks tend to organize in microstructures minimizing the surface/volume ratio, thus decreasing the interfacial energy.[1-5] For a model A-B amorphous di-block copolymer, the kind of self-assembled micro- or nanostructure that will form depends on three parameters: the Flory-Huggins interaction parameters χ, that define the chemical incompatibility between the repeating units in the A and B blocks, and it is inversely proportional to temperature (empirically, $\chi = A/T + B$), the molecular mass of

the blocks (or the degree of polymerization *N*), and the volume fraction *f* of A (or B) block. For multiblock copolymers of kind $(A\text{-}B)_n$, the number of A-B di-block units *n* connected to each other is deemed neglectable, since the same parameters that influence the phase behavior of di-block copolymers affect the phase behavior of multiblock copolymers in a much deeper way.

In the case of a model di-block copolymer, the self-assembly process may lead to the formation of cubic arrays of spheres, hexagonal arrays of cylinders, bi-continuous cubic phases or lamellae, depending on the volume fraction of the blocks (see Figure 2).

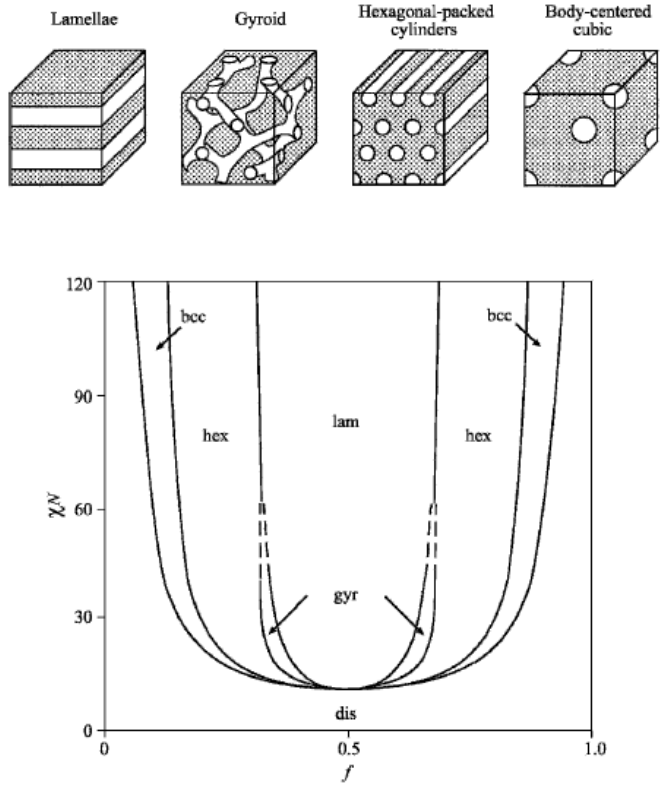

Figure 2. Phase diagram for model di-block copolymers, along with illustrations of the equilibrium morphologies. Reprinted from Developments in Block Copolymer Science and Technology, Chapter 1, Hamley, I. W, John Wiley & Sons Ltd, 2004, with permission from Wiley (2021).

It is worth noting that, depending on the temperature, order-order transitions, that is transitions between different kind of nanostructures, and order-disorder transitions, that is transitions from an ordered phase to a disordered phase (and vice versa), may occur. The temperature at which an order-disorder transition occurs is defined as Order Disorder Temperature (ODT). Since the Flory-Huggins parameter χ is correlated to the temperature, the parameter χN can be considered a measure of the degree of incompatibility; hence, the higher the χN value, the higher the segregation strength. An increase in the value of χN can be achieved decreasing the compatibility between blocks (i.e., changing the kind of comonomers), increasing the molecular mass of the blocks, or changing the temperature. As shown by a typical phase diagram of an amorphous di-block copolymer (see Figure 2), at low values of χN ($\chi N << 1$) the system is in a homogeneous disordered state and the polymer chains behave as in the unperturbed Gaussian state. If χN is asymptotically increased up to χN_{ODT}, a disorder-order transition is induced; in this case, the polymer chains are mostly unperturbed, because the interaction between the incompatible blocks are weak. This regime is known as weak segregation limit. Finally, when χN is higher than the critical value χN_{ODT}, the system gives rise to the formation of a periodically ordered structure with neat and narrow interfaces (this regime is defined as strong segregation limit), and the corresponding geometry depends on *f*. In this case, the chains are in a perturbed state, given the opposite tendency the blocks are subjected to, arising from incompressibility constraints, entropic loss due to the extended chain configuration at the interface, and the need of minimizing the surface area at the interface.[1]

1.2. Effect of Dispersity of Block Length

When discussing phase behavior, another factor that has to be considered is polydispersity. Based on random phase approximation calculations,[6] polydispersity has been deemed capable of stabilizing ordered morphology and inducing the formation of larger separated domains. Early efforts in introducing polydispersity in block copolymers included blending block copolymers with different molecular weights of the constituting units and different block compositions,[7-13] or synthetizing ad hoc series of asymmetric block copolymers with a monodisperse block and with a block of varying dispersity.[14-16] These early works have the merit to have shown that, first, contrary to the prediction of the self-consistent field theory, the increasing in the χN values is matched with a relative increase in the domain periodicity.[13-16] In other words, domain spacing increases linearly with increasing polydispersity index and segregation strength, while based on theoretical calculations it is expected that the slope of relative increase in domain spacing would decrease with increasing χN,[14,16,17] as shown in Figure 3. Secondly, it was shown that, by increasing the polydispersity, the χN_{ODT} value (the value of the χN parameter corresponding to the order-disorder transition) decreases only when the disperse blocks are the minor component and not on the entire composition range.[15] Later works widened the attainable degree of polydispersity, thanks to the development of new synthetic routes or the modification of existing polymerization strategies such as living anionic polymerization using functional initiators or followed by catalytic hydrogenation and transesterifications, combinations of ring-opening metathesis polymerization (ROMP) techniques and other living strategies, atom transfer radical polymerizations (ATRP), reversible addition-

fragmentation chain-transfer polymerizations (RAFT), and nitroxide-mediated polymerizations (NMP), as clearly described in Ref. 18.

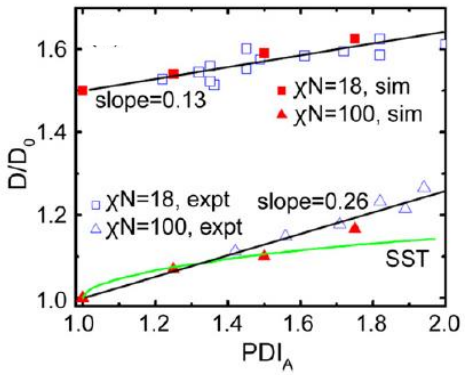

Figure 3. Domain broadening ratios as a function of polydispersity for A block in systems with low and high χN values. D_0 is the domain spacing of a monodisperse system. Red solid symbols are experimental values, while blue open symbols represent simulated values, both extracted from Refs. 14 and 16. The green line is the theoretical prediction of self-consistent field theory. Reprinted from Recent Progress on Polydispersity Effects on Block Copolymer Phase Behavior, Kim, I., Li, S., Polymer Reviews, 59 (3), 561-587, 2019, with permission from Elsevier (2021).

Concerning the increase in domain periodicity, it should be considered that polydispersity reduces the loss of entropy associated with extended chain conformation at the interface with respect to what happens for monodisperse systems, since longer chains tend to arrange in the central part of a domain, leaving the shorter chains at the interfaces (short chains shield longer one from unfavorable interactions).[19-22] This results in an increasing of the domain spacing. In addition, for very short blocks in a polydisperse system it can be energetically favorable to migrate from the interface of a domain to a surrounding domain of opposite composition (a phenomenon known as pull-out), acting as compatibilizers and inducing a further enlargement.[17,20] These two effects justify the increasing trend of domain periodicity with increasing

polydispersity and segregation strength. The domain broadening that comes with increased polydispersity can reach hundreds of nanometers, as apparent in Refs. 23-25, in which olefin-based di-block copolymers obtained through chain shuttling polymerization (CSP, vide infra) formed large lamellar structures (>100 nm) under flow alignment or exhibited photonic properties. In another study, this time on olefin-based multiblock copolymers by CSP, polydispersity in block molecular mass and number of blocks/chain leads to a further increase in domain broadening due to phase mixing,[26] because for small values of χN near to the order-disorder transition the inter-block mixing is eased by the low energy barrier. For these polyolefin-based systems, domains were found to be 3 to 5 times larger than domains in monodisperse systems of similar composition and molecular weight.[25,26] Other works that further confirmed the correlation between domain broadening and segregation strength in polydisperse systems focused on tri-block copolymers such as PS-PB-PS, PEO-PB-PEO, and PLA-PB-PLA copolymers with weak, moderate and high segregation strength, respectively.[27-31] This time, domains were found to be 2-2.5 times larger than the monodisperse counterparts in the case of the weakly and moderately segregated tri-block copolymers, whereas for the highly segregated tri-block copolymer enlargement was only 1.3 times higher. These results confirm the general trend of increased domain size with increased polydispersity and point out that the lower the χN value, the higher the inter-block mixing and the enlargement. To sum up, polydispersity in the molecular mass, composition, and number of blocks leads to reduced entropic factors associated with the stretching of polymer chains at the interphase between adjacent domains, enhanced migration of short blocks from interface to surrounding regions (pull-out) and inter-block mixing, and finally to domain broadening in comparison to monodisperse systems.

Polydispersity can also cause changes in the phase boundaries of block copolymers, leading to increases or decreases in the χN_{ODT} and χN_{OOT} (which is the value of χN corresponding to an Order-Order Transition, OOT) values with respect to monodisperse symmetric systems. Concerning the shift of the χN_{ODT} values which is observed at increasing block polydispersity, in a number of studies on asymmetric polydisperse di-block copolymers,[15,19,32-34] a downward shift was observed when the disperse block was the minority component,[19,32] as shown in Figure 4, whereas χN_{ODT} values increased when the disperse block was the majority block.[15] The opposite trends of "destabilization induced by composition fluctuations" in a melt and "stabilization due to phase separation" were taken into account for a possible explanation. When the destabilization effects are prevalent, the unexpected increase in χN_{ODT} is verified. A remarkable decrease in the χN_{ODT} has been, instead, noticed in the case of di-block or multiblock copolymers where every block is polydisperse.[25,26] For polydisperse olefin-based di-block copolymers χN_{ODT} values were found to be between 6 and 10.[25]

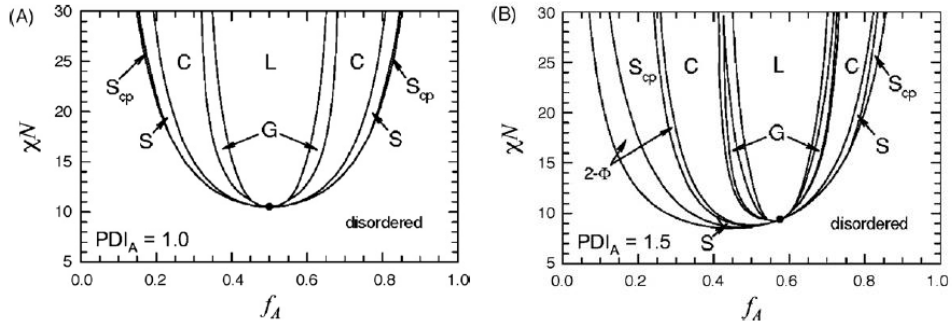

Figure 4. Phase diagrams for a model A-B di-block copolymer (a) and for the same di-block copolymer in which the polydispersity index of block A has been increased to 1.5, keeping block B monodisperse (b). Self-assembled structures geometries are indicated: biphasic regions (2-Φ), close-packed spheres (S_{cp}), body-centered cubic array of spheres (S), hexagonal-packed cylinders (C), gyroid (G), lamellar (L). Reprinted from Polydispersity and

Block Copolymer Self-Assembly, Lynd, N. A., Meuler, A. J., Hillmyer, M. A., Progress in Polymer Science, 33 (9), 875–893, 2008, with permission from Elsevier (2021) and reprinted with permission from Matsen, M. W., Polydispersity-Induced Macrophase Separation in Diblock Copolymer Melts, Physical Review Letters, 99 (14), 148304, 2007. Copyright (2021) by the American Physical Society.

The position of the order-order transition is also subjected to shifts as a consequence of polydispersity. For A-B di-block[14,15] and A-B-A tri-block copolymers,[28,29,31] the increasing in polydispersity of one of the blocks induced for instance transition from gyroid to lamellar morphology[14] or from bi-continuous to lamellar morphology.[28] Since in asymmetric polydisperse systems longer chains are located at the center of each polydisperse domain whereas shorter chains are at the interfaces, packing is efficient and the entropic contribution to chain stretching is alleviated, creating an interface whose curvature is towards the disperse domain.[10,14,19,28,29] In fact, it should be considered that for symmetric di-block copolymers, interfaces are flat in order to ensure free energy minimum in the packing of the block junctions. In asymmetric copolymers, in order to have a flat interface, longer blocks should stretch more than short blocks, so to avoid entropic penalties the interface bends towards the interfacial short blocks, allowing long blocks to relax at the center of the domain.[13] As polydispersity is enhanced, the entropic factors balance the increased interfacial enthalpic factors in the phase-separated system and, as a consequence the order-order phase boundary is modified.[13] In addition, the pull-outs of the shorter chains from the interphase and their dissolution in the surrounding monodisperse domains, lead to a broadening of the monodisperse domain.[20,29] This two phenomena are behind the changes in domain morphology and χN_{OOT} position. In conclusion, polydispersity affects in a deep way the domain spacing, inducing the pull-out phenomenon of the

shorter chains and inter-block mixing, and the phase boundaries, namely the values of χN at which order-disorder and order-order transition occurs. In particular, the χN_{ODT} upward or downward shift depends on the prevalence of destabilizing fluctuations over the stabilizing effect of having a phase segregation driven by long chains and vice versa.

1.3. Solid-state Morphology of Block Copolymers Containing a Crystallizable Block

For a semicrystalline block copolymer, in which at least one of the two segments is able to crystallize, the phase behavior in the solid-state is further complicated by the competition between the phase segregation and the crystallization, the latter, in turn, taking place in a homogeneous or a heterogeneous melt.[3,4] If crystallization starts in a phase separated melt, four situations may occur: break-out, confined, templated, and pass-through crystallization (see Figure 5). A break-out crystallization mode, typical of weakly segregated melt, is verified when crystallization completely destroys the ordered melt and leads to the formation of a lamellar crystalline morphology and to the possible organization of the lamellae in spherulitic superstructures.[35-38] If the domain-structured morphology of the melt is preserved upon crystallization, confined crystallization is verified.[39] This kind of crystallization mode is typical of systems in the strong segregation limit and involves nucleation events and crystal growth, both confined in each single domain. In the case of the templated crystallization,[35,39,40] typical of melts with medium to low segregation strength, the ordered structure of the melt is preserved as in the confined crystallization, with the important difference residing in the sporadic occurrence of bridging events. In a bridging event,

multiple crystalline domains are generated from a single nucleus, thus accelerating the kinetic of crystallization. The pass-through crystallization[26] is found in the weak segregation limit and it is characterized by a preservation of the general segregated morphology of the melt, confined crystallization with lamellar bridges connecting the different domains, and no crystal orientation.

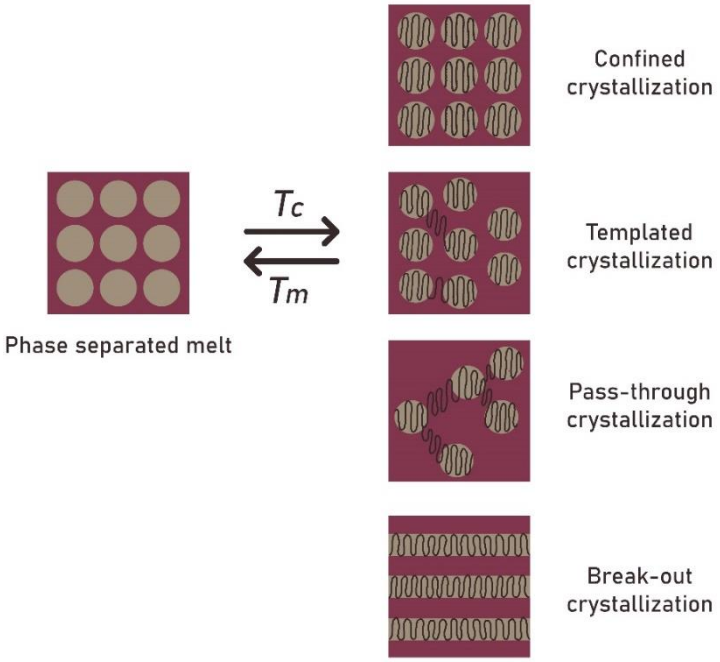

Figure 5. Crystallization modes for a semicrystalline block copolymer.

Concerning semicrystalline block copolymers containing only one crystallizable block in the weak segregation limit, it should be noted that their phase behavior depends on the length and number of blocks, on the crystallization temperature of the blocks able to crystallize, on the glass transition temperature of the amorphous block, and on the order-disorder transition temperature of the system (T_c, T_g, T_{ODT}, respectively). If the

crystallizable blocks have a higher volume fraction *f* (i.e., they are the majority component) and $T_c < T_{ODT}$ (which means that crystallization is starting from a ordered melt), break-out morphology will take place, regardless of the T_g of the amorphous block.[41,42] If the crystallizable block is the minor component and, again, crystallization is taking place in a heterogeneous melt, two possible outcomes may verify: if $T_{ODT} > T_g > T_c$, templated crystallization occurs; if $T_{ODT} > T_c > T_g$, both templated and break-out crystallization mode are expected, which mode will prevail depending on the segregation strength and on the molecular mass of the blocks.[43] The kind of morphology that will develop in the solid state can be tailored by controlling the crystallization mode (break-out, confined, templated, pass-through) through accurate selection of the maximum temperature of the melt, the cooling rate, and through the tuning of the molecular mass of the blocks, as the segregation strength χN is proportional to the molecular mass. This means that a fine tailoring of the physical, mechanical, and rheological properties of a block copolymer with a semicrystalline block can be achieved controlling the morphology through a suitable tuning of crystallization conditions and chemical constitution.

1.4. Chain Shuttling Technology

The usual synthetic ways to produce block copolymers are the anionic polymerization, the cationic polymerization, and the controlled radical polymerization.[3,4] Another synthetic strategy for the production of block copolymers, in particular olefin-based block copolymers, relies on single-site organometallic catalysts. These (co)polymerizations are based on the sequential addition of (co)monomers in the reactor, under conditions of occurrence of rare (ideally null) termination events (living polymerization)

thus providing a precise control on the structure and over the molecular weight of the resultant polymers. All these synthetic routes expanded the properties and application ranges of polymeric materials, because they allowed to produce materials with apparently irreconcilable properties, for instance elastomers with high melting points and stiffness. However, the drawback of a living polymerization based synthetic strategy is that it entails the growth of just one polymer chain/active center. To reduce catalyst/active species consumption, coordinative chain transfer polymerization (CCTP) techniques were implemented,[44] involving the use of a single transition metal catalyst and a main group metal alkyl acting as chain transfer agent (CTA). The transfer of the growing chains from the catalyst to the CTA enables growth of multiple chains/active center, saving atom economy.[45-55] Recently, using high throughput tools, the chain shuttling polymerization was discovered as an alternative and efficient way to produce olefin block copolymers (OBCs) in a single step.[56,57]

The Chain Shuttling Polymerization (CSP, Figure 6) is an efficient synthetic way to produce OBCs in which reversible chain transfer reactions take place between couples of metalorganic catalysts through a chain shuttling agent (CSA, i.e., diethylzinc),[56-64] thus representing a peculiar kind of CCTP. As in CCTP, reversible trans-alkylations of growing polymer chains occur between a transition metal center and a main group metal center and involve the formation of a hetero-dinuclear intermediate with bridging polymeryls.[56,57,59] When a CSA molecule exchanges a ligand with the growing polymer chain coordinated to a catalytic transition metal center, a dormant polymeryl chain is generated. On the other hand, when the dormant chain is delivered back to a metallic center of the catalyst by the CSA, the chain growth starts again through a succession of coordination and insertion events of the

comonomers in the feed. The comonomers, typically ethylene and α-olefins, are copolymerized in a single reactor containing the two metalorganic catalysts and the CSA. The process relies in the use of two different catalysts endowed with remarkable differences toward comonomer incorporation ability, so that the repeated exchange of the polymeryl chains between the CSA and the catalytic centers produce copolymers with multi-block microstructures.[56-64] In addition, as a result of the stochastic homo- and hetero-shuttling process, a statistical distribution in the block lengths and number of blocks/chain is obtained.

In the specific case of Infuse™ (by The Dow Chemical Company), which are the first example of multiblock copolymers produced with CSP, ethylene and 1-octene are copolymerized using a bis(phenoxyimine)Zr complex and a (pyridylamido)Hf complex (Cat1 and Cat2, respectively, see Figure 6) as transition metal catalysts and $ZnEt_2$ as CSA.[56,57] The Hf-based complex is much more reactive towards octene (and in general towards other α-olefins such as 1-hexene, 4-methyl-1-pentene, 1-hexadecene) than the Zr-based catalyst. Selecting a proper couple of organometallic catalysts active in the polymerization of ethylene and α-olefins, with different selectivity toward comonomer incorporation, with good activity in the reversible transfers of the growing chains with the CSA and working in the same reaction conditions at high temperature (100°C), along with the selection of a proper CSA is not a trivial process. Indeed, as described in a seminal paper on Science,[56] in which The Dow Chemical Company announced the discovery of the CSP, high-throughput techniques were adopted to screen a vast pool of catalysts know in literature to be active in the polymerization of ethylene. By running multiple parallel ethylene polymerizations, a first screening allowed to identify the best potential catalysts and CSAs satisfying the criteria of efficiency, high

polymerization yield, low M_n suppression, and narrow distribution of molecular mass (low M_w/M_n). In a second screening, by running this time multiple parallel ethylene/1-octene copolymerizations, combinations of the best candidates among catalysts and CSAs allowed to select the best performing pair of catalysts Cat1 and Cat2 (Figures 6 and 7) and $ZnEt_2$ as CSA.[56] It is worth noting that if one uses the catalyst couple Cat1/Cat2 of Figure 6 without the CSA, one obtains ethylene/1-octene copolymers that show a bimodal molecular mass distribution and with an 1-octene content intermediate between the ones that would have been obtained if the polymerization had been carried out using the two catalysts separately (Figure 7).

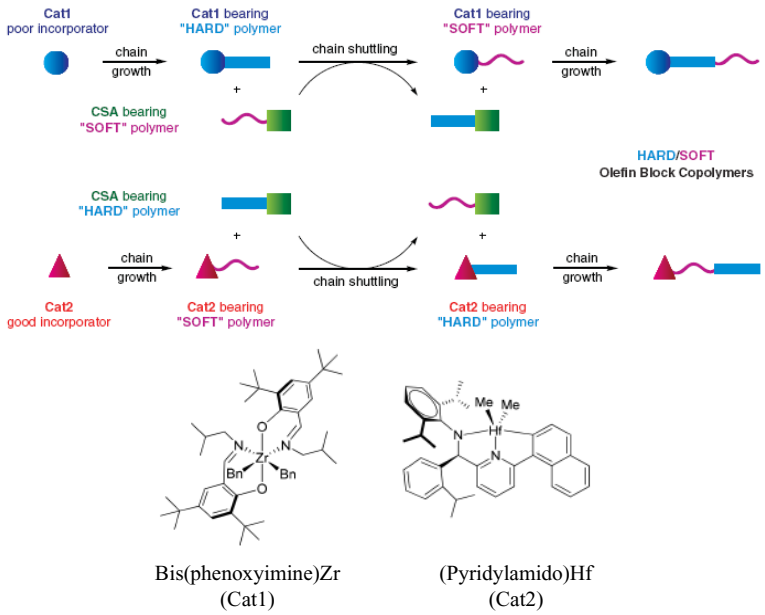

Figure 6. Schematic representation of the chain shuttling process. The chemical structure of two typical organometallic catalysts active in CST (Cat1 and Cat2) are also reported. From Arriola, D. J., Carnahan, E. M., Hustad, P. D., Kuhlman, R. L., Wenzel, T. T, Catalytic Production of Olefin Block Copolymers via Chain Shuttling Polymerization, Science, 312 (5774), 714–719, 2006. Reprinted with permission from AAAS (2021).

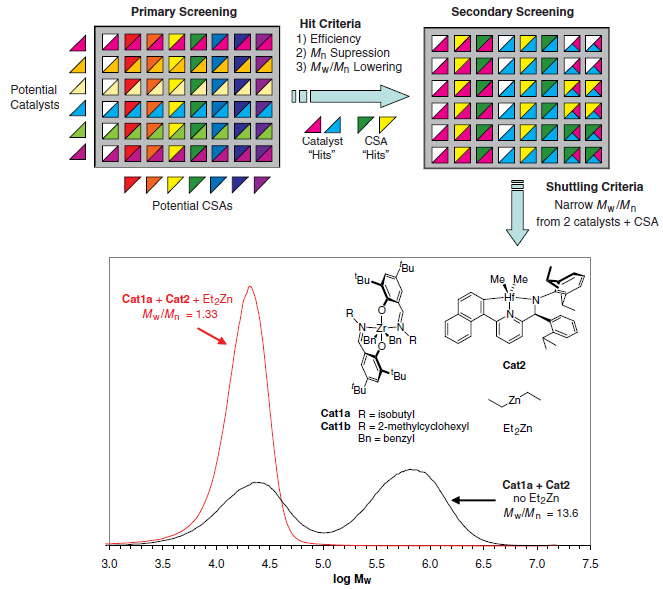

Figure 7. Two-stages high-throughput screening procedure followed in Ref. 56 to determine the best performing couple of metalorganic catalysts and the chain transfer agent to be used in ethylene copolymerizations. From Arriola, D. J., Carnahan, E. M., Hustad, P. D., Kuhlman, R. L., Wenzel, T. T, Catalytic Production of Olefin Block Copolymers via Chain Shuttling Polymerization, Science, 312 (5774), 714–719, 2006. Reprinted with permission from AAAS (2021).

Under proper conditions, the chain shuttling process yields statistical multiblock polymer chains with alternating octene-rich, amorphous segments (the 'soft' blocks) and octene-poor, semicrystalline, HDPE-like segments (the 'hard' blocks). By varying the [Cat1]/[Cat2], [Zn]/([Cat1+Cat2], and [ethylene]/[octene] mole ratios, the relative amounts of 'hard' and 'soft' blocks, as well as their average lengths and compositions, can be modulated.[56,57] OBCs with long 'hard' blocks and an excess of 'soft' blocks behave as thermoplastic elastomers,[57] with high melting temperatures, low glass transition temperatures, and low density. Therefore, contrary to random copolymers, for which the melting temperature and the mechanical properties

are controlled by the comonomer content and, hence, by a change of the density, OBCs demonstrate that this is not necessarily true. As an example, the breaking of "the longstanding product-property relationship"[56] between the density and the melting temperature is illustrated in Figure 8. It is apparent that the melting temperature of the OBCs is much higher than the melting temperature of the random counterparts with the same density.

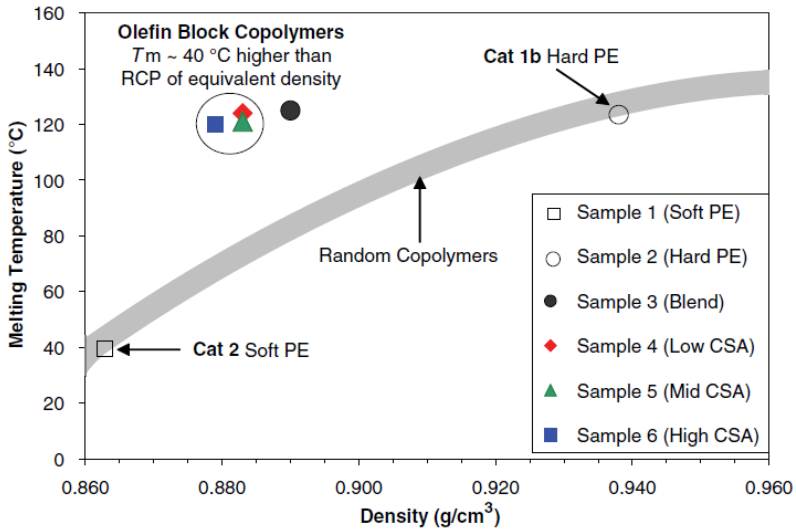

Figure 8. Melting temperature of OBCs and random ethylene-octene copolymers (RCP) as a function of density. The gray line represents the longstanding relationship between melting temperature and density, typical of random copolymers. OBCs (filled symbols) display melting temperatures more than 40° C higher than those of random copolymers of similar density. From Arriola, D. J., Carnahan, E. M., Hustad, P. D., Kuhlman, R. L., Wenzel, T. T, Catalytic Production of Olefin Block Copolymers via Chain Shuttling Polymerization, Science, 312 (5774), 714–719, 2006. Reprinted with permission from AAAS (2021).

The physical and mechanical properties of OBCs, as well as their tendency toward self-separation and assembly of the different blocks into micro-sized or nano-sized domains in the melt and solid-state, critically depend on the length

of the blocks, the distributions of block length and number of blocks/chain, and on the state of the melt.

The effect of the microstructure of the chains (i.e., comonomer content in the hard and soft blocks, fraction of hard and soft blocks, average length of the blocks, the distributions of block length, and number of blocks/chain) on the phase behavior in the solid and melt state and on the structure and mechanical properties of the OBCs has been widely investigated to date.[24,26,65-76] In particular, the role of the hard block fraction has been studied in multiblock copolymers with average content of the hard blocks comprised between 0 and 100%, fixing the 1-octene content in the hard and soft blocks to ≈1 and ≈20 mol%, respectively ($\Delta oct \approx 19$mol%).[65] Although the spherulitic morphology of the resultant OBCs was suggesting crystallization from a miscible melt, the segregation of the hard and soft blocks in separated domains was indicated by the high and constant melting temperature of the hard blocks at around 120 °C and the occurrence of distinct β- and α-relaxations in the dynamic mechanical spectra as a function of temperature.[65] Furthermore, compared with the random ethylene/1-octene copolymers, the OBCs with analogous octene content show significant differences, in that they crystallize forming space-filling spherulites against the tendency of the random copolymers to form fringed micellar-like crystalline aggregate. In addition, the OBCs are characterized by a faster crystallization kinetics, lower values of the glass transition temperature, higher values of the Young's modulus, and superior elastic performances, especially at high temperatures.[65-69] The possible occurrence of mesophase separation in the melt and the solid-state morphology, taking place upon cooling as a result of mesophase separation coupled with crystallization of the hard blocks in separated domains, have been extensively investigated in OBCs as a function of Δoct (difference of octene content between hard and soft blocks), that is as

a function of segregation strength between the constituting blocks.[24,26,70-75] For hard and soft blocks of a given length, indeed, the segregation strength is expected to increase with the increasing of the Δ*oct* value. In particular, it has been shown that at temperatures higher than the melting point, OBCs with Δ*oct* comprised in the range 16-30 mol% undergo remarkable concentration fluctuations of hard and soft blocks at chain length scale and mesophase separation transition in the melt.[24,26,70-75] The solid-state morphology is controlled not only by the Δ*oct* values, but also by the crystallization conditions.[69-72] Indeed, the crystallization of hard blocks taking place from a mesophase separated melt occurs in confined domains and prevents the formation of radial lamellae arranged in stacks, and the consequent organization of the stacks in spherulitic superstructures.[69-72] At high Δ*oct* values and/or after imposing a long annealing time at temperatures favoring the mesophase separation in the melt, the spherulitic morphology is replaced by isolated fragmented lamellar structures.[70] Similar spherulitic morphologies are instead obtained regardless of the Δ*oct* values, under crystallization conditions that prevent efficient mesophase separation in the melt.[70] However, direct evidence of mesophase separation in the melt by small angle X-ray scattering (SAXS) measurements could not be demonstrated, due to the small contrast in electron density between the soft and hard blocks. It has been instead revealed resorting to melt rheology analysis,[24,26,72-75] as the occurrence of concentration fluctuations at length scales larger than the coil size, ascribable to a mesophase separated (heterogeneous) melt, causes failure of the time temperatures superposition at frequency lower than a threshold.[76,77]

It is worth noting that the simultaneous presence of hard blocks of short and high length generated by effect of the chain shuttling process should give rise to formation of different families of lamellar stacks by effect of molecular

mass segregation. However, the analysis of the dependence of the properties and the structural arrangement of the chains in the melt and solid state on the chain microstructure of the OBCs is quite complex. It has been shown that samples characterized by small differences in molecular properties (such as the content of octene units in the hard and soft blocks, the average octene content and the fraction of hard blocks), values of octene content in the hard and soft blocks of ≈ 0.5 and 20 mol%, respectively, but having different molecular mass and average length of the blocks show largely different mechanical properties and morphology.[75,78-80] These latter features are related to differences in the length of the blocks and number of blocks per chain and to the non-uniform microstructure of the chains.[75,78-80] In particular, as the chain shuttling process entails a random chain transfer mechanism, OBCs should be regarded as a reactor blend of chains with statistical distributions in the length of blocks and in the number of blocks per chain that vary not only from chain-to-chain but also within the same chain. The interchain constitutional heterogeneity of the OBCs is clearly indicated by some results of analytical crystallization elution fractionation (aCEF),[58] that reveal the presence of a low temperature elution peak relative to an amorphous fraction consisting of soft blocks and/or soft blocks linked to short hard blocks, and of broad elution peaks at higher temperatures due to semicrystalline fractions consisting of chains made up of hard and soft blocks of different length covalently linked to each other. Further evidence of the constitutional heterogeneity of OBCs at inter-chain level derives from analytical temperature rising elution fractionation (ATREF) analysis,[64] and from preparative extraction tests using solvents.[26,58,79,80] For instance, it has been shown that prolonged extraction performed at room temperature with *n*-hexane allows to isolate a low fraction (less than 3 wt%) of a soluble amorphous component, namely consisting of soft blocks.[26] The

presence of soluble and insoluble fractions was also revealed resorting to exhaustive Kumagawa extractions with boiling *n*-hexane and diethyl ether.[64,78,79] In particular, it has been shown that the amount of the fractions soluble in *n*-hexane in Ref. 64 and diethyl ether in Refs. 78 and 79 included in the corresponding analyzed OBCs samples is around 40-50 wt%[64] and 5-10 wt%,[78,79] respectively. Although the studies performed to date have somehow evidenced the non-uniform constitution of the chains in OBCs belonging to the different fractions, the non-uniform length of the blocks covalently linked to one another within the same chains has been only indirectly addressed. In other terms, to date, the intrinsic characteristics of constitutional heterogeneity of the OBCs occurring not only at the inter-chain but also at intra-chain level have been overlooked. Furthermore, whereas all general chemical and physical principles behind the chain shuttling process are clear, the details (including basic features such as average block numbers, lengths, and distributions thereof) are ill-defined and very difficult to work out.

1.5. The Interdisciplinary Approach: Objective and Layout of the Work

As described above, OBCs obtained through chain shuttling polymerization are too complex for a conventional chain-of-knowledge investigation because data pertaining to individual elements of the chain are susceptible of multiple interpretations; this evidently calls for a more holistic approach. Hence, the intricate and still poorly defined OBC structure-properties relationships has to be unraveled by means of an *inter*-disciplinary high-throughput approach with disambiguation loops encompassing adjacent elements of the chain-of-knowledge, from polymer synthesis to microstructure, down to structural, mechanical, and rheological properties. The

high-throughput approach allows a systematic screening of the variable hyperspace of ethylene/1-alkene copolymerization, elucidating the microstructure and architecture of these advanced materials.

Three research groups with three different fields of expertise, under the umbrella of the Dutch Polymer Institute (Project DPI#817, Figure 9), cooperated along the chain of knowledge in an inter-disciplinary effort to disambiguate the relationships between microstructure, structure, morphology, and rheology: the Laboratory of Stereoselective Polymerizations (LSP) for polyolefin catalysis and microstructure, the Polymer Physics Laboratory (PPL, which this PhD candidate belongs to) for structure and properties, and the Laboratory of Soft Matter, Complex Fluids and Rheology (LSMR) for rheology.

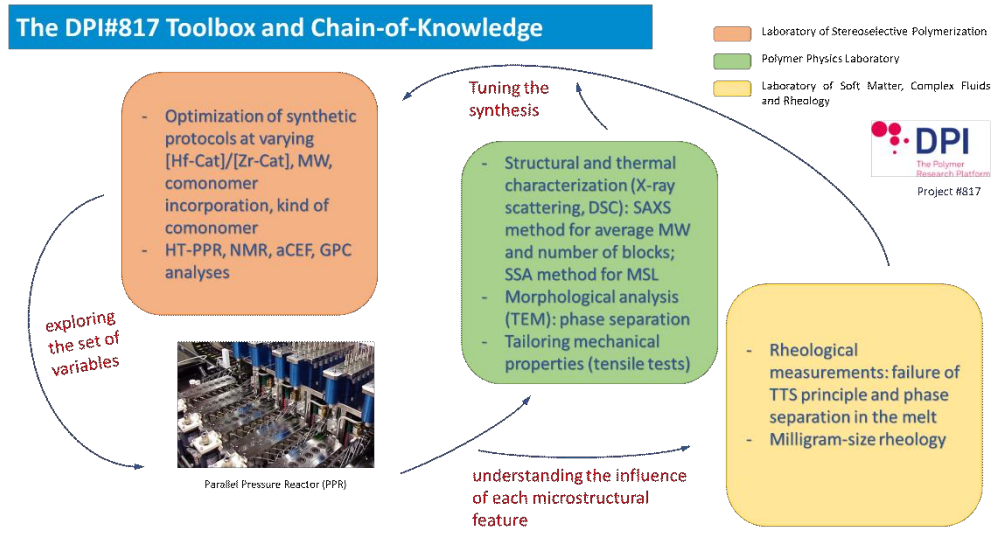

Figure 9. Workflow of Project DPI#817.

The peculiar and intriguing properties of ethylene/1-alkene OBCs result from their complex and statistically distributed molecular microstructure and architecture. Average block compositions and lengths, number of blocks per

chain, and their distributions, are all important parameters in this respect. Microphase separation, in particular, depends on the segregation strength of the blocks: the higher the difference in composition between hard and soft segments, and the longer the blocks are, the higher the segregation strength. Subtle variations of any chain microstructural parameters can determine important effects on physical and mechanical properties of OBCs. Therefore, reaching true understanding is exceedingly difficult without integrating chemical and physical competences.

In view of the above, in the present PhD thesis, a systematical and thorough analysis on the chain microstructure, thermal, structural, mechanical, and morphological properties of commercial grades Infuse™ and of samples synthetized ad hoc in a Parallel Pressure Reactor system (PPR) has been carried out with the aim to understand the influence of each microstructural feature of the chain on the melt- and solid-state morphology, and therefore on the final properties. The samples have been characterized by means of an array of techniques including NMR, GPC, aCEF, DSC, WAXS, SAXS, TEM, and mechanical and rheological testing. Chapter 2 is dedicated to the description of all the experimental procedures and techniques employed in this work.

The commercial grades have been selected as benchmarks, since they are available in large quantity, and used to test the different experimental and characterization tools aimed at assessing the non-uniform polydisperse microstructure, the average molecular mass and number of blocks, and the distribution of methylene sequence length that have been set up for these complex systems. The extensive characterization of the commercial Infuse™ grades has been described in Chapter 3. The high-throughput approach, on the other hand, allows to explore the entire set of variables (molecular mass, comonomer content, segregation strength, hard and soft blocks weight fraction

and so on) through the preparation and characterization of a suitably wide range of OBCs, thus helping to shed light on the melt- and solid-state behavior of these systems. Hence, Chapter 4 deals with the structural, mechanical, and morphological analysis of series of OBCs synthetized using a state-of-the-art high-throughput polymerization platform at varying parameters such as the kind of comonomer, the difference of comonomer incorporation between soft and hard blocks, and the ratio between the weight fraction of soft and hard blocks. Chapter 5 illustrates the results of a solid-state NMR analysis performed on an exemplary Infuse™ commercial sample and on a home-made OBC with high segregation strength with the aim to relate the segmental dynamics to the complex microstructure of these systems. The solid-state NMR experiments have been carried out with the help of Dr. Robert Graf of the Max-Planck-Institut für Polymerforschung (Mainz, Germany) during a 6-months remote training (in lieu of a 5-months stay that could not take place due to the pandemic situation). The main conclusions of this work are presented in Chapter 6. In our opinion, by closing the disambiguation loop, it has been possible to determine OBCs microstructure and architecture and correlate these univocally to material structure and morphology. The final Appendix sections to the thesis contains the NMR and GPC results of all the OBCs synthetized ad hoc for this work, along with the procedures for the calculation of the interphase distribution function of a biphasic multilayered system (IDF) and the calculation of the mono-dimensional self-correlation function of the electron density fluctuations (CF) applied to the small-angle scattering data to extract lamellar values, as well as complementary data used as support for the main results reported in the Chapters.

2. Experimental

2.1. Synthesis of Olefin Block Copolymers

All the Olefin Block Copolymers (OBCs) have been synthetized by the collaborating Laboratory of Stereoselective Polymerization (LSP) of Professor Busico at the Department of Chemical Sciences of the University of Naples "Federico II" using a Freeslate (former Symyx) parallel pressure reactor (PPR)[81] high-throughput experiment (HTE) platform, featuring 48 reaction cells (6.0 mL working volume each) arrayed in six 8-cell modules. The system is contained in a triple MBraun LabMaster glovebox operated under N_2. The Freeslate PPR HTE setup is shown in Figure 1. For all the syntheses, each cell has been loaded with a mixed alkane solution (ISOPAR-G), ethylene, α-olefin, methylalumoxane as scavenger (MAO, 5 μmol and 7.5 μmol for a total operating pressure of 160 and 250 psi_g, respectively) and N,N-dimethylaniliniumtetrakis-perfluorophenylborate in a toluene solution as activator (1.2 ratio with respect to total catalyst amount). A feed of ethylene is ensured until the desired conversion is achieved, operating at constant temperature, pressure, and stirring rate (800 rpm).[58] The system is finally quenched with dry air. Samples are then recovered from the PPR cells, centrifugated, and dried overnight. Dr. Antonio Vittoria and Dr. Felicia Daniela Cannavaciuolo are kindly acknowledged for all the syntheses of the OBCs and their help and collaboration, together with all the members of the LSP team. In particular, Prof. Roberta Cipullo is also acknowledged for the analysis of the chain microstructure of the PPR OBCs.

Figure 1. PPR HTE system used in this thesis work to synthetize olefin block copolymers.

2.1.1. Synthesis of ethylene/1-hexene OBCs at Δhex ≈ 20 mol% and w_s/w_h ≈ 80/20

A set of PPR experiments has been executed in ethylene/1-hexene chain shuttling reactions at [Cat2]/[Cat1] ratio (Figure 2) of 4:1. The reactions have been carried out at 100°C in 5.15 mL of alkane solution with $ZnEt_2$ as the chain shuttling agent ([Zn]/[Cat1+Cat2] = 50) and using 0.850 mL of 1-hexene. The operative pressure of ethylene was 160 psi_g. The total catalyst amount was 20 nmol (4 and 16 nmol of Cat1 and Cat2, respectively).[58] The obtained Δ*hex* (difference between the 1-hexene content of soft and hard blocks) was ≈ 20 mol%, and the w_s/w_h ratio (ratio between the weight fraction of soft and hard blocks) was 80/20. After preliminary characterization, the yields of the different PPR cells have been combined through complete dissolution in boiling xylene followed by re-precipitation in acetone, in order to have a larger amount of sample available to perform the characterization of the mechanical properties in tensile tests.

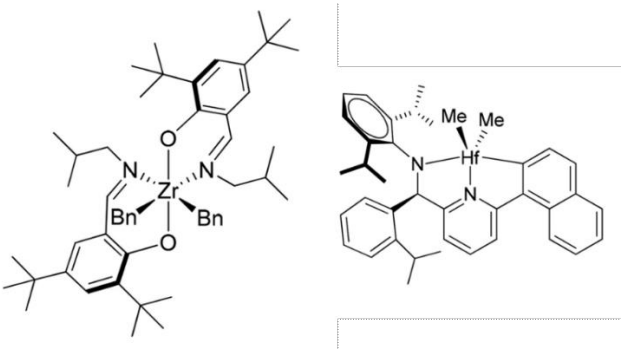

Figure 2. The bis(phenoxyimine)Zr Cat1 (left) and (pyridylamido)Hf Cat2 (right). Bn = Benzyl.

2.1.2. Synthesis of ethylene/1-hexene OBCs at Δhex ≈ 20 mol% and w_s/w_h ≈ 50/50

A set of PPR experiments has been executed in ethylene/1-hexene chain shuttling reactions. The operative pressure of ethylene has been raised from 160 to 250 psi_g and the 1-hexene feeding (1.350 mL per reactor) has been adjusted accordingly to keep a constant ethylene/1-hexene ratio. The reactions have been carried out at 100°C in alkane solution (4.65 mL) and $ZnEt_2$ has been used as the chain shuttling agent ([Zn]/[Cat1+Cat2] = 50). The [Cat2]/[Cat1] ratio has been fixed to 1:1. The total catalyst amount was 20 nmol (10 nmol for both Cat1 and Cat2). The obtained OBCs are characterized by Δ*hex* ≈ 20 mol% and w_s/w_h ratio ≈ 50/50.

2.1.3. Synthesis of ethylene/1-hexene OBCs with larger difference of co-monomer incorporation between hard and soft blocks (Δhex)

A set of PPR experiments has been executed in ethylene/1-hexene chain shuttling reactions using the usual (pyridylamido)Hf catalyst (Cat2) and replacing Cat1 (Figure 2) with a complex featuring a more sterically hindered bis(phenoxyimine) ligand (Cat3, see Figure 3), in order to overcome the molecular weight upper limitations imposed by the high propensity of Cat1 to undergo β-H elimination.[58] In particular, this was beneficial to avoid an undesired drop in OBC molecular weight which was observed upon increasing w_h over w_s with the Cat2/Cat1 pair.

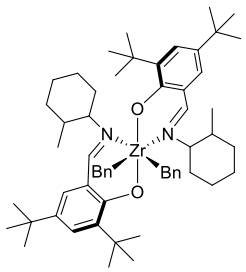

Figure 3. The structure of bis(phenoxyimine)Zr Cat3.

The new catalyst pair Cat2/Cat3 has been used to synthesize a series of OBCs with a Δ*hex* value larger than 20 mol%, at variable w_s/w_h, operating at 250 psi_g of ethylene pressure and with 2.70 mL of 1-hexene feeding per each individual reactor. The reactions have been carried out at 100°C in alkane solution (3.3 mL) and $ZnEt_2$ has been used as the chain shuttling agent ([Zn]/[Cat3+Cat2] = 50 in each polymerization). In all cases OBC samples with Δ*hex* was ≈ 30 mol% have been obtained, characterized by w_s/w_h ratio equal to 80/20, 70/30, 65/35, and 50/50. The total catalyst amount was always fixed to 20 nmol, however the catalysts ratio [Cat2]/[Cat3] changed throughout the series as follows: [Cat2]/[Cat3] = 2.5:1 for the OBCs with w_s/w_h = 80/20

(5.7 and 14.3 nmol of Cat3 and Cat2, respectively); [Cat2]/[Cat3] = 2:1 for the OBCs with w_s/w_h = 70/30 (6.7 and 13.3 nmol of Cat3 and Cat2, respectively); [Cat2]/[Cat3] = 1.5:1 for the OBCs with w_s/w_h = 65/35 (8 and 12 nmol of Cat3 and Cat2, respectively); [Cat2]/[Cat3] = 1:1 for the OBCs with w_s/w_h = 50/50 (10 nmol of both Cat3 and Cat2).

2.1.4. Synthesis of ethylene/4-methyl-1-pentene OBCs

The catalysts pair Cat2/Cat3 has been also used to synthesize a series of ethylene/4-methyl-1-pentene OBCs with similar values of the difference between the 4-methyl-1-pentene (4M1P) content of soft and hard blocks ($\Delta 4M1P \approx 20$ mol%) and w_s/w_h ratio ($\approx$ 80/20) of the ethylene/1-hexene OBCs series 1 and 2. The copolymers have been synthesized in a series of PPR experiments of chain shuttling reactions using the following set of conditions: 100°C, 250 psi_g of ethylene pressure, 1.50 mL of 4M1P feeding, 4.5 mL of alkane solution, and [Zn]/[Cat2+Cat3] = 50. The [Cat2]/[Cat3] ratio has been fixed to 4:1 and the total catalyst amount was 20 nmol (4 and 16 nmol of Cat3 and Cat2, respectively).The samples have been merged together to have a larger quantity of material to undergo structural, mechanical, and rheological characterizations. In particular, the OBCs have been dissolved in boiling xylene (in the presence of dibutylhydroxytoluene, BHT, as stabilizer) and re-precipitated in acetone.

2.1.5. Synthesis of ethylene/1-hexadecene OBCs

A series of ethylene/1-hexadecene OBCs has been synthetized using the catalysts pair Cat2/Cat3, characterized by similar values of the difference

between the 1-hexadecene (C16) content of soft and hard blocks ($\Delta C16 \approx 20$ mol%) as the ethylene/1-hexene OBCs of sections *2.1.1* and *2.1.2*, and at a variable w_s/w_h ratio. The copolymers have been synthesized in a series of PPR experiments of chain shuttling reactions using the following of experimental conditions: 100°C in alkane solution (3.5 mL total), 250 psi_g of ethylene pressure, 2.50 mL of C16 feeding per each individual reactor, [Zn]/[Cat2+Cat3] = 50. In all cases OBCs samples with $\Delta C16 \approx 20$ mol% have been obtained, characterized by w_s/w_h ratio equal to 80/20, 65/35, and 50/50.The total catalyst amount was always fixed to 15 nmol, however the catalysts ratio [Cat2]/[Cat3] changed throughout the series as follows: [Cat2]/[Cat3] = 8:1 for the OBCs with w_s/w_h = 80/20 (1.7 and 13.3 nmol of Cat3 and Cat2, respectively); [Cat2]/[Cat3] = 4:1 for the OBC with w_s/w_h = 65/35 (3 and 12 nmol of Cat3 and Cat2, respectively); [Cat2]/[Cat3] = 2:1 for the OBC with w_s/w_h = 50/50 (5 and 10 nmol of Cat3 and Cat2, respectively).

2.2. Sequential Fractionation Procedure

A sequential and exhaustive solvent fractionation procedure with a Kumagawa extractor has been applied to the commercial grades, using diethyl ether (T_{eb} = 34.6 °C), n-hexane (T_{eb} = 68 °C), and cyclohexane (T_{eb} = 80.7°C) as solvents. For the fractionation procedure, 1 g of each commercial OBC has been used. For every extraction step, about 100 mL of solvent are heated up to the boiling point. The system is kept under reflux for at least 8 hours, in order to reach the complete extraction of the soluble fraction. At the end of the extraction process, four fractions with increasing ethylene content are obtained consisting in an ether soluble fraction (sEE), an ether insoluble/n-hexane soluble fraction (iEE-sC6), a n-hexane insoluble/cyclohexane soluble fraction

(iC6-sCC6), and a cyclohexane insoluble fraction (iCC6). For each step of the sequential procedure, the solution containing the soluble fraction is first dried in a rotary evaporator and then kept overnight under vacuum to constant weight. The insoluble polymer fraction, in turn, is subjected to the successive extractions with a solvent of higher boiling temperature, up to obtain the last iCC6 fraction. The whole extraction protocol was repeated on three independent aliquots of each sample, in order to test the reproducibility and to obtain a larger quantity of each fraction for the successive characterization.

2.3. Solution ^{13}C NMR

Solution ^{13}C NMR spectra have been recorded using a Bruker Avance III 400 spectrometer equipped with a 5 mm high-temperature cryoprobe, on 45 mg mL^{-1} polymer solutions in tetrachloroethane-1,2-d_2 (with 0.40 mg mL^{-1} of 4-methyl-2,6-di-tert-butyl-phenol (BHT) added as a stabilizer). Acquisition conditions were: 45° pulse; 2.3 s acquisition time; 5.0 s relaxation delay; 1.5K transients. Broad-band proton decoupling has been achieved with a modified WALTZ16 sequence (BI_WALTZ16_32 by Bruker). Statistical analysis of the triad distributions, determined according to published methods,[82,83] has been carried out with the Copolstat software code.[84]

2.4. Gel Permeation Chromatography

Gel Permeation Chromatography (GPC) analysis has been performed using a Freeslate Rapid-GPC setup, with a set of two mixed-bed Agilent PLgel 10 μm columns and a Polymer Char IR4 detector. Calibration has been

performed with the universal method, using 10 monodisperse polystyrene samples (M_n between 1.3 and 3700 kDa).

2.5. Analytical Crystallization Elution Fractionation

Analytical Crystallization Elution Fractionation (aCEF) curves have been recorded with a Polymer Char setup, equipped with an IR5 detector, a dual capillary viscometer detector, and a column cooling unit, on 2.0 mg mL^{-1} polymer solution in orthodichlorobenzene, added with 0.40 mg mL^{-1} of BHT stabilizer.

2.6. Compression-molding

Compression-molded films (0.2-0.3mm thick) of ethylene-based multiblock copolymers have been prepared by melting the as-polymerized samples at 150°C between the heating platens of a press, by keeping them at this temperature for 5 min applying very low pressure to avoid preferred orientation in the film, and by cooling to room temperature through circulation of cold water in the press plates (estimated cooling rate ≈ 20°C/min).

2.7. Wide and Small Angle X-ray Scattering

X-ray powder diffraction (WAXS) profiles have been recorded in a θ-θ reflection geometry (with θ the halved scattering angle) using an automatic PANalytical Empyrean Diffractometer equipped with a PIXcel^{3D} detector and Ni filtered CuKα radiation (λ = 1.5418Å). The degree of crystallinity x_c(WAXS) has been evaluated, after subtraction of the background approximated by a straight line, as the ratio between the crystalline diffraction

area A_c and the total area of the diffraction profile A_t: $x_c(\text{WAXS}) = A_c/A_t$. The crystalline diffraction area A_c has been obtained by subtracting the diffraction halo of the amorphous phase A_a from the total area of the diffraction profile ($A_c = A_t - A_a$). For the commercial grades, the diffraction profile of the sEE fraction has been used to approximate the contribution of the amorphous phase, while for the home-made OBCs the amorphous diffraction halos have been obtained from the X-ray diffraction profiles of the molten samples recorded at high temperature. The profile of the melt has been translated along the *x*-axis to make the position of the maximum coincident with the 2θ value of the maximum of the amorphous phase at 25°C (2θ ≈ 19°).

SAXS patterns have been collected at room temperature with a compact small angle apparatus Anton Paar (SAXSess) in a linear collimation geometry, using the Cu Kα radiation. SAXS images have been recorded on film BAS-MS "Imaging Plate" (FUJIFILM) and digitalized by a digital reader Cyclone Plus (Perkin Elmer). The analysis has been performed on the compression-molded specimens. The SAXS data have been deconvoluted with the primary beam profile with help of the SAXSquant2D and SAXSquant1D softwares by Anton Paar, to calculate the equivalent mono-dimensional profiles that would be collected using a point collimation geometry (desmearing). After careful subtraction of the dark current, the empty sample holder, and of a constant background due to thermal density fluctuations, the SAXS data have been elaborated to extract lamellar parameters such as lamellar periodicity and thickness of the amorphous and crystalline layers, resorting also to the calculation of the interface distribution function and of the mono-dimensional self-correlation function of electron density fluctuations (see Appendix A1).

2.8. Differential Scanning Calorimetry

Calorimetric measurements have been performed with a differential scanning calorimeter (DSC-822) by Mettler Toledo, in a flowing N2 atmosphere at a scan rate of 10°C/min. As-polymerized samples, as well as melt crystallized compression-molded samples, have been first heated up to melting from -30°C to 180°C (first heating scan), then cooling from 180°C to -30°C (cooling scan) and finally heated again from -30°C to 180°C (second heating scan). The degree of crystallinity x_c(DSC) (= $\Delta H_m/\Delta H_{m0}$) has been evaluated as the ratio between the melting enthalpy of the sample ΔH_m and the thermodynamic melting enthalpy of a 100% crystalline polyethylene ΔH_{m0} = 293 J/g (a fixed value of the reference enthalpy was chosen in this case).[85] For the integration procedure, a linear baseline covering the entire temperature range of each exothermic/endothermic phenomenon was considered.

Self-nucleation and annealing (SNA)[86] and Successive self-nucleation and annealing (SSA)[87] experiments have been performed with the DSC-822 calorimeter. The SNA protocol has the following steps according to Ref. 86: a) the sample is heated up to 180°C at 10°C/min and is kept at this temperature for 5 min to erase the former thermal history; b) the sample is cooled to 25°C at 10°C/min, creating a standard crystalline state; c) the sample is then heated up to a self-seeding temperature T_s at 10°C/min and maintained for 5 min at the T_s (self-nucleation step); d) the sample is cooled down to 25°C at 10°C/min. Steps a-d are cyclically repeated for increasingly lower T_s. The adopted SNA protocol is shown in Scheme 1.

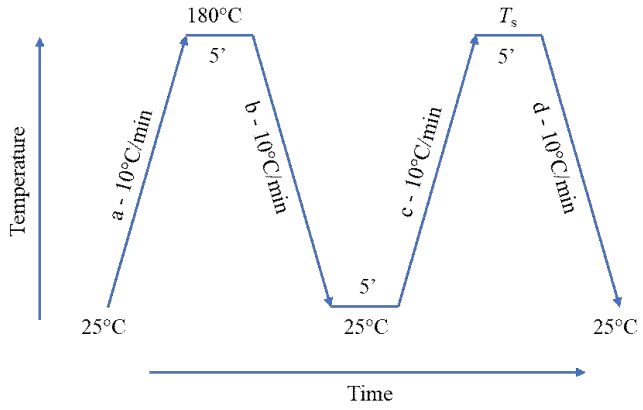

Scheme 1. SNA protocol adopted in the present thesis work.

The SSA procedure, following Ref. 87, have been performed in this way: a) the sample is heated up to 180°C at 10°C/min and held at this temperature for 5min; b) the sample is now cooled down to 25°C at 10°C/min, creating a standard crystalline state; c) the sample is heated to the ideal self-seeding temperature $T_{s\ ideal}$ at 10°C/min and kept for 3 min at this temperature; d) the sample is cooled to 25°C at 10°C/min; steps c and d are repeated for increasingly lower T_s, separated by 5°C, covering the melting range. At the end of the thermal fractionation, a melting scan is performed at 10°C/min up to 180°C. The adopted SSA thermal protocol is shown in Scheme 2.

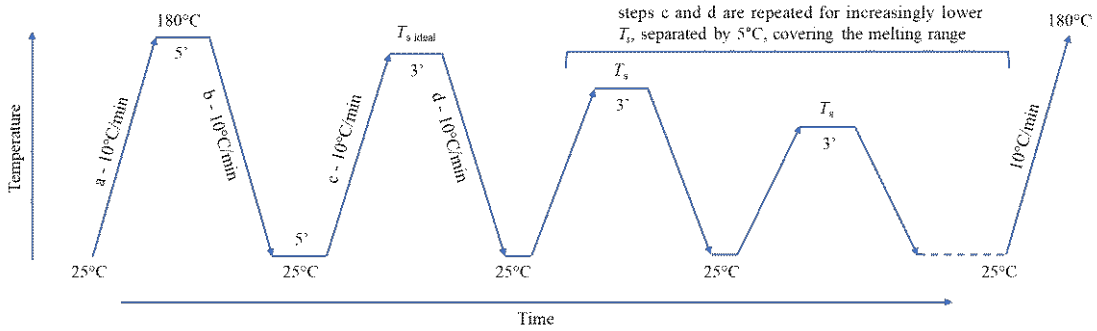

Scheme 2. SSA protocol adopted in the present thesis work.

The $T_{s\ ideal}$ of the SSA experiment is the temperature corresponding to the maximum self-nucleation density without the occurrence of annealing. It can be estimated by means of a SNA procedure. In particular, the criterion for the selection of the $T_{s\ ideal}$ was the occurrence of the annealing peak in the melting curve of step a in the SNA procedure (see above). Hence, if an annealing peak is detected in the endotherm of step a at a certain T_s, the immediately preceding self-seeding temperature is selected as $T_{s\ ideal}$.

For the deconvolution of the final multimodal endotherm of the SSA procedure, a baseline has been first subtracted to the DSC melting curve recorded at the end of the SSA protocol, and then the Peak Analyzer tool available in Origin with Gaussian fitting functions has been used. The final multimodal endotherms can be considered as the sum of Gaussian area functions allowing the calculation of the area under the melting peak of each thermal fraction (A_{fn}). The percentage area of each thermal fraction $A\%_{fn}$ is then calculated as $A_{fn}/A_{tot} \cdot 100$, where A_{tot} is the total area of the melting endotherm.

2.9. Stress-strain Curves

Mechanical tests have been carried out on rectangular specimens 5 mm wide, cut from the compression-molded films, with an Instron 5566H1543 electro-mechanical machine at room temperature and with a "Zwicky" mechanical tester by Zwick Roell equipped with a temperature-controlled chamber at 60°C and -15°C, following the standard test method for tensile properties of thin plastic sheeting ASTM D882-83. The deformation rate v (mm min^{-1}) has been set equal to 10 L_0 and 0.1 L_0 (with L_0 the initial distance between two benchmarks drawn on the unstretched samples in the transversal

direction perpendicular to the gauge length) to measure the mechanical properties up to the break and the Young's modulus, respectively. The permanent deformation achieved by the specimens after break (tension set at break, t_b) has been determined following the ASTM standard D412-8. Accordingly, 10 min after breaking, the two broken pieces have been fit closely together along the fracture line and the distance between two benchmarks L_r have been measured. The tension set has been determined as $t_b = (L_r - L_0)/L_0$. The stress-strain curves and the values of the mechanical parameters have been obtained as a result of at least five independent, reproducible experiments and successive averaging.

2.10. X-ray 2D Diffraction Data of Oriented Fibers

2D fiber diffraction patterns have been collected at room temperature and at -15°C with an automatic Bruker-Nonius Kappa CCD diffractometer (using Mo Kα1 radiation, λ = 0.70926Å), equipped with an Oxford 600 series Cryostream liquid N_2 cooler unit, and recorded on an area detector. The distance between sample and detector has been fixed equal to 100 mm. Oriented fibers have been obtained by stretching compression-molded rectangular specimens, 5 mm wide and 0.2-0.3 mm thick, using a hand-made dynamometer up to selected values of deformation ε (0%, 400%, 1000%). The deformation ε is defined as $100\cdot(L_f - L_0)/L_0$ where L_0 and L_f are the initial and final distances, respectively, between two benchmarks drawn on each specimen perpendicularly to gauge length. For each temperature (25°C and -15°C), a single specimen has been stretched at increasing values of deformation ε (0%, 400%, 1000%), making sure that the area of the specimen in-between the two benchmarks and involved in the deformation was always

illuminated by the focused X-ray beam and facing the N_2 cooling flux coming from the nozzle of the cooling unit (the latter in the case of the -15°C measurements). X-ray 2D diffraction patterns have been recorded as well on the relaxed fibers after the removal of tension from the maximum elongation. The 2D diffraction patterns have been analyzed with the FIT2D software (available online at http://www.esrf.fr/computing/scientific/FIT2D). Mono-dimensional X-ray intensity profiles as a function of 2θ have been obtained from the 2D diffraction patterns by integrating the intensity along the azimuthal angle. X-ray intensity profiles as a function of the azimuthal coordinate χ have been also obtained by integrating the intensity along the azimuthal angle at selected values of 2θ (9.9° and 11°, corresponding to (110) and (200) reflections of PE).

2.11. Transmission Electron Microscopy

Transmission Electron Microscopy (TEM) analysis has been carried out with a FEI TECNAI G2 200 kV TEM apparatus equipped with a 4K Eagle CCD Camera, operating at a voltage of 120 kV. Thin films of uniform thickness (50 - 70 nm) have been prepared by drop-casting 0.5wt% solutions of OBCs in p-xylene on glass slides. The so-obtained films, after solvent evaporation, have been melted at 180 °C, kept at this temperature for at least 5 min, and then crystallized by cooling to 25 °C at 10 °C/min. The films have been then covered with carbon, removed from the glass slides, floated on distilled water, and transferred to 200 mesh grids. Finally, prior to TEM observation, the grids have been exposed to RuO_4 vapors to selectively mark the amorphous fraction and enhance the morphological features, by introducing contrast between the involved phases.

2.12. Rheological Measurements

Rheological measurements have been carried out by the collaborating Laboratory of Soft Matter, Complex Fluids and Rheology (LSMR) of Professor Grizzuti at the Department of Chemical, Materials, and Industrial Engineering of the University of Naples "Federico II". Rheological tests have been performed on a Physica MCR702 (Anton Paar) in single-motor configuration equipped with 25 mm parallel plates and a convection oven for temperature control (CTD 450). Nitrogen atmosphere was used to prevent thermal degradation of the samples. The samples have been shaped to discs having thickness of 1–2 mm and diameter of 8 mm by means of vacuum compression molding. Dynamic measurements have been performed in the range from 100 rad/s to 0.03 rad/s. The applied strain was such that linear regime was insured at all temperatures. Besides dynamic tests, creep measurements have been performed in order to extend the range of probed timescales. The applied stress was such that creep tests were in linear regime. The conversion of the creep compliance into viscoelastic moduli have been performed using a NLReg software based on the Tikhonov regularization method. The time-temperature superposition principle has been used to build master curves of the viscoelastic moduli. Dr. Salvatore Costanzo is kindly acknowledged for the rheological tests.

2.13. Solid-state NMR

Solid-state NMR experiments have been performed with a Bruker 400 MHz standard bore NMR spectrometer, equipped with a AVANCE III HD

console, a BCU 1 (-40 to 50°C) variable temperature unit, and a 3.2 mm triple resonance magic angle spinning (MAS) probe.

2.13.1. ^{13}C single pulse high-power decoupling experiment

The acquisition conditions for the high-power decoupling single pulse ^{13}C experiments are: 90° pulse duration of 1.5 μs, 40.96 ms acquisition time, 3.0 s relaxation delay.

2.13.2. ^{13}C INEPT-MAS experiment

For the INEPT (Insensitive Nuclei Enhanced by Polarization Transfer) experiment, observing highly mobile components under MAS conditions, the following parameters have been used: a 3 s relaxation period, a 90° and 180° ^{1}H and ^{13}C pulses of, respectively, 4 μs and 8 μs, an inter-pulse delay optimized to $1/(4\ {}^{1}J_{CH})$ (1.72 ms), and a refocusing delay optimized to $1/(6\ {}^{1}J_{CH})$ (1.15 ms). The synchronization between the MAS frequency and the INEPT delays is not required.

2.13.3. ^{13}C CP MAS experiments

For the ^{1}H-^{13}C cross polarization (CP) experiments, the ^{1}H 90° pulse length was 2.5 μs, while a contact time of 6.5 ms and a recycle delay of 5s have been used. All the experiments were performed at room temperature (25°C). The MAS speed has been set to 10 kHz.

2.13.4. 2D WISE NMR experiments

For the 2D WISE NMR experiments, the ^{1}H 90° pulse length was 4 μs. The CP contact time was 300 μs to minimize the spin diffusion, and the relaxation delay was 2 s.

2.13.5. Relaxation experiments

For the ^{13}C T_1 relaxation experiments following the CP inverse recovery method (a modified Torchia experiment, using Bruker pulse sequence cpxt1), a cross-polarization step with a contact time of 6.5 ms has been used, along with 90° ^{13}C pulses of 2.4 μs. The selected values of relaxations delays are the following: 0.001, 0.07, 0.2, 0.3, 0.4, 0.5, 0.8, 1, 1.25, 1.5, 1.75, 2, 2.25, 2.5 and 3 s.

2.13.6. Spin diffusion with dipolar filters

For spin diffusion with dipolar filter experiments, loops of a 12-pulse dipolar filter have been applied to select the magnetization from the mobile phases. The strength of the filter can be enhanced by increasing the delay time *t* between the pulses or by increasing the number of loops. Several delay times have been tested associated with increasing number of loops, namely: 10 μs and 1 loop; 10 μs and 3 loops; 12 μs and 1 loop; 12 μs and 3 loops. Best results have been obtained using 12 μs and 1 loop as parameter of the filter. All the dipolar filter experiments have been recorded at room temperature.

Spin diffusion experiment has been performed with the above-mentioned dipolar filter parameters, 6.5 ms as contact time, and 4 μs as ^{1}H 90° pulse length. The spin diffusion with dipolar filter experiments have been recorded

at 25°C (298K) and 45°C (318K). Mixing times of increased length have been selected: 0.00001, 0.002, 0.005, 0.01, 0.02 and 0.05 s.

3. Structural Characterization of Ethylene/ 1-Octene Commercial Multiblock Copolymers

As already stated in Chapter 1, ethylene/1-octene multiblock copolymers synthesized by Chain Shuttling Technology (OBCs) consist of a complex mixture of chains having different block lengths and number of blocks. The first part of this work has been devoted to an extensive investigation of the inter- and intrachain constitutional heterogeneity of these materials, as well as of the distribution of crystallizable methylene sequences, in order to provide a description of the multivariate distribution of the molecular mass of the blocks and of the number of blocks/chains that characterizes the complex chain architecture of OBCs.

Five commercial grades (Infuse^{TM}) provided by The Dow Chemical Company have been selected as benchmark samples, because they represent the "classical" example of multiblock copolymers synthetized through the chain shuttling process;[56] in addition, they are available in large amount, allowing to set up and test different experimental and semi-empirical tools aimed at assessing the non-uniform polydisperse microstructure of the chains, that characterizes these complex systems.

The main features of the set of Infuse^{TM} grades, such as molecular mass, fraction of hard blocks, total amount of octene, are reported in Table 1. For all the five samples, the octene content in the hard HDPE-like block and in the soft amorphous block is 0.5 mol% (2 wt%) and 19 mol% (48.3 wt%), respectively.

Table 1. Melt flow index, density, number and mass average molecular masses M_n and M_w, polydispersity index Đ (=M_w/M_n), total amount of octene units x_O, and fraction of hard blocks w_h for the five commercial grades selected as model.

Sample ID	MFI (g/10min)	density (g/cm^3)	M_n (kDa)[a]	M_w (kDa)[a]	Đ	x_O (wt%)[b]	x_O (mol%)[b]	w_h (wt%)
Sample 1	0.5	0.877	60	155	2.6	38.4	13.1	27.7
Sample 2	1	0.877	56	134	2.4	37.8	12.8	27.5
Sample 3	5	0.877	33	86	2.6	36.9	12.4	29.6
Sample 4	15	0.877	17	71	4.3	38.4	13.1	23.5
Sample 5	0.5	0.866	70	177	2.5	41.4	14.6	15.4

a. From GPC analysis. b. From solution ^{13}C NMR analysis.

3.1. In-depth Analysis of the Non-uniform Chain Microstructure through Solvent Fractionation

To account for the interchain and intrachain non-homogeneous constitution, a sequential and exhaustive fractionation procedure with solvents of increasing boiling temperature has been carried out in a Kumagawa extractor as detailed in Chapter 2. The used solvents are diethyl ether (T_{eb} = 34.6°C), *n*-hexane (T_{eb} = 68°C) and cyclohexane (T_{eb} = 80.7°C). Four fractions of increasing average ethylene content, hard block content, and degree of crystallinity, that is a fraction soluble in diethyl ether (sEE), a fraction insoluble in diethyl ether/soluble in *n*-hexane (iEE-sC6), a fraction insoluble in *n*-hexane/soluble in cyclohexane (iC6-sCC6), and a fraction insoluble in cyclohexane (iCC6) were obtained. The analyses were focused on two representative samples, namely Samples 1 and 3, and the corresponding fractions. The results of solvent fractionation, GPC, solution ^{13}C NMR analysis, and aCEF characterization on the unfractionated Samples 1 and 3 and

the corresponding fractions are reported in Tables 2, 3. The aCEF curves are shown in Figure 1, whereas the X-ray powder diffraction profiles and the DSC thermograms are reported in Figures 2, 3. The thermal data extracted from DSC analysis are reported in Table 4.

The results of the chain microstructural analysis indicate that the unfractionated samples and the corresponding fractions show a molecular masses dispersity index in the range 2.1-2.6 and that the molecular masses of the fractions iC6-sCC6 and iCC6 are similar to those of the corresponding unfractionated samples ($M_w \approx$ 160-165 and $\approx$ 93 kDa for the Samples 1 and 3, respectively), whereas they are halved for the sEE and iEE-sC6 fractions ($M_w \approx$ 50-75 and 40-55 kDa for the Samples 1 and 3, respectively). It should also be considered that although the two raw samples feature similar 1-octene incorporation (12.4 mol% for Sample 1 vs. 13.1 mol% for Sample 3) and weight fraction of hard blocks (25 wt% for Sample 1 vs. 27 wt% for Sample 3), the distribution of the fractions is somewhat different. The major differences occur for the relative amount of the iC6-sCC6 and iCC6 fractions ($\approx$ 50 and 35 wt% for Sample 1 vs. $\approx$ 78 and 5 wt% for Sample 3). These differences cannot be ascribed to different 1-octene incorporation x_O and/or hard block content w_h, as these quantities are similar for the two samples (see Table 2).

Table 2. Relative amount of the extracted fractions from the Samples 1 and 3, and corresponding values of the average content of octene units x_O, weight fraction of the hard blocks w_h, number average M_n and mass average M_w molecular mass, dispersity index Đ (=M_w/M_n), average crystallinity index extracted from WAXS data of Figure 2 x_c(WAXS), and crystallinity index relative to the sole hard blocks $x_c(WAXS)/w_h$.[85,88] Data relative to the unfractionated samples are also reported.

Sample	wt%	x_O (mol%)	w_h (wt%)	M_n (kDa)	M_w (kDa)	Đ	x_c(WAXS) (%)	$x_c(WAXS)/w_h$ (%)
1-unfractionated	/	13.1	24.9	60	155	2.6	12	48
1-sEE	7.5	20.1	*	20	52	2.6	<1	-
1-iEE-sC6	6.7	19.1	4.2	33	75	2.2	≈2	≈47
1-iC6-sCC6	50.5	13.2	27.2	68	158	2.3	16	59
1-iCC6	35.3	12.9	30.7	74	166	2.2	16	52
3-unfractionated	/	12.4	26.9	33	86	2.6	14	52
3-sEE	9.2	20.3	*	16	40	2.6	<3	-
3-iEE-sC6	7.9	18.3	11.5	26	55	2.1	5	43
3-iC6-sCC6	78.2	12.5	26.7	39	94	2.4	19	71
3-iCC6	4.7	11.9	28.2	40	93	2.3	19	67

* not detected

To gain further information on the non-uniform chain microstructure of the commercial ethylene/1-octene copolymers, the unfractionated samples and the corresponding fractions have been characterized with analytical crystallization elution fractionation (aCEF). The aCEF traces are reported in Figure 1, whereas the elution temperature and the relative amount of the completely amorphous component (AF), eluting at subzero temperature, are reported in Table 3.

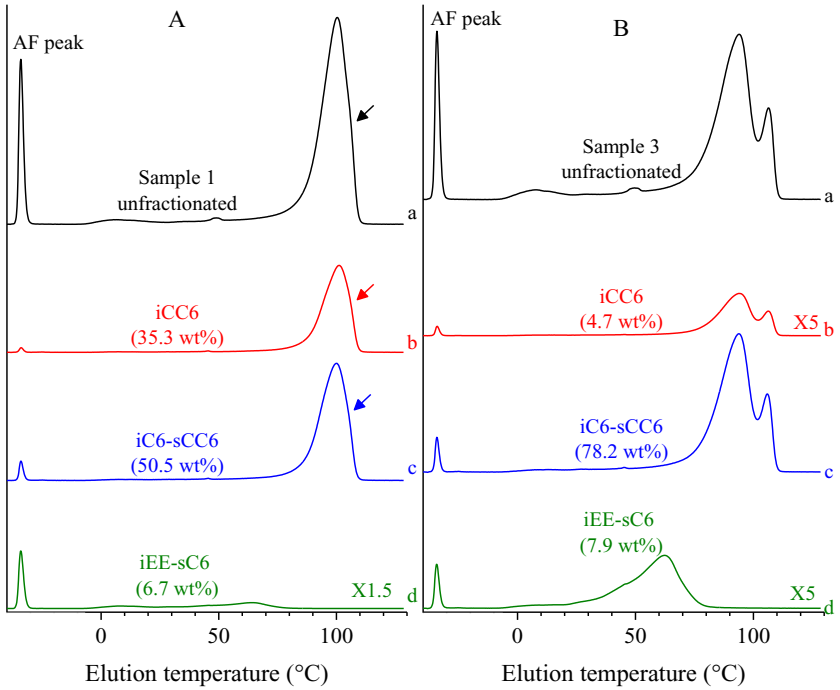

Figure 1. aCEF traces of the Samples 1 (A) and 3 (B) and of the corresponding fractions. The areas behind the curves of the fractions are normalized to the area of the unfractionated sample times the percentage of the corresponding fraction and a suitable amplification factor equal to 1.5 (d in A) and 5 (b and d in B). The arrows in A indicate a faint shoulder of the main elution peak (see Table 3). The aCEF traces of the sEE fractions are not reported as they show the sole AF peak at sub-zero temperature.

The aCEF curves of the unfractionated samples show the presence of crystalline components eluting at ≈ 100°C with a faint shoulder at ≈ 104°C for Sample 1 (curve a of Figure 1A), and at ≈ 94°C and 107°C for Sample 3 (curve a of Figure 1B). Both samples contain ≈ 10 wt% of an amorphous or scarcely crystalline component (AF component in Table 3), and less than 7 wt% of a slightly crystalline component eluting in the temperature range 0-80°C, with a not well pronounced maximum at ≈ 60°C.

Table 3. Data extracted from the aCEF elution curves of Figure 1.

Sample	AF (wt%)	T_{el} (°C)	M_H (kDa)	M_S (kDa)	$[M_H\text{-}M_S]_n$**
1-unfractionated	11.3	100.3; 105.9	1.6; 3.0	4.0; 5.7	$[2H\text{-}4S]_{11}$; $[3H\text{-}6S]_7$
1-sEE*	100	-	-	20	$[20S]_1$
1-iEE-sC6	53.5	64.2	0.3	6.2	$[0.3H\text{-}6S]_5$
1-iC6-sCC6	2.4	99.9; 105.2	1.5; 2.9	3.5; 6.8	$[2H\text{-}4S]_{14}$; $[3H\text{-}7S]_7$
1-iCC6	1.0	101.1; 106.1	1.6; 3.1	3.2; 6.1	$[2H\text{-}3S]_{15}$; $[3H\text{-}6S]_8$
3-unfractionated	10.0	93.9; 106.9	1.0; 2.7	2.4; 6.5	$[1H\text{-}2S]_{10}$; $[3H\text{-}7S]_4$
3-sEE*	100	-	-	16	$[16S]_1$
3-iEE-sC6	7.0	62.3	0.3	1.9	$[0.3H\text{-}2S]_{12}$
3-iC6-sCC6	3.0	93.8; 106.4	1.0; 2.7	2.2; 5.9	$[1H\text{-}2S]_{12}$; $[3H\text{-}6S]_5$
3-iCC6	2.0	94.0; 106.4	1.1; 2.7	2.1; 5.4	$[1H\text{-}2S]_{13}$; $[3H\text{-}5S]_5$

*The sEE fraction shows the sole AF peak at sub-zero temperature indicating that it is almost completely amorphous. This fraction essentially consists of soft blocks not linked to hard blocks or linked to very short hard blocks.

**The values of M_H and M_S in the square brackets are in kDa; the apparent value of the number of HS repetition units of an equivalent regular chain including HS units of only one length n is calculated as $n = M_n/(M_H+M_S)$.

The sEE fractions are both completely amorphous as they mainly consist of a truly random ethylene/1-octene copolymer with a 1-octene content of 20 mol% (Table 2). The iEE-sC6 fractions differ significantly for the AF content (50.5% and 7 wt% in the iEE-sC6 fractions of Sample 1 and Sample 3, respectively), in line with the fact that the hard block content w_h is ≈ 4 and 11% for the iEE-sC6 fractions of the Samples 1 and 3, respectively (Table 2). Since they both show a scarcely crystalline fraction eluting at 62-64°C, it can be inferred that these fractions consist mainly of soft segments linked to short hard segments able to crystallize. The aCEF profiles of the iCC6 and iC6-sCC6 fractions (curves b and c of Figure 1) show faint AF peaks (1-3 wt%), no elution peaks in the temperature range 0-80°C and high temperature elution

peaks, resembling those of the unfractionated samples (Figure 1 and Table 3). In particular, the double elution peaks at high temperatures suggest that the iCC6 and iC6-sCC6 fractions contain at least two populations of chains consisting of hard blocks of different length alternating with soft blocks, where the hard blocks are long enough to account for the formation of well-developed polyethylene (PE)-like crystals melting at ≈ 120-124°C, as shown in the X-ray diffraction profiles and DSC thermograms of Figures 2 and 3.

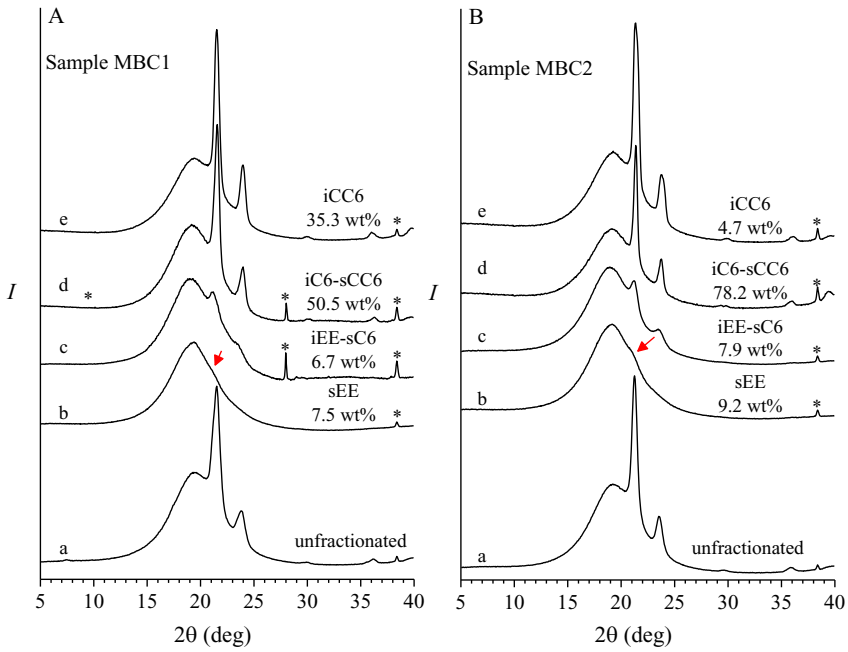

Figure 2. X-ray powder diffraction profiles of the unfractionated Samples 1 (A), 3 (B) (pellets) and of the corresponding (as recovered from extracting solvent) fractions. The starred peaks are due to catalyst/co-catalyst remnants. The arrows point at the 110 reflection of a small population of crystals in the orthorhombic form of polyethylene present in the sEE fraction.

Therefore, the aCEF results of Figure 1 and Table 3 allow assessing that for the unfractionated samples, the low-temperature elution peak at sub-zero temperatures is ascribable to the sEE fraction, the broad elution peak in the range 0-80°C is ascribable to the low-crystalline fraction iEE-sC6, whereas the

high-temperature elution peaks are due to the most crystalline fractions iC6-sCC6 and iCC6.

The results of the structural analysis (Figures 2-3, Table 4) essentially confirm the results obtained from aCEF measurements. The diffraction profiles of Figure 2 show that the unfractionated samples and the corresponding iCC6 and iC6-sCC6 fractions crystallize in the orthorhombic form of polyethylene (PE), as indicated by the well pronounced 110 and 200 reflections at $2\theta = 21.4°$ and 24°, overlaying an amorphous halo centered at $2\theta \approx 19°$ (curves a, d, e of Figure 2). The 110 and 200 reflections are less pronounced for the iEE-sC6 fractions (curves c of Figure 2), whereas for the sEE fractions only the 110 reflection appears as a faint shoulders (curves b of Figure 2), indicating that these fraction are fairly less crystalline and/or almost completely amorphous in the case of the sEE fractions.

The results of thermal analysis indicate that the fractions showing the highest degree of crystallinity, i.e., the iC6-sCC6 and the iCC6 fractions, present sharp melting and crystallization peaks, at around 121°C, 123°C and 99°C, 103°C, respectively, for Sample 1, and 121°C, 124°C and 107°C, 108°C, respectively for Sample 3, the melting and crystallization temperatures of the iCC6 fractions being slightly higher than those of the iC6-sCC6 fractions (Figure 3 and Table 4). This confirms that these fractions possess long hard blocks able to crystallize in well-developed lamellar crystals of PE, and that the lamellar crystals present in the iCC6 fractions are on average thicker than those present in the iC6-sCC6, fractions. The unfractionated samples possess instead melting and crystallization temperatures in between those of the corresponding iC6-sCC6 and the iCC6 fractions. The iEE-sC6 fractions of Samples 1 and 3 show melting peaks at ≈ 100°C and crystallization peaks at ≈ 70°C, coherently with the presence of hard segments of short length

crystallizing in tiny lamellar crystals (Figure 3 and Table 4). Finally, the sEE fractions show shallow melting endotherms at 34°C and 55°C for Samples 1 and 3, respectively, (Figure 3 and Table 4) due to the crystallization of long ethylene sequences in the soft blocks and/or of hard blocks of very short length, formed as a result of the rapid exchanges of the chains between the active metal centers of the catalysts and the CSA.

Therefore, in agreement with the aCEF results, the main differences between the iEE-sC6 fraction melting at around 100°C and the iC6-sCC6 and iCC6 fractions melting at around 120°C, reside in the average length of the hard blocks, that is chains characterized by a prevalence of short hard blocks (0.3 kDa) melting at ≈ 100°C, whereas chains with a prevalence of long hard blocks of average molecular mass higher than or equal to 3-4 kDa, melting at ≈ 120°C.

Table 4. First (T_{mI}) and second melting temperatures (T_{mII}), crystallization temperatures (T_c) and corresponding enthalpies (ΔH_{mI}, ΔH_{mII}, and ΔH_c) of the Samples 1 and 3 and of the corresponding fractions.

Sample	wt%	T_{mI} (°C)	T_c (°C)	T_{mII} (°C)	ΔH_{mI} (J/g)	ΔH_c (J/g)	ΔH_{mII} (J/g)
1-unfractionated	/	122.5	96.9	120.2	36.4	37.1	38.1
1-sEE	7.5	40.7	/	33.7	5.3	/	1.8
1-iEE-sC6	6.7	103.4	73.4	103.9	13.0	12.1	10.7
1-iC6-sCC6	50.5	120.9	99.1	120.1	47.2	41.8	42.1
1-iCC6	35.3	123.5	103.3	120.6	43.2	37.8	41.3
3-unfractionated	/	123.7	99.2	122.7	34.7	43.7	38.7
3-sEE	9.2	39.3	/	54.6	6.5	/	4.8
3-iEE-sC6	7.9	103.5	75.4	103.5	14.3	11.8	11.0
3-iC6-sCC6	78.2	121.3	107.1	122.6	53.8	48.0	49.1
3-iCC6	4.7	124.3	108.2	123.5	51.3	46.9	48.6

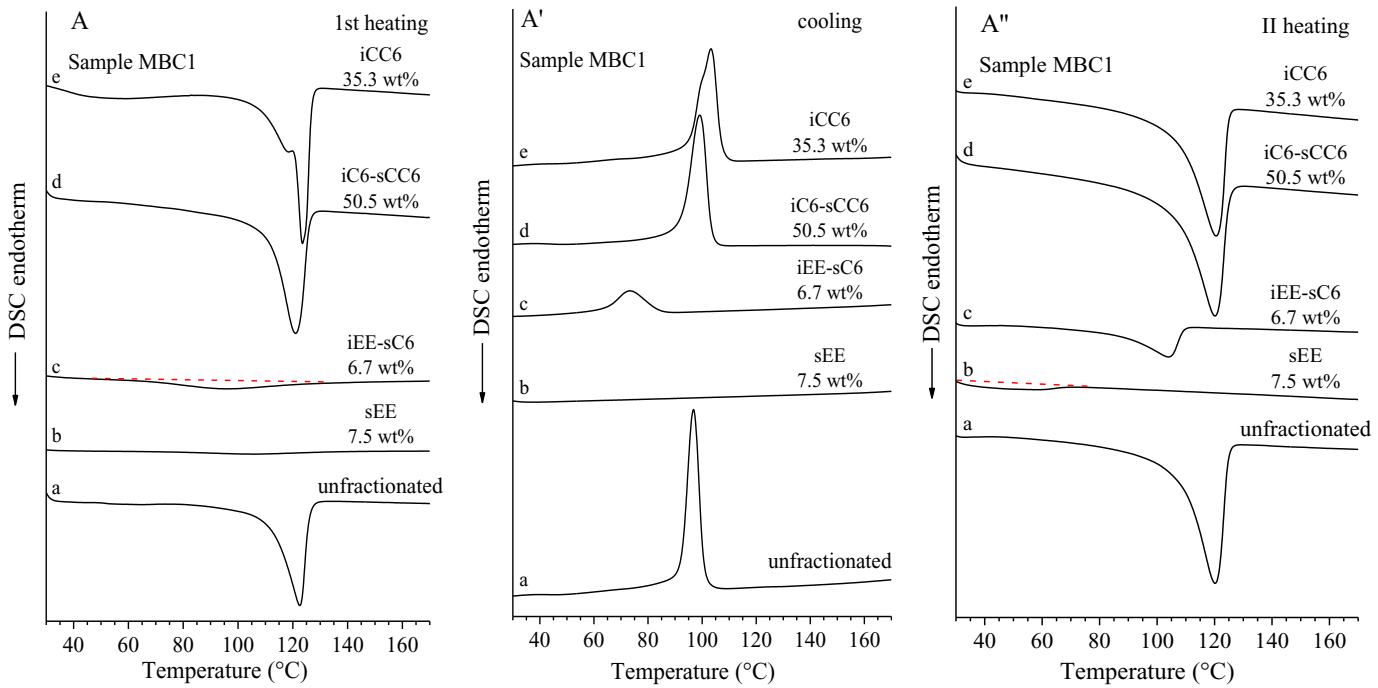
A
1st heating
Sample MBC1
iCC6
35.3 wt%
iC6-sCC6
50.5 wt%
iEE-sC6
6.7 wt%
sEE
7.5 wt%
unfractionated
DSC endotherm
Temperature (°C)
A'
cooling
Sample MBC1
iCC6
35.3 wt%
iC6-sCC6
50.5 wt%
iEE-sC6
6.7 wt%
sEE
7.5 wt%
unfractionated
DSC endotherm
Temperature (°C)
A"
II heating
Sample MBC1
iCC6
35.3 wt%
iC6-sCC6
50.5 wt%
iEE-sC6
6.7 wt%
sEE
7.5 wt%
unfractionated
DSC endotherm
Temperature (°C)

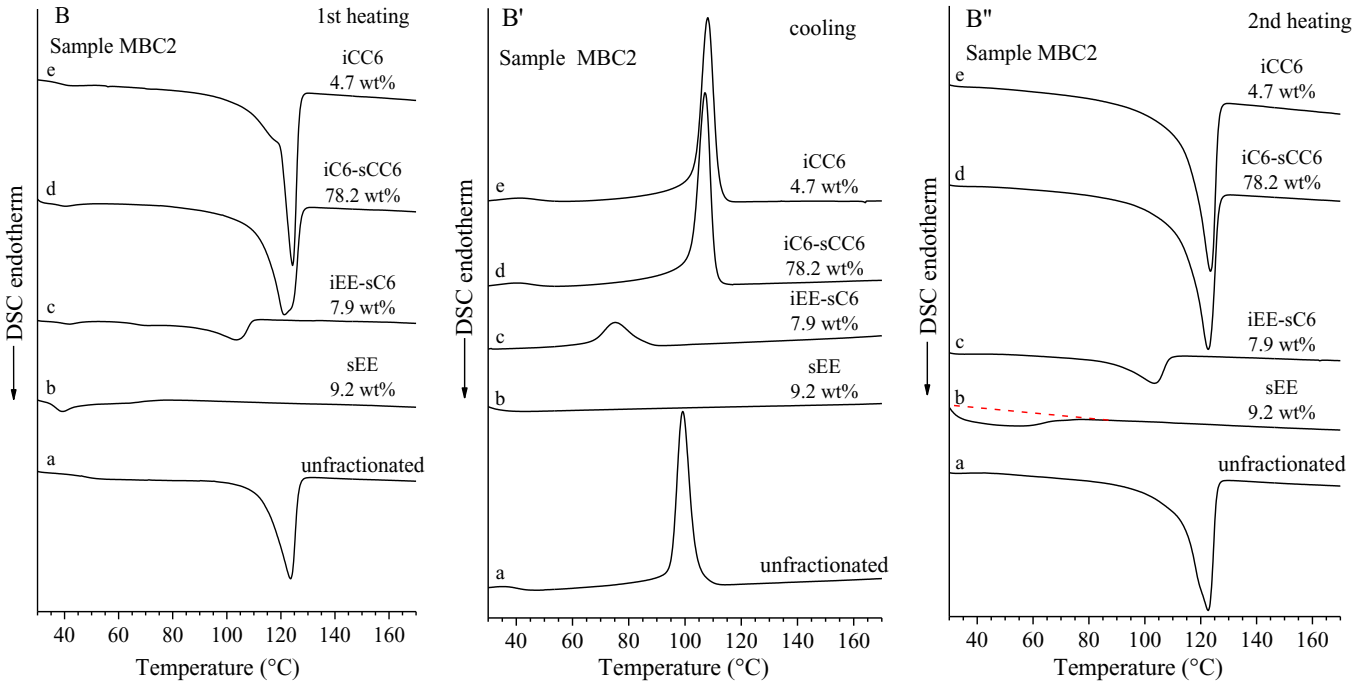

Figure 3. DSC thermograms recorded during the 1st heating (A, B), cooling (A', B') and 2nd heating (A'', B'') scans, at 10°C/min for the unfractionated Samples 1 (A, A', A'') and 3 (B, B', B'') and the corresponding fractions. The dashed lines in A, A'', and B'' outline broad endothermic peaks of the iEE-sC6 and sEE fractions of Sample 1 and of the iEE-sC6 fraction of Sample 3.

Using the approach described in Ref. 58, the values of the average molecular mass and number of blocks per chain of ethylene/1-octene multiblock copolymers may be calculated using the aCEF results. The method relies on a simple one-to-one relationship of the elution temperature of the chains with the average length of crystallizable ethylene sequences in (model) random copolymers eluting at the same temperature. In particular, assuming that the elution temperature T_{el} is only related to the length of the ethylene sequences in the hard blocks and using a correlation plot (obtained with a series of random copolymers of ethylene with different 1-hexene and/or 1-octene content), the number average molecular mass of the hard (M_H) and soft (M_S) ($M_S = M_H\,(1- w_H)\,w_H^{-1}$) blocks included within the HS building units consisting of a hard and a soft blocks linked together are calculated from the values of T_{el} of the relevant aCEF peaks. The so obtained values of M_H and M_S are reported in Table 3. Accordingly, considering that, on average, the mass of a HS building unit is M_H+M_S, the number of blocks n constituting an equivalent chain including exclusively these building units is also calculated as $n = M_n/(M_H+M_S)$. Hence, the chains of the unfractionated samples and of the corresponding fractions may be indicated through the code $[M_H\text{-}M_S]_n$, to address that they may be described in terms of an equivalent regular chain architecture including n HS repetition units, expected to elute at the same temperature of the aCEF peaks. The so-coded average composition of the unfractionated samples and of the fractions are also reported in Table 3. As discussed before, since the sEE fractions of Samples 1 and 3 include chains made up almost exclusively of soft blocks, they are coded in Table 3 as $[20S]_1$ and $[16S]_1$, where 20 and 16 kDa coincide with the M_n value of the whole fraction, respectively (Table 3). The iEE-sC6 fractions of Samples 1 and 3, instead, include chains containing 5 and 12 HS building units, respectively,

with $M_H \approx 0.3$ kDa, and $M_S \approx 6$ kDa and 2 kDa, respectively ($[0.3H\text{-}6S]_5$ and $[0.3H\text{-}2S]_{12}$, respectively). The iC6-sCC6 fractions feature two populations of chains, that are slightly different for the two samples, coded as $[2H\text{-}4S]_{14}$, $[3H\text{-}7S]_7$ for Sample 1 (curve c of Figure 1A), and $[1H\text{-}2S]_{12}$, $[3H\text{-}6S]_5$ for Sample 3 (curve c of Figure 1B). The same holds for the iCC6 fractions also, that consist of chains coded as $[2H\text{-}3S]_{15}$ and $[3H\text{-}6S]_8$ for Sample 1, and $[1H\text{-}2S]_{13}$, $[3H\text{-}5S]_5$ for Sample 3 (Table 3). From Table 3, it is also apparent that for the unfractionated sample the molecular mass of the HS building units included in the chains eluting at high temperature is in between those included in the chains eluting in the same temperature range for the iC6-sCC6 and iCC6 fractions.

It is worth noting that the two populations of chains, constituted by HS building units of different average length, cannot be separated by extraction with boiling solvents since they are present in both the iC6-sCC6 and the iCC6 fractions. This may suggest that the multi-block chain architecture arising from the stochastic exchange process of the CSA with the two catalysts entails not only a non-uniform interchain distribution of the length of hard and soft blocks but also a non-uniform intrachain distribution. The chains included in the superior fractions, indeed, include hard blocks alternating with soft blocks of different length. It may be inferred that within each fraction, the chains characterized by a major content of long soft blocks and/or a minor content of short hard blocks elute at lower temperature. Furthermore, within each sample, the chains eluting around the same temperature belonging to the iC6-sCC6 are characterized by a major content of long soft blocks and/or of short hard blocks than those belonging to the iCC6 fractions.

Furthermore, it is also worth noting that the molecular description of the chain constitution deduced from aCEF measurements does not take into account the possible presence of long HS building units, since chains including

hard blocks of length above a threshold value are expected to elute at the same temperature.[58] Therefore, the values of M_H and M_S deduced from aCEF data should be considered as a sort of lower bound of the distribution of the molecular mass of the hard and soft blocks in the superior fractions (iCC6 and iC6-sCC6). The presence of a significant concentration of long HS building units in the OBC chains is indicated by the mesophase separated morphologies often observed in the solid state by transmission electron microscopy (TEM) images[72,75] and by the occurrence of fluctuations of concentration of the hard and soft blocks at length scales larger than the coil size, causing failure of the time-temperature superposition at low frequency in melt rheology measurements.[73,75]

In order to reach a complete description of the chain architecture, SAXS measurements of melt crystallized samples have been exploited with the aim to extract relevant information about the structural organization of the chains at lamellar length scale. In particular, the rationale of this approach lies on the observation, emerged from small angle neutron scattering experiments of partially deuterated samples, that the square root of the mean squared value of the gyration radius R_g of the polymer chain changes only slightly by effect of crystallization from the melt, regardless of the cooling rate.[89-93] This observation can be explained resorting to the so-called "Erstarrungsmodell" (i.e., solidification model) entailing that the chains, upon crystallization, do not experience relevant diffusion processes in the long-range; rather, they are subjected to straightening,[89-91] through the establishment of significant intramolecular associations already in the undercooled melt.[92,93] In particular, since R_g scales as the square root of the average molecular mass $M^{1/2}$, by comparing the values of the lamellar periodicity (long spacing) L extracted from SAXS measurement and those of $M^{1/2}$ for some PE samples crystallized

under similar conditions, a linear relationship has been empirically established between L and $M^{1/2}$ ($\equiv R_g$).[94,95] It is worth noting that since the values of the thickness of lamellar crystals l_c are independent of the molecular mass, as they depend only on the crystallization conditions, a linear relationship holds also between the values of the thickness of the interlamellar amorphous layers l_a (= L - l_c) and $M^{1/2}$. It has been argued that the observed scaling relationships originate from the balance between two effects. The first effect derives from the enthalpy gain achieved by inclusion of consecutive polymer segments along the chain within growing crystals placed at separation distance $L \approx R_g$. The second effect derives from the consequent energy penalty experienced by the connecting amorphous segments, the relaxation and/or disentanglement of which is prevented by the too fast crystallization of the adjacent stems. As a consequence, the amorphous chains in the interlamellar regions are frozen in a state of non-equilibrium.[94,95] In particular, for PE samples crystallized from the melt at (relatively) fast cooling rates, namely ≥30 °C/min, the following relationship has been found between l_a and a suitable average value of the molecular mass M_g:

$$l_a = k_1 + k_2 M_g^{1/2} \quad (1)$$

In Equation 1, the value of k_1 is equal to 1.2 nm for PE samples with molecular mass higher than 10 kDa and is expected to extrapolate to zero for samples with M_n lower than 10 kDa. The value of k_2, instead, is 0.04 Da^{-1} nm, whereas the quantity M_g is defined by the mean:

$$M_g = \left(\sum_i w_i M_i^{\frac{1}{2}} \right)^2 \quad (2)$$

where w_i represents the weight fraction of chains with molecular mass M_i. According to Equation 2, the values of M_g are in between the values of the number (M_n) and mass (M_w) average molecular masses.[94,95] Therefore, in the

hypothesis that for the unfractionated samples and the corresponding most crystalline iCC6 and iC6-sCC6 fractions the crystallization of the hard blocks occurs in well separated domains, with little or no inclusion of the soft blocks in the interlamellar amorphous layers, the values of l_a extracted from SAXS data analysis may be used in Equation 1, to obtain the values of the average molecular mass of the hard blocks M_H. Upon further elaborations according to the method of Ref. 78, the values of the average molecular mass of soft blocks M_S in a HS building unit may be also determined. For the low crystalline iEE-sC6 and sEE fractions, instead, which are characterized by the formation of sporadic crystals organized in small sheafs, the inclusion of soft blocks in the interlamellar amorphous regions may not be excluded, making the use of Equation 1 and the method of Ref. 78 not applicable.

The SAXS profiles before and after correction for the Lorentz factor relative to the compression molded films of the unfractionated samples and of the corresponding fractions are shown in Figures 4 and 5, respectively. The fractions iEE-sC6 and sEE show SAXS profiles with broad or no humps (curves d, e of Figure 4). After correction for the Lorentz factor, the iEE-sC6 fractions of both samples (curves d of Figure 5) and the sEE fraction of Sample 1 (curve e of Figure 5A) show a broad correlation peak at $q_1 \approx 0.2\text{-}0.44$ nm^{-1}, indicating that these fractions contain small lamellar sheaves disorderly arranged to each other at higher length scales. In particular, for the sEE and iEE-sC6 fractions of the Sample 1 and the iEE-sC6 fraction of the Sample 3, as the correlation peaks are broad, the values of the characteristic correlation distances L_1 ($\approx 2\pi/q_1$) dominating the structural organization of the crystalline and amorphous phases span a wide region comprised between ≈ 10 and 30 nm. For the sEE fraction of Sample 3 (curve e of Figure 5B), instead, the SAXS profile shows a monotonic decrease with the increasing of q. The q^{-3} power

law dependence of SAXS intensity of Figure 4B (curve e) suggests that this fraction essentially consists of isolated lamellae. The SAXS profiles of the unfractionated samples and of the most crystalline fractions iC6-sCC6 and iCC6, instead, are characterized by two well defined humps, intersecting at 0.55-0.60 nm^{-1}. In the corresponding Lorentz corrected SAXS profiles the humps are replaced by a double correlation peak, consisting of a strong maximum at $q_1 \approx 0.1\text{-}0.2$ nm^{-1} (curves a, b and c of Figures 4 and 5) and a broad and less intense maximum at $q_2 \approx 0.7\text{-}0.8$ nm^{-1} (curves a', b' and c' of Figure 4 and 5). The area of the less intense peak is less than 20% of the total area. According to Refs. 78 and 79, the double correlation peak can be ascribed to a microphase separated morphology, originating from a hierarchical organization of the polydisperse hard and soft blocks spanning diverse levels. In particular, the presence of the two broad correlation peaks at q_1 and q_2 may be attributed to the simultaneous presence of different population of lamellar stacks originating from the tendency of the hard blocks with high and low molecular mass to crystallize in well separated stacks embedded in the matrix of the soft blocks according to average correlation distances $L_1 \approx 2\pi/q_1$ higher than 20 nm, and $L_2 \approx 2\pi/q_2$ lower than ≈ 10-11 nm. The position of the observed correlation peaks q_1 and q_2 in Figure 6 and the values of the corresponding correlation lengths L_1 and L_2 are reported in Table 5.

Table 5. Values of the position of the main correlation peaks (q_1 and q_2) and corresponding characteristic correlation distances (L_1 and L_2) observed in the Lorentz corrected SAXS profiles of the melt crystallized Samples 1 and 3 and the corresponding sEE, iEE-sC6, iC6-sCC6, and iCC6 fractions.

		Bragg Law			
Sample ID	**wt%**	q_1 **(nm^{-1})**	L_1 **(nm^{-1})**	q_2 **(nm^{-1})**	L_2 **(nm)**
1-unfractionated	100	0.2	31	0.78	8.05
1-iCC6	35.3	0.21	30	0.79	7.95
1-iC6-sCC6	50.5	0.21	30	0.77	8.16
1-iEE-sC6	6.7	0.28	22	/	/
1-sEE	7.5	0.44	14	/	/
3-unfractionated	100	0.14	45	0.73	8.61
3-iCC6	4.7	0.15	42	0.72	8.72
3-iC6-sCC6	78.2	0.17	37	0.74	8.49
3-iEE-sC6	7.9	0.21, 0.29[a]	30, 22[a]	/	/
3-sEE	9.2	/	/	/	/

a. The Lorentz corrected curve shows a double peak.

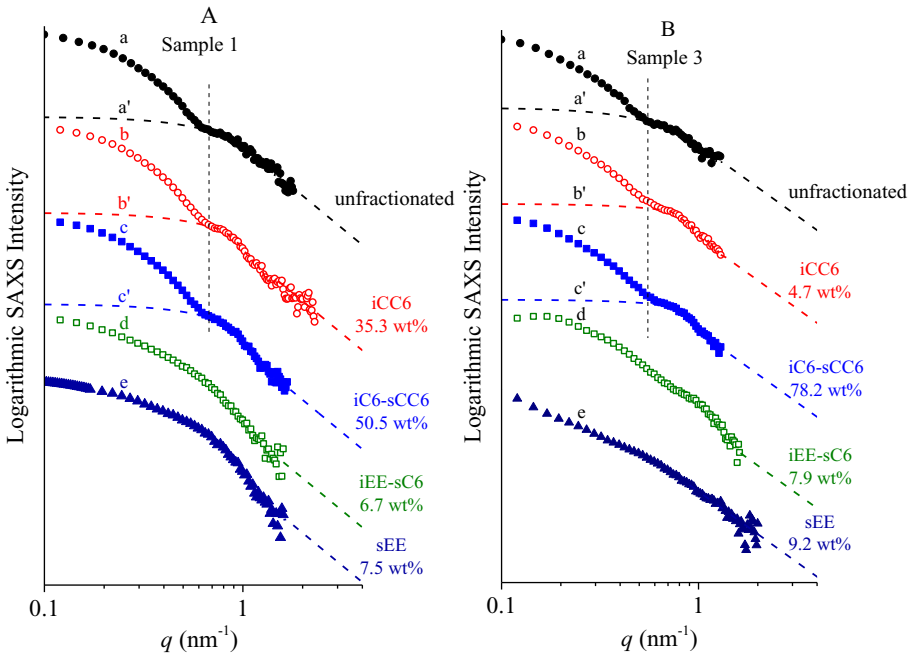

Figure 4. SAXS profiles of the unfractionated Samples 1 (A) and 3 (B) and of the corresponding fractions (a-e), crystallized from the melt at fast (uncontrolled) cooling rate (≈30 °C/min, on average), after subtraction for a flat background. Curves a', b' and c' are the contribution to SAXS intensity from a population of lamellar stacks of PE crystals characterized by hard blocks of short length (see the text). The dashed lines in the low q region indicate the extrapolation of SAXS intensity with the Debye-Bueche function. In the tail, the SAXS intensity follows a q^{-4} power law dependence, in agreement with the Porod law. This corresponds to crystalline and amorphous layers separated by a sharp interface.

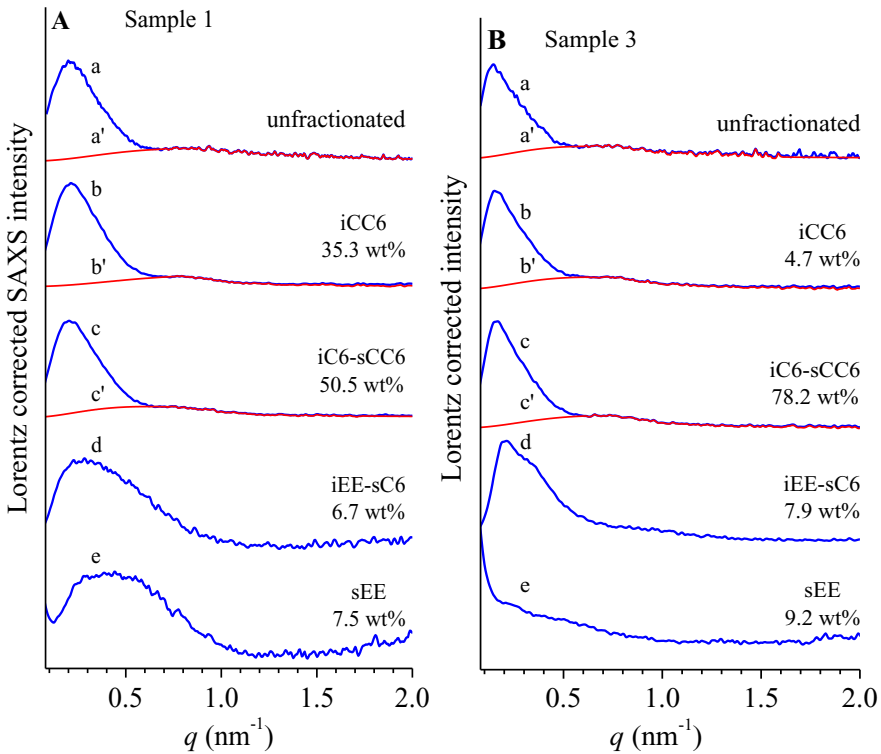

Figure 5. Lorentz corrected SAXS profiles of the unfractionated Samples 1 (A) and 3 (B) and of the corresponding fractions (a-e). Curves a', b' and c' are the contribution to the SAXS intensity from a population of lamellar stacks of PE crystals characterized by hard blocks of short length (see the text). Curves a', b', and c' have been obtained applying Lorentz correction to the dashed lines of Figure 4.

In order to extract the values of the lamellar parameters characterizing the lamellar stacks, the SAXS intensity data *I*(q) have been elaborated to calculate the interface distribution function IDF.[96] The interface distribution function of the unfractionated samples and of the corresponding fractions has been calculated with the following Equation:

$$IDF(z) = K\int_0^\infty [K_P - q^4(I(q) - I_{bk})] \exp(-\sigma^2 q^2) cos(qz)\, dq \quad (3)$$

The obtained curves are shown in Figure 6, whereas the values of the lamellar parameters extracted from the IDF are shown in Table 6. The IDF curves show a single maximum due to the strong overlap of the peaks centered at l_c and l_a for the sEE and iEE-sC6 fractions belonging to Sample 1 (curves d, e of Figure 6A) and two well-distinguishable maxima for all the remaining fractions and the unfractionated samples (curves a-c of Figure 6A and a-d of Figure 6B). For all the samples a diffuse undulated minimum that gradually approaches the horizontal zero line of the IDF is also observed.

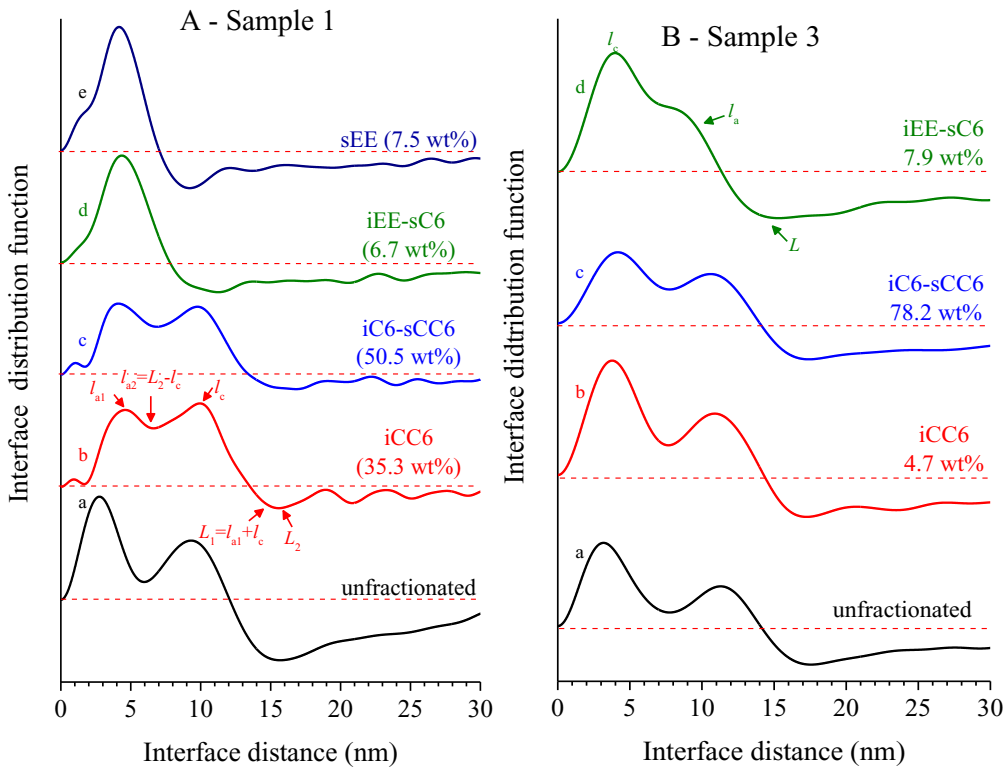

Figure 6. Distribution function of the interface distances. The center of distribution functions of interfaces distances occurring at l_{a1}, l_c, $L_1=l_{a1}+l_c$ and l_{a2}, l_c, $L_2=l_{a2}+l_c$ are indicated in A for the curve b, corresponding to the simultaneous presence of at least two different populations of lamellar stacks with parameters l_{a1}, l_c, L_1 and l_{a2}, l_c, L_2.

Table 6. Values of the lamellar periodicity (L_i) and thickness of amorphous (l_{ai}) and crystalline (l_{ci}) layers in the different populations of lamellar stacks, deduced from SAXS data (Figure 5 and 6) through the calculation of the self-correlation function of electron density

fluctuations (correlation function, CF) and the interface distribution function (IDF) of the melt crystallized Samples 1 and 3 and the corresponding sEE, iEE-sC6, iC6-sCC6, and iCC6 fractions.

				Correlation function				Interface distribution function			
Sample ID	**wt%**	**x_c(WAXS)/w_h (%)**	**φ_c(WAXS)[a] (%)**	***L*** **(nm)**	**l_c (nm)**	**l_a (nm)**	**l_c/L(CF)**	**L_1; L_2 (nm)**	**l_c (nm)**	**l_{a1}; l_{a2} (nm)**	**l_c/L_1(IDF); l_c/L_2(IDF)**
1-unfractionated	100	48	44	8.2	6.3	1.9	0.77	12.0; 15.6	9.3	2.8; 6.3	0.77; 0.60
1-iCC6	35.3	52	48	7.8	5.5	2.3	0.70	14.6; 15.6	9.9	4.7; 5.7	0.68; 0.63
1-iC6-sCC6	50.5	59	55	8.2	5.5	2.7	0.67	14.0; 16.3	9.8	4.1; 6.5	0.70; 0.60
1-iEE-sC6	6.7	≈47	≈43	/	/	/	/	11.3	4.4	6.9	0.39
1-sEE	7.5	/	-	/	/	/	/	9.2	4.2	5.0	0.46
3-unfractionated	100	52	48	9.4	7.4	2.0	0.72	14.5;17.4	11.3	3.2; 6.1	0.78; 0.65
3-iCC6	4.7	67	63	8.4	6.4	2.5	0.70	14.7; 17.2	10.9	3.8; 6.3	0.74; 0.63
3-iC6-sCC6	78.2	71	68	8.3	5.8	2.5	69.9	14.8; 17.4	10.6	4.2; 6.8	0.72; 0.61
3-iEE-sC6	7.9	43	39	/	/	/	/	15.3	3.9	11.4	0.26

a. The volume fraction of crystalline phase φ_c(WAXS) normalized with respect to the weight fraction of the hard blocks w_h is calculated from x_c(WAXS)/w_h as $\varphi_c(\text{WAXS}) = \rho_c^{-1} (x_c(\text{WAXS})/w_h) / [\rho_c^{-1} x_c(\text{WAXS})/w_h + \rho_a^{-1} (1- x_c(\text{WAXS})/w_h]$ where $\rho_c = 1$ g/cm^3 and $\rho_a = 0.855$ g/cm^3 are the density of crystalline and amorphous PE, respectively.[85]

The sEE and iEE-sC6 fractions are poorly crystalline, show a small melting endotherm at ≈ 100°C for the iEE-sC6 fractions, and a faint diffuse melting endotherm spanning the temperature range from 20 to 80°C for the sEE fractions (Figure 3). The IDF curves of these fractions suggest that they contain a single population of lamellar crystals disorderly stacked along the lamellar normal at separation distance L, the value of which corresponds to the position of the first minimum in the IDF at ≈ 10 nm for the sEE and iEE-sC6 fractions of Sample 1 and at ≈ 15 nm for the iEE-sC6 fraction of Sample 3 (Table 6). The values of the thickness of the crystalline lamellae l_c and amorphous layer l_a, instead, correspond to the position of the first maximum in the IDF curves at ≈ 4 nm for l_c and to the difference L - l_c, for l_a (Table 5). In Table 6, the values of the linear crystallinity index φ_c(IDF) calculated as the ratio $\varphi_c(IDF) = l_c/L$ are also reported. It is worth noting that the values of φ_c(IDF) are close to the values of the volume fraction of the crystalline phase φ_c(WAXS) deduced from the crystallinity index relative to the sole hard blocks (x_c(WAXS)/w_h), extracted from WAXS data of Figure 2 (Table 6).[85,88] The results of the IDF analysis suggest that the sEE fraction of Sample 1 and the iEE-sC6 fractions of both samples contain small amounts of chains, crystallizing in small, tiny domains, where the inclusion of soft blocks within the amorphous layers (thickness ≥ 5 nm) separating the crystalline lamellae (thickness ≈ 4 nm) may not be excluded. A lower bound for the average molecular mass of the hard blocks M_H constituting the building units of the crystallizing chains may be hence estimated, considering that the number of -CH2- units included in a stem of length l_c ≈ 4 nm should be close to 30 (≈ 4/0.127), where 0.127 nm is the halved chain periodicity of the PE chains in the orthorhombic crystals. This corresponds to an average molecular mass of the hard blocks M_H higher than 0.4 kDa, which is of the same order of

magnitude of the M_H value deduced from aCEF results (≈ 0.3 kDa, see Figure 1 and Table 3) of the iEE-sC6 fractions.

For the unfractionated samples and the corresponding iCC6 and iC6-sCC6 fractions, the attribution of the maxima in the IDF curves (curves b-c of Figure 6), is less straightforward. As discussed before, these samples experience little or no inclusion of the soft blocks within the interlamellar amorphous regions. This exclusion may be the result either of microphase separation of the hard and soft blocks in different domains already in the melt, or of segregation of the hard blocks in separated domains by effect of crystallization. In particular, according to the principle that under similar crystallization conditions the thickness l_c of the lamellar crystals does not depend on the values of the molecular mass of the hard blocks M_H characterizing the different fractions for M_H values higher than a threshold,[89-93] the values of l_c in the unfractionated samples and in the corresponding iCC6 and iC6-sCC6 fractions should be identical. As a consequence, the values of l_c may be assumed to correspond to the position of the second maximum of the IDF located at ≈ 9-10 nm for Sample 1 and at slightly higher values of ≈ 11 nm for Sample 3. This attribution is in agreement with the fact that the melting temperatures of the unfractionated samples and the corresponding iCC6 and iC6-sCC6 fractions are nearly identical, and with the fact that they are slightly lower (120 -121°C) for Sample 1 than those of Sample 3 (123-124°C) (see Figure 3 and Table 4, second heating scans). At least two populations of lamellar stacks may be identified from the IDF (curves a-c of Figure 6) assuming that l_{a1} corresponds to the position of the first maximum, and $L_1 \approx l_c + l_{a1}$, for the first population, and that L_2 corresponds to the position of the minimum and $l_{a2} \approx L_2 - l_c$ for the second population (curve b of Figure 6A as an example and Table 6) (see Appendix A1). The values of linear crystallinity φ_c(IDF) calculated for the first

and second populations of lamellar stacks are in good agreement with the values of the volume fraction of the crystalline phase φ_c(WAXS) deduced from the crystallinity index relative to the sole hard blocks (x_c(WAXS)/w_h), extracted from WAXS data of Figure 2 (Table 6).[85,88]

Therefore, in the hypothesis that the soft blocks are a little or not included at all in the amorphous layers located in between the lamellar crystals in the leading stacks of the unfractionated samples and the iCC6 and iC6-sCC6 fractions, the values of the average molecular mass M_{Hi} (i=1,2) in the building HS units characterizing the chains belonging to the two different populations of stacks may be calculated using the values of l_{ai} in Equation 1, by placing, for the sake of simplicity, k_1 = 1.2 nm for $M_{Hi} \geq$ 10kDa, and k_1 = 0 for M_{Hi} < 10KDa.[94,95] The values of the average molecular mass of the HS building units M_{HSi} and of the corresponding soft blocks M_{Si} can be then evaluated as $M_{HSi} = M_{Hi}\, w_h^{-1}$ and $M_{Si} = M_{HSi} - M_{Hi}$.[1] The average number of blocks included in a hypothetical chain consisting of the identical repetition of HS building units with average molecular mass M_{HSi} can be also evaluated as a figure comprised in between the ratio of the number average molecular mass M_n and M_{HSi} ($n_{ni} = M_n\, M_{HSi}^{-1}$) and of the mass average molecular mass M_w and M_{HSi}, ($n_{wi} = M_w\, M_{HSi}^{-1}$). The so-obtained values of M_{Hi}, M_{Si}, M_{HSi}, n_{ni} and n_{wi} along with the codes $[M_{Hi}\text{-}M_{Si}]_{nni/nwi}$ are reported in Table 7. They are compared with the values of the molecular mass of the HS building units deduced from aCEF results.

The results of Table 7 indicate that SAXS probes the presence of non-interfering populations of lamellar stacks due to the separate crystallization of the hard blocks with different molecular mass M_H. It is worth nothing that, on inspection of Table 7, it is apparent that for both samples, the chains belonging to the iCC6 fractions include HS units characterized by M_H values (10-13 kDa)

lower than those included in the chains belonging to the iC6-sCC6 fractions (13-16 kDa). This result suggests that the different solubility in boiling cyclohexane and *n*-hexane of the multiblock ethylene/1-octene is not controlled by the mass of the hard blocks M_H, but rather by the average mass of the attached soft blocks M_S, which is in all cases up to 3-4 times higher than the M_H value. In other terms, the chains including long hard blocks are more soluble in *n*-hexane than chains including short hard blocks, because the length of the attached soft blocks is also long.

As a further remark, it is noted that the values of molecular mass of the HS building units deduced from aCEF results are lower than those deduced from IDF analysis. The IDF, indeed, does not account for the possible existence of a third (minor) population of lamellar stacks, constituting less than 20% of the total crystalline phase, as the corresponding contributions to the IDF is almost completely concealed by the contribution from the dominant populations.

In the hypothesis that this third population of lamellar stacks contributes additively to the SAXS intensity distribution, the corresponding lamellar parameter are evaluated resorting to the calculation of the self-correlation function of electron density fluctuations (correlation function, CF, see Figure 7) utilizing the curves a'-d' of Figures 4 and 5 and completely neglecting the SAXS intensity at $q < 0.55\text{-}0.6$ nm^{-1} relative to the dominant correlation peak (see Appendix A1). The so-obtained values of the lamellar parameters and M_H and M_S of the corresponding building units are reported in Table 6 and 7. It is apparent that the so-calculated values of the lamellar thickness l_c are only slightly lower than those of the leading population of lamellae extracted from the IDF. Furthermore, the values of the molecular mass of the HS building units deduced from the CF are close to those calculated from the aCEF

maxima. Accordingly, based on the separation of SAXS curves at q values lower and higher than 0.55-0.6 nm^{-1} (curves a-c vs. a'-c' in Figures 4 and 5) such low molecular mass HS building units contribute by only 20% to the total crystalline phase. As discussed above, the resultant values of M_H and M_S correspond indeed to the lower limit of the distribution of the molecular mass of the hard and soft blocks in the iCC6 and iC6-sCC6 fractions.

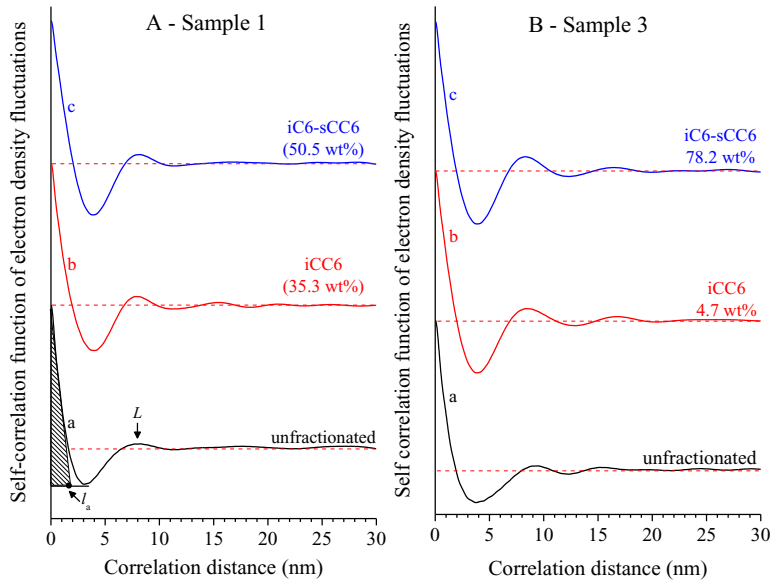

Figure 7. Correlation functions of electron density extracted from the SAXS data (curves a'-c') of Figures 4 and 5. The main self-correlation triangle (delineated with the striped pattern), the average periodicity L and the average thickness of the amorphous layers l_a are indicated in A.

Table 7. Average molecular masses of hard and soft blocks within the HS building units, and hypothetical constitution of a multiblock chain consisting (on average) of the repetition of identical HS building units, evaluated with the methods of Refs. 58 and 78.

Sample ID	aCEF-based method[58]	SAXS-based method (CF)[78]			SAXS-based method (IDF)[78]		
	$[M_{n,Hi}\text{-}M_{n,Si}]_{ni}$	M_H (kDa)	M_S (kDa)	$[M_H\text{-}M_S]_{nn/nw}$	M_{Hi} (kDa)	M_{Si} (kDa)	$[M_{Hi}\text{-}M_{Si}]_{nni/nwi}$
1-unfractionated	$[2H\text{-}4S]_{11}$; $[3H\text{-}6S]_{7}$	1.9	5.6	$[2H\text{-}6S]_{8/21}$	3.9; 13.4	11.9; 40.5	$[4H\text{-}12S]_{4/10}$; $[13H\text{-}41S]_{1/3}$
1-iCC6	$[2H\text{-}3S]_{15}$; $[3H\text{-}6S]_{8}$	2.7	6.2	$[3H\text{-}6S]_{8/19}$	6.0; 10.2	13.5; 23.1	$[6H\text{-}13S]_{4/9}$; $[10H\text{-}23S]_{2/5}$
1-iC6-sCC6	$[2H\text{-}4S]_{14}$; $[3H\text{-}7S]_{7}$	3.7	10.1	$[4H\text{-}10S]_{5/11}$	8.7; 14.5	23.2; 38.8	$[9H\text{-}23S]_{2/5}$; $[15H\text{-}39S]_{1/3}$
3-unfractionated	$[1H\text{-}2S]_{10}$; $[3H\text{-}7S]_{4}$	2.1	5.6	$[2H\text{-}6S]_{4/11}$	5.3; 12.4	14.4; 33.7	$[5H\text{-}14S]_{2/4/}$; $[12H\text{-}34S]_{1/2}$
3-iCC6	$[1H\text{-}2S]_{13}$; $[3H\text{-}5S]_{5}$	3.2	8.2	$[3H\text{-}8S]_{3/8}$	7.4; 13.4	19.0; 34.2	$[7H\text{-}19S]_{2/4/}$; $[13H\text{-}34S]_{1/2}$
3-iC6-sCC6	$[1H\text{-}2S]_{12}$; $[3H\text{-}6S]_{5}$	3.2	8.9	$[3H\text{-}9S]_{3/8}$	9.1; 16.2	25.0; 44.4	$[9H\text{-}25S]_{1/3}$; $[16H\text{-}44S]_{1/2}$

In summary, the long and short hard blocks belonging to the iCC6 and iC6-sCC6 fractions crystallize forming lamellar crystals with nearly identical thickness ($l_c \approx$ 8-11 nm) regardless of the M_H value, separated by amorphous layers with thickness l_a scaling as $M_H^{1/2}$. The presence of a non-negligible portion of chains including hard and soft blocks with molecular mass M_H higher than 10 kDa and M_s higher than 20 kDa accounts well for some (indirect) evidence of microphase separation occurring in the melt, namely based on melt-rheology experiments.[24,26,73-75] The fractionation behaviour along with the specification of the composition of representative HS building units included in the different fractions is illustrated in Figure 8. The inferior fractions (sEE and iEE-sC6) include chains consisting of short hard blocks alternating with short soft blocks in the iEE-sC6 fractions, linked to long soft blocks in the sEE fractions. Furthermore, the sEE fractions include also chains constituted by soft blocks not linked to any hard blocks. The superior fractions (iC6-sCC6 and iCC6), instead, consist in the random enchainment of long and short HS units in which the molecular mass of the hard M_H and soft M_S blocks is comprised in between 2 and 16 kDa and 6 and 44 kDa, respectively, even though the possible inclusion of shorter HS units may not be excluded.

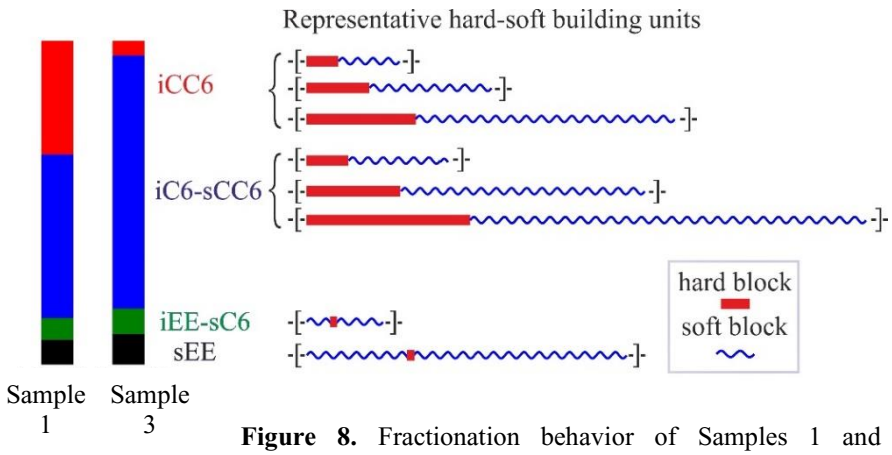

Figure 8. Fractionation behavior of Samples 1 and 3 and specification of the composition of representative HS building units included in the different fractions. The length of the vertical rectangles on the right is proportional to the relative amount of each fraction. Black: diethyl ether soluble fraction (sEE); green: diethyl ether insoluble/*n*-hexane soluble fraction (iEE-sC6); blue: *n*-hexane insoluble/cyclohexane soluble fraction (iC6-sCC6); red: cyclohexane insoluble fraction (iCC6). The compositional heterogeneity of ethylene/1-octene entails not only differences in the average length of the HS building units that varies from chain to chain, but also the random enchainment of HS units of different length within the same chain.

3.2. Transmission Electron Microscopy Analysis of the Ethylene/1-Octene Multiblock Copolymers

In this part of the study, the effect of the complex chain microstructure of the OBCs on the solid-state morphology that sets up upon crystallization from the melt has been investigated, resorting to transmission electron microscopy (TEM) analysis. Within this context, the tendency of OBC to give rise to mesophase separated morphologies is investigated in detail. It is worth noting that, following the consideration of Ref. 73, the term "mesophase separation" is used instead of "microphase separation" to address that the phase separation occurring in OBCs spans domains much larger (100 nm) than those involved

in monodisperse di- and triblock copolymers (15-25 nm) (vide infra). The term microphase separation, instead, is used to address the conventional morphology shown by the conventional monodisperse block copolymers.

In particular, the TEM investigation was performed not only on the five raw samples, but also on the fractions obtained by Kumagawa exhaustive extraction in boiling diethyl ether, *n*-hexane and cyclohexane, namely the sEE, iEE-sC6, iC6-sCC6 and iCC6 fractions. The relative amount of the extracted fractions, the molecular mass, comonomer content and percentage of hard blocks of the Samples 1 and 3 (already reported in Table 1) are compared with those of the Samples 2, 4 and 5 in Table 8.

Table 8. Relative amount of the extracted fractions from the Samples 1-5, and corresponding values of the average content of octene units x_O, weight fraction of the hard blocks w_h, number average M_n and mass average M_w molecular mass and dispersity index Đ ($=M_w/M_n$). Data relative to the unfractionated samples are also reported.

Sample	wt%	x_O (mol%)	w_h (wt%)	M_n (kDa)	M_w (kDa)	Đ
1-unfractionated	/	13.1	24.9	60	155	2.6
1-sEE	7.5	20.1	*	20	52	2.6
1-iEE-sC6	6.7	19.1	4.2	33	75	2.2
1-iC6-sCC6	50.5	13.2	27.2	68	158	2.3
1-iCC6	35.3	12.9	30.7	74	166	2.2
2-unfractionated	/	12.9	25.8	56	134	2.4
2-sEE	4.6	19.8	*	15	43	2.8
2-iEE-sC6	10.5	18.5	6.4	36	77	2.1
2-iC6-sCC6	67.3	13.6	24.4	60	143	2.4
2-iCC6	17.5	12.2	29.5	63	146	2.3
3-unfractionated	/	12.4	26.9	33	86	2.6
3-sEE	9.2	20.3	*	16	40	2.6
3-iEE-sC6	7.9	18.3	11.5	26	55	2.1
3-iC6-sCC6	78.2	12.5	26.7	39	94	2.4
3-iCC6	4.7	11.9	28.2	40	93	2.3
4-unfractionated	/	13.8	24.4	17	71	4.3
4-sEE	12.1	19.1	3.0	8.3	37	4.4
4-iEE-sC6	13.6	17.5	9.1	11	52	4.7
4-iC6-sCC6	71.0	12.8	27.4	23	77	3.4
4-iCC6	3.3	11.2	34.0	24	69	2.9

5-unfractionated	/	14.9	13.5	70	177	2.5
5-sEE	12.0	19.4	*	26	75	2.9
5-iEE-sC6	20.8	17.7	5.7	61	129	2.1
5-iC6-sCC6	59.9	14.7	17.6	104	211	2.0
5-iCC6	7.4	14.2	18	91	197	2.2

*not detected

It is apparent that, the Sample 1 and 2 have similar chain microstructure and similar fractionation behavior. The mass average molecular mass of these samples is ≈ 140-150 kDa, the average 1-octene content is ≈ 13 mol%, whereas the percentage of hard blocks is ≈ 25-28 wt%. These samples contain about 5-8 wt% of a sEE fraction, about 7-11 wt % of an iEE-sC6 fraction, a relatively high amount of an iC6-sCC6 fraction equal to ≈ 50-60 wt%, and a comparable amount (≈ 18-35 wt%) of an iCC6 fraction. Also the Samples 3 and 4 are similar as far as the chain microstructure and the fractionation behavior. In particular, the mass average molecular mass of these samples is ≈ 70-80 kDa, the average 1-octene content is ≈ 12-13 mol% and the percentage of hard blocks is ≈ 24-27 wt%. These samples contain ≈ 9-12 wt% of a sEE fraction, ≈ 8-13 wt % of an iEE-sC6 fraction, ≈ 70-80 wt% of an iC6-sCC6 fraction, and only ≈ 3-5 wt% of an iCC6 fraction. Finally, the Sample 5 is singular, as the mass average molecular mass is ≈ 180 kDa, the average 1-octene content is higher than that of the other samples, ≈ 15 mol%, whereas the percentage of hard blocks is only ≈ 19 wt%. It contains about 12 wt% of a sEE fraction, ≈ 20 wt % of an iEE-sC6 fraction, ≈ 60 wt% of an iC6-sCC6 fraction, and ≈ 7 wt% of an iCC6 fraction. For all the samples the inferior fractions (sEE and iEE-sC6) are namely constituted by soft blocks not linked to hard blocks or linked to short hard blocks, whereas the superior fractions (iC6-sCC6 and iCC6), contain long hard blocks alternating with long soft blocks, even though the enchainment of short hard blocks may not be excluded. Furthermore, the molecular mass of the superior fractions is only slightly higher than that of the

unfractionated samples, whereas it is significantly lower for the inferior fractions. The X-ray powder diffraction profiles and DSC thermograms of the unfractionated Samples 2, 4, and 5 and of the corresponding fractions are reported in the Appendix A2 (Figures A2-1-3). In the Appendix A2, the thermal parameters and the crystallinity indices extracted from thermal and diffraction data are also reported (Table A2-1). Similar to the Samples 1 and 3 (Figures 2 and 3) the unfractionated Samples 2, 4, and 5, and the corresponding superior fractions crystallize in the orthorhombic form of PE, show a melting and crystallization temperatures of ≈ 120 and 90-100°C, respectively, and a crystallinity index, normalized to the sole hard block, content of 40-70%.

The TEM images of the Samples 1-5 of the unfractionated samples and the corresponding fractions are reported in Figures 9-23. In particular, for the Sample 1, the TEM images of the unfractionated sample and of all the fractions are shown (sEE, iEE-sC6, iC6-sCC6, iCC6), whereas for Samples 3, and 4, only the TEM micrographs of the unfractionated samples and of the iC6-sCC6 and iCC6 fractions are reported. For Samples 2 and 5, the TEM micrographs have been collected only for the unfractionated sample and for the iC6-sCC6 fraction.

Bright field TEM images at low magnification of the unfractionated Sample 1 (Figures 9A and B) show sheaves of lamellae splaying from point-nuclei, typical of spherulitic superstructures, spotted by bright round-shaped entities (≈ 150-200 nm wide), especially in the regions with a high concentration of lamellar crystals (see Figure 9A). At higher magnification, as shown in Figures 9C and D, the round-shaped domains appear populated by tightly stacked lamellar crystals laying on edge with a separation distance of ≈ 20 nm. The surrounding dark regions appear sporadically crossed by edge-on lamellae arranged in stacks, at less regular separation distance. The average

thickness of the lamellar crystals inside and outside the round entities is identical and equal to ≈ 10 nm. The TEM images indicate that Sample 1 tends to crystallize in a phase separated morphology at mesoscale, where the bright round regions are hard-block-rich domains and the surrounding dark regions are soft-block-rich regions. In the hard-block-rich domains, crystallization of the orthorhombic form of PE takes place,[13,65,68,78,79] thus producing well organized lamellar stacks, separated by amorphous layers including only a negligible fraction of soft blocks. However, the good inter-block mixing induces the formation of additional PE lamellar crystals emanating from the round hard domains and passing through the soft matrix. The values of lamellar thickness and of the separation distances are of the same order of those ones deduced from SAXS analysis through IDF calculations. However, it is not possible to visualize lamellar stacks characterized by separation distances of the order of 10 nm because they constitute less than 20% of the crystalline phase.

The sEE fraction of Sample 1 essentially consists of a random ethylene/1-octene copolymer not attached to hard blocks or attached to hard blocks of short length. It shows a homogeneous morphology sporadically crossed by isolated lamellar crystals laying edge-on (Figure 10). Also the morphology of iEE-sC6 fraction is characterized by a homogeneous matrix populated by soft blocks. In the TEM image at low magnification (Figure 11A) open structures of thin lamellar crystals organized in star-like aggregates are visible. The star-like entities appear separated by rather sharp boundaries, due to impingement. At higher magnification (Figure 11B) the texture appears more homogeneous and includes thin lamellar crystals crossing the amorphous matrix in all the directions. Finally, iC6-sCiC6 and iCiC6 fractions present bright domains of rounded shape populated by tightly stacked edge-on lamellar crystals, due to

confined crystallization of hard blocks. The bright domains are separated by homogeneous, dark regions, crossed by lamellae according to the pass-through morphology (Figures 12 and 13). However, while the morphology of the iCC6 fraction is similar to the morphology of the corresponding unfractionated sample, for the iC6-sCC6 the bright domains appear coarser, with low defined boundaries and of much larger size (500-1000 nm vs. 100-200 nm) (Figures 12 and 13).

For the Sample 2, the TEM images of Figures 14 reveal the interior of well-defined spherulites, with lamellar crystals splaying from central nuclei. The whole image is speckled with bright spherical domains populated by hard blocks, as in the solid-state morphology of the Sample 1. At high magnification (Figures 14C, D) the round domains, with diameter of 100-200 nm, appear densely occupied by edge-on lamellae arranged in stacks, with little or no inclusion of soft segments. Pass-through lamellae emerging outside the hard domains and crossing the soft matrix, are also present as for the Sample 1 (Figure 9). The iC6-sCC6 fraction shows TEM images with no significant differences compared with the unfractionated sample (Figure 15).

The Sample 3, along with the corresponding iC6-sCC6 and iCC6 fraction, instead, shows sheaf-like superstructures of branched lamellae laying on edge on the support, uniformly filling the space, with no remarkable phase separation (Figures 16-18). In the TEM images at high magnification (Figures 16B-D, 17B and 18B) it appears that there are regions covered by stacks of lamellae running in parallel at a separation distance of ≈ 20 nm, as well as regions covered by curved lamellae at average separation distance higher than 50–60 nm. The high and low interlamellar distances correspond to interlamellar amorphous layers characterized by a high inclusion or a low or no inclusion of the soft segments, respectively.

The Sample 4 and the corresponding iC6-sCC6 and iCC6 fractions show solid state morphologies (Figures 19-21) similar to those of the Sample 3 and its fractions (Figures 16-18). Also in this case, indeed, the morphology is characterized by sheaves of lamellar crystals filling the spaces trough splaying and branching. The lamellar sheaves are surrounded by region of the sample in which lamellar crystals are less frequent or totally absent, especially for the unfractionated sample that contains a non-negligible amount of chains belonging to the less crystalline sEE and iEE-sC6 fractions (Figure 19).

Finally, the Sample 5 and its iC6-sCC6 fraction show again a mesophase separated morphology, featuring the presence of round domains speckling a dark matrix, crossed by edge-on lamellae directed in all the direction (Figures 22 and 23). Also in this case, the rounded domains are populated by hard blocks crystallized forming stacks of densely packed lamellae, with little or no inclusion of the soft blocks within the interlamellar amorphous layers. It is also apparent that part of the lamellar crystals included in the hard block rich domains emerges outside the round domains, cross the soft-block-rich matrix, up to eventually bridge adjacent round domains, according to an interconnected network, as in the pass-through morphology (Figures 22 and 23). However, the speckling coverage is less dense than the one observed for the Samples 1 and 2, in agreement with the lower hard blocks content (w_h) that characterizes the Sample 5 (i.e., w_h = 15.4% for the Sample 5 and ≈27-28% for the Samples 1, 3, see Tables 1 and 8).

The main results of the TEM analysis consist in having identified two kinds of solid-state morphologies. The Samples 1, 2, and 5 of high molecular mass and the corresponding superior fractions show a pass-through morphology, due to the tendency of the long hard blocks to crystallize in well separated domains. The weak segregation strength established between the soft

and hard blocks induces the growth of the lamellar crystals located in the hard block rich domain to grow also outside across the soft matrix, giving rise to a sort of interconnected network, that defines the pass-through morphology, typical of these systems.[72] The low molecular mass of the Sample 3 and 4, instead, give rise, upon crystallization, to a more uniform morphology, with lamellar crystals radiating outside point nuclei. Domains, with not well-defined boundaries, are also formed, constituted by lamellar crystals running in parallel, arranged in stacks at small separation distance.

In all the unfractionated samples and the corresponding superior fractions, the value of the lamellar thickness is centered around 10 nm, and the separation distance is about 20 nm. It is worth noting that these lamellar parameters are only slightly higher than those deduced from SAXS analysis (Table 6). The TEM images, indeed, do not allow to make precise measurements, neither discerning the presence of different populations of lamellar stacks, the formation of which is ascribable to molecular fractionation occurring upon crystallization. Accordingly, it is not possible to detect the small population (less then 20 % of the total crystalline fraction) of lamellar stacks formed by hard blocks of molecular mass of 2-3 kDa, stacked at distance of only ≈10 nm.

The phase separated morphology of the Samples 1, 2, and 5 and of the corresponding superior fractions is in agreement with presence of a non-negligible fraction of HS building units of high molecular mass. These high molecular mass HS units are present also in the Samples 3 and 4 and in the corresponding superior fractions. The more uniform morphology observed for these samples entails that the relative amount of these building units is too low.

Based on TEM analysis the question arises as to whether the observed mesophase separation occurs already in the melt or it is driven by the tendency of the hard blocks to crystallize in separate domains. Mesophase separation in

the melt may not be directly probed by small angle X-ray scattering (SAXS) because of the small contrast in electron density between the soft and hard blocks. In the next paragraph it is shown that rheology can give relevant information on this issue.

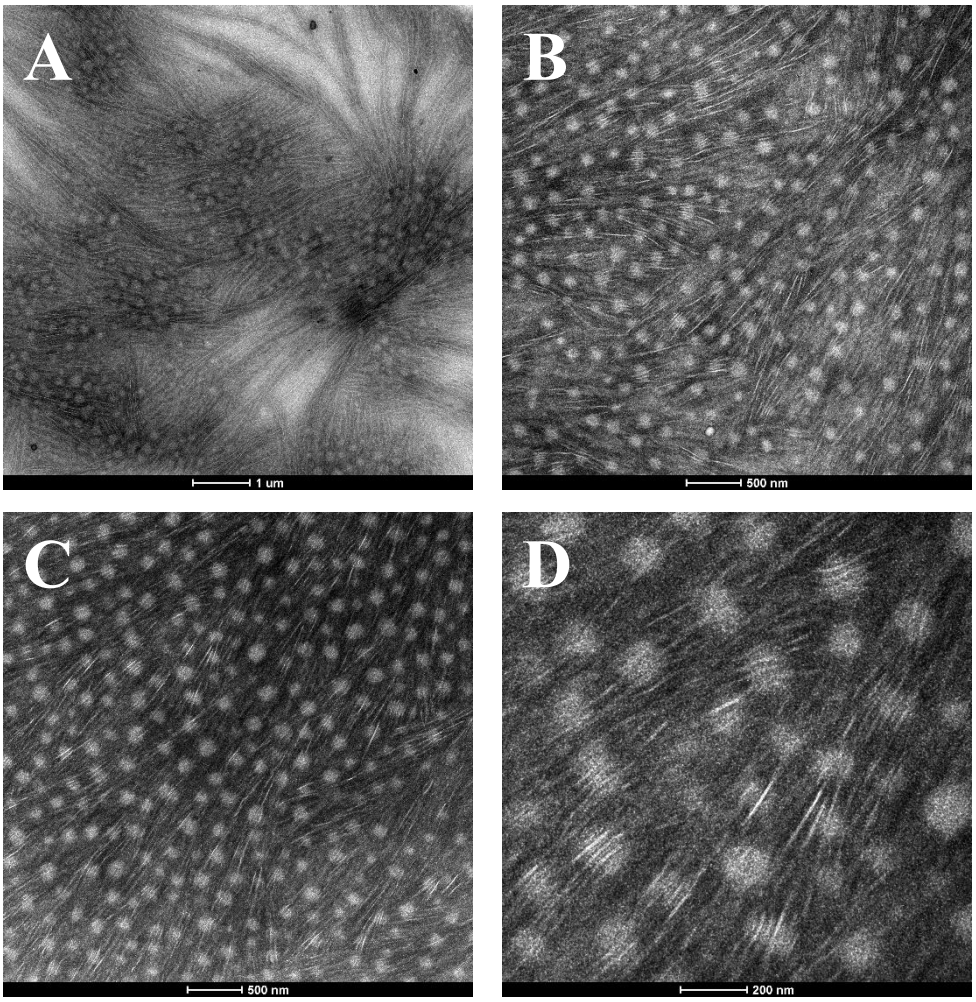

Figure 9. Bright field TEM micrographs of the Sample 1 at different magnifications. The sample is RuO_4 stained for several hours, in order to enhance the contrast between the lamellar crystals (bright), and the amorphous regions (dark).

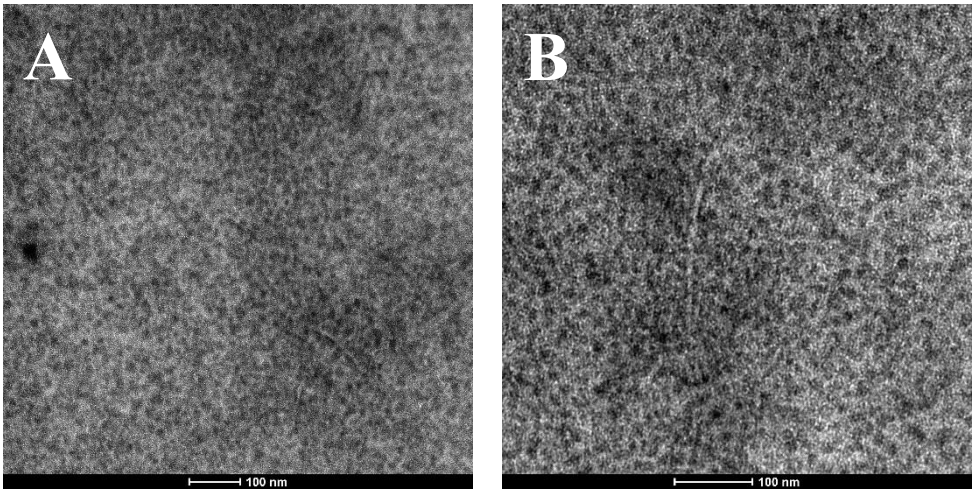

Figure 10. Bright field TEM micrographs of the sEE fraction of the Sample 1 at different magnifications. The sample is RuO_4 stained for several hours, in order to enhance the contrast between the lamellar crystals (bright), and the amorphous regions (dark).

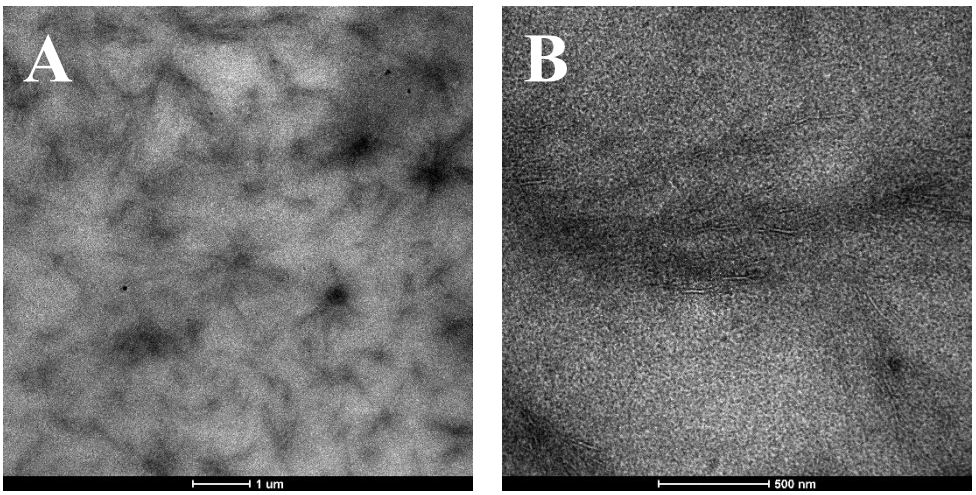

Figure 11. Bright field TEM micrographs of the iEE-sC6 fraction of the Sample 1 at different magnifications. The sample is RuO_4 stained for several hours, in order to enhance the contrast between the lamellar crystals (bright), and the amorphous regions (dark).

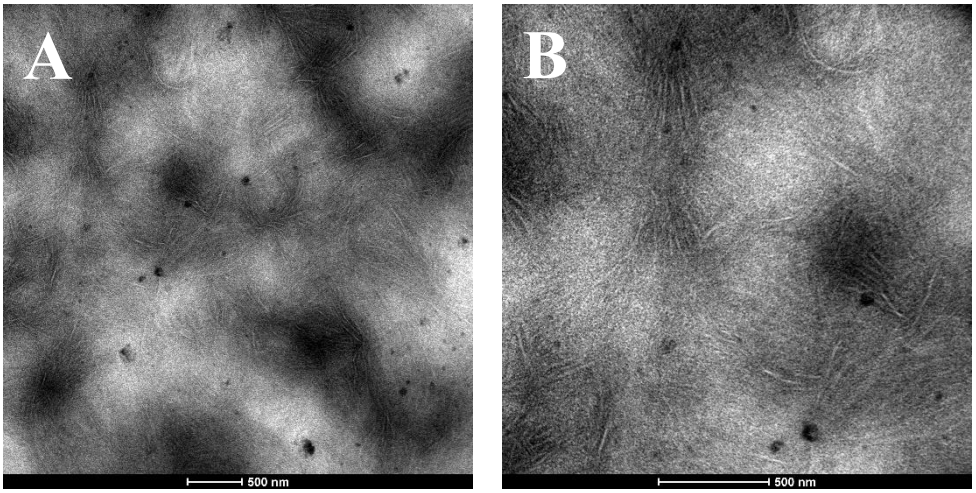

Figure 12. Bright field TEM micrographs of the iC6-sCC6 fraction of the Sample 1 at different magnifications. The sample is RuO_4 stained for several hours, in order to enhance the contrast between the lamellar crystals (bright), and the amorphous regions (dark).

Figure 13. Bright field TEM micrographs of the iCC6 fraction of the Sample 1 at different

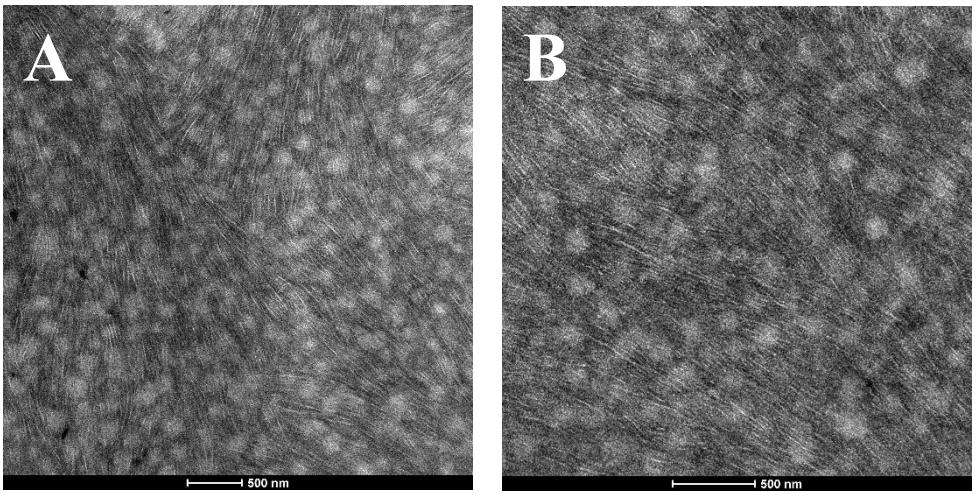

magnifications. The sample is RuO_4 stained for several hours, in order to enhance the contrast between the lamellar crystals (bright), and the amorphous regions (dark).

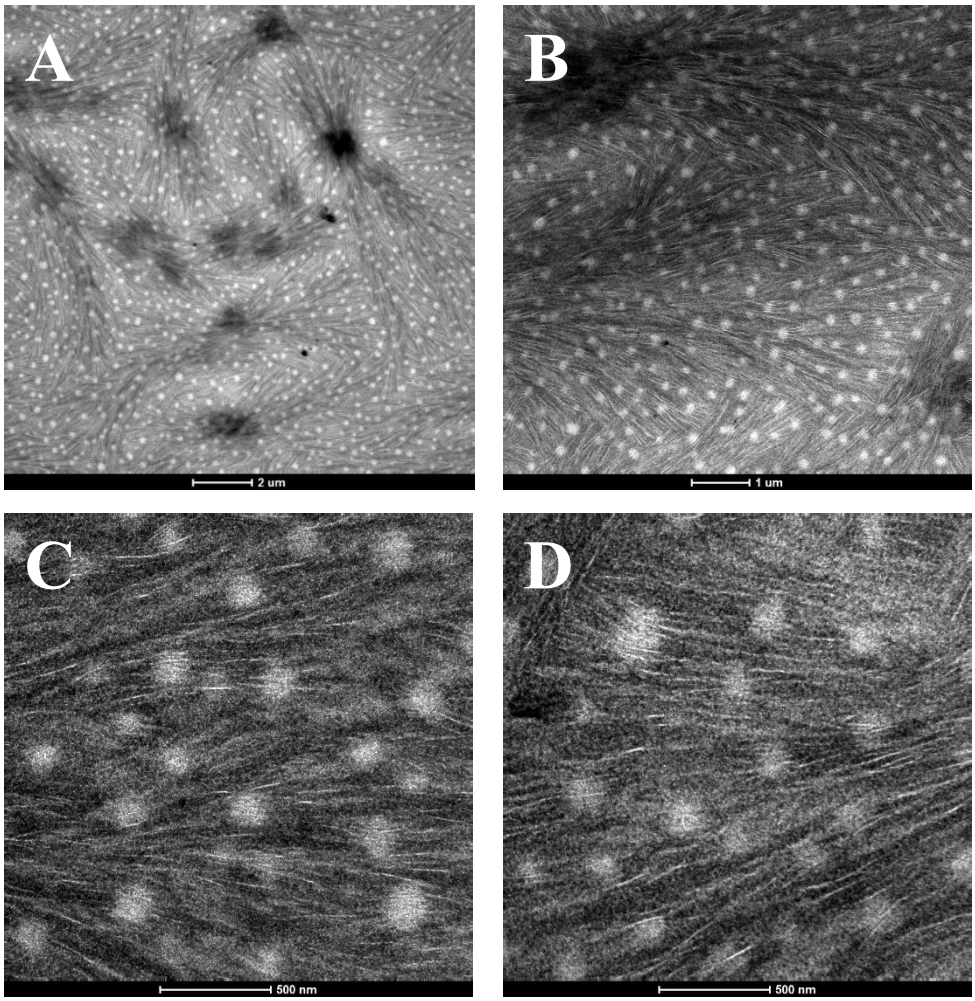

Figure 14. Bright field TEM micrographs of the Sample 2 at different magnifications. The sample is RuO_4 stained for several hours, in order to enhance the contrast between the lamellar crystals (bright), and the amorphous regions (dark).

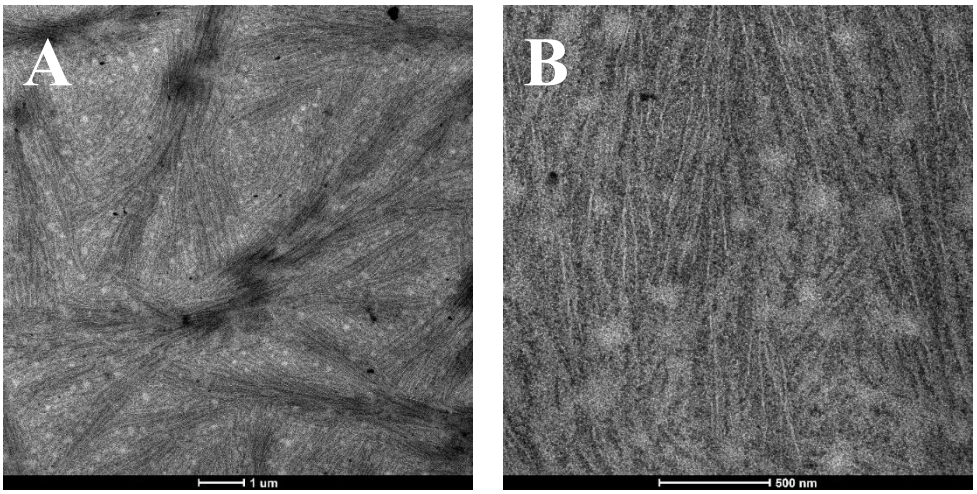

Figure 15. Bright field TEM micrographs of the iC6-sCC6 fraction of the Sample 2 at different magnifications. The sample is RuO_4 stained for several hours, in order to enhance the contrast between the lamellar crystals (bright), and the amorphous regions (dark).

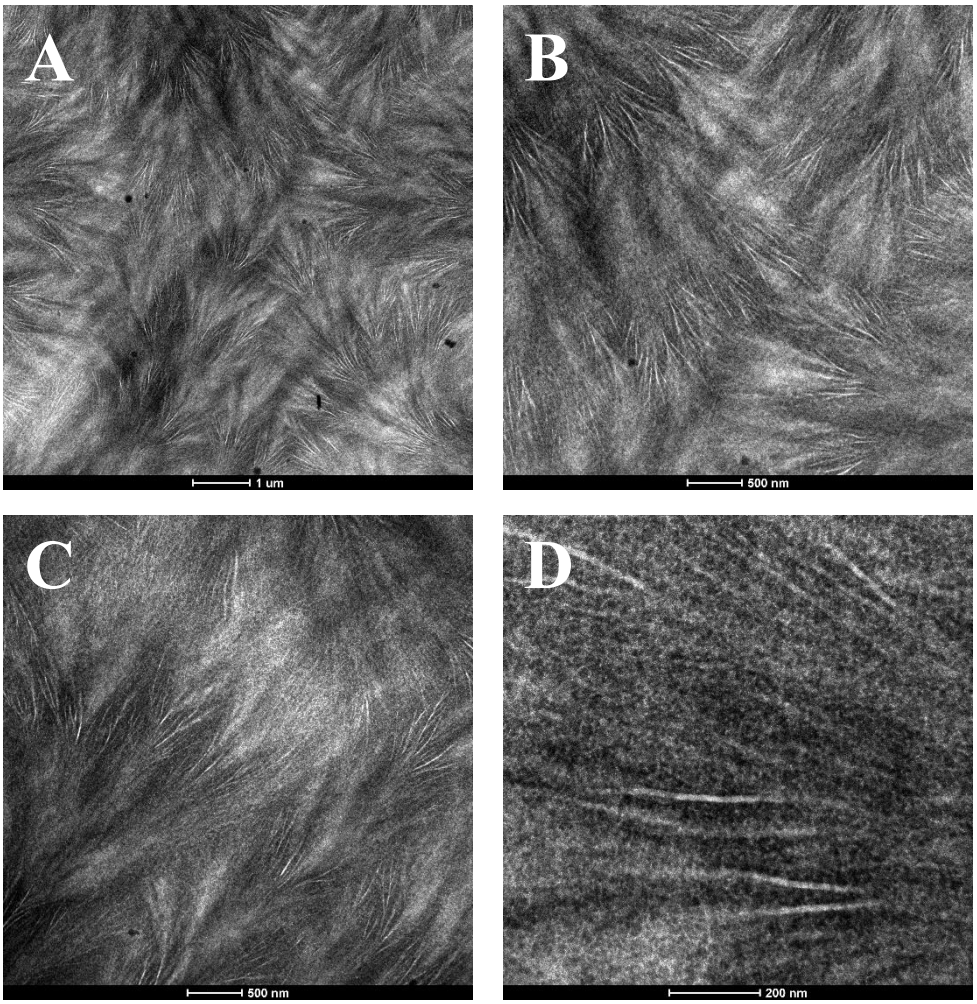

Figure 16. Bright field TEM micrographs of the Sample 3 at different magnifications. The sample is RuO_4 stained for several hours, in order to enhance the contrast between the lamellar crystals (bright), and the amorphous regions (dark).

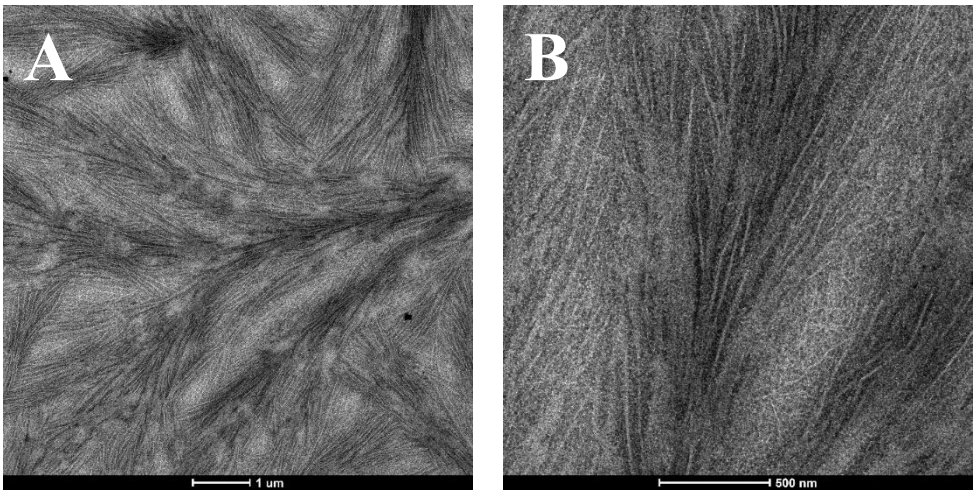

Figure 17. Bright field TEM micrographs of the iC6-sCC6 fraction of the Sample 3 at different magnifications. The sample is RuO_4 stained for several hours, in order to enhance the contrast between the lamellar crystals (bright), and the amorphous regions (dark).

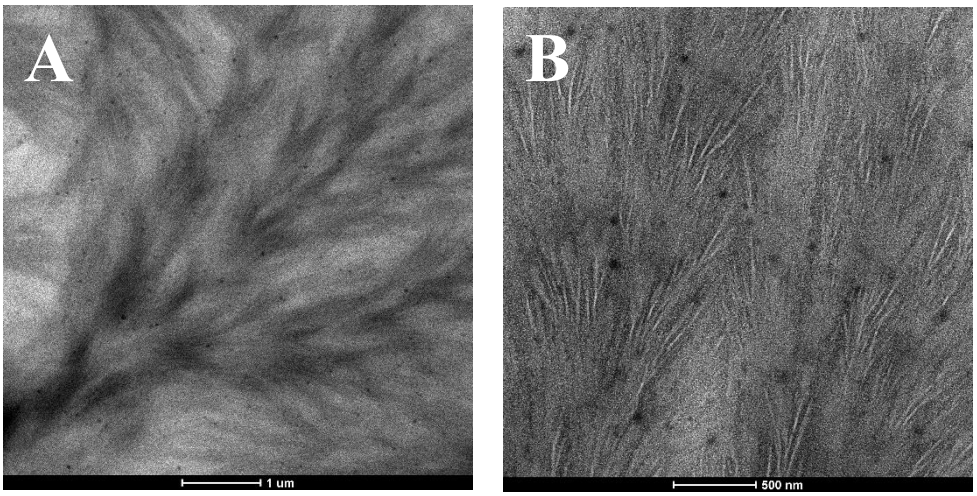

Figure 18. Bright field TEM micrographs of the iCC6 fraction of the Sample 3 at different magnifications. The sample is RuO_4 stained for several hours, in order to enhance the contrast between the lamellar crystals (bright), and the amorphous regions (dark).

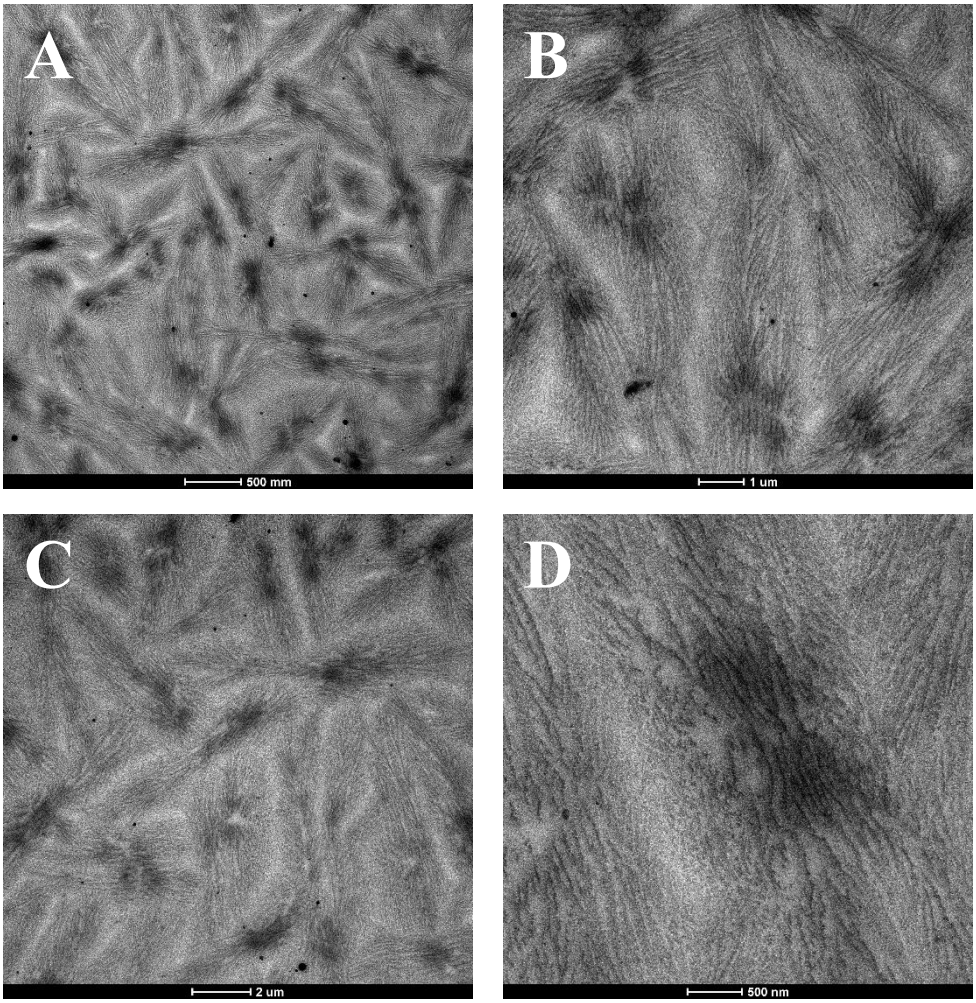

Figure 19. Bright field TEM micrographs of the Sample 4 at different magnifications. The sample is RuO_4 stained for several hours, in order to enhance the contrast between the lamellar crystals (bright), and the amorphous regions (dark).

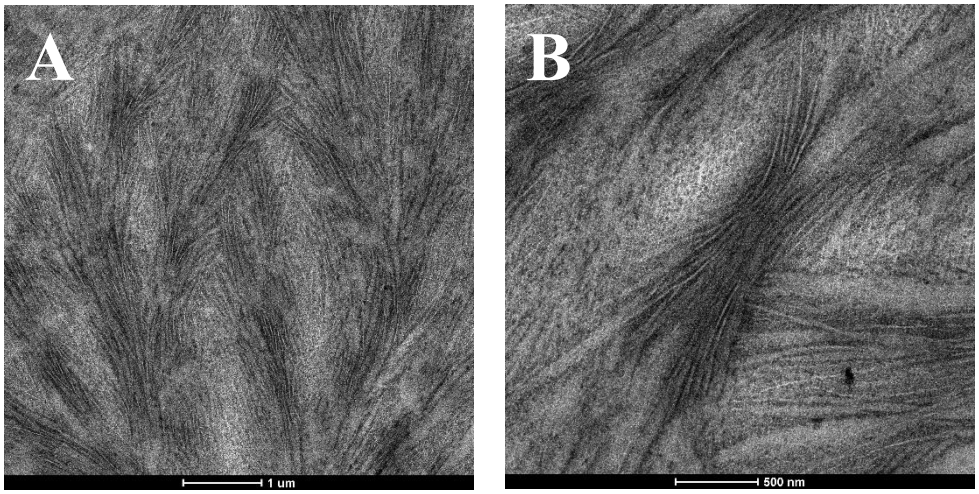

Figure 20. Bright field TEM micrographs of the iC6-sCC6 fraction the Sample 4 at different magnifications. The sample is RuO_4 stained for several hours, in order to enhance the contrast between the lamellar crystals (bright), and the amorphous regions (dark).

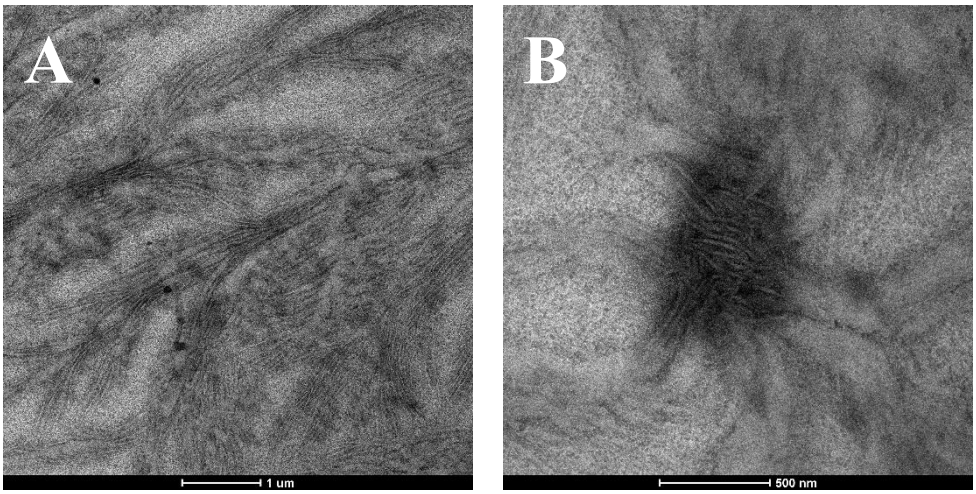

Figure 21. Bright field TEM micrographs of the iCC6 fraction of the Sample 4 at different magnifications. The sample is RuO_4 stained for several hours, in order to enhance the contrast between the lamellar crystals (bright), and the amorphous regions (dark).

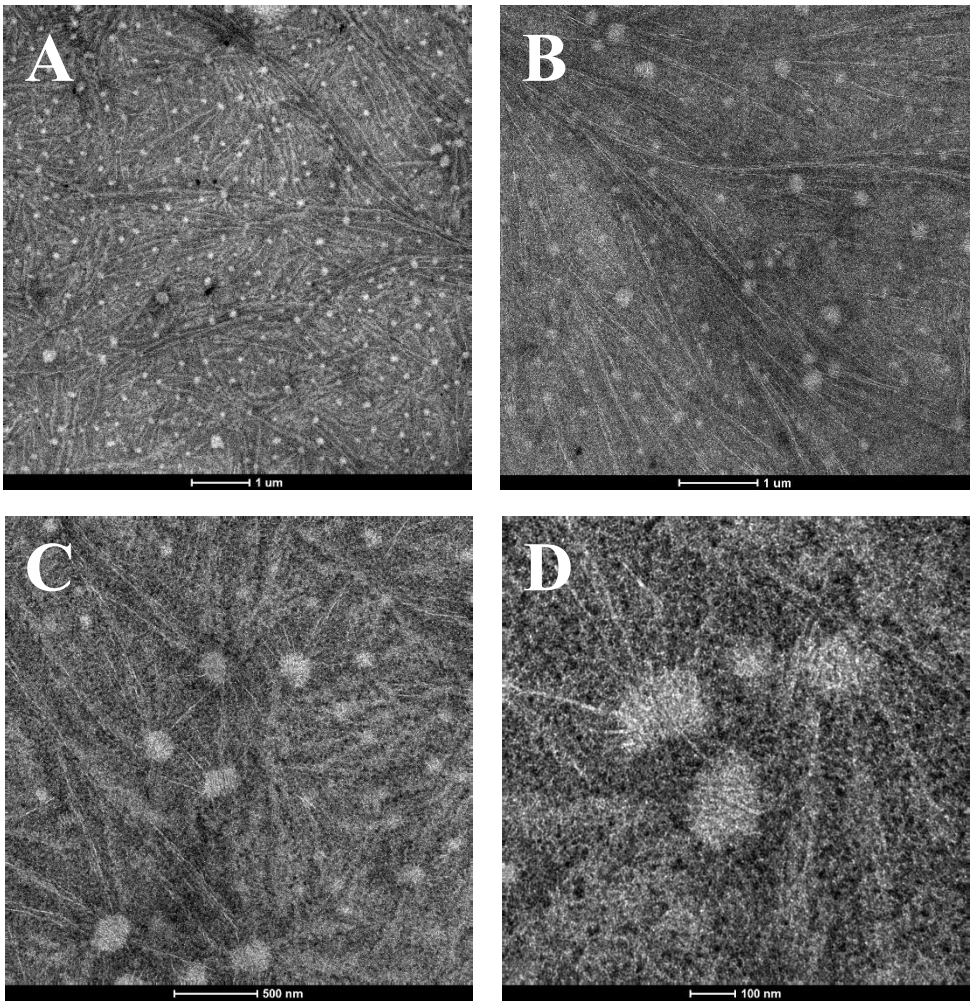

F**igure 22.** Bright field TEM micrographs of the Sample 5 at different magnifications. The sample is RuO_4 stained for several hours, in order to enhance the contrast between the lamellar crystals (bright), and the amorphous regions (dark).

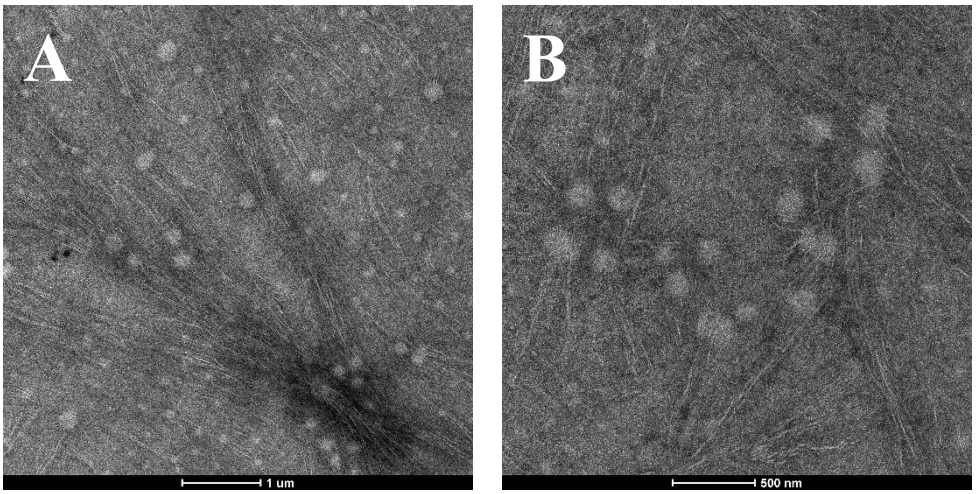

Figure 23. Bright field TEM micrographs of the iC6-sCC6 fraction of the Sample 5 at different magnifications. The sample is RuO_4 stained for several hours, in order to enhance the contrast between the lamellar crystals (bright), and the amorphous regions (dark).

3.3. Melt Rheology of OBCs

The effect of multiblock chain architecture and dispersity in block length on micro/meso-phase separation transition has been investigated in numerous studies so far.[18,19,24,26,32,97-106] It has been found that in monodisperse systems the order-disorder transition from a microphase separated morphology into a homogeneous state is essentially controlled by the average length of the blocks and only marginally by the number of blocks/chain, in agreement with theoretical predictions.[103-105] As for the effect of dispersity, an increase of dispersity of block length may lead to stabilization or destabilization of the ordered phase.[32,33,100,107,108] In particular, with increasing dispersity, two competitive effects come into play, that is the role of the chains with long blocks which tends to stabilize microphase separation on one hand,[32,100] and the enhancement of concentration fluctuations which tends to destabilize microphase separation, on the other hand.[33,106-108] Which one of the two effects

will prevail depends on the composition and the molecular mass of the polymer chains. Therefore, in disperse systems of multi-block copolymers the final morphology obtained at room temperature is not only function of the average block segregation strength, and average volume fraction of the blocks, but also of the disperse nature of the blocks, as the number of blocks/chain plays a minor role.[32,33,100,106-108] In the case of block-copolymers containing crystallizable blocks, the final morphology is further complicated by the possible crystallization from a homogeneous or heterogeneous melt, and in the latter case by occurrence of crystallization in confined domains with consequent preservation of melt morphology or through complete destruction of it and consequent formation of lamellar stacks organized in spherulitic superstructures, similar to those ones occurring in a homopolymer, or deriving from a homogeneous melt.[43]

It is worth noting that spotted morphologies similar to those observed for Samples 1, 2, and 5 and the corresponding superior fractions in Figures 9, 12-15, 22, and 23 were obtained in Ref. 72 in the case of ethylene/1-octene samples with M_w of ≈ 182 and 250 kDa, hard block content of ≈ 17–18 mol% and difference in octene concentration between hard and soft blocks Δ*oct* of 23 and 33.6 mol%, respectively, crystallized from the melt by epitaxy, using benzoic acid (BA) as substrate. The obvious difference with respect to the pass-through morphology shown by Samples 1, 2, and 5 consists in the high degree of orientation of the lamellar crystals by effect of BA epitaxy. In absence of BA, the sample with Δ*oct* = 23 mol% showed stacks of lamellar crystals homogeneously distributed all over the film, whereas the sample with Δ*oct* = 33.6 mol% showed confined crystallization of the hard blocks in domains of not well-defined shape, embedded in the soft-block-rich matrix.[72] As both samples were shown to crystallize from a phase separated melt, it was inferred

that the observed crystallization behavior was due to the differences in octene concentration between hard and soft segments (Δ*oct*), resulting in significant differences in segregation strength. Moreover, depending on the mixing state in the melt and crystallization temperature, confined and/or unrestricted crystallization of hard blocks was also observed in Ref. 69, in the case of ethylene/1-octene multiblock copolymers with M_w ≈ 90 kDa, hard block content of ≈ 20 and 35 wt%, and Δ*oct* of ≈ 21–22 mol%. In particular, the formation of crystals meandering the soft-block-rich domains, eventually bridging the crystals formed in adjacent hard-block-rich domains was attributed to the non-negligible solubility of the hard blocks in the soft matrix, even when crystallization occurred from a pre-mesophase separated melt.

On this ground, it may be hypothesized that the crystallization behavior of the here analyzed Samples 1 - 5 is controlled by the state of the melt. One should expect that mesophase separation occurs already in the melt for the Samples 1, 2, and 5, and does not occur at all for the Samples 3 and 4. The possible occurrence of mesophase separation in the melt is in contrast with the low segregation strength of the analyzed samples. In particular, the value of segregation strength $N_{HS}\chi$ may be calculated with Equation:

$$N_{Hs}\chi = \frac{M_{HS}}{\rho RT}(\delta_{soft} - \delta_{hard})^2 \quad (4)$$

In Equation 4, N_{HS} is the number of monomers in a HS building unit, χ is the Flory interaction parameter, ρ is the density of the multiblock copolymers in the melt (≈ 0.77 g/cm^3, at 170 °C), *R* the gas constant and *T* the absolute temperature.[26] The symbols δ_{soft} and δ_{hard} indicate the solubility parameters for the soft and hard blocks, respectively, modeled, as in Ref. 26, following the empirical equation $\delta_{soft} - \delta_{hard} = -0.95\, x_O$ MPa$^{0.5}$, where δ_{soft} and δ_{hard} correspond to the solubility parameters of an ethylene/1-octene random copolymers with

x_O octene molar content ($x_O \approx 0.2$) and of PE, respectively. Considering that the highest molecular mass of the HS building units in the OBC samples estimated through SAXS analysis is of the order of 50-60 kDa (Table 7), values of segregation strength of the order of 2-3 (at 170°C) may be calculated through Equation 4. Therefore, the possible microphase separation occurring in the melt may not be predicted using conventional thermodynamics schemes.

In order to probe the role of the melt on the solid-state morphology developed at nanoscale by the commercial grades Samples 1 to 5, rheological measurements in the linear regime have been performed within a collaboration with the Laboratory of Soft Matter, Complex Fluids and Rheology (LSMR) at the Department of Chemical, Materials, and Industrial Engineering of the University of Naples "Federico II". Linear rheology, indeed, allows to investigate the state of a melt, as this technique is highly sensitive to the presence heterogeneity, such as those arising from mesophase separation.[73] In fact, mesophase separation in the melt state induces a failure of the time-temperature superposition principle (TTS) at low frequencies, that is, at length scales beyond that of the single chains.[73]

Measurements are shown for the unfractionated Samples 1 and 3, as examples of OBCs showing solid state morphologies characterized by heterogeneous features in the lamellar arrangement (Figure 9) and more conventional lamellar morphology (Figure 16), respectively.

The master curves of the Samples 1 and 3 have been obtained by measuring frequency-dependent viscoelastic moduli (or by converting creep compliance at low frequencies) at different temperatures, namely 135, 150, and 170°C, and applying the TTS principle using 150°C as reference temperature (see Figure 24). It is apparent that the TTS principle is valid for the Sample 3 (Figure 24A) over the entire frequency range, thus showing that for this sample no phase

separation occurs in the melt, in agreement with the homogeneous distribution of lamellae in the corresponding TEM images (Figure 16).

Conversely, in the case of the Sample 1, at low frequencies the viscoelastic modulus measured at different temperatures deviate from a single master curve (see Figure 24B). According to Kossuth et al., such a behavior corresponds to a disordered state with ordering fluctuations.[109] The TTS failure shown by the Sample 1 in the low frequency tail region clearly indicates mesophase separation in the melt and accounts well for the heterogeneous solid-state morphology shown in Figure 9.

A possible explanation of the remarkable differences in the solid-state morphology and melt state of the two samples may reside in the molecular masses and in their intrinsic polydispersity. Indeed, compared with the Sample 1, the Sample 3 has nearly halved molecular mass, smaller number of blocks/chain, and higher block length (Table 6). It is argued that the low molecular mass fraction of chains in Sample 3 acts as diluent, preventing an efficient long-range segregation of the hard blocks. Furthermore, as discussed in the previous paragraph, the more uniform morphology observed for the Samples 3 may also be due to the too low concentration of the long HS building units.

All in all, the Samples 1 and 3 represent an exemplary case of polydisperse multiblock copolymers with a statistical distribution of the block length and number of blocks/chain, where two competitive effects responsible for the phase behavior come into play to a different extent. For the Sample 1, of high molecular mass, the role of the chains with long blocks in stabilizing mesophase separation prevails.[32,100] For the low molecular mass Sample 3, instead, the effect of concentration fluctuations is enhanced,[33,106-108] with consequent destabilization of mesophase separation, both in the melt and solid state.

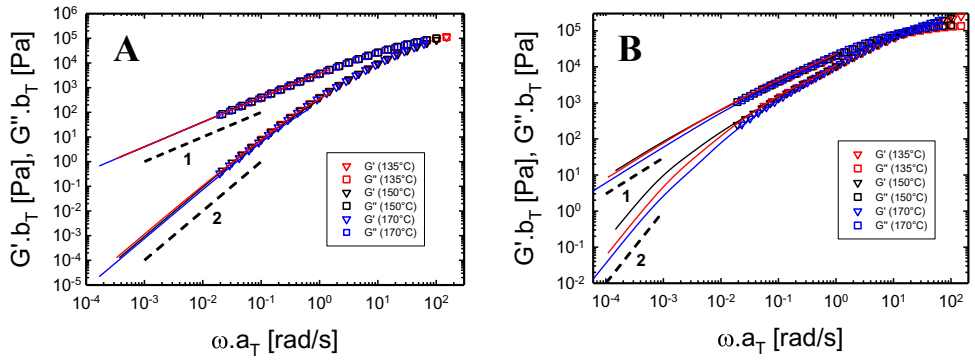

Figure 24. Master curves of the viscoelastic storage (*G*') and loss (*G*'') modulus at the reference temperature T_{ref} of 150°C for the Sample 3 (A) and the Sample 1 (B). The horizontal shift factors were 1.50 at 135 °C and 0.62 at 170 °C. No vertical shift factor was applied.

3.4. Thermal Fractionation

As a further step of the present investigation of the complex chain microstructure of the OBCs, the five commercial samples and the corresponding superior (iC6-sCC6 and iCC6) fractions (Table 8) have been subjected to thermal fractionation, resorting to a Successive Self-nucleation ad Annealing (SSA) protocol.[87] The SSA technique has been devised to resolve

the complex wide melting endotherms of polymers including defects that interrupt the regular sequences of the crystallizable units along the chains, in terms of "elementary melting processes".[87] As detailed in Chapter 2, the attitude of regular sequences of monomeric units of different length to crystallize separately is exploited resorting to successive events of a heating step up to a given self-seeding temperature T_s, a short isotherm (3 min) at T_s, and a successive cooling step to room temperature. The adopted scanning rate in the cooling and heating steps is 10°C/min (see Chapter 2). According to the Scheme 2 of Chapter 2, the regular sequences of monomeric units of higher length crystallize in the cooling step forming lamellar crystals of virtually any thickness, while the defects (1-octene units) and the soft blocks are rejected in the surrounding amorphous regions. In general, the thickest and most perfect crystals melt at high temperatures, whereas the thinnest and more imperfect crystals melt at lower temperatures. As a consequence, in the successive heating scan, since the highest temperature reached in consecutive SSA steps (the self-seeding temperature T_s) is gradually decreased in step of 5°C in the adopted protocol, not all the crystals melt, but the thickest and most perfect crystals that are formed in the preceding cooling steps survive, being merely subjected to consecutive annealing steps during the short isotherms. Therefore, at any selected T_s annealing and self-seeding processes occur, allowing the gradual fractionated crystallization of the sample across the SSA steps covering the whole melting range, through the formation of crystals with increasingly lower thickness. At the end of SSA procedure, the sample is heated up to high temperatures while recording a DSC thermogram, which reveals the presence of multiple endothermic peaks. The multiple peaks replace the broad endothermic phenomena of the pristine sample recorded in a standard DSC scan on the unannealed sample. The melting peaks correspond to the

melting of crystals of different thickness formed during the SSA protocol. Therefore, the distribution of melting peaks reflects the distribution of crystalline thickness in the sample, that in turn, for polymers with irregular chains, should reflect the distribution of the defects along the backbone. In the case of the OBCs, owing to the intrinsic polydispersity in the hard block length, the distribution of melting peaks should reflect not only the distribution of branching points along the chain backbone of the long hard blocks, but also the distribution of the hard block length. In order to establish which one of the two effects prevails, a model random copolymer synthetized with the Zr-based catalyst Cat1, containing 0.55 mol% of octene units, mimicking the octene-poor hard blocks, has been selected as reference sample. The main characteristics of the random copolymers are summarized in Table 9.

Based on a well-established protocol,[87] after creating an "initial standard semi-crystalline state" (see Chapter 2), the SSA protocol is applied starting from a first value of the self-seeding temperature, known as $T_{s\ ideal}$. It has been shown that the first self-seeding temperature is crucial. At this temperature, indeed, the sample should not experience annealing, but only self-seeding. A correct selection of the $T_{s\ ideal}$ is conveniently done[87] by performing Self-nucleation and Annealing (SNA) experiments[86] (see Chapter 2 for more details). In particular, the value of $T_{s\ ideal}$ is selected, with the help of a SNA protocol, as the temperature that causes maximum self-nucleation without producing annealing (see below).

Table 9. Number and mass average molecular masses M_n and M_w, polydispersity index Đ, total amount of octene units x_O, and fraction of hard blocks w_h for the random copolymer selected as reference for the SSA protocol.

Sample ID	M_n (KDa)	M_w (KDa)	Đ	x_O (wt%)	x_O (mol%)	w_h (wt%)
RC	44	91	2.1	/	0.55	/

As an example, the DSC curves recorded during the SNA protocol applied to the Sample 1 are reported in Figure 25 (a similar behavior is observed for the all the other commercial grades and the reference sample RC, see Appendix A3). In particular, the DSC thermograms recorded by cooling the sample from a T_s value to 25°C are reported in Figures 25A and 25B, whereas the subsequent heating thermograms recorded from 25 °C up to melting are reported in Figures 25C and 25D. The crystallization temperatures T_c extracted from the DSC thermograms of Figures 25A, B are reported in Figure 26 as a function of the seeding temperature T_s. These data allow to define the classical three SNA domains.[86] For the Sample 1, domain I exists for $T_s > 125$°C. Within domain I, that is at temperatures higher than a threshold, all the self-nuclei are destroyed; as a matter of fact, T_c vs T_s remains constant (Figure 26) and no shift of the crystallization peaks in the cooling curves of Figure 26A is observed. Domain II is located roughly between 125°C and 123°C. In this quite narrow domain, the values of T_c increase rather steeply with the decrease of T_s (Figure 26). The decrease of T_c during cooling entails an increase in crystallization rate, ascribable to the presence of self-nuclei, the concentration of which increases with decrease of T_s. Domain III starts from $T_s < 123$°C, with the appearance of an endothermic peak at high temperature in the melting thermograms of Figure 25D, due to the melting of annealed crystals. That is, for $T_s < 123$°C the sample undergoes self-seeding and annealing. Since the appearance of this annealing-related peak is the hallmark of the transition from the domains II to the domain III, we selected the T_s immediately preceding the T_s at which this peak appears as $T_{s\,ideal}$.

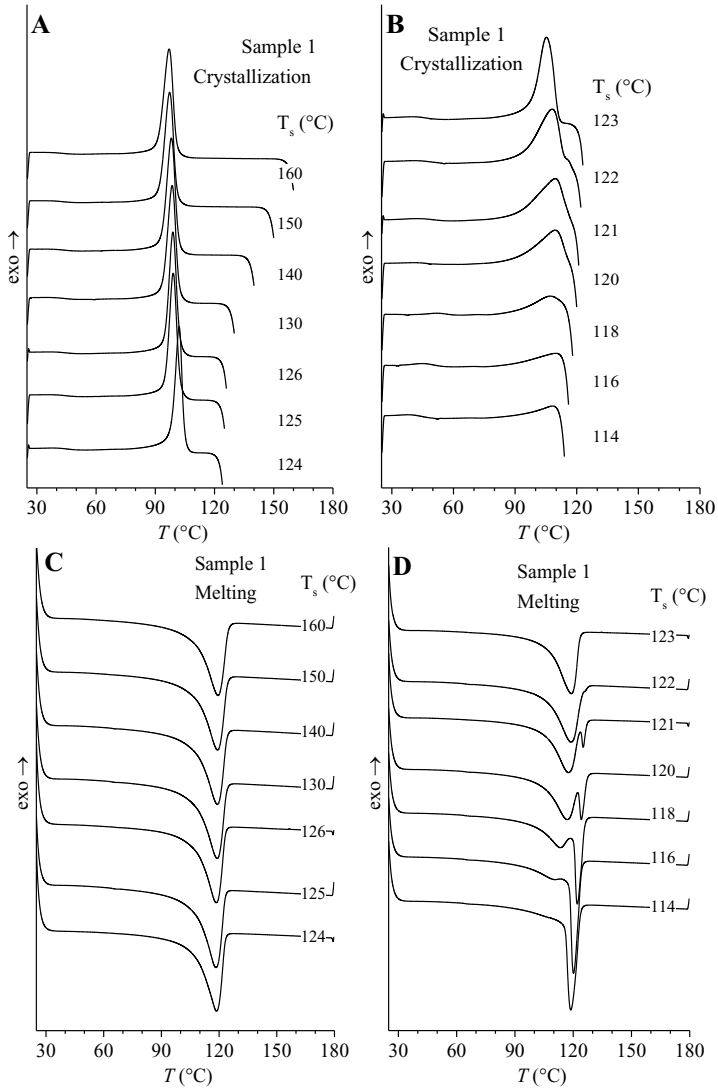

Figure 25. DSC thermograms recorded in the SNA protocol for the Sample 1, during the DSC cooling steps from the selected T_s to 25 °C (A, B) and the subsequent heating DSC scans (C, D). The scanning rate is 10°C/min.

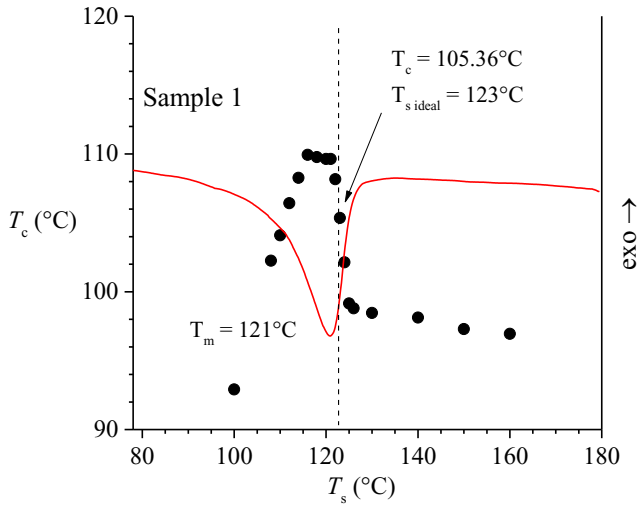

Figure 26. Crystallization temperatures T_c as a function of the seeding temperature T_s extracted from the SNA cooling scans of Figures 25A, B. The (T_s, T_c) diagram defining the domains I-III overlies the standard DSC melting curve recorded at 10°C/min, which is indicated with a red line. The values of $T_{s\ ideal}$ and the corresponding values of T_c on the *y*-axis, along with the melting temperatures T_m obtained from standard DSC analysis are also indicated.

Table 10. Values of $T_{s\ ideal}$ for the five OBCs samples and the random copolymer selected as benchmark.

Sample ID	$T_{s\ ideal}$ (°C)
Sample 1	123
Sample 2	124
Sample 3	124
Sample 4	124
Sample 5	123.5
RC	126.5

The values of $T_{s\ ideal}$ found for all the five samples and the random copolymer RC selected as benchmark are reported in Table 10. It is apparent that the values of $T_{s\ ideal}$ for the Samples 1-5 are similar, and are comprised in the range 123-124 °C, whereas for the RC samples the value of $T_{s\ ideal}$ is higher, and equal to 126.5°C.

The DSC thermograms recorded during the SSA protocol for the Samples 1-5, their corresponding superior fractions, and the random copolymer are reported in the Appendix A4. The final SSA melting DSC thermograms relative to the unfractionated OBC samples and the reference random copolymer RC, instead are reported in Figure 27, whereas the final SSA melting curves relative to the unfractionated Samples 1-5 are compared with those one relative to the corresponding superior (iC6-sCC6 and iCC6) fractions in Figure 28. In Figures 27 and 28, for each sample, the final SSA heating scan is compared with the corresponding standard non-isothermal heating scan, recorded after cooling from the melt at 10 °C/min. The heating rate is in all cases of 10°C/min.

All the samples show a series of sharp melting peaks in the DSC heating thermograms recorded at the end of the SSA protocol. The number of peaks correspond to the number of SSA steps, that is to the number of the selected T_s values minus one, since the initial step, performed up to $T_{s\,ideal}$ does not induce annealing, but only self-seeding.[86] An additional broad melting peak is also present in the tail at low temperatures (60-90°C) due to the melting of the crystals that are formed during the cooling from the lowest employed value of T_s.

The DSC thermogram of the random copolymer RC recorded at the end of the SSA protocol (curve a of Figure 27) includes one relevant sharp peak, followed by four sharp peaks of low area. The melting peak distribution of the RC sample is in agreement with the low concentration of defects (0.55 mol%), the random distribution of the comonomeric units along the chain, and the consequent rather high values of the average length of crystallizable methylene sequences (methylene sequence length MSL) (equal to two times the inverse

of the fractional amount of 1-octene units, i.e., $2/5.5\ 10^{-3} \approx 400$ methylene units).

The OBC samples and the corresponding fractions, instead, show a more complex distribution of the melting peaks. All the samples and the corresponding fractions show 5-6 sharp peaks. For the Samples 1, 3, and 4 and the corresponding fractions, except for the iCC6 fraction of the Sample 1, the first melting peak occurring at high temperatures is dominant and has an area which is at least 4 times the area of the other peaks at lower temperatures. For the iCC6 fraction of the Sample 1, and the Samples 2 and 5, instead, the first two peaks at high temperature show comparable area, while all the other peaks are less pronounced. The more complex distribution of the melting peaks shown by the OBCs arises from a more complex distribution of methylene crystallizable sequences (MSL), than that occurring for the Sample RC. In particular, due to the high concentration of 1-octene units (≈ 19 mol%), the soft blocks do not include methylene sequences long enough to crystallize in the adopted SSA protocol. Therefore, the distribution of melting peaks observed in the final SSA DSC heating scans essentially reflects the distribution of MSL belonging to the sole hard blocks. These sequences are interrupted not only by the presence of 0.5 mol% 1-octene units along the backbone but also by the intrinsic statistical multiblock architecture of the OBCs and the corresponding superior fractions. In other terms, only in the hypothesis that the hard blocks were very long, the melting point distribution in the SSA final melting scan of the OBCs would be similar to that of the reference sample RC. However, since the length of the hard blocks is not too high and is polydisperse (Table 7), the SSA behavior of the OBCs should necessary also reflect the distribution of the hard block length. On this basis, it may be inferred that the melting peaks distribution shown by the OBCs reflects a distribution of lamellar thickness

that includes long and short methylene sequences belonging to the hard blocks. Due to molecular fractionation occurring upon crystallization, the longer the methylene sequences, the higher the crystal thickness and the higher the melting temperature.[110,111] In principle, chain folded and unfolded lamellar crystals may both form, depending on the MSL value. In particular, as long paraffins begin to fold at a chain length that includes around 150 carbon atoms, [112-114] the lamellar crystals including stems of length lower than 150 methylene units are expected to be unfolded.

The values of the MSL have been calculated from the temperatures of the multiple melting peaks of Figures 25 and 26 (black curves), using the two empirical equations suggested by Zhang and by Keating,[115-117] and the Gibbs-Thomson equation.[88] In the works of Zhang[115] and Keating,[117] the relationship between the temperature of each peak T_m(MSL) in a SSA melting curve and the MSL value was obtained through calibration curves based on SSA[115,117] and stepwise crystallization[116] experiments on linear hydrocarbons of known MSL values. The calibration equations are:

$$ln\,(X) = 0.3451 - \frac{142.2}{T_m(MSL)} \quad (5)^{115}$$

$$ln\,(X) = 0.331 - \frac{135.5}{T_m(MSL)} \quad (6)^{117}$$

where X is defined as the mole fraction of carbon atoms in a methylene unit. X can be easily transformed in the values of methylene sequence lengths (MSL) as it follows:

$$MSL = \frac{2X}{1-X} \quad (7)^{115}$$

An alternative approach to convert the final SSA endotherms to methylene sequence lengths is based on the Gibbs-Thomson equation:

$$T_m(MSL) = \frac{T_m^0\,(1 - 2\sigma_e)}{l_c \Delta H_m^0} \quad (8)$$

where T_m^0 is the equilibrium melting temperature (415K), σ_e is the fold surface free energy, l_c is the lamellar thickness, and ΔH_m^0 (280 MJ/m^3) is the melting enthalpy of the defect-free PE crystal in the orthorhombic form. Two different values of σ_e can be adopted: 90 mJ/m^2, which is valid for extended chain crystals of PE, and 44 mJ/m^2, valid for folded chain crystals of PE.[88] Hence, for each value of T_m(MSL), a value of lamellar thickness l_c can be calculated and the MSL values can be obtained as the ratio between l_c and the chain periodicity c of PE in the orthorhombic form (0.254 nm), multiplied by 2. The MSL values obtained with the three different methods for the five commercial grades, for their superior iC6-sCC6 and iCC6 fractions, and for the standard random copolymer are reported in Table 11, along with the melting temperature of each major detectable peak T_m(MSL) and the percentage area of each thermal fraction A(MSL). In particular, in the evaluation of the A(MSL) values from the individual melting peaks centered at T_m(MSL) in the final SSA heating thermograms, the possible presence of humps spanning the temperature range 65-90 °C value has been neglected. These subsidiary endotherms, indeed, corresponds to the melting of crystals formed during cooling from the lowest T_s, and do not correspond to the crystals formed in the SSA protocol. In all cases their relative amount is less than 10%.

The values of MSL obtained with the calibration curves of Zhang and Keating are in good agreement with those calculated with the Gibbs-Thomson equation adopting 90 mJ/m^2 as σ_e, in particular for the peaks at low temperatures (Table 11). For all the samples, the sequence lengths are rather short and range from 50 CH_2 groups up to 180 CH_2 groups.

It is worth noting that the calibration curve of Keating et al. yields values of MSL that are higher than those obtained with the equation found by Zhang et al. because they used stepwise crystallization, rather than SSA experiments. In the case of the Gibbs-Thomson equation with σ_e = 44 mJ/m^2, the MSL values are significantly lower, going from 20 to 60 carbon atoms. In all cases the MSL values are lower than 150, and only for the lamellar crystals melting at the highest T_m(MSL), values close to 180-200 are obtained using to the Keating equation.[117] All in all, this suggests that the MSL values extracted from SSA experiments correspond to the number of CH_2 units in a stem, included in unfolded lamellar crystals, and therefore they mimic to a good approximation the effective values of the hard block length.

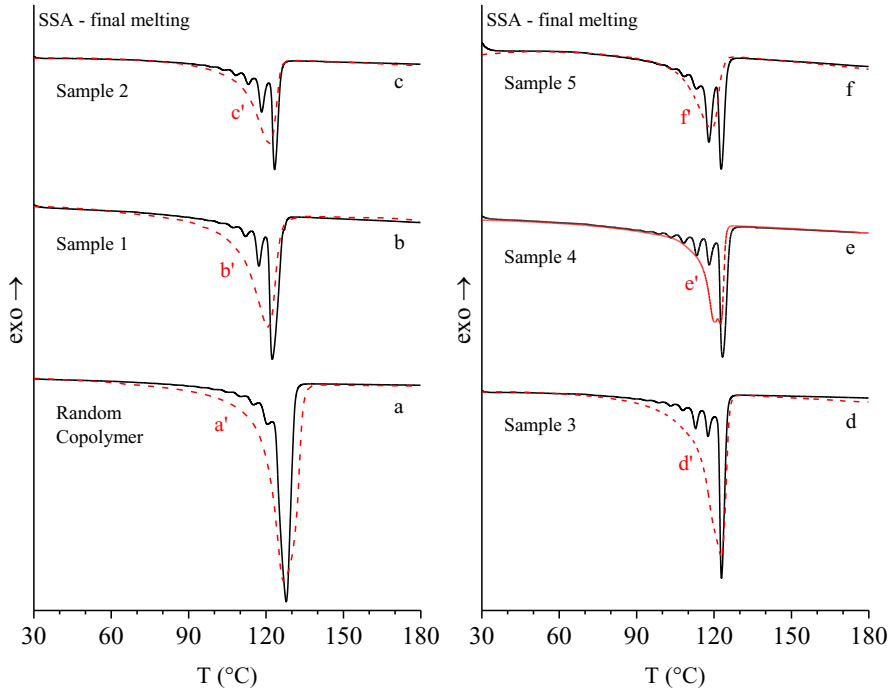

Figure 27. SSA final heating DSC thermograms (a-f, black curves) and standard DSC heating scans (a'-f', red dashed lines) relative to the OBC Samples 1-5 and the random copolymer RC used as benchmark. The heating rate is 10°C/min. The standard heating scans (a'-f') are recorded after cooling from the melt at 10 °C/min.

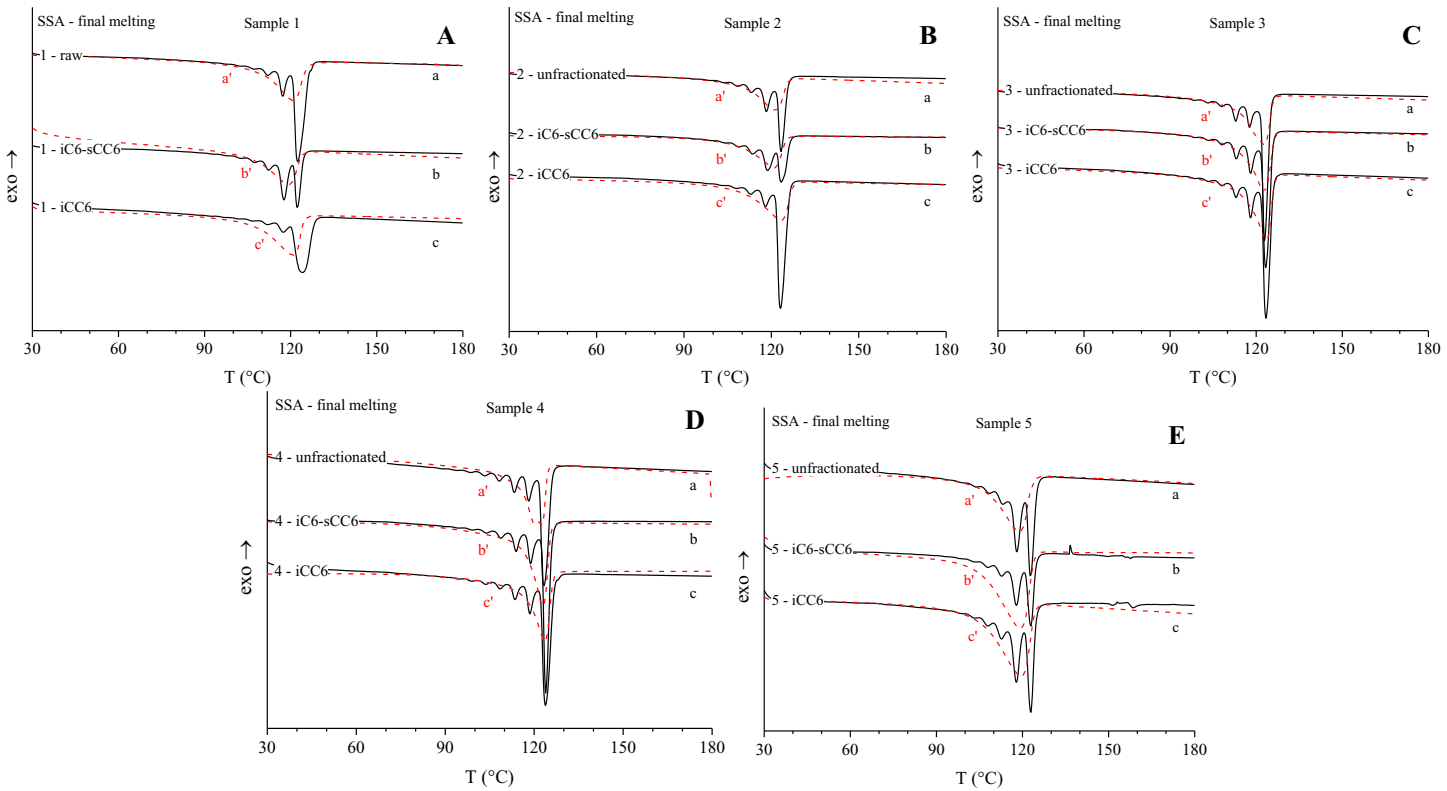

Figure 28. SSA final heating DSC thermograms (a-c, black curves) and standard DSC heating scans (a'-c') red dashed lines relative to the unfractionated OBC Samples 1-5 (a,a') and the corresponding iC6-sCC6 (b,b') and iCC6 (c,c') fractions. The heating rate is 10°C/min The standard heating scans (a'-c') are recorded after cooling from the melt at 10 °C/min.

Table 11. Percentage of iC6-sCC6 and iCC6 fractions, melting temperature T_m(MSL) and percentage area A(MSL) of each melting peak in the SSA final heating DSC thermograms, methylene sequence lengths (MSL) obtained with three different methods and degree of crystallinity x_c extracted from WAXS.

				Gibbs-Thomson				Zhang[115]	Keating[117]	
				σ_e (90 mJ/m^2)		**σ_e (44 mJ/m^2)**				
Sample	**wt%**	**T_m(MSL) (°C)**	**A(MSL) (%)**	**l_c (nm)**	**MSL**	**l_c (nm)**	**MSL**	**MSL**	**MSL**	**x_c(WAXS) (%)**
1	/	123.0	67.3	14.2	112	6.9	55	144	181	12
		117.3	15.3	10.9	86	5.3	42	104	124	
		112.5	9.7	9.1	72	4.4	35	84	97	
		107.3	1.8	7.7	61	3.8	30	69	78	
		103.9	5.9	7.0	55	3.4	27	61	70	
1-iC6-sCC6	50.5	122.5	32.0	13.8	109	6.7	53	139	173	20
		117.8	35.8	11.1	87	5.4	43	106	127	
		112.7	17.8	9.1	72	4.5	35	84	98	
		107.5	7.9	7.8	61	3.8	30	69	79	
		103.1	3.2	6.9	54	3.4	27	60	68	
		99.0	3.2	6.2	49	3.0	24	53	59	
1-iCC6	35.3	124.1	72.4	15.0	118	7.3	58	154	196	20.2

		117.4	10.3	10.9	86	5.3	42	104	125	
		112.5	12.7	9.1	71	4.4	35	84	97	
		106.7	3.0	7.6	60	3.7	29	67	77	
		102.6	1.5	6.8	53	3.3	26	59	66	
2	/	123.5	44.6	14.6	115	7.1	56	149	188	12
		118.5	26.5	11.4	90	5.6	44	110	132	
		113.5	12.9	9.4	74	4.6	36	87	102	
		108.4	9.4	8.0	63	3.9	31	71	82	
		103.7	2.1	7.0	55	3.4	27	61	69	
		100.1	4.5	6.4	50	3.1	25	55	61	
2-iC6-sCC6	67.3	123.8	33.7	14.8	116	7.1	57	151	192	13.2
		118.9	26.4	11.6	92	5.7	45	113	136	
		113.8	18.5	9.5	75	4.7	37	89	104	
		108.7	9.6	8.1	63	3.9	31	72	83	
		104.4	4.5	7.1	56	3.5	27	63	71	
		100.1	7.2	6.4	50	3.1	25	55	61	
2-iCC6	17.5	123.5	64.1	14.5	114	7.1	56	148	187	18
		118.2	12.9	11.3	89	5.5	43	109	130	

		113.2	9.3	9.3	73	4.6	36	86	101	
		108.2	2.0	7.9	62	3.9	31	71	81	
		105.1	5.4	7.3	57	3.5	28	64	72	
		96.7	6.2	5.9	47	2.9	23	50	56	
3	/	123.1	53.2	14.2	112	6.9	55	145	182	14
		118.0	20.1	11.2	88	5.5	43	108	129	
		112.9	11.2	9.2	73	4.5	36	85	99	
		108.3	10.4	7.9	63	3.9	31	71	82	
		102.9	3.7	6.9	54	3.4	26	60	67	
		98.8	1.3	6.2	49	3.0	24	53	59	
3-iC6-sCC6	78.2	123.5	57.2	14.6	115	7.1	56	149	188	12.5
		118.3	20.6	11.3	89	5.5	44	109	131	
		113.2	11.7	9.3	73	4.6	36	86	100	
		108.4	6.4	8.0	63	3.9	31	72	82	
		103.6	1.4	7.0	55	3.4	27	61	69	
		100.8	2.6	6.5	51	3.2	25	56	63	
3-iCC6	4.7	123.6	55.9	14.6	115	7.2	56	149	189	25
		118.2	19.5	11.3	89	5.5	43	109	130	

		113.1	10.8	9.3	73	4.5	36	86	100	
		108.3	6.1	8.0	63	3.9	31	71	82	
		103.6	1.4	7.0	55	3.4	27	61	69	
		101.5	6.3	6.6	52	3.2	25	57	64	
4	/	123.6	60.3	14.6	115	7.1	56	149	189	18
		118.4	16.7	11.4	89	5.6	44	109	131	
		113.5	12.0	9.4	74	4.6	36	87	102	
		108.5	6.9	8.0	63	3.9	31	72	82	
		103.4	3.2	6.9	55	3.4	27	61	68	
		98.6	0.9	6.2	49	3.0	24	52	59	
4-iC6-sCC6	71.0	124.1	57.4	15.0	118	7.3	58	154	197	18.1
		119.1	19.2	11.7	92	5.7	45	114	137	
		114.0	11.2	9.6	75	4.7	37	89	104	
		109.0	7.3	8.1	64	4.0	31	73	84	
		104.1	2.2	7.1	56	3.5	27	62	70	
		99.9	2.8	6.4	50	3.1	24	54	61	
4-iCC6	3.3	124.1	53.7	15.0	118	7.4	58	155	197	28.5
		118.7	16.4	11.5	91	5.6	44	112	134	

		113.7	12.5	9.5	75	4.6	37	88	103	
		108.7	9.3	8.0	63	3.9	31	72	83	
		103.9	5.5	7.0	55	3.4	27	61	70	
		99.6	2.6	6.3	50	3.1	24	54	61	
5	/	122.9	33.1	14.1	111	6.9	54	143	179	3
		118.2	30.6	11.3	89	5.5	43	109	130	
		113.5	17.6	9.4	74	4.6	36	87	102	
		108.4	9.2	8.0	63	3.9	31	71	82	
		104.1	4.9	7.1	56	3.5	27	62	70	
		100.1	4.6	6.4	50	3.1	25	55	62	
5-iC6-sCC6	59.9	122.8	34.3	14.0	111	6.9	54	142	178	6.9
		117.9	32.4	11.2	88	5.5	43	107	128	
		112.9	18.8	9.2	73	4.5	36	85	99	
		108.1	8.2	7.9	62	3.9	30	71	81	
		103.8	5.7	7.0	55	3.4	27	61	69	
		98.7	0.6	6.2	49	3.0	24	53	59	
5-iCC6	7.4	122.8	30.4	14.0	110	6.9	54	142	178	18.5
		117.9	29.2	11.2	88	5.5	43	107	128	

		112.9	17.3	9.2	73	4.5	35	85	99	
		108.0	8.9	7.9	62	3.9	30	71	81	
		103.8	3.8	7.0	55	3.4	27	61	69	
		100.0	10.5	6.4	50	3.1	25	55	61	
RC	/	127.5	69.3	18.6	146	9.1	72	203	277	58
		121.1	20.3	12.9	101	6.3	50	127	157	
		114.9	3.0	9.9	78	4.8	38	93	109	
		111.3	3.6	8.7	69	4.3	34	80	92	
		106.4	3.8	7.5	59	3.7	29	67	76	

Plotting the fractional amount of crystals of a given lamellar thickness melting at a given T_m(MSL) value (A(MSL)) as a function of MSL, a distribution mimicking the distribution of the MSL values in the hard blocks for the various samples and the corresponding fractions may be obtained. These distributions, along with the corresponding cumulative distributions, are reported in Figures 29-33. The values of MSL calculated following Zhang et al.[115] (Equation 5), have been used to build the distributions of Figures 29-33, as an example. Similar results would be obtained using the MSL values calculated through the Keating[117] (Equation 6) and/or the Gibbs-Thomson (Equation 8) approach. From the observation of Figures 29-33 it is clear that the relative amount of methylene sequences tends to increase with the increasing of the MSL value, for all the samples. In particular, the distributions of the MSL values of the unfractionated Samples 1-5 are compared with the distributions of the random copolymer in Figure 29. It is apparent that the MSL distribution of the random copolymer is completely different from that one of the OBCs. As an example, the 50% of the methylene sequences have length higher than 140 units for the RC, 100 units for the Samples 1 and 2, 90 units for the Samples 3 and 4 ,and 80 units for the Sample 5 (Figure 29B). The Samples 1 and 2 show similar cumulative distributions (Figure 29B), even though the relative distributions of the MSL sequences are dissimilar. The Samples 3 and 4 show similar relative and cumulative distributions (Figure 29A and B). The Sample 5, instead, shows a different behavior, as the MSL distribution reaches a quasi-plateau for MSL values in the range 100-140 units. The different SSA behavior of the Sample 5 with respect to the Samples 1-4 is due to differences in the fractional amount of hard blocks w_H that corresponds to ≈ 15 wt% for the Sample 5 and to 23-27 wt% for the other samples.

The relative and cumulative distributions of the MSL value for the unfractionated Samples 1-5 are compared with those of the corresponding superior fractions in Figures 30-33. It is apparent that the relative and cumulative distributions of the unfractionated Sample 1 follow that of the iC6-sC6 fraction for MSL values lower than 100 units and increases steeply due to the contribution from the iCC6 fraction for MSL values higher than 100 units. The iCC6 fraction, in particular, contains a high amount of segments with MSL values higher than 100 units. The relative and cumulative MSL distributions of the Samples 2-4 (Figures 31, 32) essentially follow those of the iC6-sCC6 fractions. In particular, the unfractionated Samples 3 and 4 and their superior fractions show similar MSL distributions (Figure 32). Finally, for the Sample 5 (Figure 33) the relative and cumulative distributions of the superior fractions account for less than 70% of the MSL distribution of the unfractionated sample, at both low and high MSL values, in agreement with the presence of about 30 wt% of an sEE and an iEE-sC6 fractions (Table 8).

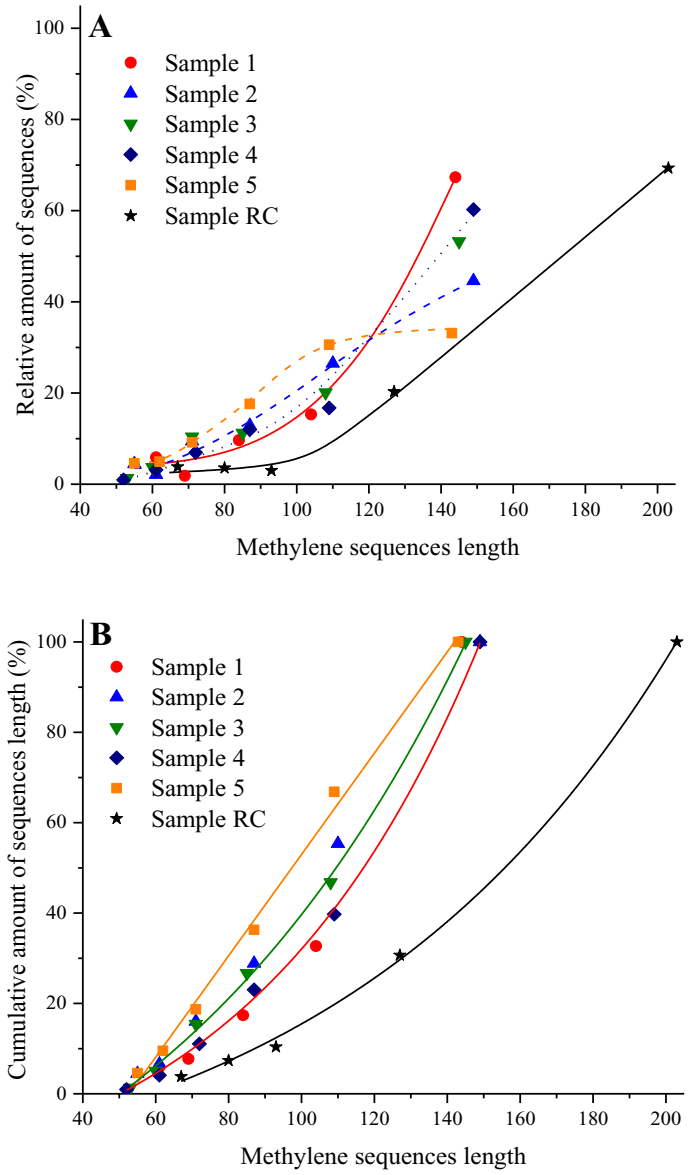

Figure 29. Relative (A) and cumulative (B) distribution of methylene sequences in a stem as a function of the methylene sequence length, calculated following Zhang et al.[115] for the five commercial grades and the random copolymer chosen as reference.

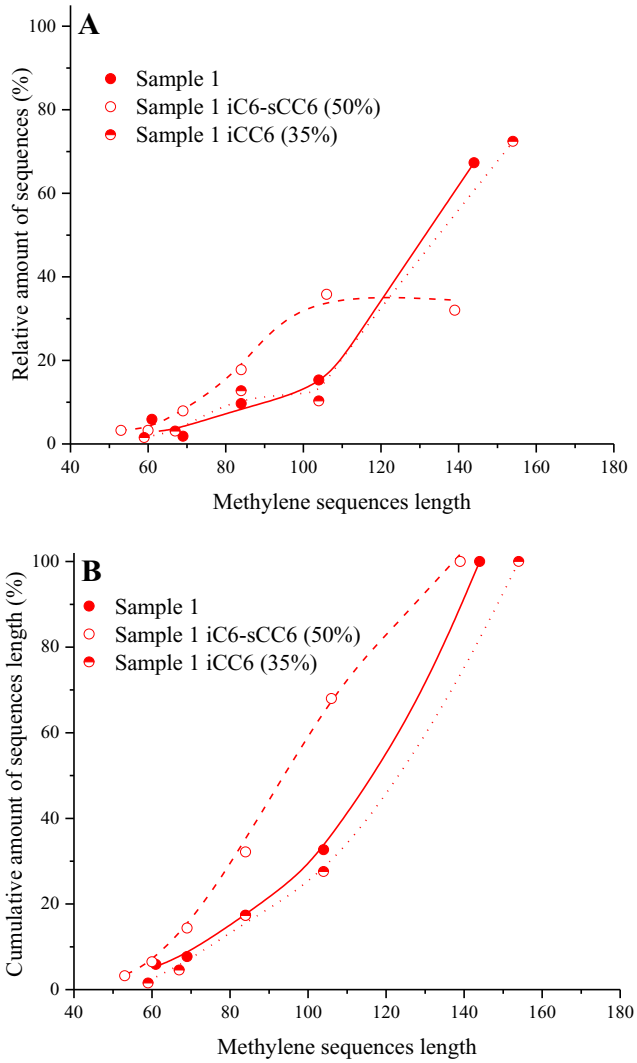

Figure 30. Relative (A) and cumulative (B) distribution of methylene sequences length, calculated following Zhang et al.[115] for the Sample 1 and the corresponding iC6-sCC6 and iCC6 fractions.

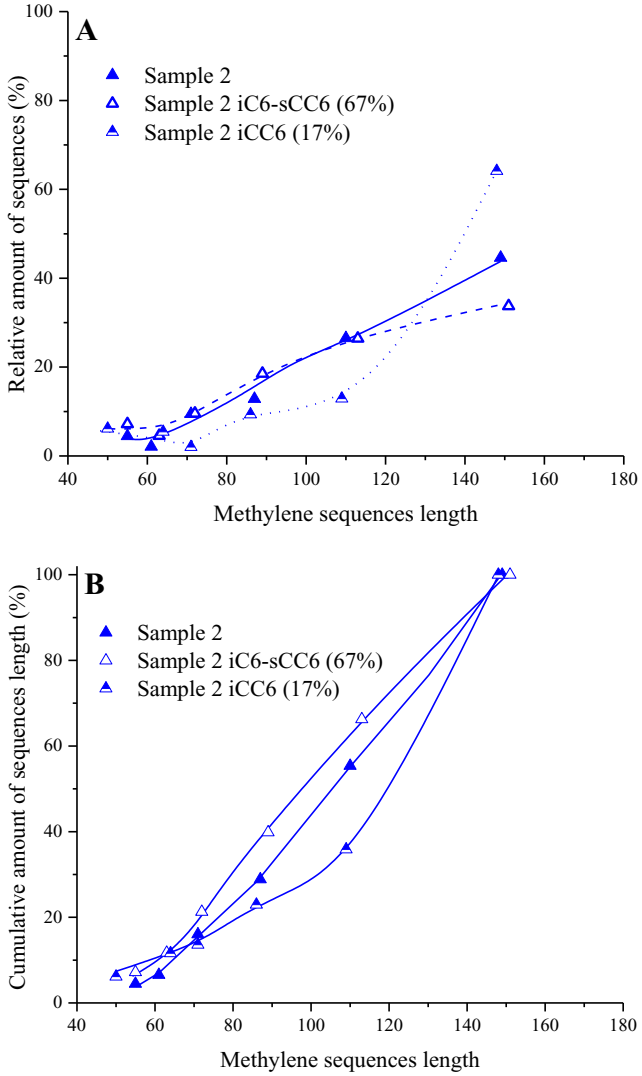

Figure 31. Relative (A) and cumulative (B) distribution of methylene sequences length, calculated following Zhang et al.[115] for the Sample 2 and the corresponding iC6-sCC6 and iCC6 fractions.

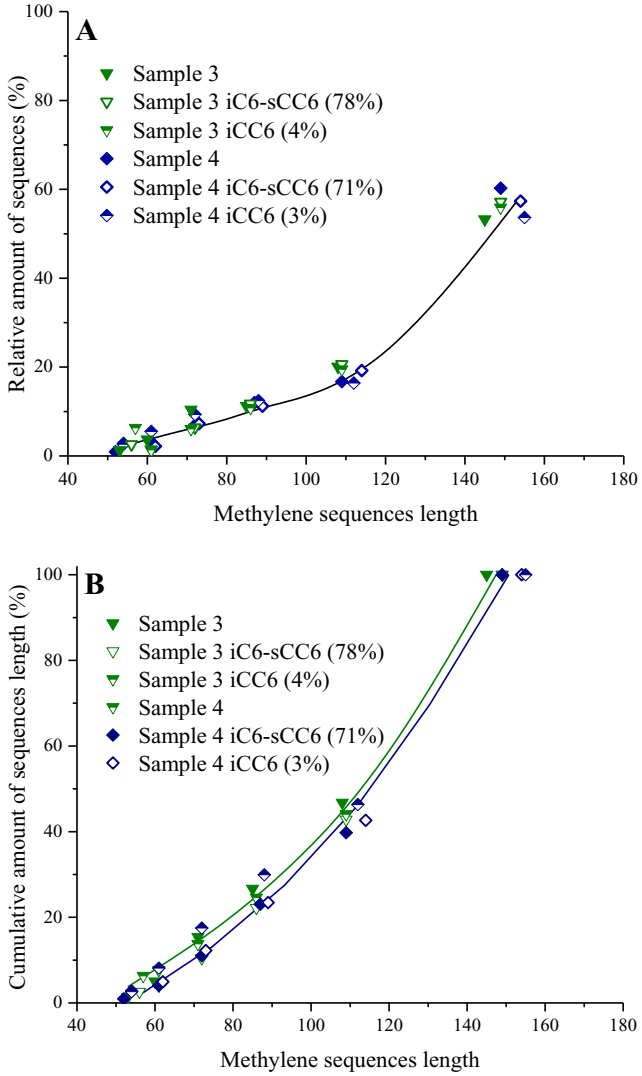

Figure 32. Relative (A) and cumulative (B) distribution of methylene sequences length, calculated following Zhang et al.[115] for the Sample 3 (down triangles) and Sample 4 (lozenges) and the corresponding iC6-sCC6 and iCC6 fractions.

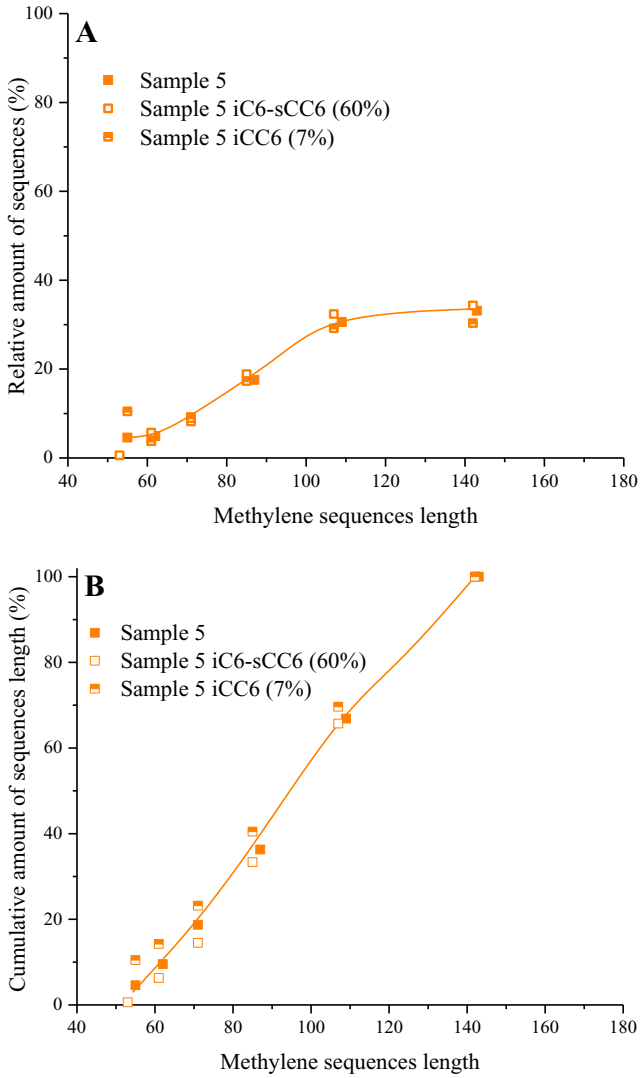

Figure 33. Relative (A) and cumulative (B) distribution of methylene sequences length, calculated following Zhang et al.[115] for the Sample 1 and the corresponding iC6-sCC6 and iCC6 fractions.

The most important result of this analysis consists in having evidenced that the MSL distribution of the OBCs is a good approximation of the effective distribution of the hard block length. In general, the most abundant iC6-sCC6 fraction controls the chain microstructure of the OBCs and hence also the

crystallization properties in the SSA protocol. Even though the SSA technique does not allow probing directly differences in the MSL distribution occurring at intra and intermolecular level within the different fractions, it is a powerful tool that allows highlighting the wide constitutional heterogeneity of the OBCs complex systems.

3.5. Conclusions

The inter- and intrachain non-uniform constitution of the ethylene/1-octene statistical multiblock copolymers from the Dow Chemical Company (OBCs) has been studied focusing on a microstructural, structural, morphological, and thermal analysis. The study has been carried out on both as-polymerized samples and on the four fractions obtained through exhaustive solvent fractionation in boiling solvents. In particular, thanks to the combination of aCEF, SAXS, and TEM analysis, it was revealed that these systems are reactor blends of chains having different constitutions. The four fractions consist of two poorly crystalline fractions, namely a sEE and an iEE-sC6 fraction, constituted by soft blocks not linked to hard blocks or linked to short hard blocks able to crystallize and form tiny lamellar crystals, and two semicrystalline fractions, namely an iC6-sCC6 and an iCC6 fractions, which include long ethylene sequences and are able to crystallize in lamellar stacks organized in well-formed spherulitic superstructures. aCEF analysis reveals that the chains within the fractions are, in turn, non-uniform, as indicated by the presence of broad and multiple elution peaks in the corresponding traces. By applying a semi-empirical method based on the high temperature elution peaks of aCEF traces, a lower bound for the values of the molecular mass of the hard (M_H) and soft (M_S) blocks in a HS building unit was calculated,

corresponding to 1-2 kDa and 3-4 kDa, respectively. The similar aCEF profiles for the iC6-sCC6 and iCC6 fractions and in particular the presence of elution peaks at identical temperatures, suggest that the main differences between them namely consist in differences in the distribution of the hard and soft blocks length. These similarities suggest that the iC6-sCC6 fractions contain a lower relative amount of long hard blocks and/or a higher relative amount of long soft blocks than the iCC6 fractions.

A more in-depth analysis shedding light on the intrachain and interchain distributions of block length, also revealed that in the unfractionated samples and in the most crystalline fractions at least three different population of HS building units exist, accounting for the similarities between these two fractions and the unfractionated samples. Resorting to IDF analysis of SAXS data, two populations of HS building units have been identified, showing values of the molecular mass of the hard blocks M_H corresponding to 4-9 kDa and 10-16 kDa and values of the molecular mass of the soft blocks M_S equal to 12-20 kDa and 30-44 kDa (Table 7). A third population of lamellar stacks has also been identified, the molecular masses of the hard M_H and soft M_S blocks in a HS building unit being calculated resorting to the CF analysis. They are in good agreement with the lower bound values deduced from the aCEF method, that is 2-3 kDa and 6-8 kDa by CF-based analysis *vs*. 1-2 kDa and 3-4 kDa by aCEF-based analysis. Therefore, based on this combined structural and microstructural analysis, it has been possible to establish that the sEE fractions include chains constituted by long soft block not linked to hard blocks and/or linked to hard blocks of molecular mass M_H lower than 1 kDa; the iEE-sC6 fractions include chains made up of short hard blocks (M_H <1kDa) alternating with soft blocks of average molecular mass $M_S \approx$ 3-4 time higher than M_H; the iC6-sCC6 and iCC6 fractions consist of chains characterized by the random

enchainment of hard blocks with molecular mass M_H comprised in the range 2-16 kDa alternating with soft blocks with M_S values comprised between 6 and 44 kDa. However, no quantitative information about the distribution of the hard block length could be obtained.

TEM analysis of these OBC samples and of top fractions iC6-sCC6 and iCC6 indicates a lamellar morphology, characterized by formation of roundish hard block domains populated by tightly stacked lamellar crystals, interconnected by lamellar crystals crossing the surrounding regions mainly populated by soft blocks, according to a web-like arrangement, that defines the pass-through morphology.

In an attempt to obtain more quantitative information about the distributions of the molecular mass of the hard blocks, the SSA thermal fractionation technique was selected, as it represents an effective tool that allows to fractionate, with a high resolution and in a short time, polymers that incorporate along the chain defects, such as comonomeric units, stereo- and regio-defects or cross-links, that interrupt the regular sequences of the crystallizable units. It was shown that, due to the intrinsic polydispersity in the hard block length, the distribution of melting peaks in the final endotherm measured at the end of a SSA protocol reflects the distribution of the hard block length. Hence, a good approximation of the real distribution of the hard block length was built up, through cumulative and relative distributions of methylene sequences length for the unfractionated samples and the most crystalline fractions. It was observed that the sequence lengths are rather short and range from 50 to 150 CH_2 units. Therefore, the maximum value of the average length of methylene units in a stem (MSL_{max}) is about 150. The value of MSL_{max} is lower than the average number of consecutive methylene units in the hard blocks, that is the average number of methylene units comprised in between

two interruptions (octene units), which is equal to about 400 (≈ 200/0.5, with 0.5 mol% the octene concentration in the hard blocks). This entails that the lamellar crystals include chain-folded, rather than fully-extended, ethylene sequences. The chain folded crystals including stems of length MSL_{max} are markedly shorter than those which would develop in a random ethylene/octene copolymer with an identical octene concentration and high molecular mass. In general, it may be noticed that the melting peaks distribution shown by the OBC samples reflects a distribution of lamellar thickness that includes long and short methylene sequences belonging to the hard blocks and that the relative amount of methylene sequences tends to increase with the increasing of the MSL value. Furthermore, the cumulative and relative distributions of methylene sequence length help to better understand why the samples behave in such a different way, despite having similar molecular parameters, such as average content of hard and soft blocks, molecular masses, average content of octene and polydispersity index, since the most crystalline fractions, which are the leading fractions in all the samples, have very different MSL distribution between the samples.

In conclusion, the combination of such a large number of characterization techniques has successfully contributed to the elucidation of the wide compositional heterogeneity at inter- and intrachain level of the ethylene/1-octene statistical multiblock copolymers produced through the chain shuttling process. Although the distributions of block length that have been derived in this work are still approximations, these approximations are really good, as they reflect quite well the complex chain microstructure of these complex systems.

4. Structural Characterization of OBCs Synthetized in a High-throughput Parallel Pressure Reactor

High-throughput tools in polyolefins have been extensively used throughout the last decades as a powerful and efficient way to discover and improve catalysts and to build structure-properties relationship databases since they offer the chance of screening the variables hyperspace to study complex chemical processes. Ethylene/1-alkene chain-shuttling copolymerization, aimed at producing olefin block copolymers (OBC) with alternating hard crystallizable blocks and soft amorphous blocks, represents in this latter respect an exemplary case. Given the features of the chain shuttling polymerization (discussed in Chapter 1), the final materials are a reactor blend of non-uniform multiblock chains, each chain having a statistical distribution in both block length and number of blocks. The intrinsic polydispersity and inhomogeneity of OBCs is mainly governed by catalysts ratio Cat2/Cat1. It must be recalled that the couple of catalysts used in chain shuttling polymerization for the synthesis of OBCs differs in monomer incorporation ability (paragraph 1.4 of Chapter 1). The Cat2/Cat1 ratio, indeed, determines the probability of chain shuttling events between the same or different transition metal catalytic species. In particular, whenever catalyst formulations with an excess of the good incorporator catalyst are used, an amorphous fraction and a semicrystalline fraction are obtained. The amorphous fraction, which is only due to 'homo' chain shuttling events between active species of the good incorporator catalyst, has a composition coinciding to that of a

random ethylene/1-alkene copolymer that would be produced by the sole good incorporator catalyst at the same comonomer feed. The semicrystalline fraction is instead an OBC formed by 'hetero' chain shuttling events between the two organometallic catalyst active species.

To address the complexity of these systems and to expand their field of application, it is necessary (in addition to the systematic study of the paradigmatic Infuse™ commercial samples, which has been dealt with in Chapter 3) to grasp what is the effect of the different operating parameters in the chain shuttling copolymerization on the microstructure, on phase separation, and on the final properties through the setting up of a chain-of-knowledge in which a high-throughput synthetic stage (in a Parallel Pressure Reactor, PPR) and a characterization stage (in high-throughput regime as well, when possible) are closely interrelated.

The first step that had to be taken in this workflow from catalytic process to microstructure, down to structure, morphology, rheology, and end-use properties was to validate the high-throughput PPR approach to mimic the properties of commercial OBC samples. The downscaling of the high-temperature and high-pressure synthesis of statistical OBCs in PPR microreactors has been successfully carried out as described in Ref. 58. Although it was shown that it is possible to prepare OBC featuring a microstructure similar to that of commercial OBC, it was still not clear whether the miniaturized reactors were able to produce materials mimicking all industrially relevant properties of the commercial ones. In view of the above, efforts were made in demonstrating that PPR replicas are microstructurally similar to each other, with no significant differences with respect to the physical and mechanical properties, and that they fairly well reproduce the main features of the commercial grades taken as benchmark.

The second step of the workflow was tailoring the OBC properties through changes in chain microstructure by PPR approach. As a matter of fact, by synthetizing and characterizing libraries of OBCs, it is possible to assess the effect of different molecular masses, different [pyridylamido)Hf]/[bis(phenoxyimine)Zr] catalysts ratios (in turn, different w_s/w_h, that is the ratio between the weight fraction of hard and soft blocks), different comonomers (1-hexene, 1-octene, 4-methyl-1-pentene, 1-hexadecene), different comonomer concentration between hard and soft blocks (Δcom), different values of segregation strength (χN values), and differences in the distribution of block size.

4.1. Mimicking the Commercial Grades: Synthesis and Characterization of Ethylene/1-Hexene OBCs at $\Delta hex \approx 20$ mol% and $w_s/w_h \approx 80/20$

Replicas of commercial OBCs, mimicking a commercial sample, have been prepared in a PPR using the two catalysts shown in Chapter 2 in CSP regime at 100°C under the same experimental conditions to verify the reproducibility of the synthetic protocol (details on the synthesis are reported in Chapter 2). We focused on the 4:1 [(pyridylamido)Hf]/[bis(phenoxy imine)Zr] catalysts ratio to obtain OBCs featuring the weight fraction of soft blocks around 80%, as in the reference commercial sample. In Table 1, the main characterization results achieved via GPC, ^{13}C NMR spectroscopy, and aCEF are summarized and compared with those of the commercial Sample 5, used as reference. Sample 5 is part of the set of commercial Infuse™ ethylene-1-octene block copolymers provided by The Dow Chemical Company and studied in Chapter 3. It is worth reminding that this multiblock sample has a non-uniform chain constitution, as it includes hard PE-like blocks with low

comonomer content and soft random ethylene-1-octene blocks with high comonomer concentration, alternating along the chains. In particular, the concentration of octene is 0.5 mol% (less than 2 wt%) in each hard block and ≈19 mol% (≈48 wt%) in each soft block. The main features of this benchmark sample are listed in Table 1.

Table 1. Main features of the ethylene-1-hexene multiblock copolymers with $\Delta hex \approx 20$ mol% and $w_s/w_h \approx 80/20$ and of the reference sample 5: Yield, number average molecular mass (M_n), mass average molecular mass (M_w), polydispersity index (Đ), molar percentage of 1-hexene units x_H, molar percentages of 1-hexene units in each soft block $x_{H,s}$, molar and weight percentage of soft blocks w_s, weight fraction of the amorphous component AF, and elution temperatures $T_{el,\,max}$ (extracted form aCEF data).

Sample ID	Yield (mg)	M_n (kDa)	M_w (kDa)	Đ	x_H (mol%)	$x_{H,s}$ (mol%)	w_s (mol%)	w_s (wt%)	AF (wt%)	$T_{el,\,max}$ (°C)
164260 6C	128	53	102	1.9	0.153	19.5	77.6	82.8	21.8	96.4 104.9
164260 4E	133	50	100	2.0	0.160	21.0	76.2	82.0	26.8	97.3 105.2
164260 4G	135	48	99	2.1	0.161	20.8	76.4	82.1	23.9	95.5 104.1
164260 5E	156	55	108	2.0	0.160	20.8	76.4	82.1	31.5	95.4 104.2
164260 2E	175	44	80	1.8	0.158	20.6	75.6	81.4	16.9	92.7 104.9
Sample 5*	/	70	177	2.5	0.146	19.5	77.3	84.4	27.2	94.8 104.8

* Comonomer, 1-octene

The reproducibility on all measured values is truly remarkable, considering the complexity of the chain shuttling chemistry. The GPC traces were almost superimposable with Đ values of 1.9 ± 0.1 (see Appendix A5), and a relative standard deviation (rSD) on the measured values of M_n and M_w of 15-17% (Table 1, columns 2−3), which is within the specifications of the method. The comonomer incorporation determined by ^{13}C NMR spectroscopy

is 15.6% with a relative standard deviation (rSD) of 5%, which well compares with the 14.6 mol% in the commercial sample. The statistical analysis of the ^{13}C NMR triad distributions revealed that the weight fraction of soft blocks is 82.1 ± 0.7 wt% (84.4 wt% in Sample 5), featuring a comonomer content of 20.5 mol% (19.5 mol% in Sample 5). The AF fraction in the aCEF traces (see Figure 1), which is the amount of polymer eluted at sub-zero temperature, ranges from 17 wt% to 31.5 wt%, and consists of a random ethylene-1-hexene copolymer resulting from chain shuttling events between active transition metal species of Cat2. The semicrystalline part of the aCEF traces (Figure 1) shows two distinctive peaks at elution temperatures $T_{el,max}$ of 95 ± 2°C and 104 ± 1°C, the relative intensities of which differ from sample to sample, due to statistical fluctuations of polymerization conditions in the miniaturized reactors.

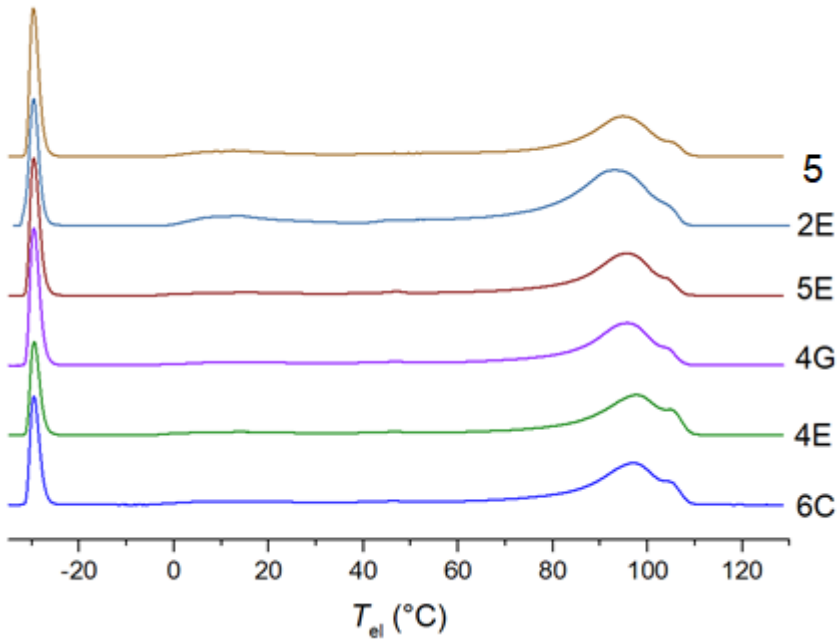

Figure 1. aCEF profiles for the samples of Table 1.

Overall, it is possible to conclude that the PPR replicas are microstructurally very similar, although not identical, and well reproduce the main feature of the commercial Sample 5, except for the molecular mass, which is almost halved. This is due to the relatively high propensity of the Zr-based catalyst to β-H elimination.

To understand whether such differences impact on the properties of the materials, we performed a comparative thorough structural, thermal, morphological, and rheology study of the PPR replicas and of the commercial Sample 5, in a high-throughput mode.

The X-ray powder diffraction (WAXS) profiles of the PPR replicas are reported in Figure 2A. They are compared with the WAXS profile of the commercial Sample 5, that we selected as reference. All the samples show the presence of the 110 and 200 reflections of the orthorhombic form of polyethene (PE) at 2θ ≈21° and 24°, overlying an amorphous halo at 2θ ≈19°, due to the crystallization of long ethylene sequences constituting the hard blocks. The soft blocks, with comonomer content of ≈ 20 mol% (Table 1), instead, are amorphous, as the average length of consecutive ethylene units is not long enough to be able to crystallize. The values of the crystallinity index x_c(WAXS), extracted from the WAXS profiles, are reported in Table 2. They are comprised in the range 15-18%. When normalized to the amount of hard blocks (1-w_s) measured via ^{13}C NMR spectroscopy, the degree of crystallinity is in the range 85-90% (Table 1).

The DSC thermograms are reported in Figures 2B and C. Only the melting thermograms recorded in the first heating and successive cooling scans are shown. The values of the melting and crystallization temperatures and the corresponding enthalpy extracted from DSC analysis are reported in Table 2.

All PPR replicas show similar values of melting/crystallization parameters. In particular, the values of the melting temperature in the first and second (data not shown) heating scans are similar and correspond to 120.3 ± 0.3 °C and 119.2 ± 0.2 °C, respectively. The crystallization temperature corresponds to 99 ± 1°C. The higher standard deviation for the crystallization temperature value is due to the fact that crystallization is much more sensitive than melting to small fluctuations in the chain microstructure of polymers. The melting and crystallization enthalpies are similar (25-27 J/g). The degree of crystallinity calculated from the melting enthalpy in the first heating scan x_c(DSC) corresponds to 9 ± 1%, and is lower than x_c(WAXS), probably because of the occurrence of melting and partial recrystallization phenomena of the hard blocks during heating. All in all, the DSC analysis essentially confirms that the PPR replicas not only are characterized by the presence of long ethylene sequences belonging to the hard blocks crystallizing in the orthorhombic form of PE, but also that their properties are statistically similar each to other, and also similar to those of the benchmark.

Table 2. Values of crystallinity index x_c(WAXS) deduced from WAXS analysis, of the melting temperature (T_m^I, T_m^{II}) and enthalpy (ΔH_m^I, ΔH_m^{II}) measured in the first (T_m^I, ΔH_m^I) and second heating (T_m^{II}, ΔH_m^{II}) scans, of the crystallization temperature (T_c) and enthalpy (ΔH_c) and degree of crystallinity (x_c(DSC)) relative to the PPR replicas and the benchmark Sample 5, extracted from DSC analysis.

Sample ID	x_c(WAXS) (%)	T_m^I (°C)	ΔH_m^I (J/g)	T_m^{II} (°C)	ΔH_m^{II} (J/g)	T_c (°C)	ΔH_c (J/g)	x_c(DSC) (%)[a]
164260-6C	15.1	120.2	26.0	119.1	24.5	98.6	24.3	9
164260-4E	16.0	120.6	31.8	119.3	27.5	99.9	26.7	11
164260-4G	17.7	120.7	29.2	119.9	26.6	100.3	25.1	10
164260-5E	15.1	119.9	20.3	118.6	18.9	96.6	19.8	7
164260-2E	17.2	119.9	30.4	119.1	28.4	100.1	28.4	10
Sample 5	17.0	120.0	16.0	119.0	16.0	94.0	18.0	5

a. Calculated as x_c(DSC) = 100 ΔH_m^I / ΔH_m^0 with ΔH_m^0 = 293 J/g, the melting enthalpy of 100% crystalline PE.[85]

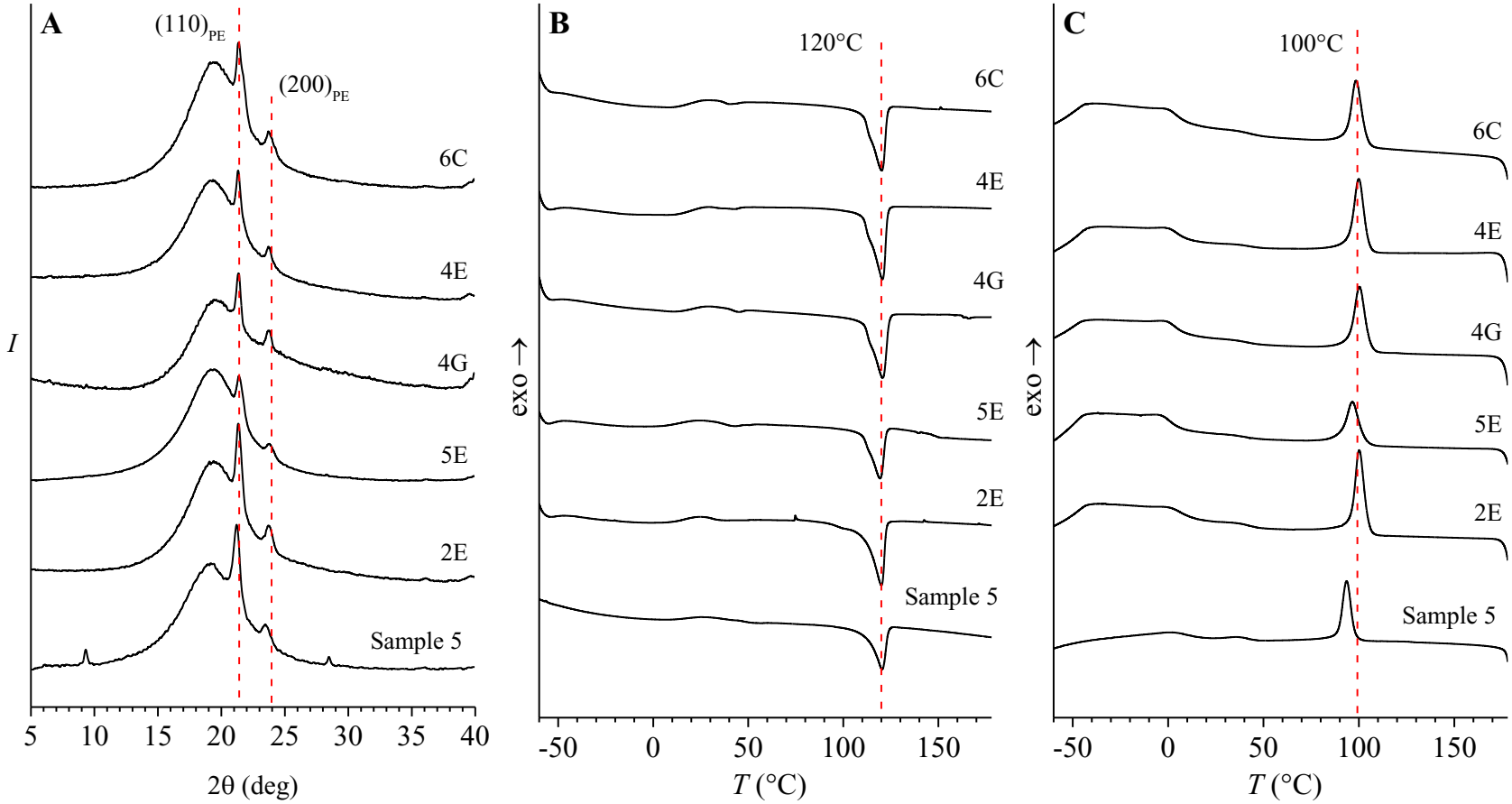

Figure 2. Wide angle X-ray scattering (WAXS) profiles (A) and DSC heating (B) and cooling curves of the PPR replicas and of the commercial grade Sample 5 taken as reference.

The small angle X-ray scattering (SAXS) profiles of the PPR replicas and the reference Sample 5 are reported in Figure 3, before and after correction for the Lorentz factor. The samples show SAXS profiles having similar shape characterized by the presence of two bumps separated at $q \approx 0.52$ nm^{-1} (Figure 3A). The two bumps, in the corresponding Lorentz corrected profiles (Figure 3B), appear as maxima centered at q values comprised in range $q_1 = 0.17$-0.19 nm^{-1} and $q_2 = 0.74$-0.78 nm^{-1}. The exact values of the maxima, along with the corresponding correlation distances L_1 and L_2, evaluated using the Bragg law, are reported in Table 3. For the PPR samples the average position of the maxima correspond to $q_1 = 0.18 \pm 0.01$ nm^{-1} and $q_2 = 0.76 \pm 0.02$ nm^{-1}, whereas the average position of the correlation distances corresponds to $L_1 = 35 \pm 2$ nm and $L_2 = 8.2 \pm 0.2$ nm. The modulation of SAXS intensity derives from independent contributions due to the tendency of the hard blocks of different lengths to crystallize in separated domains, with little or no inclusion of the soft blocks in the interlamellar amorphous phase.[75] These results indicate that the PPR samples show similar characteristics at mesoscale, even though the values of the correlation distance L_1 are spread over a wide range centered around 35 nm. These large fluctuations may be due to the complex multiblock architecture of OBCs, that include chains with a statistical distribution of block length and number of blocks/chain, that varies not only from chain to chain but also within the same chain.

All in all, the present analysis strongly validates the PPR approach for the study of the structure and properties of OBCs. Furthermore, the SAXS curves of the OBCs and the structural parameters extracted from them can be considered in good agreement with the data relative to the commercial Sample 5 (Figure 3 and Table 3), thus confirming that the OBCs synthetized in the PPR well mimic the structural behavior of the commercial grades.

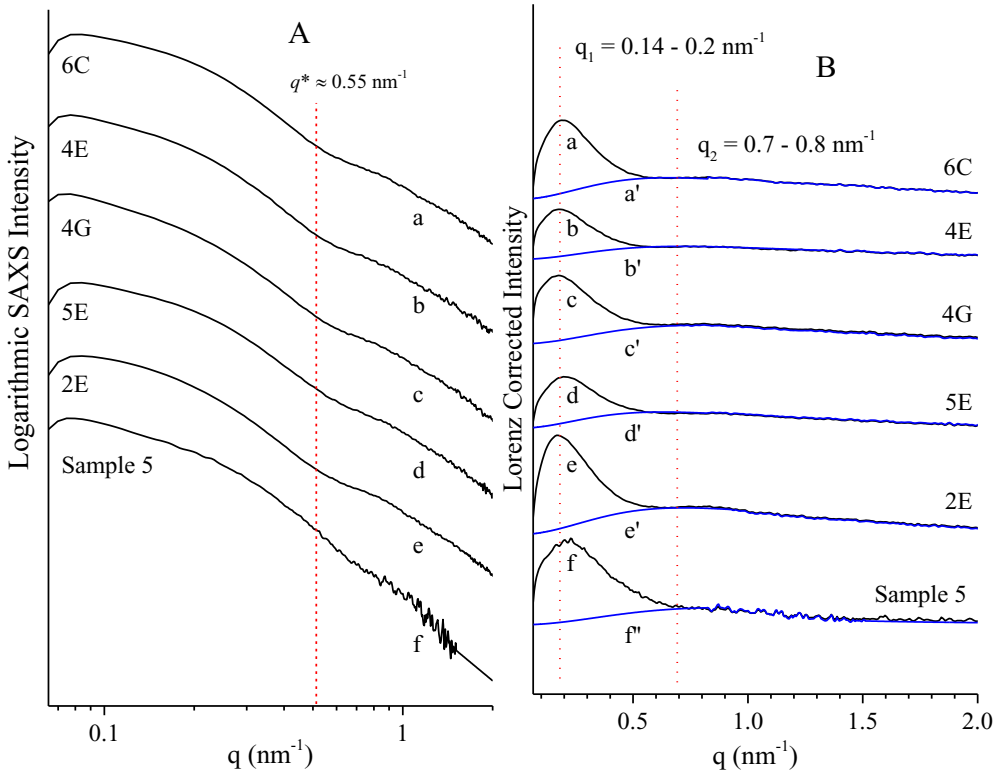

Figure 3. SAXS intensity profiles before (A) and after correction for the Lorentz factor (B) (a-f) relative to the PPR replicas and the commercial Sample 5, taken as reference. The vertical red line at $q^* \approx 0.52$ nm^{-1} in A marks the value of q of intersection between the two contributions deriving from the structural organization of the chains at correlation distances $D > 2\pi/ q^*$ and $D < 2\pi/ q^*$. The position q_1 and q_2 of the two maxima in B are indicated by the vertical red lines. The blue curves a'-f' in B indicate the contribution to the SAXS intensity of the chains at correlation distances $D < 2\pi/ q^*$.

Table 3. Positions of the two correlation peaks q_1 and q_2 in the Lorentz corrected curves and corresponding correlation distances.

Sample ID	q_1 (nm^{-1})	q_2 (nm^{-1})	L_1 (nm)	L_2 (nm)
164260-6C	0.189	0.750	33.2	8.38
164260-4E	0.182	0.785	34.5	8.00
164260-4G	0.175	0.777	35.9	8.09

164260-5E	0.196	0.730	32.0	8.61
164260-2E	0.168	0.777	37.4	8.09
Sample 5	0.214	0.740	29.3	8.49

Furthermore, as shown in Chapter 3, SAXS analysis allows to evaluate the average molecular mass of hard blocks and soft blocks, and the average number of blocks/chain for the OBCs. In particular, by adopting the empirical approach recently proposed in Ref. 78, the average molecular mass of the hard block (M_H) has been determined using the lamellar parameters extracted from SAXS self-correlation functions. The method is based on the consideration that the values of long spacing L and thickness of amorphous layers l_a of semicrystalline polymers scale as the square root of the mean square gyration radius of the chains in the unperturbed state R_g ($\approx M_H^{1/2}$), according to a linear relationship set up in Ref. 95 for polyethylene. As discussed in Chapter 3, in the hypothesis that the SAXS profiles are dominated by the contribution from lamellar stacks involving crystallization of the hard blocks in separated domains with little or no inclusion of the soft blocks in the interlamellar amorphous regions, the values of M_H have been evaluated by determining the lamellar parameters extracted from the SAXS intensity profiles of Figure 3. For the sake of simplicity and without loss of generality, the calculations have been performed focusing on the sole contribution to SAXS intensity deriving from the population of lamellar stacks including hard blocks with short length, that is extracting the mono-dimensional correlation function of fluctuations of electron density (correlation function, CF) using the curves a'-f' of Figure 3B (see paragraph 3.1 of Chapter 3). The so calculated CF curves are reported in the Appendix A6.

The values of average molecular mass (M_{HS}) of a di-block HS building unit including consecutive hard (average molecular mass M_H) and soft

segments (average molecular mass M_S) are calculated as M_{HS} (= M_H + M_S) = $M_H\, w_h^{-1}$, where w_h is the average fraction of hard blocks. The average number of blocks/chain, instead, is determined as a quantity in between $n_1 = M_n\, M_{HS}^{-1}$ and $n_2 = M_w\, M_{HS}^{-1}$, where M_n and M_w are the number and mass average molecular mass of the OBCs, respectively. In Table 4, the symbol $[HM_H\text{-}SM_S]_{n1/n2}$ specifies the average molecular mass of hard and soft blocks in an HS building unit in a hypothetical chain constituted by HS units of only one length, whereas the subscripts n1 and n2 indicate average number of blocks/chain. Calculations have not been extended to the evaluation of the whole distribution of hard and soft block length as performed for the commercial samples (Chapter 3), since the aim of this section and of the following ones is just to assess the reliability of the PPR approach in reproducing the structure and properties of the OBCs and to extend the PPR approach toward obtaining new OBCs with tailored properties.

In general, all the OBCs show a similar average molecular mass of the hard block (2 kDa), which is slightly lower than that of Sample 5 (3 kDa). The average molecular mass of the soft unit M_s in the OBC samples 6C, 4E, and 4G is equal to 7-8 kDa, whereas for the OBC samples 2E and 5E and the reference Sample 5 it is almost doubled (11-16 kDa). This variability, once again, reflects the intrinsic statistical multiblock architecture of the OBCs. The average numbers of blocks/chain (n1 and n2) are, instead, similar.

Table 4. Average molecular masses M_n and M_w; weight fraction of hard blocks w_h; values of long spacing L, thickness of lamellar crystals l_c and of the amorphous layer l_a; values of interdomain spacing L_{HS}; average molecular mass of hard M_H and soft M_S blocks and of HS building units $M_{HS;}$ average number of blocks/chain n_1 and n_2; symbol specifying the average mass of blocks and number of blocks/chain $[HM_H\text{-}SMs]_{n1/n2}$ for all the PPR OBC samples of Table 1 and Sample 5.

Sample ID	M_n **(kDa)**	M_w **(kDa)**	w_H **(wt%)**	**L (nm)**	l_c **(nm)**	l_a **(nm)**	L_{HS} ***(nm)***	M_H **(kDa)**	M_{HS} **(kDa)**	M_S **(kDa)**	n_1	n_2	$[HM_H\text{-}SM_S]_{n1/n2}$
164260-6C	53	102	18.3	12.04	10.23	1.81	33.2	1.7	9.2	7.6	5.7	11.0	$[2H\text{-}8S]_{6/11}$
164260-4E	50	100	17.8	9.8	8.06	1.74	34.5	1.6	8.8	7.2	5.7	11.4	$[2H\text{-}7S]_{6/11}$
164260-4G	48	99	17.3	8.48	6.67	1.81	35.9	1.7	9.8	8.1	4.9	10.1	$[2H\text{-}8S]_{5/10}$
164260-5E	55	108	12.6	11.91	9.79	2.12	32.0	2.3	18.4	16.1	2.9	5.9	$[2H\text{-}16S]_{3/6}$
164260-2E	44	80	16.7	8.65	6.54	2.11	37.4	2.3	13.8	11.5	3.2	5.8	$[2H\text{-}11S]_{3/6}$
Sample 5	70	177	15.4	7.10	4.8	2.3	31.4	2.7	17.7	15.0	3.8	9.9	$[3H\text{-}15S]_{4/10}$

Representative bright field transmission electron microscopy (TEM) images of the PPR replicas and the reference Sample 5 are shown in Figure 4. The PPR replicas show similar morphological features, so that the TEM images shown in 4A-E, relative to the different replicas, correspond to different magnifications, and only the TEM images of the reference Sample 5 correspond to different magnifications. The low magnification images (Figure 4A-B) show sheaves of lamellar crystals laying on edge onto the support that spread out from point nuclei within spherulitic superstructures. The whole area is covered by rounded spots, of diameter equal to 100-200 nm. The TEM images taken at higher magnification (Figure 4C-E) allow distinguishing the inner structure of the rounded objects consisting of lamellar crystals tightly stacked one on the top of the other, at a separation distance of ≈20 nm. The surrounding regions also appear crossed by edge-on lamellae, but their relative arrangement is less regular and the separation distance is bigger than 20 nm. This kind morphology is typical of OBCs and similar to that one of the reference Sample 5 (Figure 4F, G).[75] It is generated by the tendency of the hard blocks to crystallize in separated domains, with little or no inclusion at all of the soft block in the interlamellar amorphous regions. Furthermore, given that there is not total incompatibility between the hard and soft blocks, the PE lamellar crystals are not confined into the rounded domains but come out of them, passing through the surrounding matrix populated by the soft blocks, eventually connecting adjacent hard domains (pass-through morphology).

Therefore, also the pass-through morphologies of the PPR replicas are statistically similar. Furthermore, given the similarities between the solid-state morphology shown by the TEM images of the PPR replicas with the solid-state morphology of the reference Sample 5 used as benchmark, it is confirmed that

OBCs produced in the PPR mimic well the morphology of the commercial OBCs.

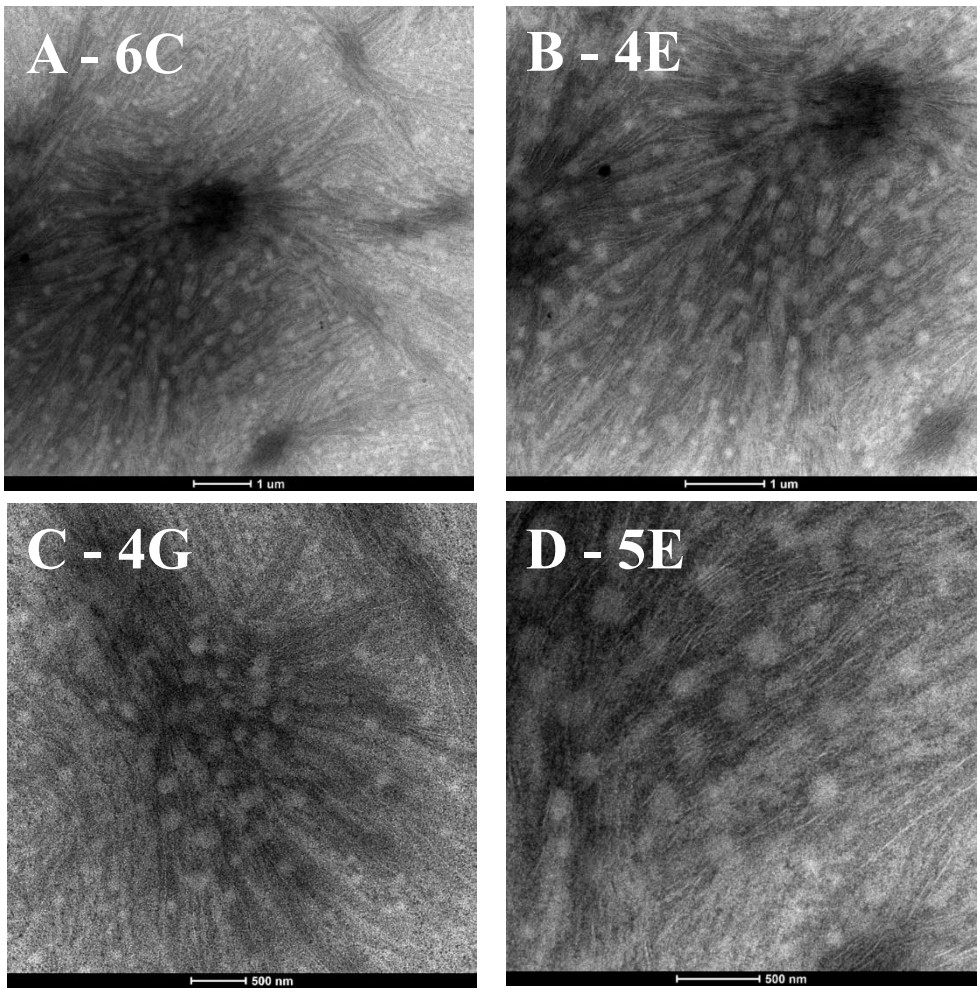

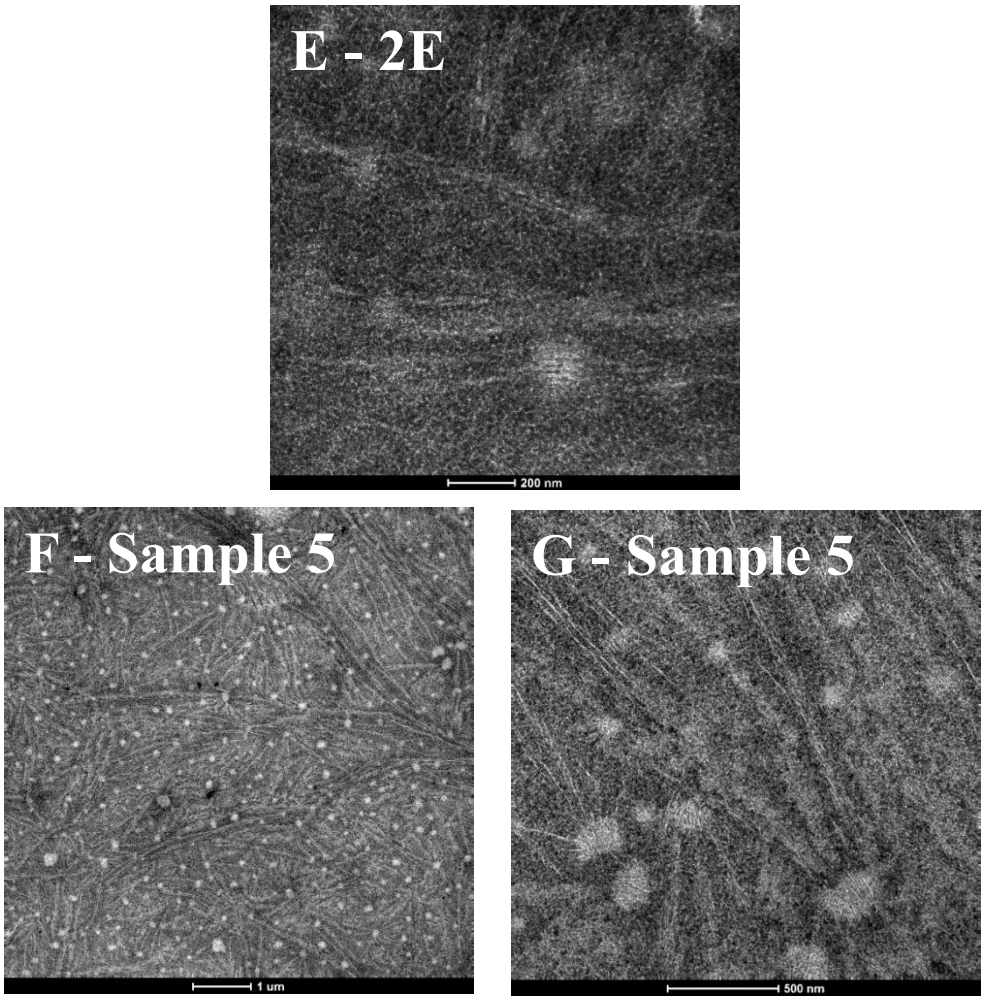

Figure 4. Bright field TEM micrographs of the PPR replicas (A-E) and of the commercial Sample 5 selected as benchmark (F, G), at different magnifications (see text). The samples are RuO_4 stained for several hours, in order to enhance the contrast between the lamellar crystals (bright), and the amorphous regions (dark).

Owing to the strict similarities of the structure of PPR replicas, they were merged together in order to have available a significant quantity of material (ca. 400 mg), suitable for the determination of the tensile properties. The crystallinity index calculated from WAXS and DSC analysis along with the values of the melting and crystallization temperature and enthalpy of the

merged sample are reported in Table 4. The WAXS profile and the DSC thermograms of the merged sample, instead, are compared with those of the Sample 5 in Figure 5. The results of Table 4 and the data of Figure 5 indicate that the structure and thermal properties of the merged sample are similar to those of the benchmark Sample 5.

Table 5. Values of crystallinity index x_c(WAXS) deduced from WAXS analysis, of the melting temperature (T_m^I) and enthalpy (ΔH_m^I) measured in the first heating scan, of the crystallization temperature (T_c) and enthalpy (ΔH_c) and degree of crystallinity (x_c(DSC)) relative to the merged PPR sample.

Sample ID	x_c(WAXS) (%)	T_m (°C)	ΔH_m (J/g)	T_c (°C)	ΔH_c (J/g)	x_c(DSC) (%)[a]
OBC PPR 4:1 merged sample	18.0	119.2	25.7	102.7	25.7	9

a. Calculated as $x_c(DSC) = 100\ \Delta H_m^I / \Delta H_m^0$ with $\Delta H_m^0 = 293$ J/g, the melting enthalpy of 100% crystalline PE.[85]

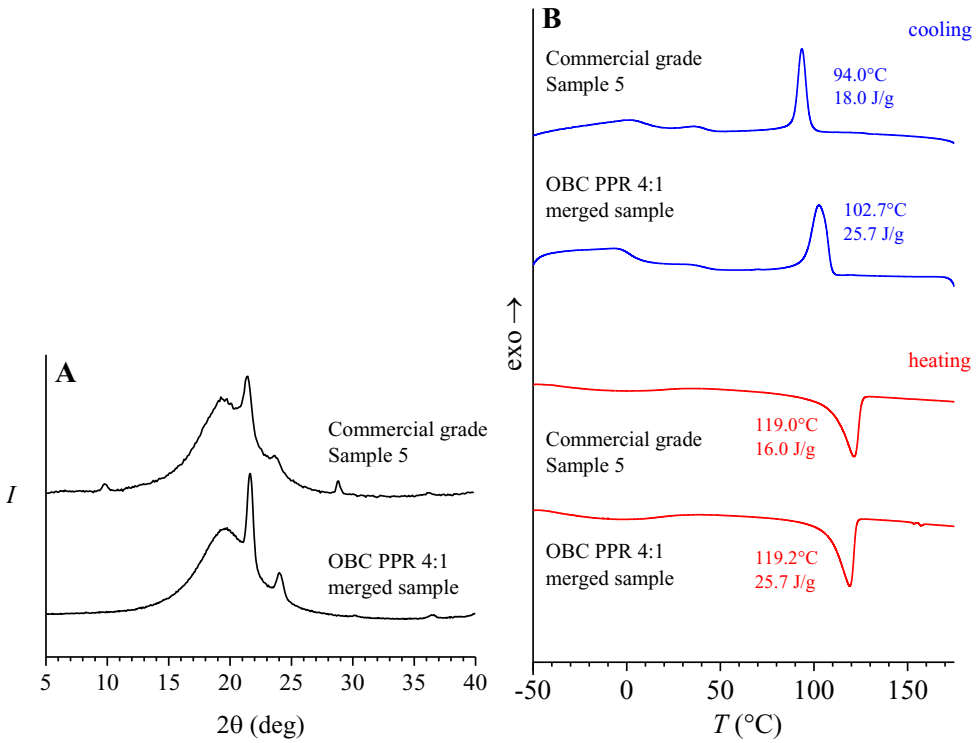

Figure 5. WAXS profiles (A) and DSC heating (B, in red) and cooling (B, in blue) thermograms for the merged sample of Table 5 and for the commercial Sample 5 selected as benchmark.

The stress-strain curve of the merged PPR sample is compared with that of the reference Sample 5 in Figure 6. The mechanical parameters extracted from the curves of Figure 6 are reported in Table 6. It is apparent that the merged sample shows a high ductility and remarkable rigidity, with values of deformation at break and Young's modulus equal to ≈ 1200% and ≈ 8 MPa. Compared with the tensile properties of the reference Sample 5, the merged sample shows a higher value of the Young's modulus (8 vs. 6MPa), similar value of tension set at break (≈200%) and stress at yield (1.2 MPa), minor differences in the value of deformation at yield (17 vs 12%) and similar values of stress at any deformation up to 500% strain. At deformations higher than

500% the stress strain behavior of the two samples diverges. As a matter of fact, at deformations higher than 500% the merged PPR sample shows strain hardening, and deformation at break equal to 1200%. The reference Sample 5, instead, shows strain hardening at deformations higher than 1000% and a significantly higher deformation at break, equal to ≈2100%. These differences might arise from the merged sample being the product of the mixing of independent PPR cells, each one yielding only a small quantity (less than 100 mg) of OBC. Unlike the values of rigidity (Young's modulus) and the yielding behavior, which are properties essentially dependent on the chain microstructure, ductility (associated with the values of deformation at break) is also sensitive to the molecular mass and preparation conditions of the specimens used in mechanical tests. The high ductility of the reference sample 5, may be explained also considering that the molecular mass is higher than that of the PPR replicas. Furthermore, considering the very limited quantity of material, defects caused by small fluctuations in the preparation conditions, such as surface imperfections or small differences in thickness, may affect the breaking behavior in a deeper way than what usually happens with respect to commercial grades, that are more massively available.

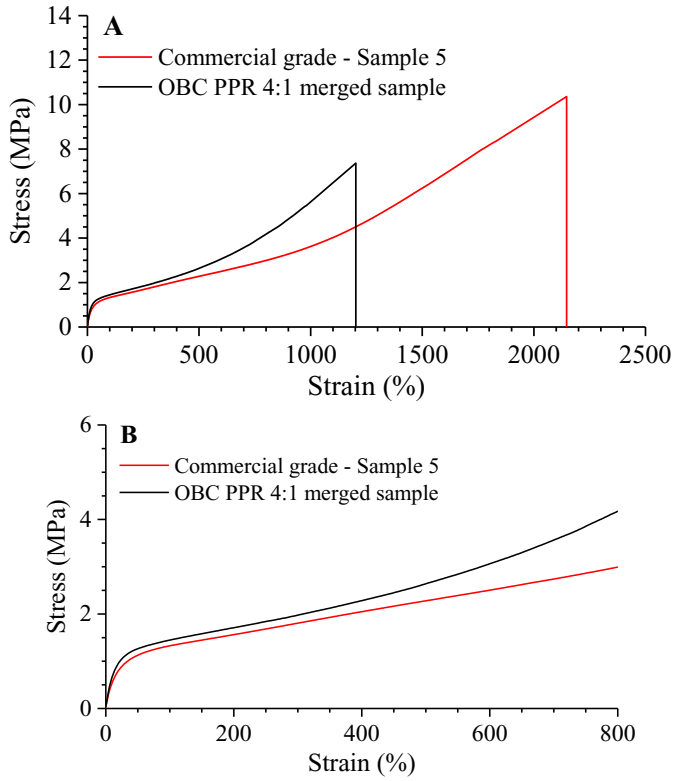

Figure 6. Stress-strain curves for the merged sample and for the commercial Sample 5 selected as benchmark (A). In B, the first part of the stress strain curve for the two samples is shown on an enlarged *y*-scale.

Table 6. Values of the Young's moduli E, tension set at break t_b, stress and deformation at yield σ_y and ε_y, stress and deformation at break σ_b and ε_b of the merged PPR sample and the reference Sample 5.

Sample ID	***E*** **(MPa)**	***t*****b** **(%)**	**σy (MPa)**	**εy (%)**	**σb (MPa)**	**εb (%)**
OBC PPR 4:1 merged sample	8.4±1.1	(22±2)·10	1.2±0.2	17±2	7.4±2.5	$(12\pm1)\cdot10^2$
Sample 5	6.0±1.0	(17±1)·10	1.2±0.2	12±2	10±2	$(21\pm3)\cdot10^2$

In conclusion, the throughout characterization of the samples prepared in a PPR platform in milligram-size quantities demonstrated the close similarity between the industrial relevant properties of the lab-prepared samples and of

the commercial ones. In particular, it was showed how a series of replicas of PPR experiments, performed in the very same set of conditions, produces identical (within the error margins) OBCs in terms of microstructural and morphological behavior. It was also established that OBCs produced in the PPR mimic the morphological behavior of commercial grades, comparing the lab-made samples against a Dow Infuse^{TM} olefin block copolymer.

4.2. Synthesis and Characterization of Ethylene/1-Hexene OBCs at $\Delta hex \approx 20$ mol% and $w_s/w_h \approx 50/50$

Once demonstrated the reliability of the synthetic protocol, a different [Cat2]/[Cat1] ratio was explored, namely a 1:1 ratio, while keeping the same experimental conditions. The results of GPC, ^{13}C NMR, and aCEF analysis are reported in Table 7. Samples with average 1-hexene content of ≈ 9 mol%, Δhex ≈ 20 mol% and mass average molecular mass of ≈ 100-120 kDa were obtained. These characteristics are similar to those of the samples of Table 1. However, since the two catalysts are used here in equimolar ratio, the amount of soft and hard blocks is nearly identical for the sample of Table 7 (i.e., $w_s/w_h \approx 50/50$ w/w). For the samples of Table 1, instead, the w_s/w_h ratio was ≈ 80/20 w/w (Cat2/Cat1 ratio equal to 4:1). Typical aCEF traces of the samples with w_s/w_h ≈ 50/50 and 80/20 are compared in Figure 7. It is apparent that the 50/50 sample shows a small AF peak and only a single elution peak at high temperature. The 80/20 sample, instead, shows a much higher AF peak at low temperature, a broad elution peak in the temperature range 0-40°C, and a double elution peak at high temperatures (Figure 7). This indicates that the distribution of block length narrows with the increasing of the hard block fraction w_h. In the hypothesis that the shuttling rate (number of shuttling

event/unit time) for Cat1 and Cat2 are identical, the narrowing of block length distribution entails that the chain homo-shuttling events involving the catalysts Cat1 and Cat2 occur to the same extent.[58]

Table 7. Molecular parameters for the OBCs samples with $\Delta hex \approx 20$ mol% and $w_s/w_h \approx 50/50$.

Sample ID	Yield (mg)	M_n (kDa)	M_w (kDa)	Đ	x_H (mol%)	$x_{H,s}$ (mol%)	w_s (mol%)	w_s (wt%)	AF (wt%)	$T_{el,max}$ (°C)
1 50/50	176	49	103	2.1	9.1	21.6	40.1	48.9	3.3	106.7
2 50/50	178	49	100	2.0	8.6	21.6	37.9	46.6	5.6	107.4
3 50/50	214	66	124	1.9	8.7	22.0	37.9	46.8	1.3	106.4

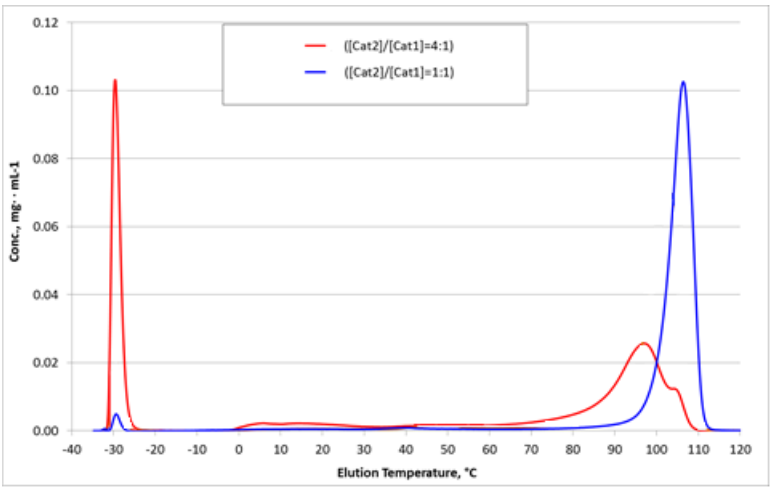

Figure 7. Representative aCEF profile for the OBCs samples with w_s/w_h equal to 50/50 of Table 7 synthetized with [Cat2]/[Cat1] ratio of 1:1 (blue trace). For comparison, a representative aCEF profile of an OBC synthetized with [Cat2]/[Cat1] ratio of 4:1 is also shown (red trace).

The WAXS profiles and the DSC thermograms of the 50/50 samples of Table 7 are reported in Figure 8, whereas the corresponding SAXS profiles and TEM images are shown in Figure 9 and 10, respectively. Finally, the results of DSC and WAXS analysis are reported in Tables 8 and 9, respectively.

All the 50/50 samples crystallize in the orthorhombic form of PE (Figure 8A) as indicated by the presence of 110 and 200 reflections, at $2\theta \approx 21$ and 24°, respectively, and show melting and crystallization peaks around 124°C and 110°C, respectively (Figure 8B,C and Table 8). The SAXS profiles of the 50/50 samples display two well-separated humps at $q \approx 0.5$ nm^{-1}, corresponding to a strong correlation peak at $q \approx 0.20$ nm^{-1} and to a broader halo at $q \approx 0.6$ nm^{-1} in the Lorentz corrected curves (Figure 9 and Table 9). The reason for the uneven distribution of SAXS intensity is due to molecular segregation induced by crystallization that generates the formation of independent lamellar stacks characterized by different periodicity, and nearly identical values of the lamellar thickness. Indeed, as discussed in the Chapter 3, hard blocks of different average length, tend to crystalize forming separated lamellar stacks. Since the lamellar thickness depends exclusively on the crystallization conditions, the values of long spacing L of the stacks (and hence of the amorphous layers l_a) scales as the square root molecular mass of the hard blocks $M_H^{1/2}$. The values of the average molecular mass of the hard and soft blocks M_H and M_S in a representative HS building unit have been hence calculated using the method of Chapter 3, focusing exclusively the calculation of correlation function CF using the curves a'-c' of Figure 9. The so calculated CF curves are reported in the Appendix A6. In Table 8 the resultant constitution of the such short HS building units in a hypothetical chain constituted by HS units of only one length $[HM_H - SM_s]_{n1/n2}$ is specified. It is apparent that the shortest HS building units are similar for the three replicas, with values of M_H equal to 1-3 kDa.

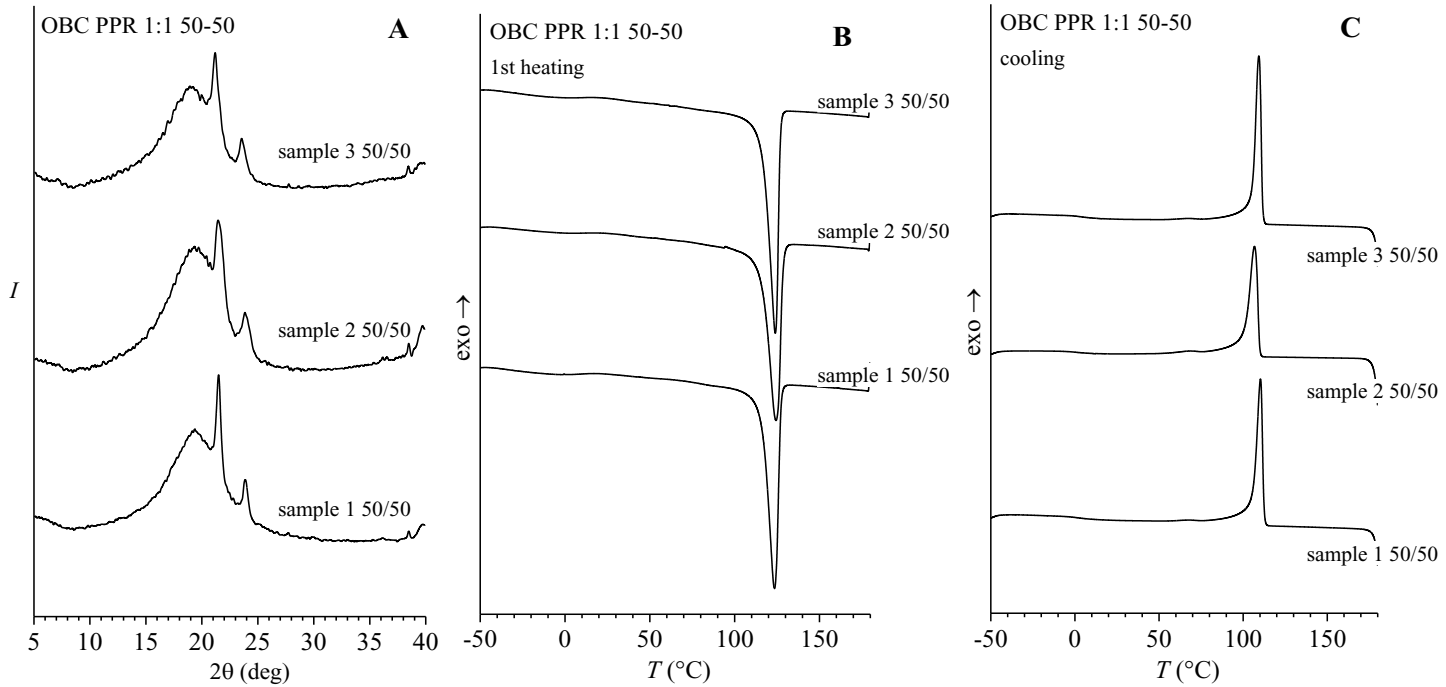

Figure 8. X-ray powder diffraction profiles (A) and DSC heating (B) and cooling (C) curves of the samples with w_s/w_h equal to 50/50 of Table 7.

Table 8. Degree of crystallinity x_c and results of thermal analysis of the OBCs samples with w_s/w_h equal to 50/50 of Table 7.

Sample ID	x_c (%)	T_m (°C)	ΔH_m (J/g)	T_c (°C)	ΔH_c (J/g)
1 50/50	22.6	123.4	94.2	110.2	82.2
2 50/50	24.2	124.3	96.2	106.8	84.7
3 50/50	22.6	123.9	96.0	109.3	87.7

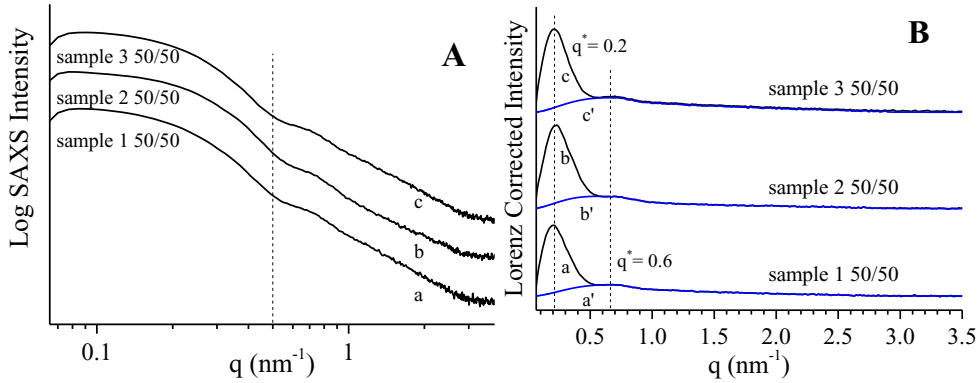

Figure 9. SAXS profiles (A) (a-c) and Lorentz corrected SAXS intensities (B) (a-c) for the OBCs samples with w_s/w_h equal to 50/50 of Table 7. The blue curves a'-c' in B indicate the contribution to the SAXS intensity of the chains at correlation distances $D < 2\pi/q^*$

Table 9. Results extracted from SAXS data analysis of the OBCs samples with w_s/w_h equal to 50/50 of Table 7.

Sample ID	x_cWAXS (%)	Φ_cSAXS (%)	q_{HS} (nm^{-1})	L_{HS} (nm)	q^* (nm^{-1})	L_B (nm)	l_a (nm)	l_c (nm)	$[HM_H - SM_S]_{n1/n2}$
1 50/50	22.6	80.1	0.210	29.9	0.637	9.86	1.97	7.98	$[2H\text{-}2S]_{14/30}$
2 50/50	24.2	78.6	0.231	27.2	0.623	10.08	2.16	7.92	$[2H\text{-}2S]_{14/19}$
3 50/50	22.6	80.1	0.210	29.9	0.630	9.97	1.99	7.98	$[1H\text{-}1S]_{24/44}$

The solid-state morphology of the samples with w_s/w_h equal to 50/50 has been investigated by means of Transmission Electron Microscopy (TEM). The bright-field TEM images of Figure 10 show the presence of sheaves of

lamellae splayed from center-nuclei, typical of spherulitic structures at all magnifications (Figures 10 A-D). Regions occupied by the lamellar sheaves rich in hard blocks alternate with featureless regions rich in soft blocks (Figures 10 B and C). The spotted pattern with hard-block-rich domains embedded in the soft matrix that was observed for the OBCs with w_s/w_h = 80/20, is not present here, indicating the low tendency of these samples to generate well-defined phase separated morphologies upon crystallization. It is worth noting that the morphology of the samples with w_s/w_h equal to 50/50 is rather similar to the conventional morphology of semicrystalline polymers. However, at variance with conventional morphologies of semicrystalline polymers, the uneven distribution of the lamellar sheaves suggests some tendency of the samples with w_s/w_h equal to 50/50 to experience mesophase separation, even though the boundaries between the different domains appear ill defined.

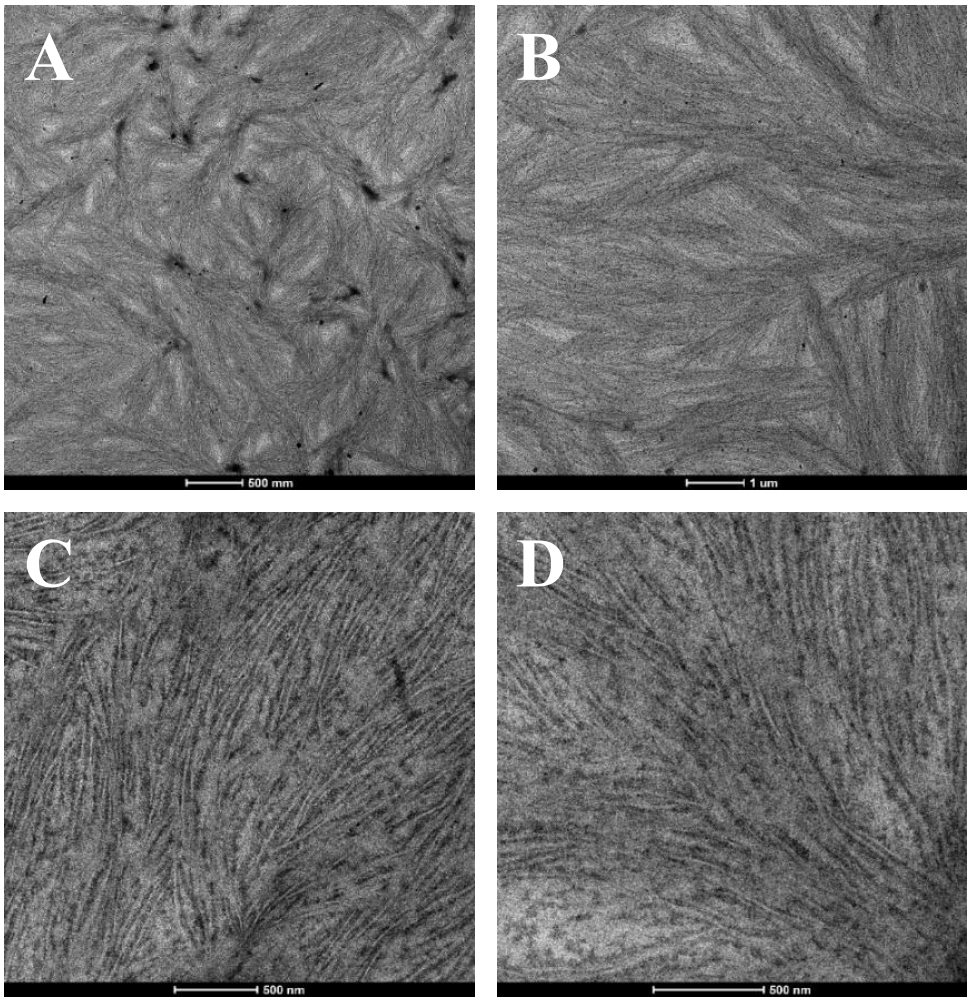

Figure 10. Bright field TEM images of OBCs samples with w_s/w_h equal to 50/50 of Table 7 stained with a RuO_4

The fact that the microphase separated morphology of the OBCs samples with w_s/w_h equal to 50/50 (Figure 10) appears less defined than that shown by the samples with $w_s/w_h \approx 80/20$ and identical $\Delta hex \approx 20$ mol% values (Figure 4) may seem in contrast with expectations. In fact, it is well known that symmetric block copolymers, i.e. block copolymers with identical block length, show, in general, a higher order-disorder transition temperature (T_{ODT})

than the asymmetric counterparts.[1-5] This is true not only for monodisperse di-block copolymers (AB), but also for multiblock copolymers $(AB)_n$, since the phase behavior of the latter systems is predicted to be equivalent to that of the corresponding (AB) base unit.[1-5] Furthermore, for polydisperse systems, mesophase separation is expected to be stabilized (higher T_{ODT} values) compared with monodisperse counterparts.[13-18] Therefore, the observed morphology of the samples with $w_s/w_h \approx 50/50$ (Figure 10) may be explained assuming that the breakout crystallization mode somehow prevails, destroying almost completely the mesophase separated morphology of the melt. The phase separated morphology of the melt may be better preserved upon crystallization of the hard blocks, instead, in OBC samples with an asymmetric base unit, as for instance for OBCs characterized by a length of the hard blocks lower than one half the length of the soft blocks (samples with $w_s/w_h \approx 80/20$). For comparable length of the hard and soft blocks, instead, the crystallization of the hard blocks may easily prevail, up to induce almost complete breakout of the melt morphology.[5,118]

4.3. Increasing the Segregation Strength: Synthesis and Characterization of Ethylene/1-Hexene OBCs with Larger Difference of Co-monomer Incorporation between Hard and Soft Blocks (Δ*hex*)

As part of the second stage of the workflow, which is devoted at exploring the set of chain shuttling operating parameters and tailoring the OBCs properties, the effect of increased difference of comonomer incorporation between the hard and soft blocks is investigated, in OBCs samples with different ratio between the soft and hard block content w_s/w_h. In particular,

samples with Δ*hex* value ≈ 30 mol% have been synthesized. The value of Δ*hex* of these series of samples is higher than that of the Infuse™ and the corresponding PPR-made OBCs, characterized by Δ*hex* value of ≈ 20 mol%. An increase in Δ*hex* value, indeed, is expected to increase the segregation strength of the blocks, and hence also the tendency of the resultant OBCs toward mesophase separation in the melt and in the solid state.[24,26,70-75]

The catalyst pair Cat2/Cat3 (Figures 2-3 in Chapter 2) was used to synthesize a series of OBCs with w_s/w_h values of about 80/20, 70/30, 65/35, and 50/50 w/w while fixing the Δ*hex* at ≈ 30 mol%, and with number average molecular mass around 60-80 kDa and values of dispersity index close to 2. The Zr-based catalyst Cat3 was selected to replace Cat1, in order to avoid undesired drops in molecular mass which were observed using the Cat2/Cat1 pair for the preparation of samples with a fractional content of hard blocks w_h higher than 20 wt% (data not shown). The main characteristics of the PPR replicas are summarized in Table 10. The details on the synthesis of the OBCs samples of Table 10 are reported in Chapter 2. The aCEF traces of representative OBCs replicas are shown in Figure 11. It is apparent that all the samples show a low temperature elution peak due to the amorphous fraction generated by chain shuttling events involving the sole catalyst Cat2, able to incorporate a high content of 1-hexene units along the chain (AF peak). Therefore, these chains are merely soft blocks either not liked to hard blocks or linked to very short hard blocks. The relative intensity of the AF peak decreases with increasing relative amount of the hard blocks, being the highest for the sample with $w_s/w_h \approx 80/20$ and the lowest for the sample with $w_s/w_h \approx 50/50$.

Table 10. Main features of the ethylene-1-hexene multiblock copolymers with $\Delta hex \approx 30$ mol% and variable w_s/w_h ratio: Cat2/Cat3 ratio, yield, number average molecular mass (M_n), mass average molecular mass (M_w), polydispersity index (Đ), molar percentage of 1-hexene units x_H, molar percentages of 1-hexene units in each soft block $x_{H,s}$, weight percentage of soft blocks w_s, weight fraction of the amorphous component AF, and elution temperatures $T_{el,\,max}$ (extracted form aCEF data).

Sample ID	[Cat2]/[Cat3]	Yield (mg)	M_n (kDa)	M_w (kDa)	Đ	x_H (mol%)	$x_{H,s}$ (mol%)	w_s (wt%)	AF (wt%)	$T_{el,\,max}$ (°C)
2	2.5	268	76	158	2.1	0.212	0.325	75.0	18	96.3
3		275	80	166	2.1	0.232	0.337	78.0	24	95.4
4		276	72	159	2.2	0.221	0.340	75.2	16	96.4
5		303	71	172	2.4	0.236	0.346	77.2	20	95.8
6	2.0	226	80	147	1.8	0.169	0.313	64.2	6	101.6
7		284	72	158	2.2	0.188	0.330	67.9	7	100.3
8		330	66	158	2.4	0.204	0.352	69.0	12	99.3
9	1.5	232	63	134	2.1	0.165	0.326	61.9	5	102.2
10		250	77	153	2.0	0.184	0.329	66.6	7	100.5
11		251	65	131	2.0	0.168	0.324	62.4	7	102.0
12	1.0	118	71	135	1.9	0.142	0.336	53.7	6	102.5
13		203	62	132	2.1	0.148	0.343	55.1	5	102.1
14		237	59	121	2.1	0.134	0.334	51.5	5	102.5
15		251	64	138	2.1	0.159	0.344	58.2	6	101.1

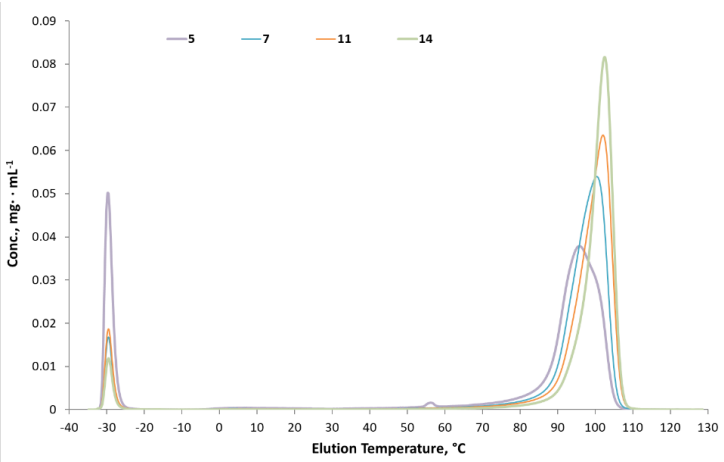

Figure 11. Representative aCEF profiles for selected OBCs of Table 10, with $\Delta hex \approx 30$ mol% and w_s/w_h ratio ≈ 80/20 (5), 70/30 (7), 65/35 (11), and 50/50 (14).

With the aim to assess the effect of a higher Δ*hex* value in samples with different weight fractions of hard and soft blocks, a thermal, structural, and morphological characterization has been carried out, along with the analysis of mechanical properties. The analysis is carried out not on each single replica but on the merged samples obtained by combining the different PPR replicas of Table 10 synthetized in the same conditions, and hence with similar w_s/w_h ratio. The results of the structural, thermal, and mechanical analysis are reported in Table 11-14, whereas the X-ray powder diffraction profiles, the DSC thermograms, and the stress-strain curves are reported in Figures 12-14. Finally, the TEM images of the merged samples are reported in Figures 15-18.

Table 11. Main chain microstructure properties of the merged OBCs with Δ*hex* = 30mol% and w_s/w_h = 80/20, 65/35, 70/30, and 50/50.

Sample ID	$\frac{[Cat2]}{[Cat3]}$	M_n (kDa)	M_w (kDa)	Đ	x_H (mol%)	$x_{H,s}$ (mol%)	w_s (wt%)	AF (wt%)	$T_{el,\,max}$ (°C)	x_c (%)
merged 80/20	2.5	77	188	2.4	0.250	0.347	80.4	29	95.6	21
merged 70/30	2.0	72	158	2.2	0.188	0.330	67.9	7	100.3	26
merged 65/35	1.5	70	152	2.2	0.189	0.341	65.6	11	101.7	29
merged 50/50	1.0	62	142	2.3	0.148	0.350	52.5	8	102.1	30

The X-ray diffraction profiles of Figure 12A show that all the ethylene-1-hexene multiblock copolymers with Δ*hex* ≈ 30 mol% and different w_s/w_h ratios crystallize in the orthorhombic form of polyethylene, as indicated by the presence of (110) and (200) reflections at 2θ equal to 21.4° and 24°, respectively. The degree of crystallinity increases with the decreasing of the w_s/w_h ratio, from 21% for the merged sample with 80/20 w_s/w_h ratio to 30% for the merged sample with 50/50 w_s/w_h ratio (Table 11). The DSC melting curves in Figure 12B show sharp endothermic peak at 120°C for all the samples with

$\Delta hex \approx 30$ mol%. In the DSC crystallization thermograms (Figure 12C), the merged samples with w_s/w_h = 80/20 and 70/30 show a sharp exothermic peak at ≈90°C (main peak) and a faint satellite peak at ≈80°C, whereas the merged samples with w_s/w_h = 65/35 and 50/50 show the main and satellite melting peaks at ≈100 and 80°C, respectively. The melting and crystallization (main) temperatures increase with the increasing of the fraction of hard blocks from 121 and 94°C, respectively, for the sample with w_s/w_h = 80/20 to 124 and 104°C, respectively, for the sample with w_s/w_h = 50/50 (Table 12). The secondary exothermic peak at 80°C is probably ascribable to the separate crystallization of portion of hard blocks in well-separated domains. The area of the melting peaks tends to increase with the increasing of the amount of hard blocks w_h, in agreement with the increasing of crystallinity (Table 12).

Table 12. Values of the melting temperature (T_m^I, T_m^{II}) and enthalpy (ΔH_m^I, ΔH_m^{II}) measured in the first (T_m^I, ΔH_m^I) and second heating (T_m^{II}, ΔH_m^{II}) scans, of the crystallization temperature (T_c) and enthalpy (ΔH_c) and degree of crystallinity (x_c(DSC)) relative to merged OBCs with Δhex = 30mol% and w_s/w_h = 80/20, 65/35, 70/30, and 50/50, extracted from DSC analysis.

Sample ID	T_m^I (°C)	ΔH_m^I (J/g)	T_m^{II} (°C)	ΔH_m^{II} (J/g)	T_c (°C)	ΔH_c (J/g)	x_c(DSC) (%)[a]
merged 80/20	121.2	28.1	116.8	22.7	93.3, 70.2	22.1	10
merged 70/30	122.1	51.9	117.9	38.6	97.4, 71.1	38.6	18
merged 65/35	123.9	57.4	119.8	47.7	100.4, 69.7	47.7	20
merged 50/50	124.3	73.0	118.7	60.7	104.1, 71.2	60.7	25

a. Calculated as x_c(DSC) = 100 ΔH_m^I / ΔH_m^0 with ΔH_m^0 = 293 J/g, the melting enthalpy of 100% crystalline PE.[85]

The SAXS profiles and the corresponding Lorentz corrected curves (Figure 13 and Table 13) show double correlation peaks at 0.28 nm^{-1} and 0.7 nm^{-1}, analogous to those shown by all OBCs investigated so far, due to the tendency of hard blocks of different length to crystallize in separated domains,

forming lamellar stacks characterized by little or no inclusion of the soft blocks in the interlamellar amorphous layers and identical values of the lamellar thickness. The semi-empirical approach of Ref. 78 has been hence applied to calculate the average value of the molecular mass of representative HS building units of short length, the average molecular mass of hard and soft blocks, and the average number of blocks, as reported in Table 13.

The stress-strain curves of the OBCs samples with $\Delta hex \approx 30$ mol% and different w_h/w_s ratio (Figure 14 and Table 14) indicate that the mechanical resistance, the Young's modulus, and the strain hardening behavior of these samples increase with the increasing of the hard block content w_h, whereas the values of the deformation at break ε_b decrease. The increase of Young's modulus with the increasing of the w_h value is in agreement with the increasing of the degree of crystallinity (Table 14).

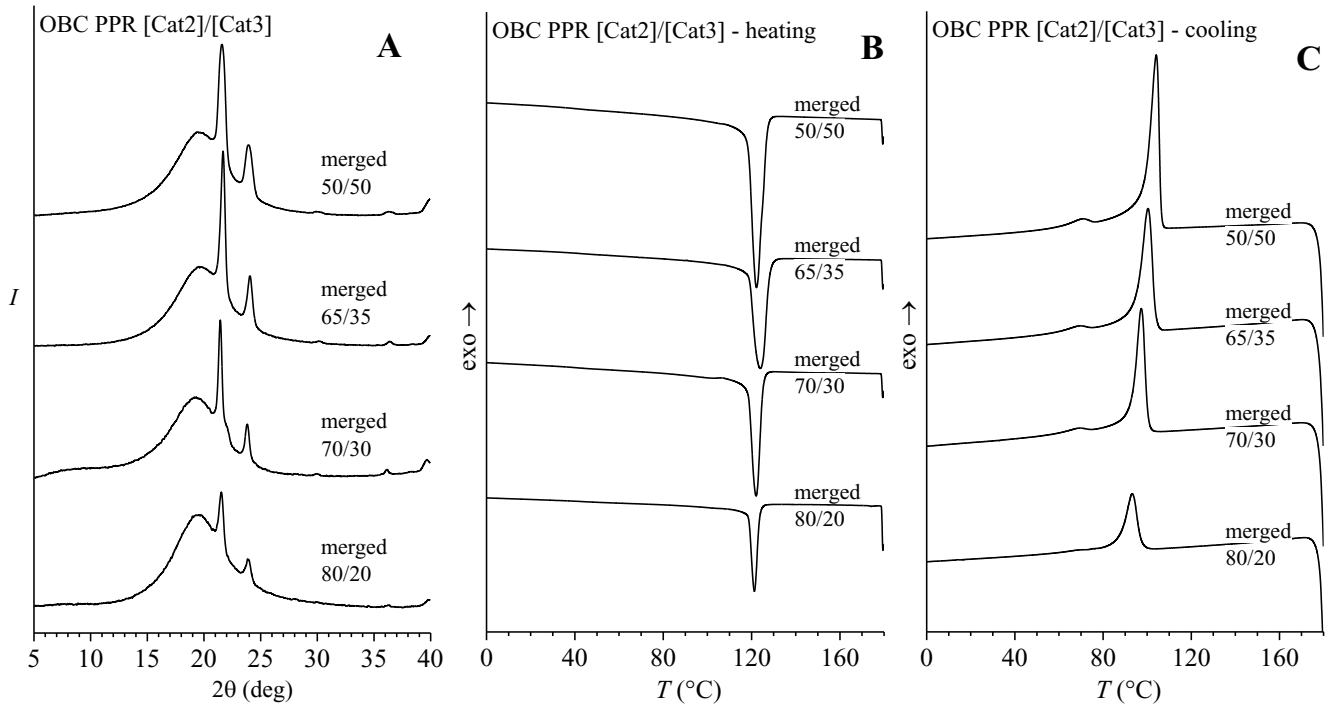

Figure 12. X-ray powder diffraction profiles (A) and DSC heating and cooling curves (B and C, respectively) for the merged OBCs samples of Table 11, with $\Delta hex \approx 30$ mol% and the indicated values of the w_s/w_h ratio.

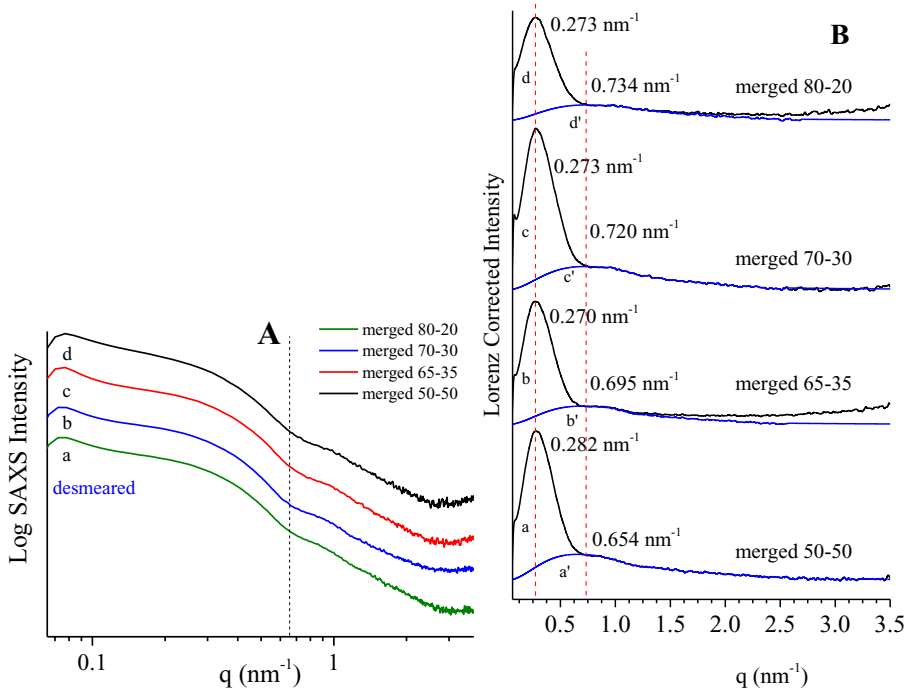

Figure 13. SAXS profiles (A) (a-d) and corresponding Lorentz corrected curves (B) (a-d) for the merged OBCs of Table 11, with $\Delta hex \approx 30$ mol% and the indicated values of the w_s/w_h ratio. The blue curves a'-d' in B indicate the contribution to the SAXS intensity of the chains at correlation distances $D < 2\pi/q^*$.

Table 13. Results extracted from SAXS data analysis of the merged OBCs of Table 11.

Sample ID	x_cWAXS (%)	Φ_cSAXS (%)	q_{HS} (nm^{-1})	L_{HS} (nm)	q^* (nm^{-1})	L_B (nm)	l_a (nm)	l_c (nm)	$[HM_H\text{-}SM_S]_{n1/n2}$
merged 80/20	21	82	0.27	23.0	0.73	8.6	1.6	7.0	$[2H\text{-}7S]_{9/18}$
merged 70/30	26	77	0.27	23.0	0.72	8.7	2.0	6.7	$[2H\text{-}5S]_{10/22}$
merged 65/35	29	74	0.27	23.3	0.70	9.0	2.3	6.7	$[2H\text{-}3S]_{13/27}$
merged 50/50	30	73	0.28	22.3	0.65	9.6	2.6	7.1	$[2H\text{-}2S]_{14/29}$

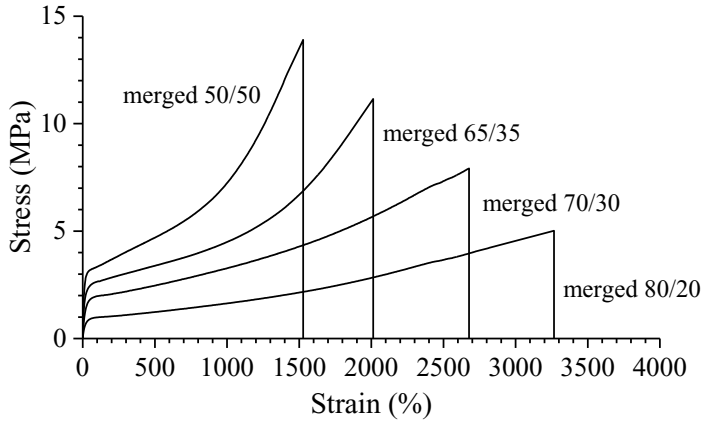

Figure 14. Stress-strain curves recorded at room temperature for the merged OBCs samples of Table 11, with $\Delta hex \approx 30$ mol% and the indicated values of the w_s/w_h ratio.

Table 14. Degree of crystallinity evaluated from WAXS data and mechanical parameters of the merged OBCs samples of Table 11, with $\Delta hex \approx 30$ mol% and the indicated values of the w_s/w_h ratio.

Sample ID	x_c (%)	E (MPa)	ε_b (%)	σ_b (MPa)	t_b (%)
merged 50/50	30	46±4	$(15\pm3)\cdot10^2$	14±4	$(38\pm3)\cdot10$
merged 65/35	29	22.9±1.5	$(20\pm2)\cdot10^2$	11±2	$(30\pm2)\cdot10$
merged 70/30	26	9.4±1.5	$(27\pm2)\cdot10^2$	7.9±0.8	$(16\pm2)\cdot10$
merged 80/20	21	8.8±1.1	$(33\pm4)\cdot10^2$	5.0±0.4	$(35\pm1)\cdot10$

Transmission Electron Microscopy bright field images of the merged OBCs with $\Delta hex = 30$ mol% and different w_s/w_h ratio are reported in Figure 15-18. The TEM micrographs of the merged sample with $w_s/w_h \approx 80/20$ (Figure 15) show bright roundish domains rich in hard blocks that include densely packed lamellae. These roundish domains have radius of 45 nm and are arranged at average (core-to-core) distance of ≈100 nm in a dark matrix mainly populated by soft blocks. This morphology is similar to that of the OBCs samples with $\Delta hex = 20$ mol% and 80/20 w_s/w_h ratio. However, contrary to the samples with $\Delta hex = 20$ mol%, the rubbery matrix appears poorly or not populated at all by the lamellar crystals sticking out from the hard domains as

in the pass-through morphology, indicating a major degree of segregation strength between the hard and soft blocks (see Figure 4 and Chapter 3). The average thickness of the lamellar crystals l_c included inside the roundish domains and sticking out of them is identical (≈ 14nm) .

For the merged samples with w_s/w_h ≈ 70/30 and 65/35, the dot-like morphology is replaced by worm-like motifs (Figures 16 and 17). The worm-like motifs are bright and include stacks of tightly packed lamellae with thickness l_c of ≈14 nm, indicating that the domains are essentially populated by hard blocks. The surrounding matrix is dark and is sporadically crossed by lamellar crystals sticking out from the worm-like domains, indicating that the matrix is essentially populated by soft blocks. However, while for the merged sample with w_s/w_h ≈ 70/30 the worm-like domains form isolated entities embedded in the dark matrix (Figure 16), for the merged sample with w_s/w_h ≈ 65/35 the worm-like motifs are largely interconnected (Figure 17). The transversal size of the worm-like motifs and of the meandering regions populated by the soft blocks are ≈ 80 and 70 nm, respectively, for the sample with w_s/w_h ≈ 70/30 and ≈ 70 and 80 nm, respectively, for the sample with w_s/w_h ≈ 65/35. In both cases, the average core-to-core distance ≈ 150 nm. Therefore, the TEM micrographs of Figures 16 and 17 suggest that both samples show only a small tendency, if any, to crystallize according to a pass-through morphology. The hard blocks, instead, tend to crystallize in confined regions wherein the soft blocks are almost completely excluded. Finally, for the merged sample with w_s/w_h ≈ 50/50 (Figures 18A and B), the TEM images show a spotted morphology wherein roundish dark spots of average size close to 100 nm are embedded in a light matrix at average distance of ≈ 200 nm. The dark spots are featureless, are enclosed within not well-defined boundaries and appear only sporadically crossed by lamellar crystals. The majority of the

lamellar crystals, instead, are included in the surrounding light matrix, forming sheaf-like entities running in all the directions. This indicates that the dark roundish spots are namely populated by soft blocks, whereas the light surrounding matrix namely include the crystallizing hard blocks. Therefore, the speckled patterns, observed for the samples with $w_s/w_h \approx 80/20$, 70/30, and 65/35, characterized by roundish and/or worm-like light domains embedded in a dark matrix, seems here to be reversed. For the OBC sample with $w_s/w_h \approx$ 50/50, indeed, the bright regions, occupied by densely stacked lamellar crystals formed by the hard blocks, constitute the matrix, wherein the roundish black domains, namely populated by soft-block, are embedded (Figures 18C and D).

It is worth noting that, based on thermodynamic arguments,[5,118] in the hypothesis that the observed morphologies shown by the OBC series with Δhex = 30 mol% in the TEM images of Figures 15-18 reflect the degree of mesophase separation already occurring in the melt, the phase separated morphology shown in the solid state by the sample with $w_s/w_h \approx 50/50$ (Figure 18) should be more pronounced than that of the samples with $w_s/w_h \approx 80/20$, 70/30, and 65/35 characterized by an asymmetric base unit (Figures 15-17). This tendency is measured by the degree of sharpness of the interfaces at the boundaries between the different domains and by how pronounced is the frequency of the lamellar crystals passing through the boundaries of the hard-block-rich domains and travelling across the soft-block-rich regions. The TEM images of Figures 15-18 indicate that the interface boundaries are sharp for the samples with $w_s/w_h \approx 80/20$ and 70/30 and less defined for the samples with $w_s/w_h \approx 65/35$ and 50/50. However, the occurrence of pass-through events decreases with the decreasing of the soft block content w_s, being sporadic for the sample with w_s/w_h ratio $\approx 80/20$, more sporadic for the samples with $w_s/w_h \approx 70/30$ and 65/35, and almost null for the sample with $w_s/w_h \approx 50/50$.

Comparing the TEM images of Figures 15 and 18 relative to the samples with Δhex = 30 mol% and $w_s/w_h \approx 80/20$ and 50/50, respectively, and of Figures 4 and 10 relative to the samples with Δhex = 20 mol% and similar w_s/w_h ratio, it appears that the increase in the difference of comonomer content between the hard and soft blocks induces a neat increase in segregation strength, and hence an increased tendency of the hard blocks to crystallize in confined domains.

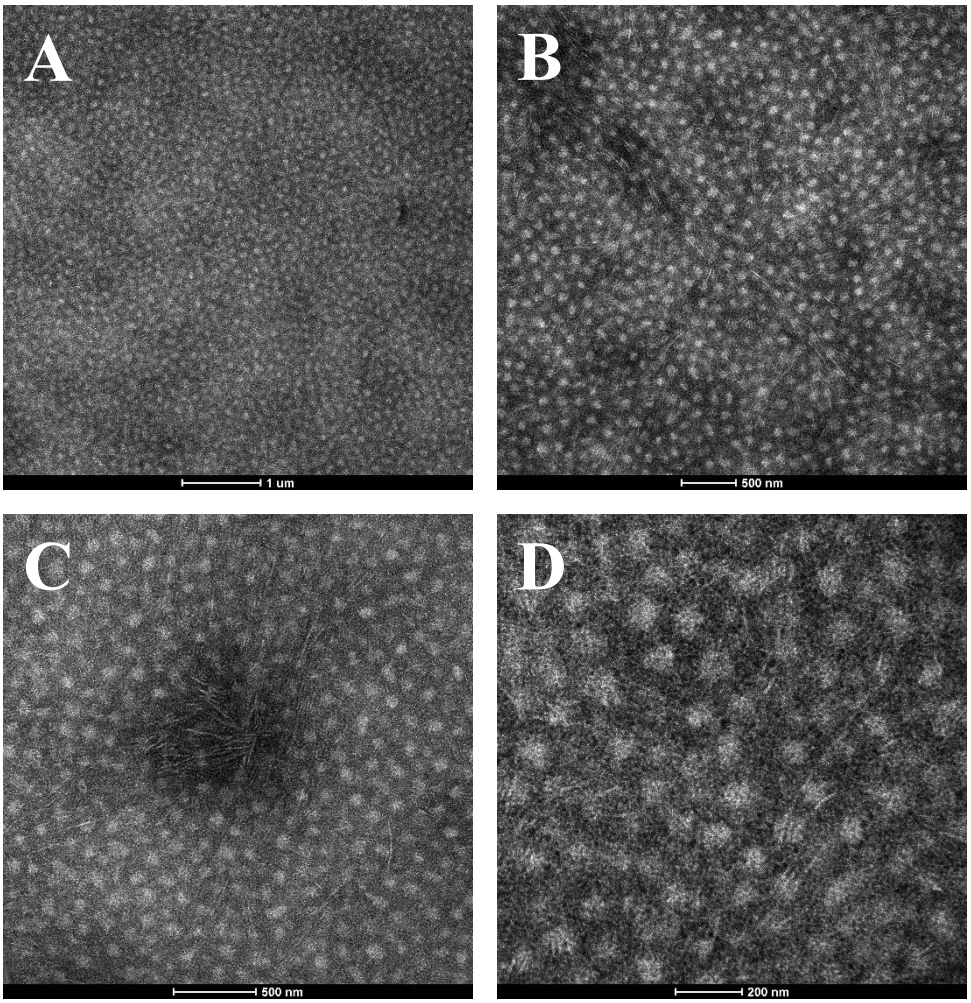

Figure 15. Bright field TEM micrographs of the OBC sample with $\Delta hex \approx 30$ mol% and w_s/w_h ratio of 80/20 at different magnifications. The sample is RuO_4 stained for several hours, in order to enhance the contrast between the lamellar crystals (bright), and the amorphous regions (dark).

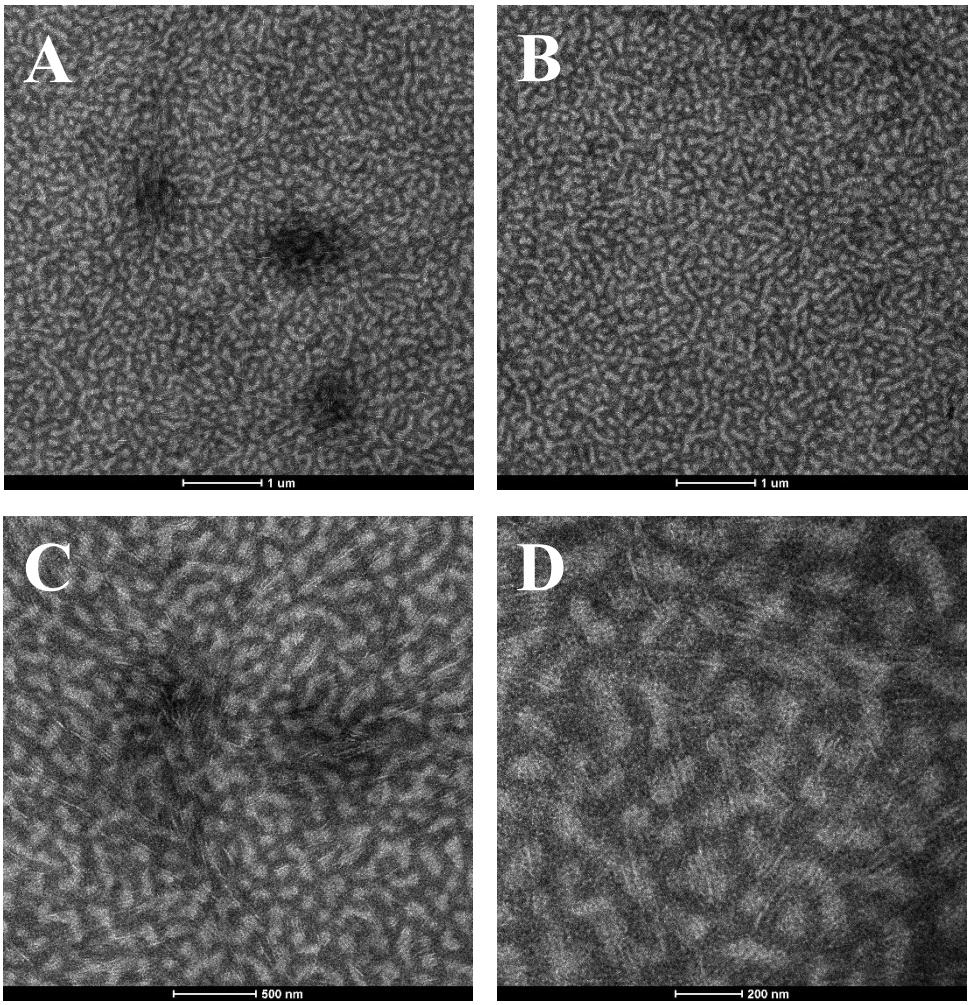

Figure 16. Bright field TEM micrographs of the OBC sample with $\Delta hex \approx 30$ mol% and w_s/w_h ratio of 70/30 at different magnifications. The sample is RuO_4 stained for several hours, in order to enhance the contrast between the lamellar crystals (bright), and the amorphous regions (dark).

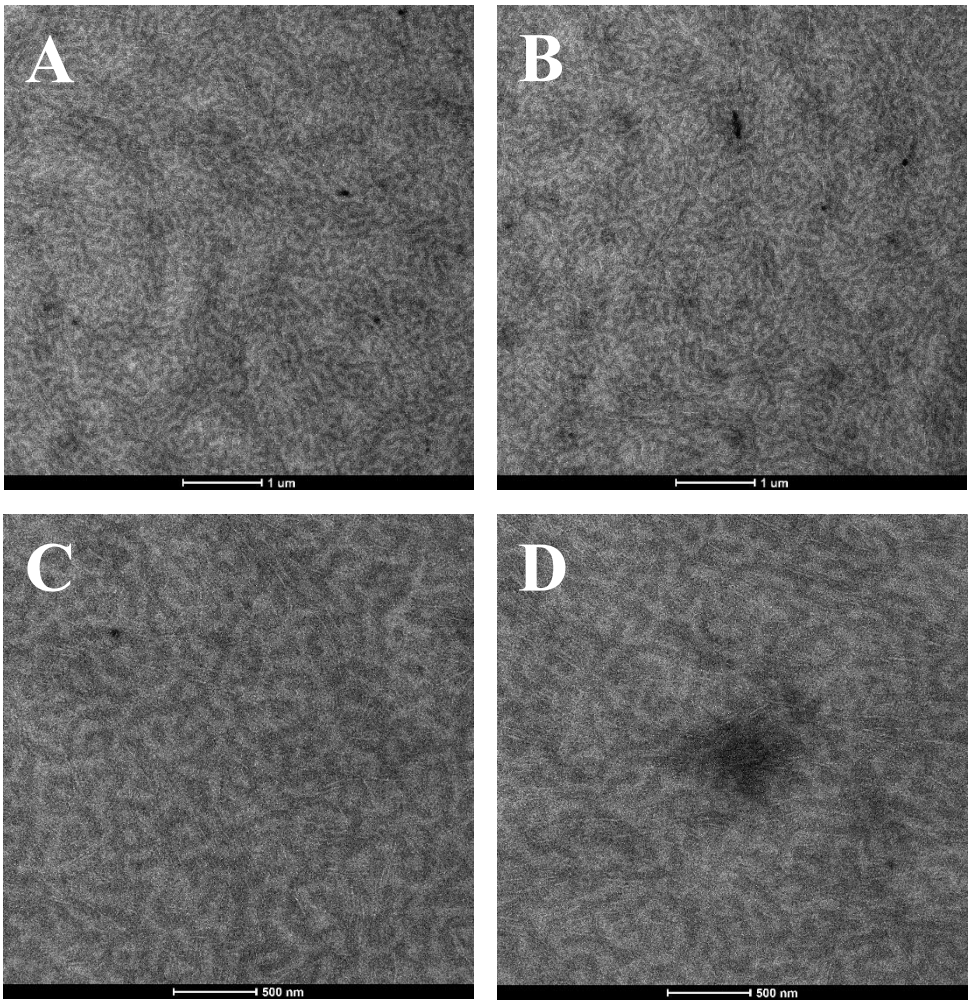

Figure 17. Bright field TEM micrographs of the OBC sample with $\Delta hex \approx 30$ mol% and w_s/w_h ratio of 65/35 at different magnifications. The sample is RuO_4 stained for several hours, in order to enhance the contrast between the lamellar crystals (bright), and the amorphous regions (dark).

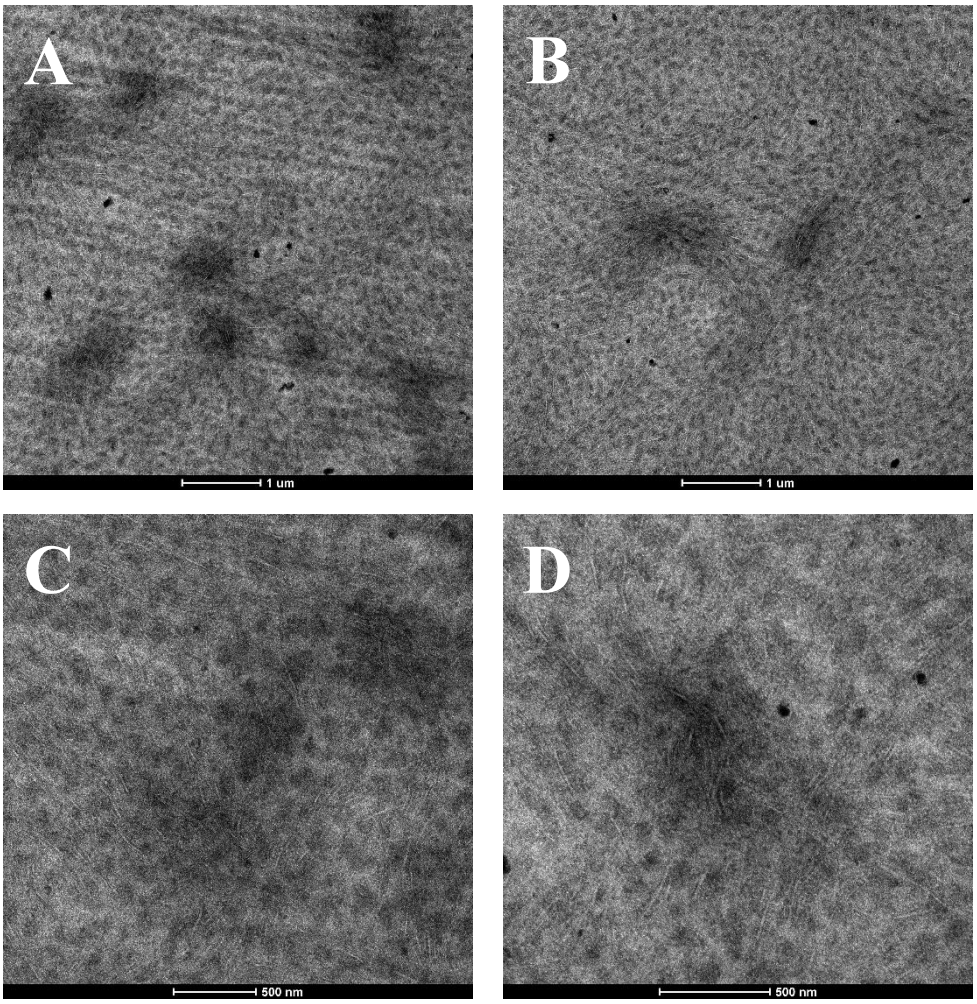

Figure 18. Bright field TEM micrographs of the OBC sample with $\Delta hex \approx 30$ mol% and w_s/w_h ratio of 50/50 at different magnifications. The sample is RuO_4 stained for several hours, in order to enhance the contrast between the lamellar crystals (bright), and the amorphous regions (dark).

4.4. Synthesis and Characterization of Ethylene/4-Methyl-1-pentene OBCs

While ethylene/1-hexene olefin multi-block copolymers are well-known and commercialized materials (i.e., Infuse^{TM} by Dow Chemical), examples of statistical OBCs made with different co-monomers are rare. In particular, no cases are reported of similar materials featuring ethylene in copolymerization with 4-methyl-1-pentene (4M1P). Compared to ethylene/1-hexene (or 1-octene) multiblock copolymers, in materials featuring 4M1P as comonomer, phase separation should be triggered more easily given the higher steric hindrance of this comonomer and hence the resultant higher segregation strength between the comonomer rich (soft) and the comonomer poor (hard) blocks.

The catalysts pair Cat2/Cat3 was used to synthesize a series of E/4M1P with 4M1P content in the soft and ($x_{4M1P,soft}$) and hard ($x_{4M1P,hard}$) blocks of ≈ 20 and 0.5 mol%, respectively, $\Delta 4M1P$ of ≈ 19 mol%, and weight ratio between the soft and hard blocks w_s/w_h of ≈ 80/20. Therefore, the chain microstructure of the so-obtained E/4M1P OBCs is similar to that of the ethylene/1-hexene OBCs investigated in paragraph 4.1 of this Chapter. The molecular mass, the average 4M1P content, the 4M1P content in the soft blocks, and the mass fraction of soft blocks of the different PPR replicas are reported in Table 15. The corresponding aCEF traced are shown in Figure 19.

Table 15. Molecular parameters for the ethylene/4-methyl-1-pentene OBCs with $\Delta 4M1P \approx 20$ mol% and $w_s/w_h \approx 80/20$.

Sample ID	Yield (mg)	M_n (kDa)	M_w (kDa)	Đ	x_{4M1P} (mol%)	$x_{4M1P,soft}$ (mol%)	w_s (wt%)	AF (wt%)	$T_{el,\ max}$ (°C)
5	174	60	120	2.0	0.158	0.230	0.753	15	100.3
6	77	63	148	2.4	0.142	0.193	0.778	19	100.5
7	171	59	153	2.6	0.152	0.202	0.796	21	99.6
8	176	74	184	2.5	0.149	0.204	0.779	12	99.9
9	121	53	134	2.5	0.145	0.199	0.776	17	101.8
10	148	65	163	2.5	0.146	0.200	0.774	15	100.3

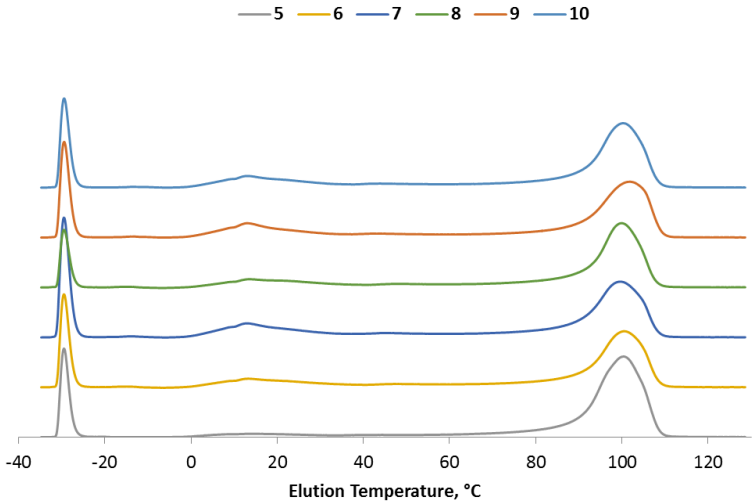

Figure 19. aCEF profiles of the OBCs replicas with $\Delta 4M1P \approx 20$ mol% and $w_s/w_h \approx 80/20$ of Table 15.

All replicas show a low temperature elution peak, due to an amorphous fraction essentially constituted by soft block (AF, Figure 19). The relative intensity of the AF peak is around 15-20% (Table 15). A broad elution peak spanning the temperature range 0-30°C is also present due to chains constituted by long soft blocks linked to very short hard blocks. The main elution peak occurs around 100°C, due to multiblock chains including long hard blocks alternated with soft blocks. Due to the similar chain microstructure (Table 15)

and aCEF traces, the PPR replicas 5-10 of Table 15 have been merged together (Mix 4M1P) using the protocol described in Chapter 2.

The structural, thermal, and mechanical properties along with the morphology of the E/4M1P merged OBC sample have been hence investigated and the results are reported in Figure 20-23 and Tables 16, 17. The merged sample Mix 4M1P crystallizes in the orthorhombic form of PE, as shown in Figure 20A by the presence of (110) and (200) reflections at $2\theta \approx 21°$ and 24°, respectively. The DSC curves show melting and crystallization peaks around 120°C and 95°C respectively (Figure 20B), as observed for all the others OBCs studied so far.

Table 16. Main properties of the merged OBC sample Mix 4M1P.

Sample ID	x_c (%)	T_m (°C)	ΔH_m (J/g)	T_c (°C)	ΔH_c (J/g)	T_g (°C)	q^* (nm^{-1})
Mix 4M1P	20.4	121.5	28.0	97.1	24.5	-49	0.20, 0.80

The SAXS profile shows two bumps, corresponding to a sharp correlation peak at $q \approx 0.20$ nm^{-1} and a broader halo at $q \approx 0.80$ nm^{-1} in the Lorentz corrected curve (Figure 21B). The double-peaked SAXS curve can be considered the hallmark of the peculiar multiblock chain architecture of the OBCs, characterized by a non-uniform length of the hard and soft blocks. In particular, the presence of hard blocks of different length generates molecular segregation upon crystallization, that is formation of different populations of lamellar stacks, characterized by similar lamellar thickness, but different long spacing and thickness of the amorphous layers, due to the tendency of the hard blocks of different molecular mass to crystallize in separated domains.

The analysis of the mechanical properties of the sample Mix 4M1P (Figure 22 and Table 17) indicates that it presents good ductility, high mechanical resistance (Young's modulus E = 9 MPa, $\sigma_b \approx 7$ MPa), and a marked strain hardening, due to the high crystallinity (x_c = 32.5%). Nonetheless, this sample shows good elastomeric properties, as shown by the tension set $t_b \approx 90\%$.

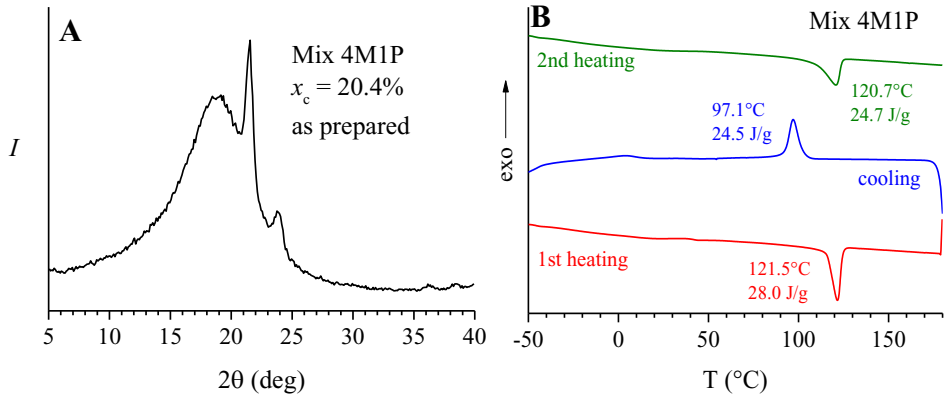

Figure 20. X-ray powder diffraction profile (A) and DSC curves (B) of the merged ethylene/4-methyl-1-pentene OBC Mix 4M1P.

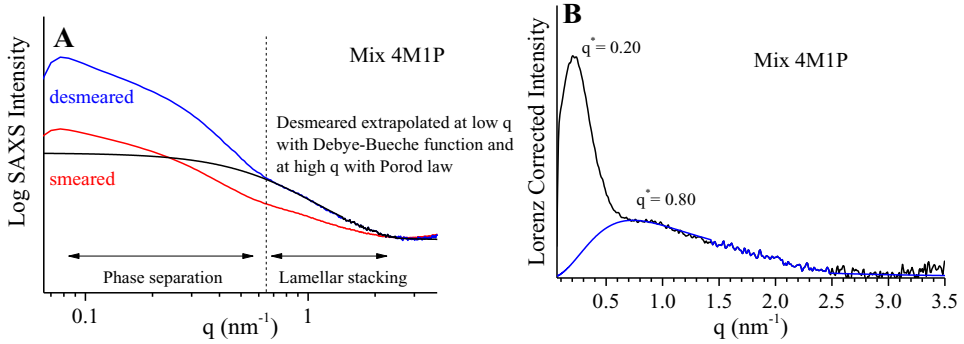

Figure 21. SAXS profile (A) and Lorentz corrected SAXS intensity (B) of the merged ethylene/4-methyl-1-pentene OBC Mix 4M1P.

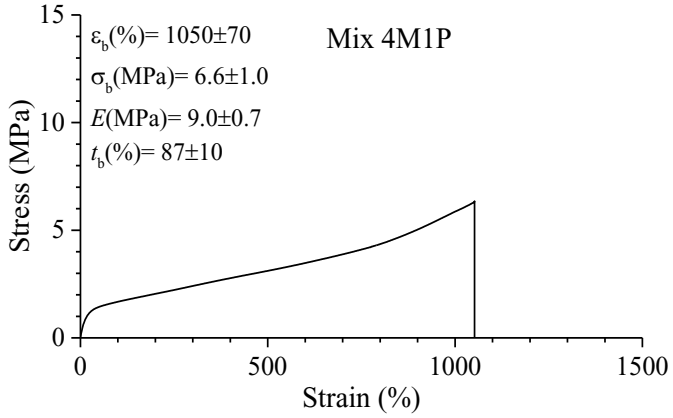

Figure 22. Stress-strain curve of the merged ethylene/4-methyl-1-pentene OBC Mix 4M1P.

Table 17. Mechanical parameters extracted from the stress-strain curves of merged OBC Mix 4M1P.

Sample ID	E (MPa)	σ_y (MPa)	ε_y (%)	σ_b (MPa)	ε_b (%)	t_b (%)
Mix 4M1P	9.0±0.7	/	/	6.6±1.0	(105±7)·10	(9±1)·10

The bright field TEM images of the merged sample Mix 4M1P show, at low magnification (Figure 23A), round-shaped bright domains constituted by hard blocks surrounded by a black soft-block-rich matrix. The interior of spherulitic structures is visible in Figures 23B-D, as indicated by the presence of lamellar sheaves splaying from a common center. At higher magnification (Figure 23E), the inside of the roundish hard domains becomes distinguishable. It is apparent that the roundish domains include tightly stacked lamellar crystals, with little or no inclusion of the soft blocks in the interlamellar layers. Passing-through lamellae are also present, creating bridges between the different hard-block-rich domains. However, the fraction of lamellar crystals crossing the soft matrix appear lower than that characterizing the homologous ethylene/1-hexene (or 1-octene) samples with Δcom = 20 mol% and w_s/w_h =

80/20 (Figure 4 and Chapter 3). The less pronounced pass-through morphology of the sample Mix 4M1P is in agreement with the high segregation strength induced by a comonomer more hindered than 1-hexene or 1-octene units.

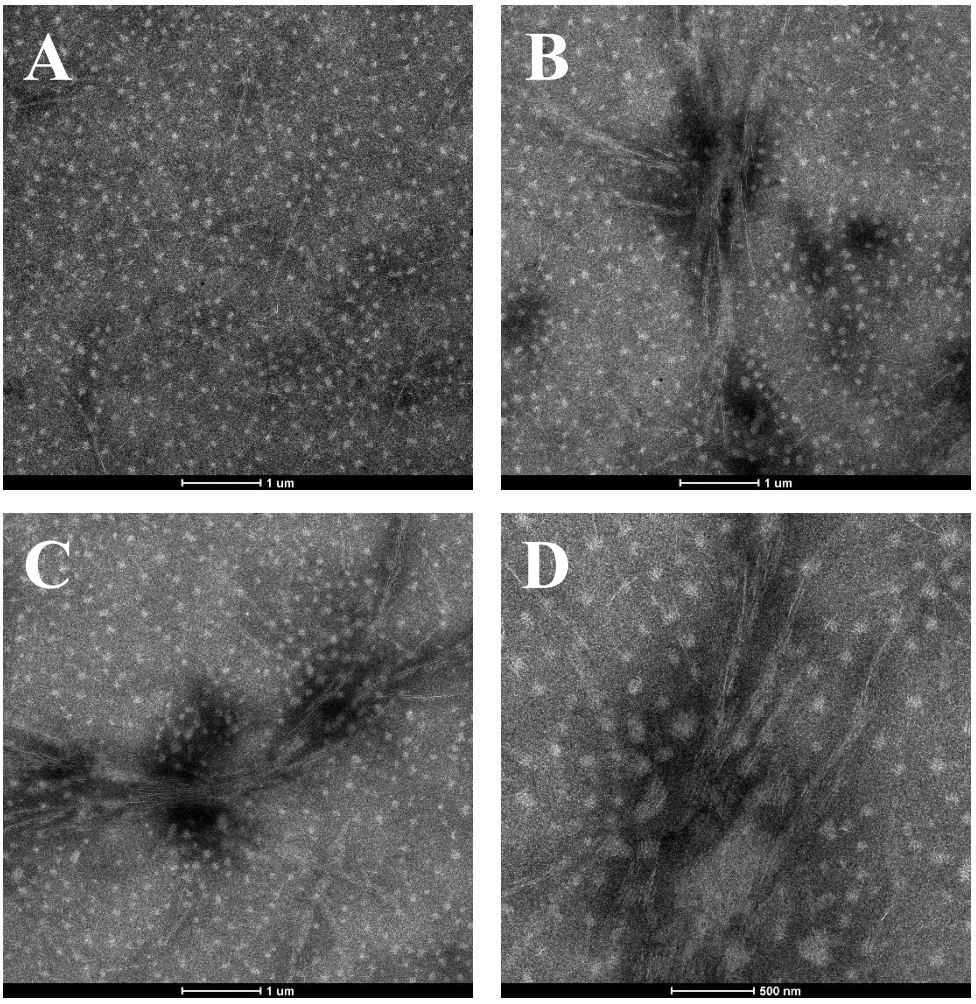

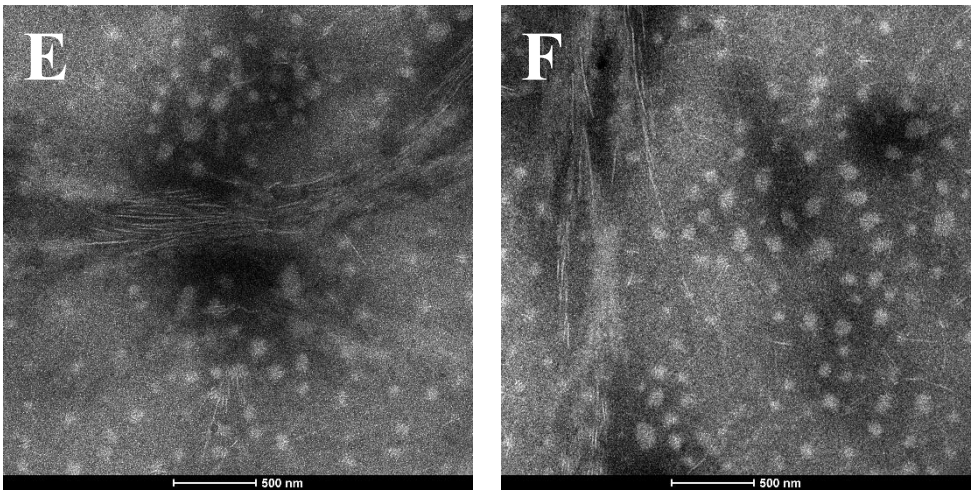

Figure 23. Bright field TEM micrographs of the 80/20 ethylene-4-methyl-1-pentene sample Mix 4M1P at different magnifications. The sample is RuO_4 stained for several hours, in order to enhance the contrast between the lamellar crystals (bright), and the amorphous regions (dark).

4.5. Synthesis and Characterization of Ethylene/1-Hexadecene OBCs

In order to investigate the effect of different kind of comonomers on the final properties and on the solid-state behavior of ethylene-based multiblock copolymers against the "classical" commercial OBCs, novel ethylene/1-hexadecene (C16) OBCs were synthetized. The use of 1-hexadecene as a comonomer in chain-shuttling copolymerization might be valuable due to the possibility of side-crystallization of the long side branch at low temperatures.[119]

In order to verify the possibility of side-chain crystallization of C16 units in ethylene/1-hexadecene copolymers, a random soft copolymer was

synthesized with only Cat2 (1-hexadecene content x_{C16} = 16 mol%) and analyzed by DSC. The results, reported in Figure 24, clearly show the low temperature crystallization (-8.9°C) and melting (9.4°C) of the side chains. Hence, the effect of side-crystallization on OBCs phase separation, morphology and mechanical properties can be studied.

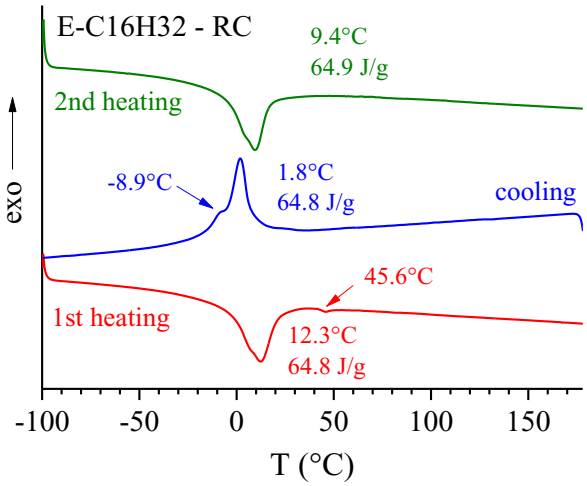

Figure 24. DSC curves of an ethylene/1-hexadecene (x_{C16} = 0.16) random copolymer.

A series of ethylene/1-hexadecene with C16 content in the soft ($x_{C16,soft}$) and hard ($x_{C16,hard}$) blocks of ≈ 0.20 and 0.5 mol%, respectively, $\Delta C16$ ≈ 20 mol%, and weight ratio between the soft and hard blocks w_s/w_h ≈ 80/20, 65/35, and 50/50 have been synthesized using the catalysts pair Cat2/Cat3. The value of Δcom is similar to that of the ethylene/1-hexene OBCs investigated in paragraph 4.1 of Chapter 4, but the values of w_s/w_h span a wider range. The E/C16 OBCs samples have been analyzed by GPC, aCEF and ^{13}C NMR techniques and the results are reported in Table 18 and Figure 25. It is apparent that the E/C16 Sample 2 of Table 18 may be considered a replica of the sample 1.

Table 18. Molecular parameters of the ethylene/1-hexadecene OBCs synthetized with variable w_s/w_h and $\Delta C16 \approx 20$ mol%.

Sample ID	Yield (mg)	M_n (kDa)	M_w (kDa)	Đ	x_{C16} (mol%)	$x_{C16,soft}$ (mol%)	w_s (wt%)	AF (wt%)	$T_{el,\ max}$ (°C)
1	276	73	196	2.7	0.136	0.218	80.3	38	98.7
2	319	91	224	2.5	0.153	0.238	81.7	47	97.6
3	193	66	167	2.5	0.106	0.233	66.5	21	105.3
4	129	60	134	2.2	0.007	0.216	51.0	6	107.6

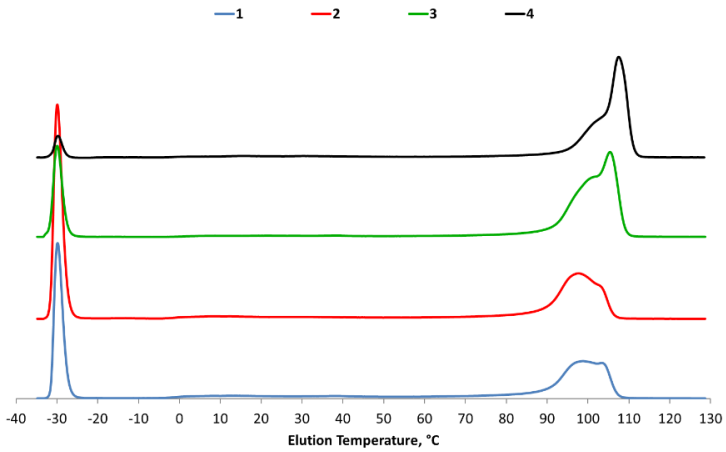

Figure 25. aCEF profiles of the ethylene/1-hexadecene OBCs from Table 18 with $\Delta C16 \approx 20$ mol% and w_s/w_h ratio of ≈ 80/20 (Samples 1 and 2), 65/35 (Sample 3), and 50/50 (Sample 4).

The aCEF traces of the E/C16 samples (Figure 25) show a sub-zero temperature elution peak, due to chains constituted by the sole soft blocks, formed through the homo-shuttling events involving almost exclusively Cat2. The relative intensity of the AF peak decreases with decreasing weight fraction of soft blocks w_s in agreement with the decreasing in the relative amounts of Cat2 used in the synthetic step. The main elution peak show two maxima at ≈ 95-100°C and at ≈ 105-107°C at temperatures that increase with the increasing of the average hard block content w_h. The double maxima of the high temperature elution peaks are due to the fact that the chain shuttling process

generates different populations of chains characterized by blocks of different length. In particular, the length of the blocks changes not only from chain to chain, but also within the same chain. Furthermore, with the decreasing of the w_s value, the relative intensity of the high temperature elution peak increases, due to the increase in the fraction of hard blocks of higher length.

The WAXS profiles and DSC thermograms of the E/C16 OBCs are reported in Figure 26, whereas the results of thermal analysis are summarized in Table 19. The WAXS profiles of the E/C16 OBCs reported in Figure 26A, recorded at room temperature, show the presence of the 110 and 200 reflections of the orthorhombic form of PE at 21° and 24°, respectively, due to the crystallization of long ethylene sequences in the orthorhombic form of PE. The DSC analysis reveals that the side branches crystallize in the temperature range -7 ÷ 2°C and melt and at 10°C, respectively (Figures 26B and C and Table 19). The long ethylene sequences included in the hard blocks, instead, have melting and crystallization of ≈ 120°C and 100°C, respectively (Figures 26B and C and Table 19). In particular, the melting and crystallization temperatures tend to increase with the decreasing of the w_s value, being ≈ 124 and 103°C, respectively, for the sample with w_s/w_h ≈ 80/20 and ≈ 127 and 111°C, respectively, for the sample with w_s/w_h ≈ 50/50.

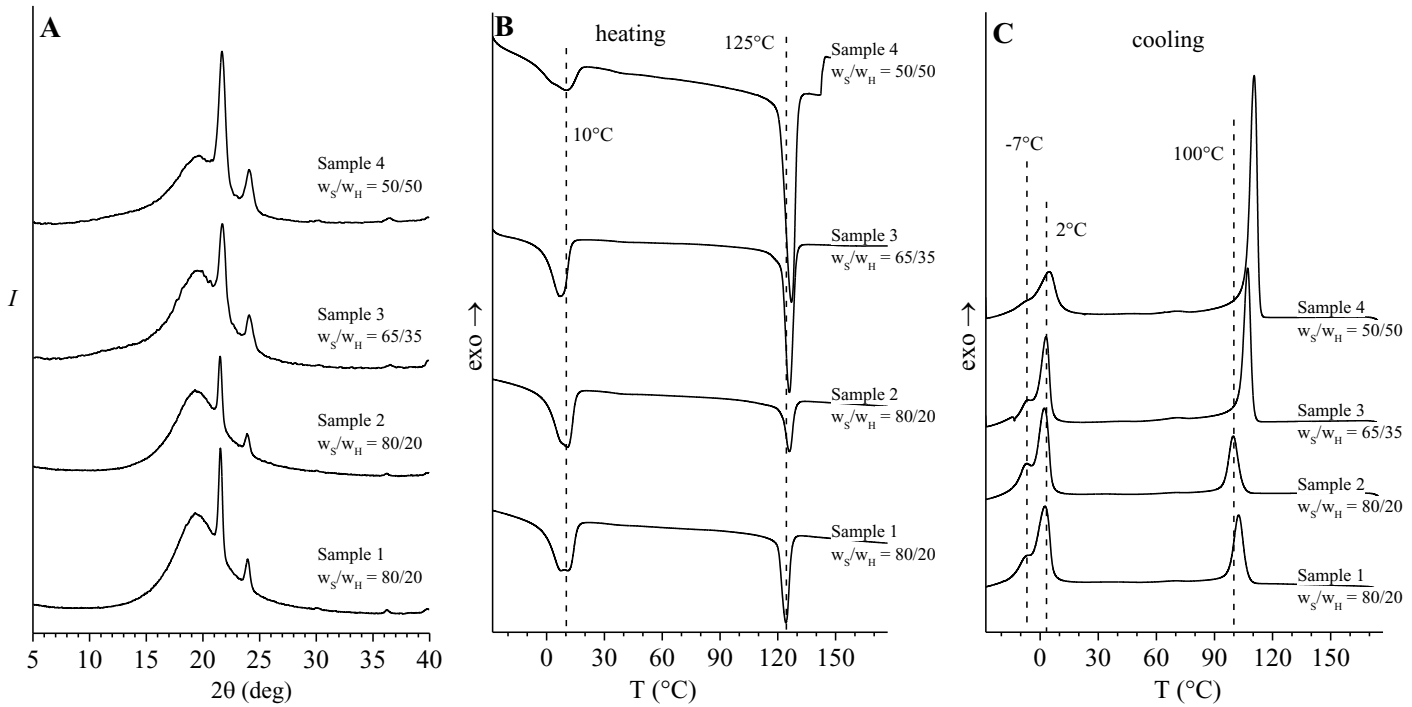

Figure 26. X-ray diffraction profiles (A) and DSC heating and cooling thermograms (B, C) for ethylene-1-hexadecene OBCs of Table 18 with $\Delta C16 \approx 20$ mol% and the indicated values of the w_s/w_h ratio. The double peaked crystallization of the side chains at low temperatures is probably due to intrinsic topological heterogeneity of the environment in which the side chains are located.

Table 19. Degree of crystallinity, melting and crystallization temperatures and corresponding enthalpies of the ethylene-1-hexadecene OBCs of Table 18 with $\Delta C16 \approx 20$ mol% and the indicated values of the w_s/w_h ratio.[a]

Sample ID	x_c (%)	T_{mI} (°C)	ΔH_{mI} (J/g)	T_{mII} (°C)	ΔH_{mII} (J/g)	T_c (°C)	ΔH_c (J/g)
1 80/20	18	7.4 124.2	37.8 26.3	9.9 120.6	37.2 23.3	-7.0; 2.5 102.5	37.1 23.3
2 80/20	17	10.7 126.0	39.4 18.6	10.2 120.0	37.8 18.6	-6.9; 2.1 99.7	37.9 18.6
3 65/35	20	7.3 126.1	32.4 47.7	8.1 121.0	32.5 38.7	-7.1; 3.1 107.2	32.4 38.4
4 50/50	26	10.0 127.1	23.7 73.4	7.8 123.9	23.5 60.8	-7.0; 4.7 110.5	23.7 60.8

a. The low melting and crystallization temperatures are relative to the side chains crystals. The corresponding melting and crystallization enthalpies are also reported.

The solid-state morphology of the E/C16 OBCs samples has been investigated by performing a TEM analysis. Samples 1 and 2 share the same molecular features and solid-state morphology, so only the TEM images of the Sample 1 are reported. The bright field images of the E/C16 samples are reported in Figures 27-29. The micrographs at low magnification of Sample 1 with w_s/w_h ratio of 80/20 (Figures 27A-D) show roundish bright domains, of average size equal to ≈140 nm, populated by hard blocks, embedded in a dark matrix essentially populated by soft blocks. Contrast arises from the preferred adsorption of the staining agent (RuO_4) within the soft-block-rich regions. In the images taken at higher magnification (Figures 27 C-F), the roundish domains appear densely packed by well-formed lamellar crystals, with thickness l_c = 14 nm, that run in parallel and extend in the surrounding soft matrix with a less dense arrangement, according to the so-called "pass-through" morphology.

In the case of Sample 3 (Figure 28), which has a ratio between the fractions of soft and hard blocks equal to 65/35, the TEM bright field micrographs show again a phase separated morphology, similar to the pass-through morphology

that develops in the 80/20 sample (Figure 27), even though the boundaries at the interphase between the different domains appear less pronounced. In particular, the morphology of Figures 28A and B appears rather uniform, and only Figure 28F shows the presence of the roundish hard-block-rich domains. The average size of the roundish domains ≈ 140 nm, whereas the average thickness of the lamellar crystals l_c is ≈ 18 nm.

Finally, for Sample 4, with a 50/50 w_s/w_h ratio, the micrographs of Figure 29 show a much more segregated solid-state morphology in comparison to the morphology of the samples with higher w_s values, in agreement with the fact that a symmetric base unit should give rise to a higher segregation strength. As a matter of fact, the shape of the (bright) hard-block-rich domains is worm-like. The average width of the worms is equal to ≈110 nm, whereas the lamellar thickness corresponds to l_c ≈ 18 nm. The meandering soft domains (dark) also appear worm-shaped and have a width of ≈ 120 nm (Figure 29D). Furthermore, in this case as well, the bright domains appear densely populated by lamellar crystals, the latter radiating outside the domains and passing-through the intervening amorphous region with a less dense packing (Figure 29).

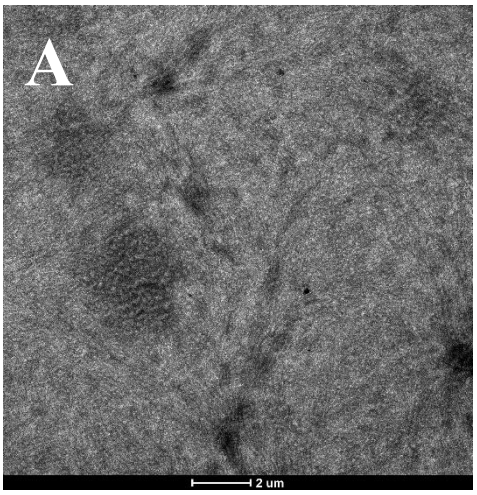

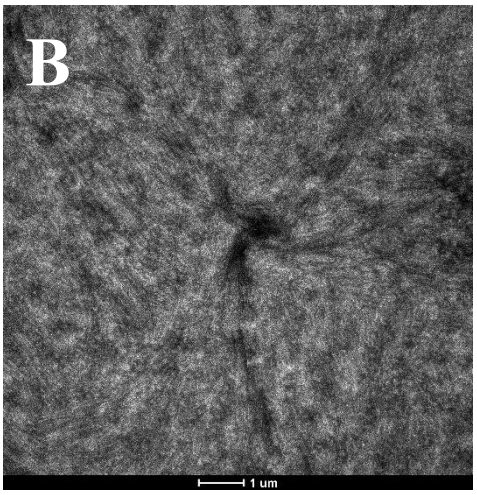

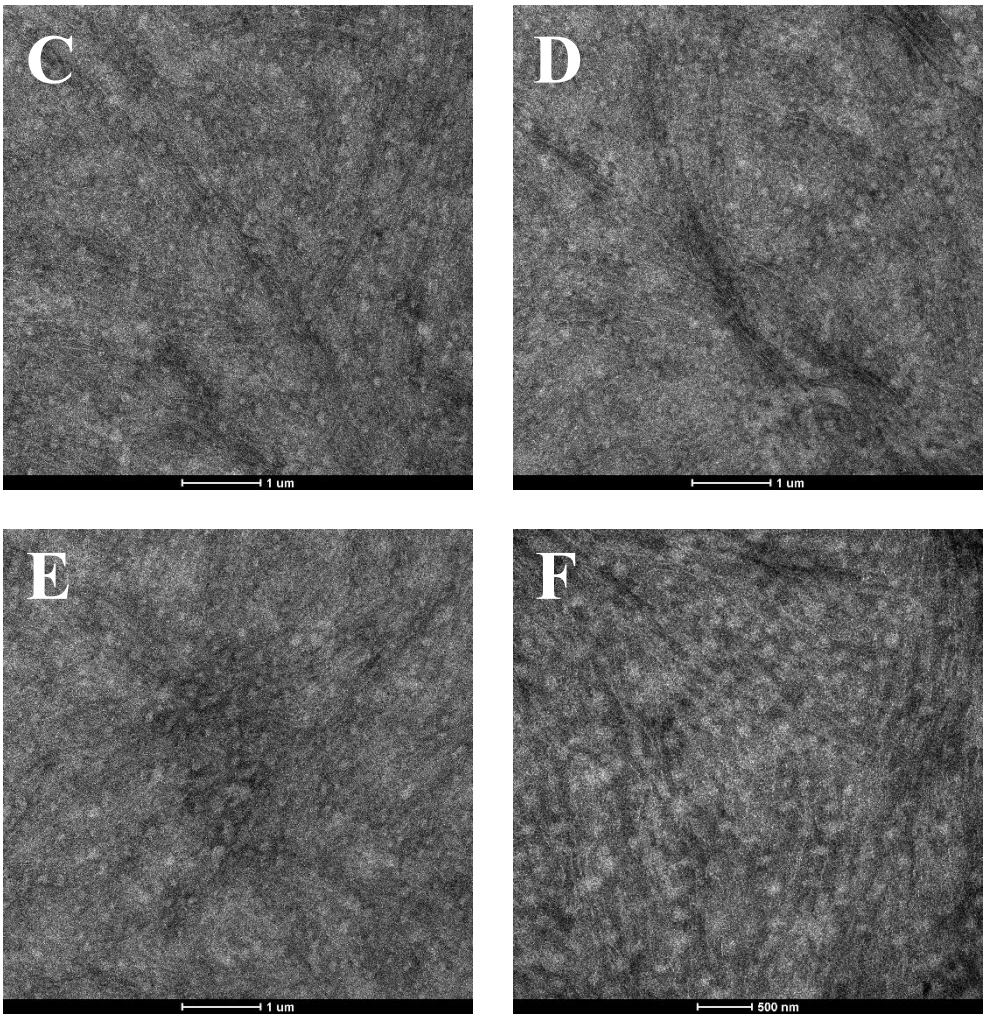

Figure 27. Bright field TEM micrographs of the ethylene-1-hexadecene OBC Sample 1 with $\Delta C16 \approx 20$ mol% and w_s/w_h ratio ≈ 80/20, at different magnifications. The sample is RuO_4 stained for several hours, in order to enhance the contrast between the hard-block-rich regions, densely populated by lamellar crystals (bright), and the amorphous soft-block-rich regions, less densely populated by the lamellar crystals (dark).

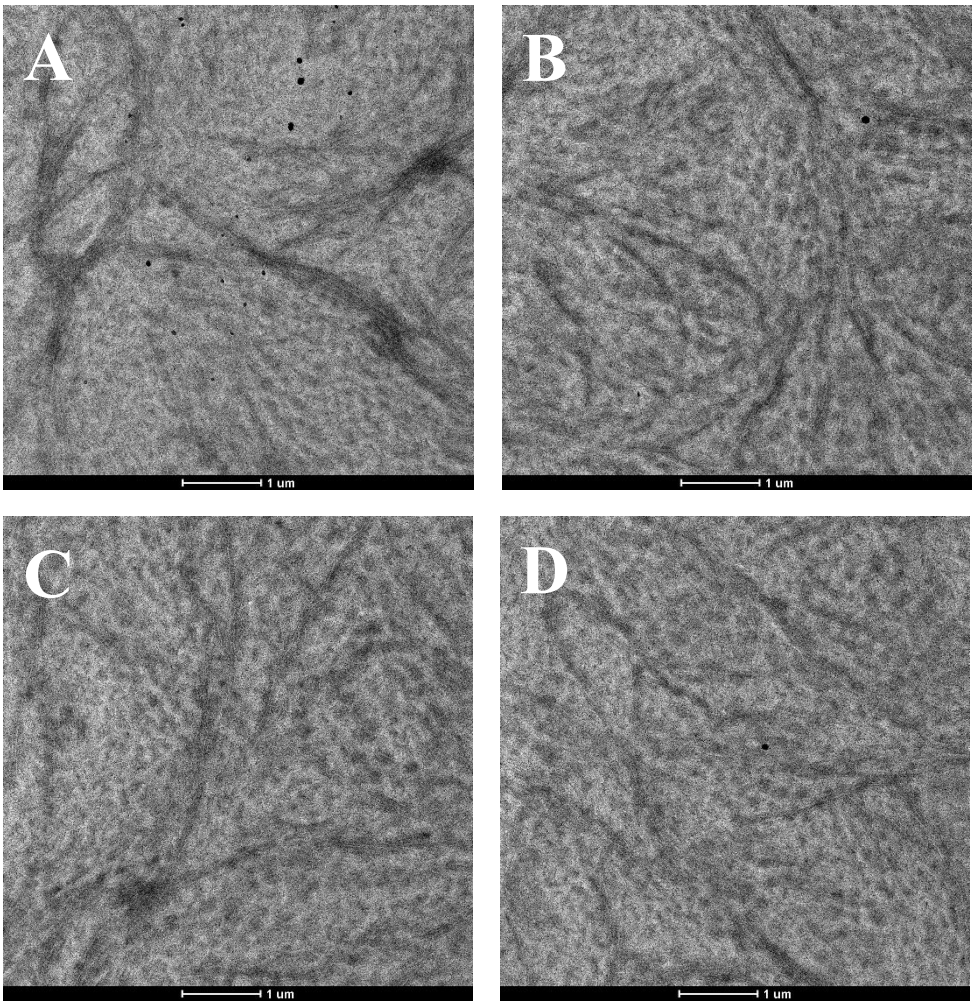
A
1 um
B
1 um
C
1 um
D
1 um

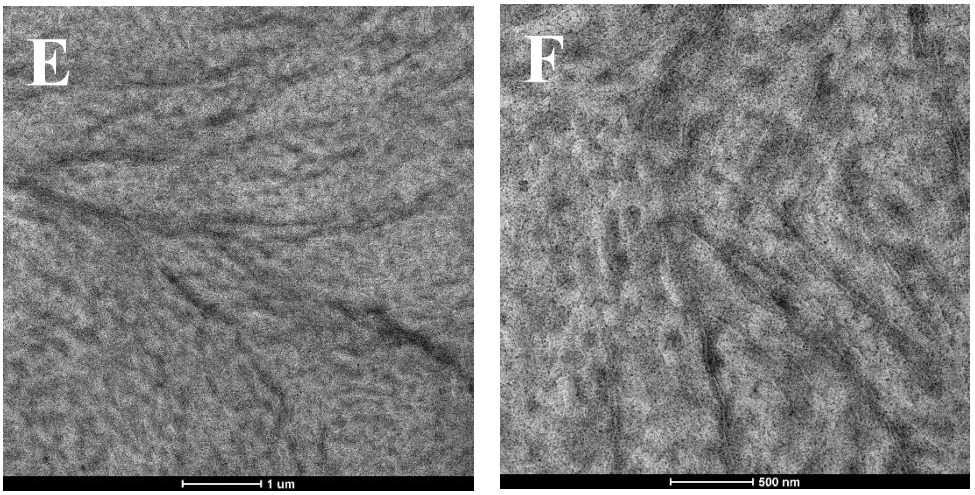

Figure 28. Bright field TEM micrographs of the ethylene-1-hexadecene OBC Sample 3 with $\Delta C16 \approx 20$ mol% and w_s/w_h ratio ≈ 65/35, at different magnifications. The sample is RuO_4 stained for several hours, in order to enhance the contrast between the hard-block-rich regions, densely populated by lamellar crystals (bright), and the amorphous soft-block-rich regions, less densely populated by the lamellar crystals (dark).

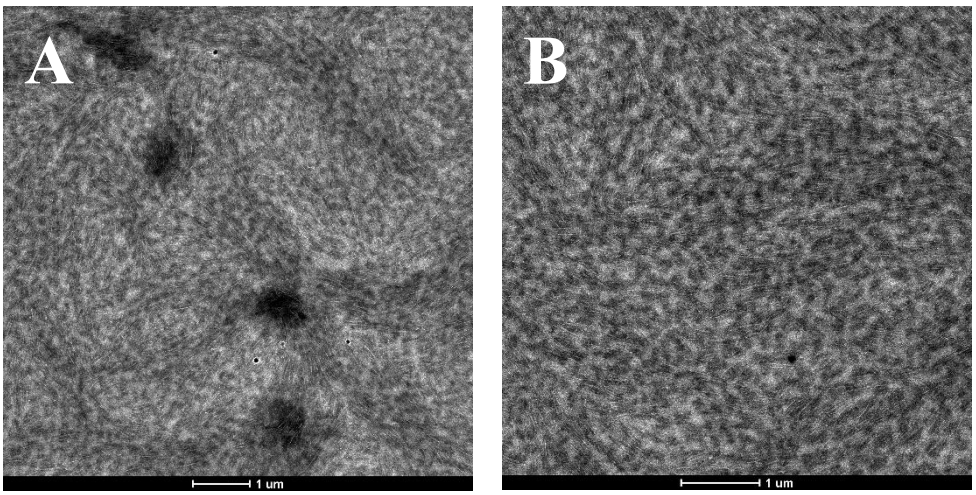

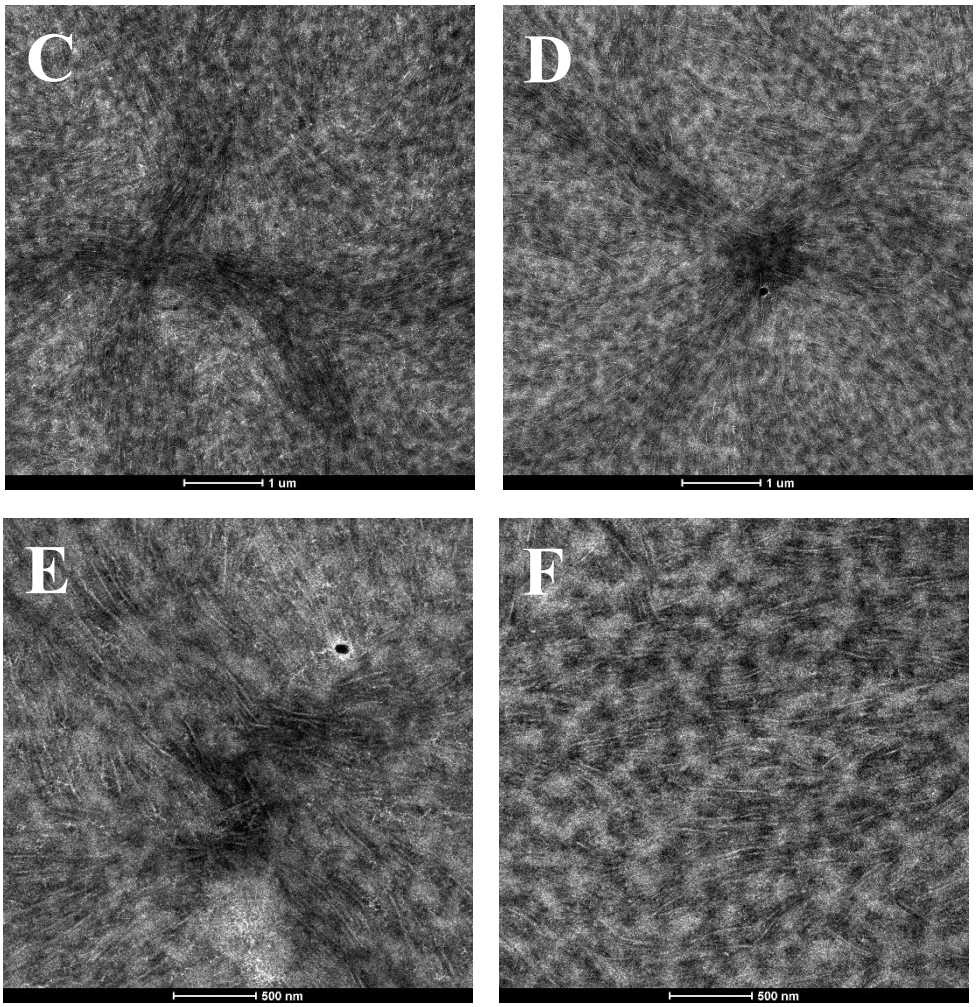

Figure 29. Bright field TEM micrographs of the ethylene-1-hexadecene OBC Sample 4 with $\Delta C16 \approx 20$ mol% and w_s/w_h ratio ≈ 50/50, at different magnifications. The sample is RuO_4 stained for several hours, in order to enhance the contrast between the hard-block-rich regions, densely populated by lamellar crystals (bright), and the amorphous soft-block-rich regions, less densely populated by the lamellar crystals (dark).

The crystallization of the side chains to crystallize taking place at low temperatures shown by the E/C16 OBC samples of Table 18 has the potential to bring some interesting mechanical properties as a function of the temperature, due to the changes in crystallinity and stiffness. Hence the PPR

replicas Samples 1 and 2 of Table 18, with $\Delta C16 \approx 20$ mol%, have been merged together in order to obtain an amount of material high enough to measure the tensile properties at -15°C and 25°C.

The stress-strain curves of the merged sample, Mix C16, recorded at 25 and -15°C are reported in Figure 30, whereas the corresponding mechanical parameters are compared in Table 20. At 25°C the merged sample Mix C16 shows a thermoplastic elastomeric behavior typical of OBCs, with no pronounced yielding, high ductility and good elastic recovery, the deformation at break ε_b and the tension set at break t_b being ≈ 1600% and ≈ 300%, respectively. Furthermore, the merged sample shows a low value of Young's modulus (≈ 2MPa) and a modest strain-hardening (curve a of Figure 30 and Table 20). On the other hand, at -15°C, the mechanical behavior changes dramatically (curve b in Figure 30). Indeed, at low temperature, the stress-strain curve shows a remarkable increase in the mechanical resistance and a decrease in the ductility, as shown by the values of Young's moduli E, elongation at break ε_b, and stress at break σ_b equal to 112 MPa, ≈800%, and 8.7 MPa, respectively, in Table 20. This increase in mechanical strength is ascribable to the formation of additional crystals from part of the side chains occurring at low temperatures. Furthermore, the strain oscillation behavior observed in the stress strain curves recorded at -15°C is due to multiple necking behavior. The origin of this mechanical instability is most likely ascribable to the crystallization of the side chains. Finally, it is worth noting that the OBC specimens stretched at low temperature, once heated back to room temperature, recover almost completely the initial size and shape.

The noticeable increase of mechanical strength by effect of the crystallization of the side chain at low temperatures and the immediate recovery of the initial size upon heating to room temperature suggests that this

novel class of OBCs may find promising applications for fabrication of mechanical devices exploiting their properties of temperature driven mechanical sensing, such as temperature sensitive food and/or drug tags.

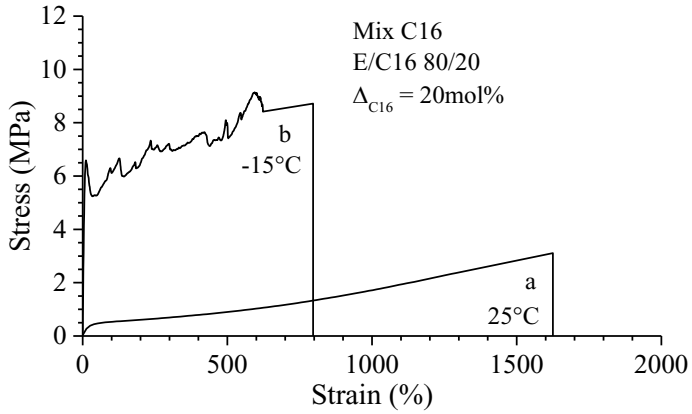

Figure 30. Stress-strain curves for the merged OBC Mix C16 with $\Delta C16 \approx 20$ mol% and w_s/w_h ratio ≈ 80/20 obtained at 25°C (a) and -15°C (b). The strain oscillation behavior at -15°C, due to multi-necking phenomena, is clearly visible.

Table 20. Values of Young's modulus E, tension set at break t_b, stress at break σ_b, deformation at break ε_b) extracted from the stress-strain curves at 25°C and -15°C for ethylene-1-hexadecene OBCs Mix C16 with $\Delta C16 \approx 20$ mol% and w_s/w_h ratio ≈ 80/20.

Sample ID	T (°C)	E (MPa)	t_b (%)	σ_b (MPa)	ε_b (%)
Mix C16	25	2.4±0.2	290±10	3.1±0.8	$(16\pm4)\cdot10^2$
	-15	110±30	/	9±5	$(8\pm2)\cdot10^2$

A structural analysis during deformation has been performed on the merged OBC Mix C16 by using an automatic diffractometer KCCD Nonius, recording the fiber diffraction patterns on an area detector (see Chapter 2 for details). These measurements have allowed to observe the crystallization of the side chains induced by the low temperatures (-15°C), the relative orientation of the newly formed crystals with respect to the pre-existing ones stable at

room temperatures (texture), and the possible increase in crystallinity during cooling and stretching.

The bidimensional (2D) X-ray fiber diffraction patterns of the OBC sample Mix C16 stretched at different deformations and the corresponding radial, equatorial, and azimuthal profiles are reported in Figures 31-34. The azimuthal profiles, in particular, are obtained in correspondence of the 110 and 200 reflections of PE in the orthorhombic form.

At $\varepsilon = 0\%$ and 25°C, only the ethylene sequences of the hard blocks are able to crystallize in the orthorhombic form of PE. The 2D diffraction pattern (Figure 31A) shows Debye-Scherrer rings in correspondence of the 100 and 200 reflections at $2\theta(\text{MoK}\alpha 1) = 9.9$ and 11° (Figure 31A'), respectively. This indicates that the crystals are not oriented. When the temperature is cooled down to -15°C, the intensity of the Debye-Scherrer rings increases (Figure 31B), indicating that the degree of crystallinity increases, due to the crystallization of the side chains in the orthorhombic form of PE (Figure 31B'). From the radial profiles (Figure 31A',B'), after subtraction of the background intensity, approximated by a straight line, the increase in the degree of crystallinity x_c due to the crystallization of the side chains Δx_c has been calculated, as the ratio between the areas subtending the profiles at -15 °C A_{15} and 25 °C A_{25}, through the equation $\Delta x_c = (A_{15} - A_{25})\, A_{25}^{-1}$. The so-determined incremental crystallinity value Δx_c corresponds to ≈8% upon cooling.

With increasing deformations at 400% (Figure 31C) and 1000% (Figure 33A) at 25°C, the degree of orientation of the crystals with the chain axes parallel to the stretching direction gradually increases, as indicated by the slight polarization of the intensity relative to the 110 and 200 reflections on the equator, overlaying the corresponding Debye-Scherrer rings. In particular, the azimuthal intensity profile relative to the 110 reflection shows, at 400%

deformation, faint maxima at value of the azimuthal angle χ equal to 90, +30, -30, 150 and -150°, that is on the equator, and at ± 30° off the meridian (Figure 32C), and only at 1000% deformation the 110 reflection becomes well-polarized on the sole equator (Figure 34A). The 200 reflection, instead, appears polarized on the equator not only at 1000% deformation (Figure 34A'), but already at 400% deformation (Figure 32C'). The four arcs polarization of the 110 reflection of PE at intermediate deformations, correspond to the breaking of the lamellar crystals to form chevron-like motifs. These motifs originate from mechanical instability of the crystals that are subjected to forces acting on the samples at microscopic level, along a direction perpendicular to the tensile stress.[120] When the stretched samples are cooled down to -15°C, for the value of deformation ε = 400%, the 110 and 200 reflections show a strong polarization on the equator, as indicated by the intensity distribution in the fiber diffraction pattern (Figure 31D) and in the corresponding azimuthal profiles (Figures 32D,D'). With the increasing of the deformation at ε =1000%, at -15°C, the equatorial maxima of the 110 and 200 reflections exhibit a further increase in intensity. Besides, the 110 reflection and partly also the 200 reflection show maxima also at values of the azimuthal angle χ equal to +30, -30, -150 and 150° (four arcs pattern) (Figures 34B,B'). The four arcs polarization does not occur at 25°C and is fairly visible in the diffraction patterns of the sample deformed at ε = 400% (Figures 32D,D'). The changes of the azimuthal intensity distribution of the 110 and 200 reflections occurring by cooling the stretched fibers from 25 to -15°C are partly due to the crystallization of the side chain triggered by the low temperature, partly to the fact that the lamellar crystals formed by the hard blocks achieve a higher degree of orientation at -15°C, compared to the behavior at 25°C. In particular, the X-ray fiber diffraction analysis of the OBC sample E/C16 with w_s/w_h ratio

≈ 80/20 during stretching indicates that at 25°C, a small fraction of the PE crystals tends to assume a low degree of orientation with the chain axes parallel to the stretching direction. The majority of the crystals remains unoriented, as the high compliance of the soft block rich matrix prevents an effective transmission of the tensile stress (Figures 31A,C, 32A,C,A',C' 33A and 34A,A'). At -15°C, instead, the soft matrix becomes less compliant (Figure 30), so that a higher fraction of the PE crystals formed by the hard blocks experience a more effective stress field. The decrease of global compliance of the OBC Mix 4M1P sample at -15°C is indicated in the stress-strain curve of Figure 30 by the remarkable increase of stress at any deformation compared to the stress experienced by the sample at 25°C. Hence, the sharp increase in the intensity maxima of the 110 and 200 reflections on the equator (Figures 31D, 32D,D', 33B and 34B,B') occurring at -15°C may be largely ascribed to the increased tendency of the hard block crystals to become oriented with the chain axes parallel to the stretching direction. Besides, the four arcs polarization of the 110 and 200 reflections occurring by cooling the stretched samples to -15°C may be ascribed to the tendency of the side chains to crystallize with the chain axes inclined by ±30° with respect to the stretching direction. However, the formation of some fraction of side chain crystals with the chain axes parallel to the stretching direction may not be excluded.

To check whether the structural/textural transformations occurring in the E/C16 sample with $\Delta C16 \approx 20$ mol% and w_s/w_h ratio ≈ 80/20 are reversible, a fiber specimen stretched at 1000% deformation has been heated from -15 °C to 25°C, while keeping the sample in tension. The corresponding diffraction pattern (data not shown) is similar to the diffraction pattern of the sample stretched at 25°C up to 1000% deformation (Figures 33A,A' and 34A,A'), indicating that, upon heating, the side chain crystals melt and the high degree

of orientation achieved by the crystals is partially lost, due to the increase in sample compliance (Figure 30). In the successive step, the stretched sample is cooled again to -15°C. The corresponding diffraction pattern is reported in Figure 33C whereas the corresponding radial, equatorial, and azimuthal profiles are reported in Figures 33C' and 34C,C', respectively. These patterns are similar to those of the pristine sample stretched at -15°C up to 1000% deformation of Figures 33B,B' and 34 B,B', respectively. In fact, when the stretched sample is cooled again down to -15°C, the diffraction patterns show that the 110 and 200 reflections of the orthorhombic form of PE are strongly polarized on the equator and in the four quadrants, at ±30° off the meridian (Figures 33C and 34C,C'). This demonstrates the reversibility of the structural/textural transformations occurring in the OBC sample. Upon removal of the tension at 25°C, the side chain crystals melt and the high degree of orientation achieved by the crystals is completely lost. This is indicated in Figures 33D and 34D,D' by the almost uniform intensity distribution of the PE reflections along the Debye-Scherrer rings. Simultaneously, the sample recovers almost completely the initial dimensions.

The results of the structural analysis allow to build a model describing the mechanical behavior of the ethylene-1-hexadecene sample at high deformations. The model is shown in Figure 35. At 25°C, when stress is applied, the crystals of PE involving the ethylene sequences of the backbone tend to orient themselves with the *c* axis parallel to the stretching direction. At -15°C, these main PE crystals are still oriented in the stretching direction. However, since crystallization of the lateral chains occurs, new PE crystals form in orthorhombic form as well, but this time with an inclination of around ± 30° of the *c* axis with respect to the direction of the applied deformation. The ±30° tilting of the side chain crystals according to a chevron-like texture

(Figure 35 B) may be due to the short length of the pendant alkyl groups and the confined space available in the intra-lamellar amorphous phase of about 40-60 nm (Figure 27).

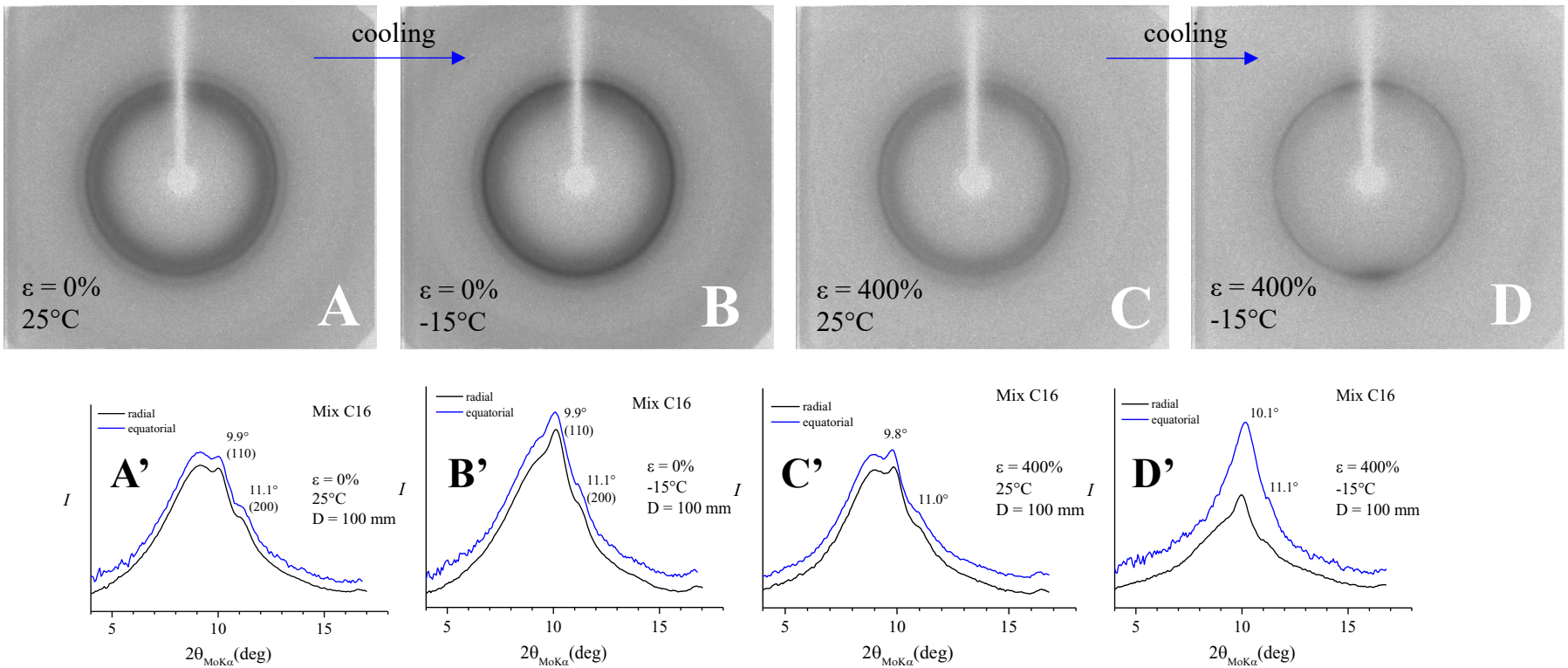

Figure 31. Bidimensional X-ray fiber diffraction patterns of the ethylene/1-hexadecene OBC sample Mix C16, recorded at the values of deformation ε = 0% (A, B) and 400% (C, D) at 25°C (A, C) and -15°C (B, D) and corresponding equatorial and radial profiles (A'-D'). The stretching direction is horizontal.

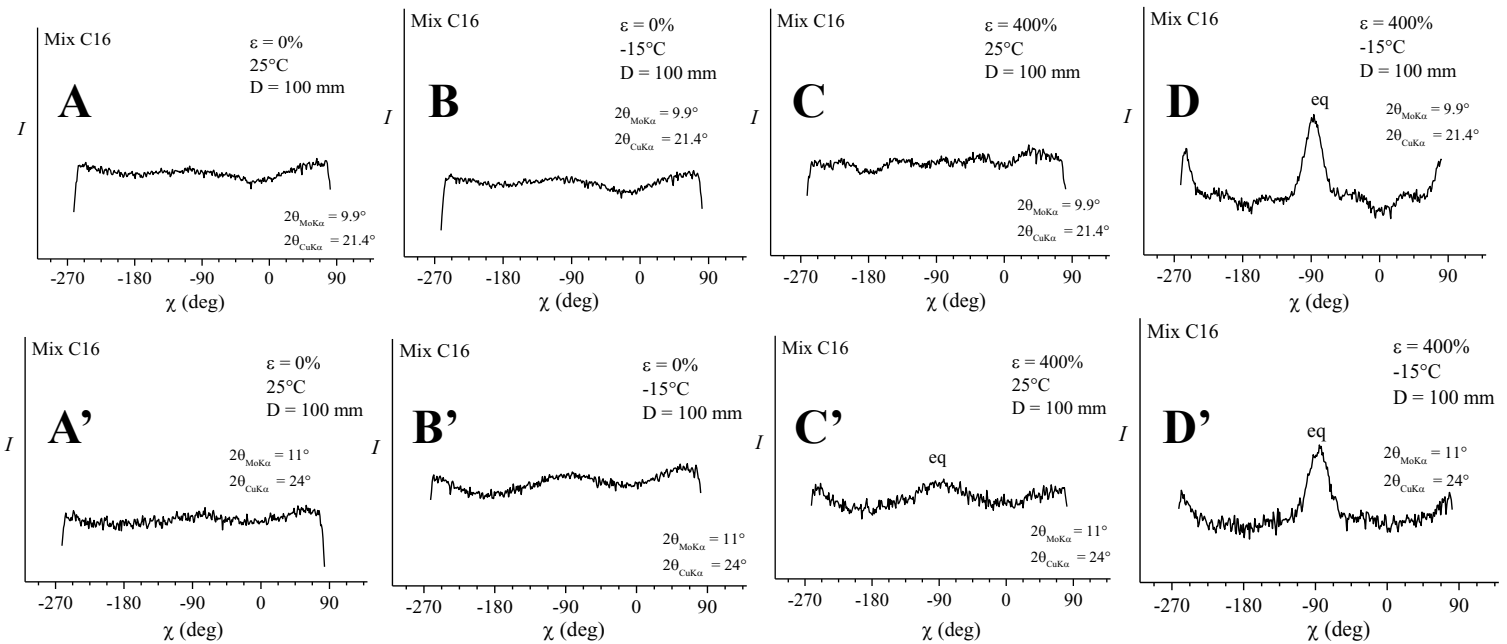

Figure 32. Azimuthal profiles of the ethylene/1-hexadecene OBC sample Mix C16 extracted from the 2D diffraction patterns of Figure 31, in correspondence of the 110 (A-D) and 200 (A'-D') reflections of the orthorhombic form of PE. The profiles are extracted from the 2D images recorded at 25°C (A, A') and -15°C (B, B') for unstretched specimens and at 25°C (C, C') and -15°C (D, D') for specimens stretched at 400% strain.

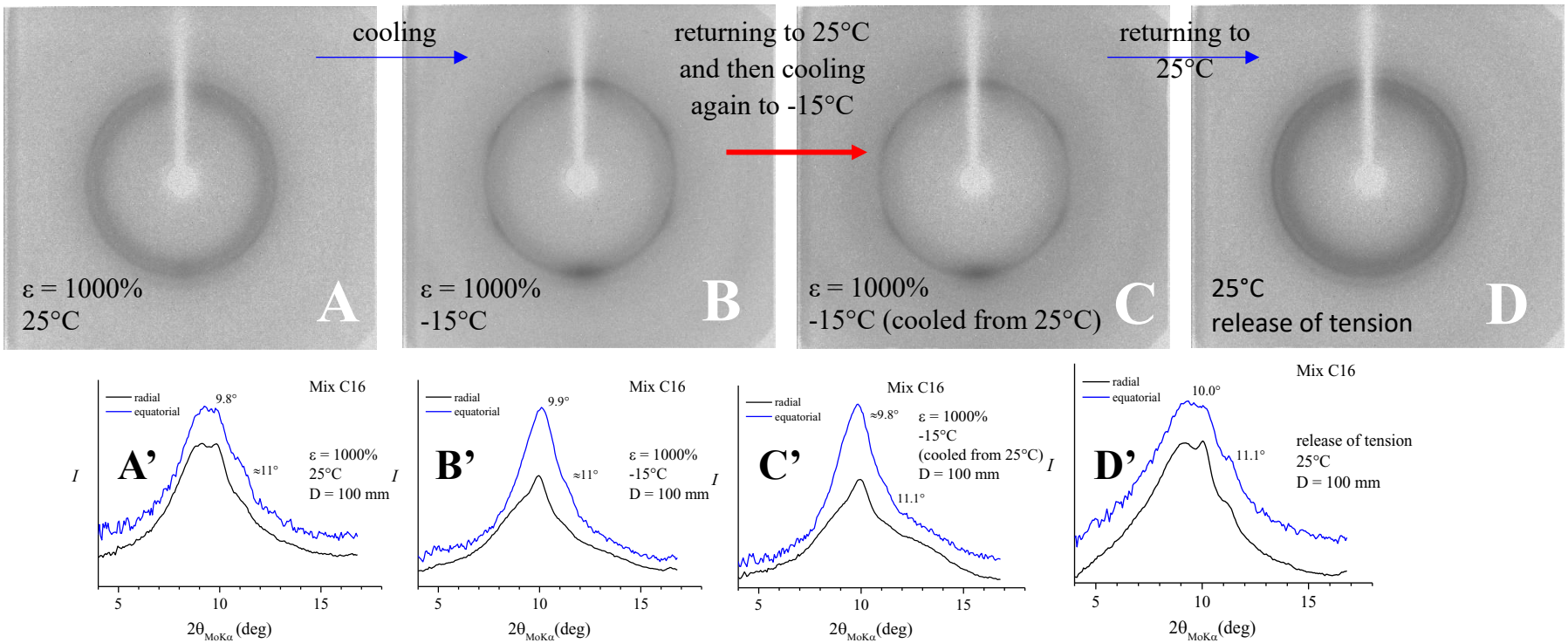

Figure 33. Bidimensional X-ray fiber diffraction patterns of the ethylene/1-hexadecene OBC sample Mix C16, recorded at the values of deformation ε = 1000% before (A, B, C) and after (D) release of the tension, at 25°C (A, D) and -15°C (B, C) and corresponding equatorial and radial profiles (A'-D'). The patterns in C, C' are relative to a sample stretched to 1000% of deformation at -15°C, then heated to 25°C, and successively cooled again to -15°C, while keeping the fiber in tension. The stretching direction is horizontal. Upon release of the tension at 25°C, the initial dimensions of the specimen are recovered.

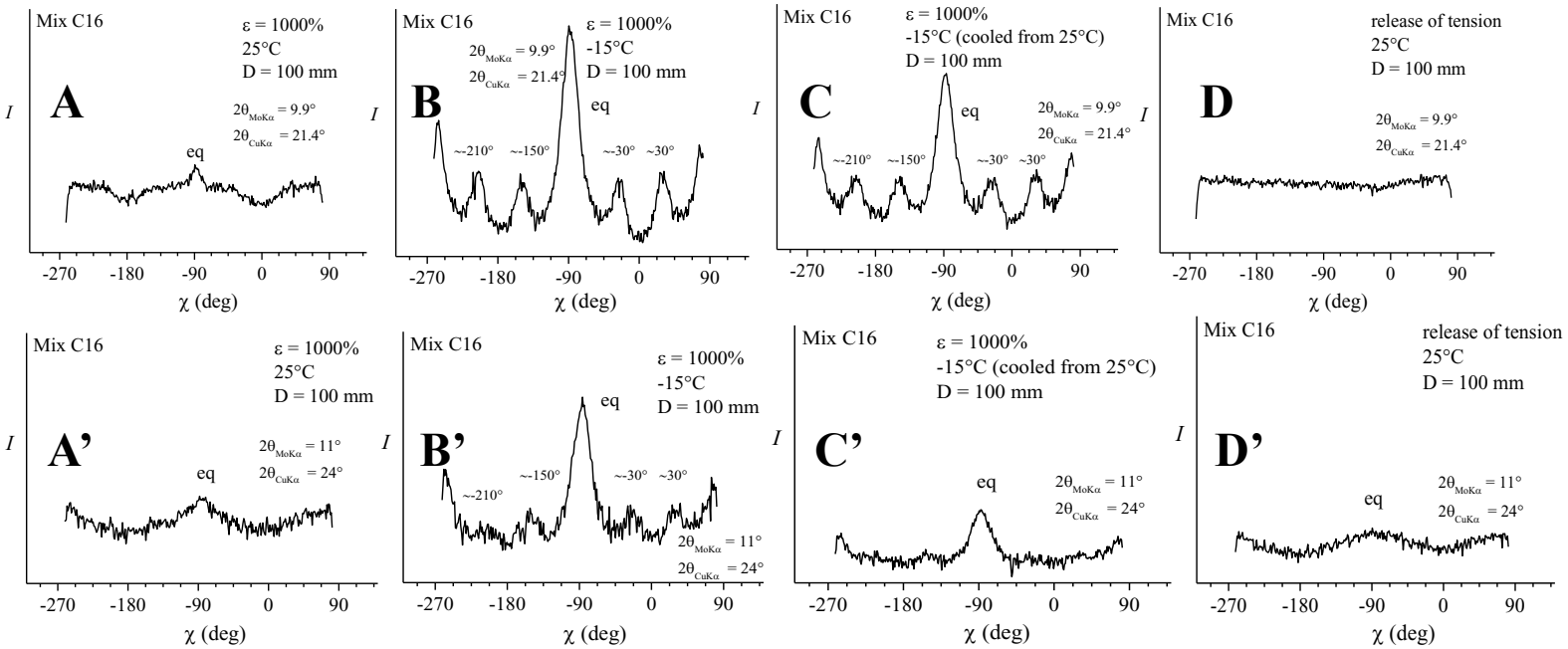

Figure 34. Azimuthal profiles of the ethylene/1-hexadecene OBC sample Mix C16 extracted from the 2D diffraction patterns of Figure 33, in correspondence of the 110 (A-D) and 200 (A'-D') reflections of the orthorhombic form of PE. The profiles are extracted from the 2D images recorded at 25°C (A, A', D, D') and -15°C (B, B', C, C') for specimens stretched at 1000% of deformation before (A, A', B, B', C, C') and after (D, D') release of tension. Upon release of the tension at 25°C, the initial dimensions of the specimen are recovered.

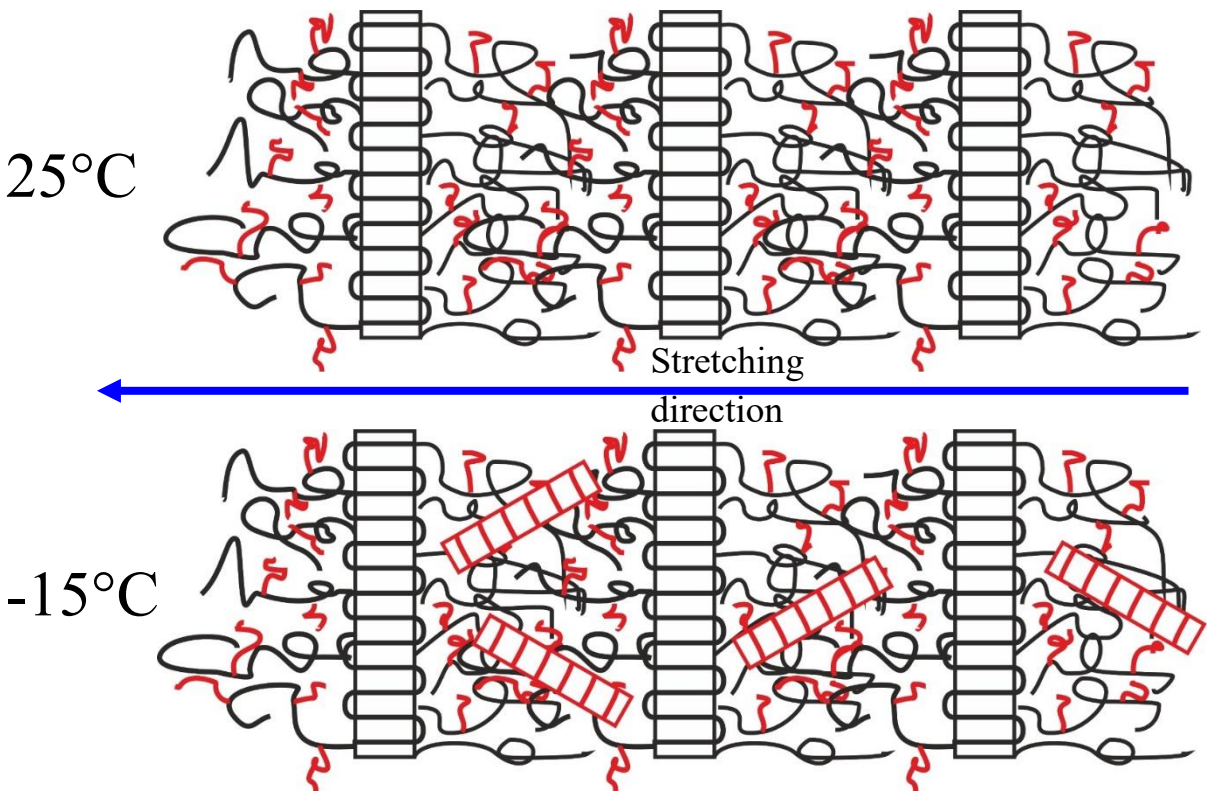

Figure 35. Simplified model for the crystallization behavior of the ethylene-1-hexadecene OBC sample stretched at high deformation at 25°C and -15°C. the model does not account for the increasing in the degree of deformation of the main chain crystals occurring at low temperature.

4.6. Conclusions

The complications introduced in blocks copolymers by polydispersity, different block composition, and competition of crystallization and phase separation have been addressed in this Chapter through high-throughput tools in both the synthetic (thanks to the collaborating group of Professor Busico) and characterization stages, since working in this regime helps to screen the large hyperspace of operating variables affecting the chain microstructure, and of course, the final properties of a polymeric material. In the early efforts of this work, it was clearly demonstrated and concluded that a Parallel Pressure Platform (PPR) working in high-throughput conditions could yield perfectly reproducible samples, within the experimental error, from the point of view of microstructural, structural, mechanical, and morphological properties, mimicking the industrially relevant properties of commercial samples.

The validation of the PPR approach allowed, then, to explore the effect of an increased segregation strength, through an increase in the parameter Δ*com*, that is the difference of comonomer content between the hard and soft blocks, with respect to the Δ*com* value of 20 mol% characterizing the Dow samples explored in the Chapter 3. It was shown that, for a high value of segregation strength, corresponding to a Δ*hex* ≈ 30 mol%, and at ever decreasing values of the w_s/w_h ratio (≈ 80/20, 70/30, 65/35, and 50/50), that is the ratio between the weight fraction of soft and hard blocks, the morphology of the samples evolves towards more confined geometries with hard blocks crystallizing in confined domains with little or no occurrence of pass-through events.

The effect of more hindered comonomers was also probed, by replacing 1-hexene or 1-octene with 4-methyl-1-pentene and 1-hexadecene. In both cases, even if the overall morphology was similar to the one obtained for the

paradigmatic Dow OBCs or for the corresponding PPR-made replicas, well-separated hard domains were observed with well-defined interfaces, together with less pronounced pass-through events. It can be also concluded that introducing a more hindered comonomer such as 1-hexadecene can trigger phase separation at lower values of χN, that is at lower Δcom values with respect to any other OBCs analyzed so far. As a matter of fact, if the morphologies of ethylene/1-hexene OBCs with $w_s/w_h \approx 50/50$ and $\Delta hex \approx 20$ and 30 mol% (Figures 10 and 18) are compared to the solid-state morphology of the ethylene/1-hexadecene with $w_s/w_h \approx 50/50$ and $\Delta C16 \approx 20$ mol% (Figure 29), it is clear that the more hindered comonomer leads to a more phase segregated system with separated crystalline domains embedded in a soft matrix even at "classical" Δcom values (20 mol%).

The introduction of 1-hexadecene as comonomer also served the purpose of exploring new fields of applications, for example as temperature-driven mechanical sensing materials, thanks to the interesting mechanical properties as a function of the temperature associated with changes in crystallinity and mechanical resistance. Indeed, the side chains are able to crystallize at subzero temperatures, inducing an increase in the degree of crystallinity and in the stiffness of the materials. It has been shown that the samples are able to recover almost completely the original size and shapes once they are heated back to room temperature. The potential of the PPR approach in the discovery of novel materials is therefore demonstrated, in the case of non-trivial complex copolymers such as OBCs, exploiting an advanced polymerization tool such as the Chain Shuttling Technology.

5. Solid state NMR

The aim of the present study is the determination of the segmental mobility of the hard and soft blocks of the ethylene-based multiblock copolymers, in the crystalline and amorphous regions, in relation to the complex chain microstructure of these systems, using solid state NMR techniques. The study is performed focusing on the Sample 1 as an example. Additional results for an ethylene/1-hexene OBC with weight fraction of the soft and hard blocks $w_s/w_h \approx 65/35$, corresponding to the merged sample 65/35 (65/35 OBC) of Chapter 4 are also reported. Molecular mass, comonomer content and hard block content of these samples are summarized in Table 1.

Table 1. Molecular parameters for commercial grade ethylene/1-octene multiblock copolymer Sample 1 and ethylene/1-hexene multiblock copolymer merged 65/35.

Sample ID	Comonomer	M_n (kDa)	M_w (kDa)	PDI	x_{com} (mol%)	$x_{com,s}$ (mol%)	w_s (wt%)
Sample 1	1-octene	60	155	2.6	13.1	19.0	72.3
merged 65/35	1-hexene	70	152	2.2	18.9	34.1	65.6

5.1. High Power Decoupling Single Pulse, INEPT, CPMAS and WISE Experiments: Resonances Assignment

The ^{13}C NMR single pulse, INEPT-MAS experiments and cross-polarization (CP) MAS spectra with high power decoupling, recorded on Sample 1 (see Chapter 3) at room temperature, are reported in Figures 1A-D. In particular, CP MAS experiments have allowed to enhance the signals of the nuclei located in predominantly rigid environment, the INEPT-MAS spectra have allowed to enhance the signals of nuclei located in predominantly mobile

environments, whereas the direct excitation ^{13}C MAS single pulse spectra have been used to obtain more quantitative information about the chemical structure of the OBCs, since the adopted T_1 relaxation time was set equal to a value longer than the longest T_1 relaxation of the ^{13}C nuclei.

The NMR signals of Figure 1 can be assigned to the Carbon nuclei belonging to the different constitutional triads EEE, EEO, EOE, OOE, OEO, OOO[83] (see Figure 2) following Ref. 121, as reported in Table 2, where the symbols E and O stand for ethylene and octene units, respectively. All spectra show resonances at the same positions, but with different intensity, depending on the pulse sequence adopted to enhance the contribution from C nuclei belonging to environments with different mobility.

In particular, the ^{13}C CP MAS spectrum of Figure 1C is dominated by the resonances of the C nuclei belonging to the rigid (crystalline) regions, as indicated by the high intensity of the resonance at 32.8 ppm, due to the backbone C atoms in the long methylene sequences in the all-trans conformation, crystallizing in the orthorhombic[121,122] form of polyethylene (PE). At ≈ 34.5 ppm another resonance is visible as a shoulder, that can be assigned to the secondary C atoms crystallizing in the monoclinic form of PE,[123] even though the 6C atoms of the hexyl groups (see Figure 2 and Table 2), also contribute (vide infra). Indeed, according to Ref. 123, for copolymers of ethylene with α-olefins bearing long branches, long backbone ethylene sequences crystallize in the orthorhombic form of PE, whereas short ethylene sequences tend to crystallize in the monoclinic form of PE. The monoclinic form of PE, indeed, can be considered as a distorted orthorhombic structure, which occurs not only for short PE stems, but also by crystallizing PE under uniaxial pressure, and/or during stretching unoriented PE samples.[124]

The peak at 30.6 ppm (Figure 1C) instead, can be attributed to secondary backbone C atoms belonging to the amorphous phase. These methylene sequences, with a high segmental mobility at room temperature, essentially belong to the soft blocks. Additional resonances of low intensity are also present in the ^{13}C CP MAS spectrum of Figure 1C, due to 1-6 C nuclei of the later groups and tertiary C atoms, located in the amorphous phase.

The INEPT-MAS NMR spectrum is reported in Figure 1B and compared with the CP MAS spectrum in Figure 1D. It is worth noting that the INEPT experiment only yields signals for nuclei belonging to mobile segments since ^{1}H coherences of rigid segments rapidly dephase under ^{1}H–^{1}H dipolar couplings during the delays of the INEPT sequence. It is apparent that the ratio between the intensity of the 38.1 ppm signal, relative to the methine groups, and the intensity of the resonance at 30.6 ppm relative to the amorphous main chain methylene groups in the INEPT-MAS NMR spectrum (Figure 1B) is higher than that observed in the single pulse spectrum (Figure 1A). Since the single pulse spectrum should be quantitative, the fact that the intensity of the resonance at 38.1 ppm is so high in Figure 1B, means that the branching points are at least as mobile as other main chain segments in non-crystalline regions of the material. This suggests that the high mobility of the side chains induces additional fluctuations to the methine groups.

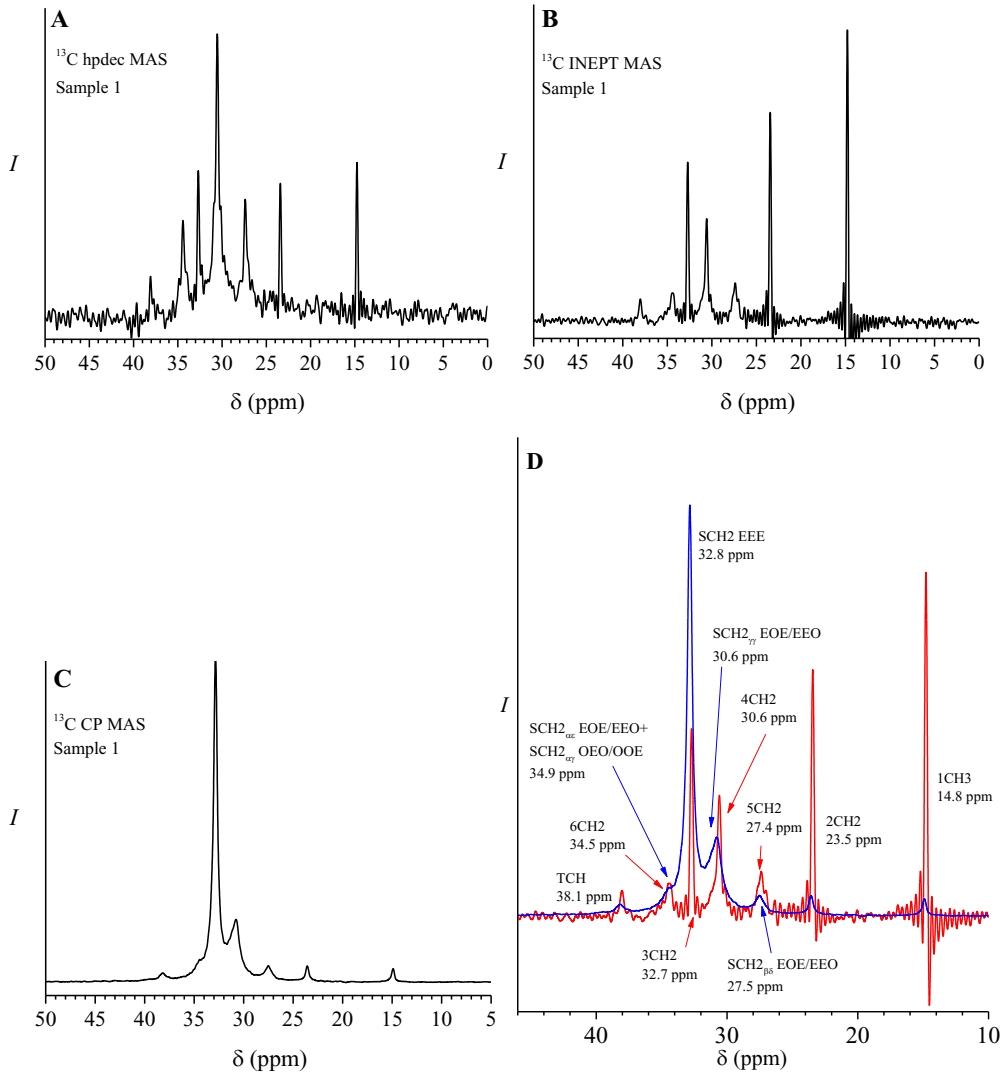

Figure 1. ^{13}C single pulse high power decoupling MAS (A), ^{13}C INEPT-MAS (B), and ^{13}C CP MAS (C) spectra of ethylene/1-octene multiblock copolymer Sample 1. In D, a comparison between the INEPT (red curve) and the CP MAS (blue curve) spectra is reported. The assignments of the NMR signals are indicated: letters T and S correspond to tertiary (methine) and secondary (methylene) Carbon atoms, respectively; the Greek subscripts indicate the distance of a carbon atom from the methine group bearing a side chain; the numbers denote the side chain carbons as counted from the methyl group. Constitutional triads are indicated by the labels EEE, EOE, EEO, OOE, OEO, OOO[83] (see Figure 2).

The comparison of the ^{13}C CP MAS and INEPT spectra (Figure 1D) allows for the complete identification of the signals due to nuclei located in a mobile environment. In particular, it is apparent that the crystalline resonances in the CP MAS spectrum at 32.8 and ≈ 34 ppm (Figure 1C) due to backbone secondary nuclei in the orthorhombic and monoclinic forms of PE are superimposed to the signals related to secondary C nuclei of the hexyl branches $3CH_2$ and $6CH_2$, respectively (Figures 1D and 2 and Table 2).

The high power decoupling single pulse MAS spectrum of the Sample 1 shown in Figure 1A presents resonance peaks in the same positions as the CP MAS and the INEPT spectra, but with different relative intensity. In particular, the peak at 30.6 ppm (Figure 1A) relative to secondary backbone C atoms belonging to the amorphous phase shows the highest relative intensity, in agreement with the low degree of crystallinity of the sample. The relative intensity of this peak is roughly 2 times higher than the intensity of the crystalline signal at 32.8 ppm, in good agreement with the value of the degree of crystallinity evaluated by WAXS analysis of about 12%. This indicates that the 3.0 s relaxation delay adopted to record the spectrum of Figure 1C allows almost full relaxation of the crystalline and amorphous nuclei.

Table 2. Assignment of peaks in Figure 1 for ethylene/1-octene multiblock copolymer Sample 1. Letters T and S correspond to secondary and tertiary carbon atoms in the methine and methylene groups, respectively; the Greek subscripts indicate the distance of a carbon atom from the methine group bearing a side chain; the numbers denote the side chain carbons as counted from the methyl group. Constitutional triads are indicated by the labels EEE, EOE, EEO, OOE, OEO, OOO.[a,83]

Peak chemical shift (ppm)	Group
38.1	TCH
34.9	SCH2 αγ EOE/EEO and SCH2 αε OEO/OOE
34.5	6CH2
32.8	SCH2 EEE
32.7	3CH2
30.7	SCH2 γγ EOE/EEO/EEE[b]
30.6	4CH2
27.5	SCH2 βδ EOE/EEO
27.4	5CH2
23.5	2CH2
14.8	1CH3

[a] NMR signals of $SCH_{2\,\alpha\alpha}$ and of $SCH_{2\,\beta\beta}$ belonging, respectively, to constitutional triads OEO, OOE, OOO at ≈ 40 ppm and OEO, OOE at ≈ 24 ppm are not visible in the spectra of Figure 1. [b] Subscript γ stands also for not spectroscopically resolved positions δ, ε, ζ and so on.

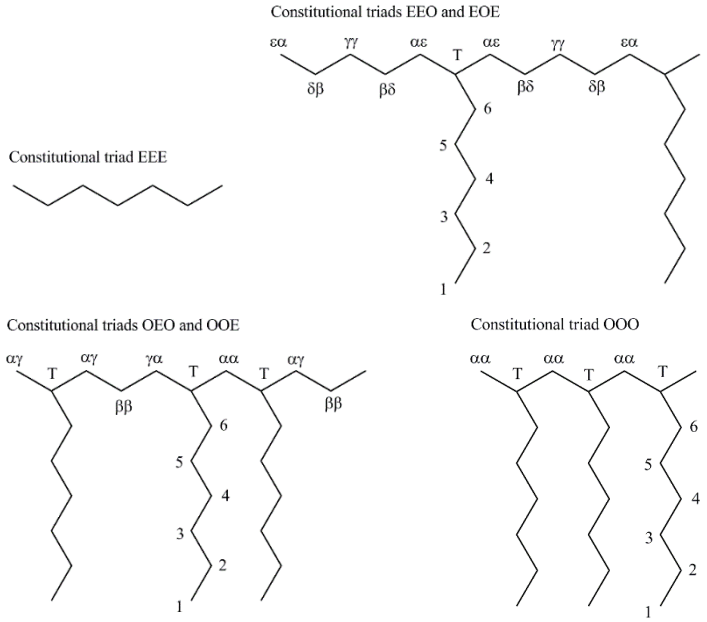

Figure 2. Constitutional EEE, EOE, EEO, OOE, OEO, and OOO triads[83] for ethylene/1-octene copolymers.

2D ^{13}C-^{1}H NMR WISE (WIdeline SEparation) experiments allow to correlate domain structure and chain segment mobility taking advantage of the structural and dynamic information that can be derived from the chemical shift in the ^{13}C dimension and the proton line width in the ^{1}H dimension. In particular, as far as the ^{1}H NMR linewidth is concerned, the higher the proton line width, the more rigid the component and vice versa. The 2D WISE spectrum (A), the ^{1}H slices resolved at ^{13}C resonances of 32.8 and 30.6 ppm (B), and the 3D projection (C) of Sample 1 are shown in Figure 3. From the proton slices, it is evident that the amorphous phase, peaked at 30.6 ppm in the ^{13}C dimension, is relatively mobile as indicated by the narrow line width ($\approx$ 1 kHz) (curve a of Figure 3B). The proton line width in correspondence of the crystalline peak at 32.8 ppm in the ^{13}C dimension, instead, spans almost the entire sampled frequencies range (Figures 2A and C) at half height, indicating

that this phase is rigid and has a reduced mobility. A narrow peak, with narrow line width (≈ 1 kHz), superimposed to the broad proton signal at ≈ 32.8 ppm in the ^{13}C dimension (curve b of Figure 3B), is also present. This peak essentially confirms the results of the analysis of the INEPT spectrum of Figure 1B, that is the strong crystalline resonance at ≈ 32.8 ppm is superimposed to the weak signal of the secondary carbon nuclei located in a highly mobile environment relative to the $3CH_2$ groups of the hexyl side chains.

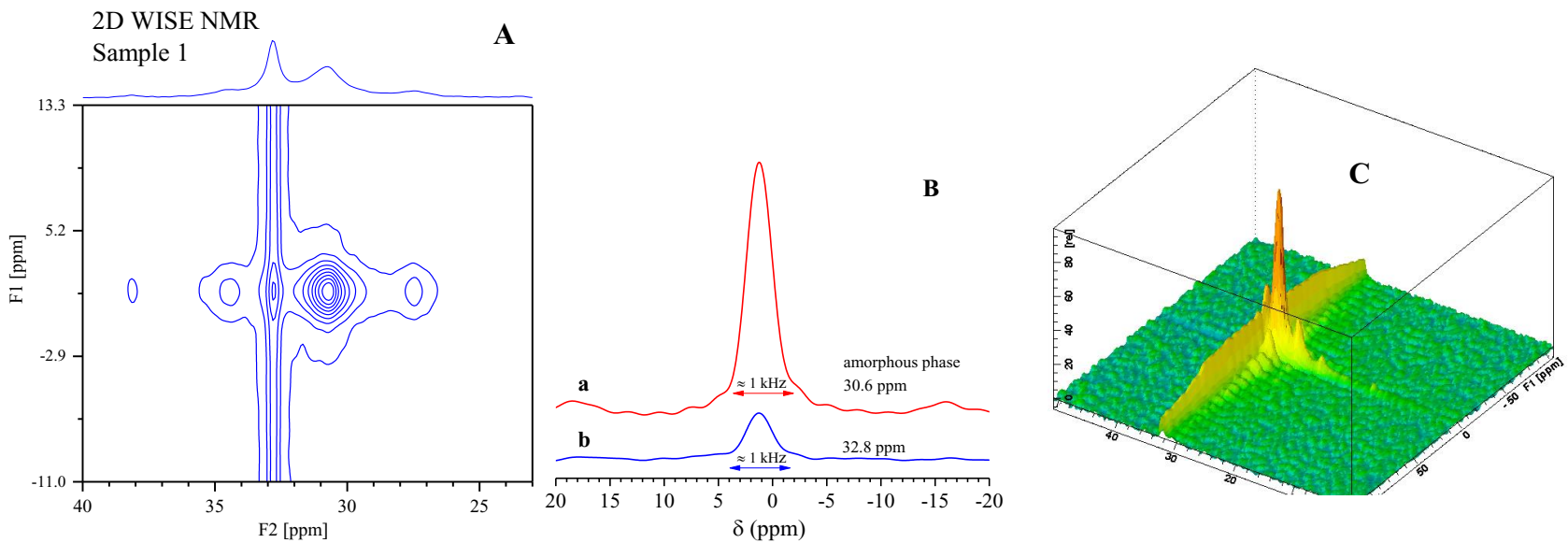

Figure 3. 2D WISE spectra for ethylene/1-octene multiblock copolymer Sample 1 (A, C): 2D contour plot (A); corresponding 3D view (C). Slice projections of 1D proton wide line spectra for the resonance at 30.6 (curve a, red) and 32.8 ppm (curve b, blue), corresponding to backbone secondary nuclei in the amorphous and crystalline regions, respectively (B).

5.2. Inversion Recovery Experiment: Determination of the Spin-lattice Relaxation Time T_1

To gain further insight into the different phases present in the analyzed ethylene/1-octene multiblock copolymer, characterized by different mobilities, relaxation experiments have been performed. In fact, the relaxation of a nuclear spin back to the equilibrium state is affected by the local magnetic field and its fluctuations experienced by the nucleus itself. The local field, in turn, is modulated by the local chemical environment and by the molecular motions of the nucleus involved. Hence, nuclei in domains with different mobilities will display a different T_1 relaxation behavior, with the amorphous regions having less restricted motions than the crystalline regions. The phenomenon of exponential relaxation of the *z*-component of the nuclear spin magnetization is described by the equation:

$$\frac{M(\tau) - M(\infty)}{M\ (0) - M(\infty)} = exp\left(-\frac{\tau}{T_1}\right) \qquad (1)$$

where $M(\tau)$ is the magnetization after a variable relaxation period τ, $M(\infty)$ is the equilibrium magnetization, $M(0)$ is the magnetization immediately following the perturbing rf pulse and T_1 is the spin-lattice relaxation time. A typical way in which the spin-lattice relaxation time T_1 can be measured is an inversion recovery experiment: first, the magnetization is inverted by a 180° pulse; then, there is a delay during which the magnetization relaxes, and a 90° pulse converts the time dependent longitudinal magnetization to transverse magnetization; finally, the FID is recorded. The disadvantage of the inversion recovery experiment is that the delay between subsequent scans needs to be significantly longer than the longest T_1 of the slowest relaxing spins in the sample. If cross-polarization from protons is possible, the initial inversion

pulse can be replaced by a cross-polarization step followed by a 90° pulse on the nucleus to be observed. Then, the required delay between scans becomes that for relaxation of the protons (Torchia experiment).[125] Following a variant of the Torchia pulse sequence (modified Torchia),[126] a relaxation experiment has been performed for the commercial Sample 1 in order to extract the T_1 longitudinal relaxation time. The modification consists in the introduction of an alternation of the phase of the contact pulse in alternate scans, which means that in a certain scan the first 90° pulse creates -*z* magnetization and in the following scan it creates +*z*. The phase cycling implies that the difference between the two scans is recorded.[126] The ^{13}C NMR spectra obtained using a modified CP inversion recovery experiment (modified Torchia)[126] are reported in Figure 4. For short relaxation delays, as apparent from the ^{13}C NMR spectra of Figure 4 (curves for 0.001 s and 0.07 s as delay times) the nuclei do not relax significantly, and so signals with maximum intensity are recorded. At longer relaxation delays (see curves in the range of delay times from 0.2 s to 0.8 s in Figure 4) the +*z* magnetization (which is larger than the equilibrium value as it is created by CP), and the -*z* magnetization both relax, and the recorded signal decays exponentially as a function of the relaxation delay. At long times both +*z* and -*z* magnetizations have relaxed back to equilibrium, and the two scans yield a zero signal, as shown by the curves of Figure 4 for delay times higher than 1 s. By integrating the area of each main peak in Figure 4 for every value of the delay list, it is possible to obtain the exponential decay of the peak intensity as a function of the delay time τ reported in Figure 5 and the values of the T_1 relaxation time reported in Table 3. The C nuclei in the crystalline regions, resonating at 32.6 ppm, have the longest relaxation time (≈ 0.6 s) in agreement with the reduced mobility of the ethylene sequences constituting the hard blocks and crystallizing in the orthorhombic form of PE

(Figure 5C). The nuclei in the amorphous mobile fractions, and in particular the C nuclei of the methine groups bearing the side branches (Figure 5A), and of the methylene units of the hexyl side chains, show T_1 relaxation times around 0.30 s (Figures 5B, E). The secondary C atoms belonging to the amorphous fraction (resonance at 30.5 ppm) (Figure 5D) show a relaxation time of ≈ 0.4 s, indicating that they are characterized by a slightly reduced mobility with respect to the side chain groups (Table 3). Finally, the C nuclei in the terminal hexyl chains, namely $1CH_3$ and $S2CH_2$ (Figure 5F and Table 3) behave very differently from the other nuclei in mobile environment, as they show longer relaxation times (>0.7 s). The possible reason for such long relaxation times may be envisaged in that the terminal groups of the lateral chains are in a fast diffusion limit or a motional averaging regime. In these conditions, indeed, as the frequency of low amplitude internal motion results of the same order of the resonance frequency of those spins, fluctuations in the magnetic field are averaged out, and the relaxation decay is delayed.

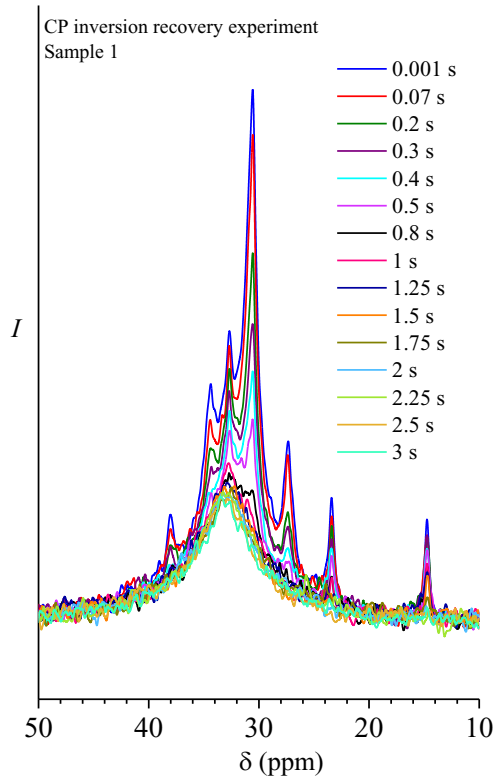

Figure 4. ^{13}C NMR spectra obtained using a modified CP inversion recovery pulse sequence (modified Torchia)[126] for the ethylene/1-octene multiblock copolymer Sample 1. The values of the delay times are indicated.

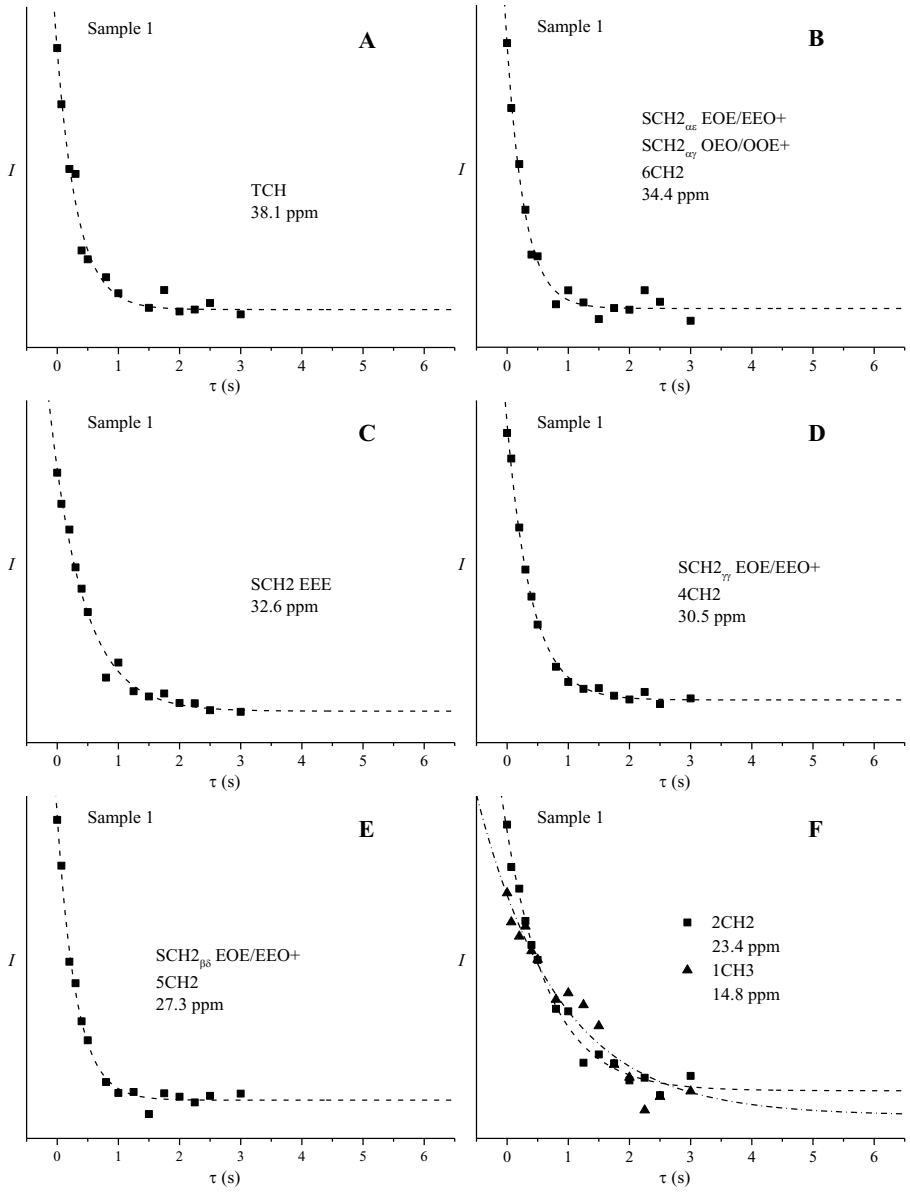

Figure 5. Peak intensities as a function of mixing time τ for each main peak of the ^{13}C NMR spectra recorded using a modified CP inversion recovery pulse sequence (modified Torchia)[126] (Figure 4) of the ethylene/1-octene multiblock copolymer Sample 1. The fit to the data (symbols) to an exponential decay function (Equation 1) is shown with a dashed line.

Table 3. Chemical shift of the peaks of Figure 4 and spin-lattice T_1 relaxation times as deduced from the exponential decay fitting of Figure 5 applied to the inversion recovery data. The nuclear species contributing to the resonances are indicated.

Peak position (ppm)	Nuclei	T_1 (s)
38.1	TCH	0.34±0.03
34.4	SCH2 αγ EOE/EEO, SCH2 αε OEO/OOE and 6CH2	0.29±0.02
32.6	SCH2 EEE	0.55±0.04
30.5	SCH2 γγ EOE/EEO and 4CH2	0.40±0.02
27.5	SCH2 βδ EOE/EEO and 5CH2	0.31±0.02
23.5	2CH2	0.71±0.06
14.8	1CH3	1.33±0.12

5.3. Spin Diffusion Experiments

In order to gain further insight on the spatial proximity between rigid crystalline and mobile amorphous regions characterizing the ethylene/α-olefins multiblock copolymers, spin diffusion experiments with dipolar filter have been collected at 298K and 318K (25°C and 45°C) for the previously analyzed Sample 1. For comparison, the study was also extended to an ethylene/1-hexene OBC with weight fraction of soft and hard blocks $w_s/w_h \approx$ 65/35 (merged sample 65/35, for details see Chapter 4). Compared with Sample 1, the concentration of comonomer in the 65/35 OBC is higher (total comonomer content, 19 vs. 13 mol%; comonomer content in the soft blocks, 34 vs. 19 mol%) (Table 1). Furthermore, despite both samples showing solid state morphologies characterized by a microphase separation between hard- and soft-block-rich domains, for Sample 1 the lamellar crystals included in the hard-block-rich domains are extended outside, crossing the soft blocks matrix to form a sort of network (pass-through morphology), whereas for sample 65/35 OBC the lamellar crystals remain better confined in the hard-block-rich

domains, due to a higher inter-block segregation strength. The molecular details of these samples are given in Table 1. In Figure 6, the ^{13}C CP MAS spectra for this two samples are compared. Even though the spectra are similar, the relative intensity of the resonances of the nuclei located in the amorphous (mobile) environment at ≈ 38, 34.5, 30.5, 27.5, 23.5, and 14.8 ppm for the sample 65/35 OBC is higher than that of the Sample 1, in agreement with the higher comonomer content.

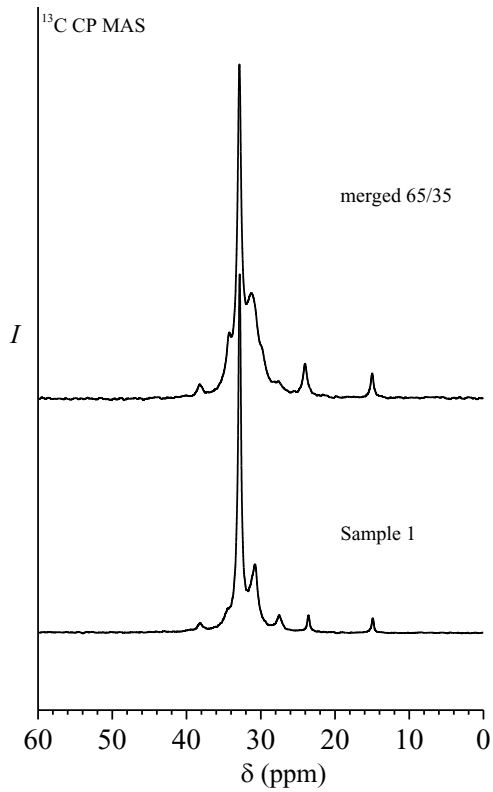

Figure 6. ^{13}C CP MAS spectra for Sample 1 and merged 65/35 OBC sample.

Information on local segmental mobility and heterogeneity of a sample can be gathered with spin diffusion experiments, in which nuclear magnetization spatially diffuses through the mediation of dipolar couplings.[127] In particular, magnetization travels spatially in the sample through successive

flip-flop events involving dipolar coupled pairs of spins. The total bulk magnetization is not changed during the process, since the ratio between the parallel and anti-parallel spin populations stays unaltered. Indeed, what is changing is the spatial distribution of the nuclear magnetization over time. A more rigid component has stronger dipolar couplings, meaning that the magnetization transfer through a flip-flop event will be more efficient. Spins in mobile regions have weaker dipolar coupling thus making magnetization transfer a less efficient process. By taking advantage of different dipolar couplings strength characterizing regions of the sample with different mobilities, one can apply a filter, which is a succession of loops of pulses, with the aim to average out all the interactions.[128] The averaging is not effective for strong dipolar couplings, so that the magnetization decays quickly. Magnetization is only retained in the more mobile parts, where the dipolar couplings are weaker and the averaging due to the filter is effective. The strength of a filter, that allows to select regions in the samples with different mobility, can be adjusted by changing the delay times between the pulses and/or by varying the number of loops. Increasing the delay times and the number of loops increases the filter strength and vice versa.

Therefore, a spin diffusion experiment coupled with a dipolar filter consists in three steps: first, the proton magnetization of the more mobile components is selected by a suitable filter to generate a nonequilibrium distribution of proton magnetization by dephasing the magnetization in the rigid parts; then ^{1}H spin diffusion, that is the spatial diffusion of nuclear magnetization through spin flip flops, occurs during a mixing time; finally, the resulting distribution of proton magnetization after the mixing time is detected in a ^{1}H spectrum or after cross-polarization in a ^{13}C spectrum.

For a proper selection of the polarization of the more mobile components, a series of dipolar filters have been tested, with varying delay times and number of loops. The results are reported in Figure 7. For Sample 1, filters with 10 and 12 μs as delay time have been tested, increasing the number of loops from 1 to 3 (Figure 7A). The filter with 12 μs and 1 loop has been considered the right compromise between suppression of the crystalline signal and retention of signals associated with the mobile components. As a matter of fact, the filter with 10 μs and 1 loop is not filtering the more rigid component at all, while the filters with 3 loops and 10 and 12 μs delay times are excessively reducing the signals of all components. Similar considerations apply to the merged 65/35 OBC, the dipolar filter with 12 μs delay time and 1 loop being again the filter giving the best results in properly selecting the signals of the mobile carbons.

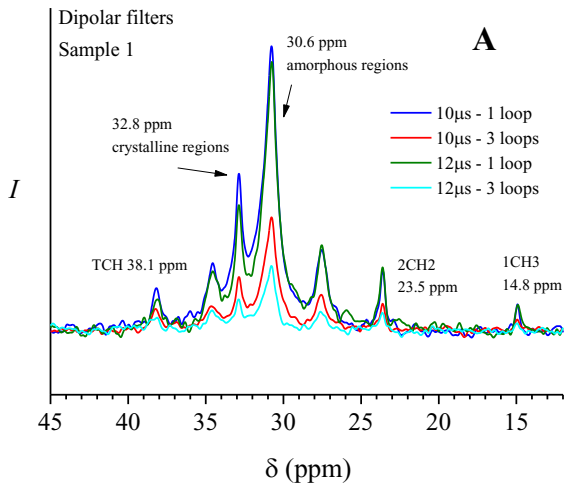

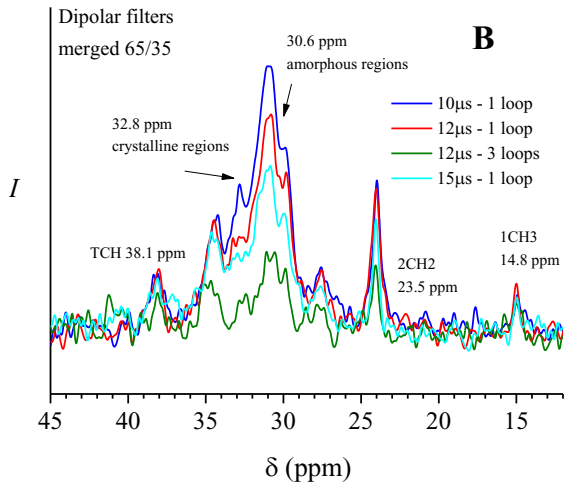

Figure 7. ^{13}C NMR MAS spectra recorded applying dipolar decoupling with the indicated values of delay time and number of loops, of the commercial grade Sample 1 (A) and the OBC merged 65/35 sample (B).

Once the dipolar filter parameters (12 μs delay time and 1 loop) are selected, spin diffusion experiments have been recorded allowing magnetization to diffuse during ever increasing delays (0.00001, 0.002, 0.005, 0.01, 0.02, and 0.05 s). The results of the spin diffusion experiments with the application of dipolar filter at 298K and 318K are reported in Figures 8 and 9 for Sample 1 and merged 65/35 OBC sample, respectively. Even though a quantitative analysis of spin diffusion cannot be currently done because ^{1}H spin diffusion did not work properly for some instrumental problems on the proton channel, useful qualitative consideration can be made to assess how polarization is transferred from more mobile components to more rigid fractions.

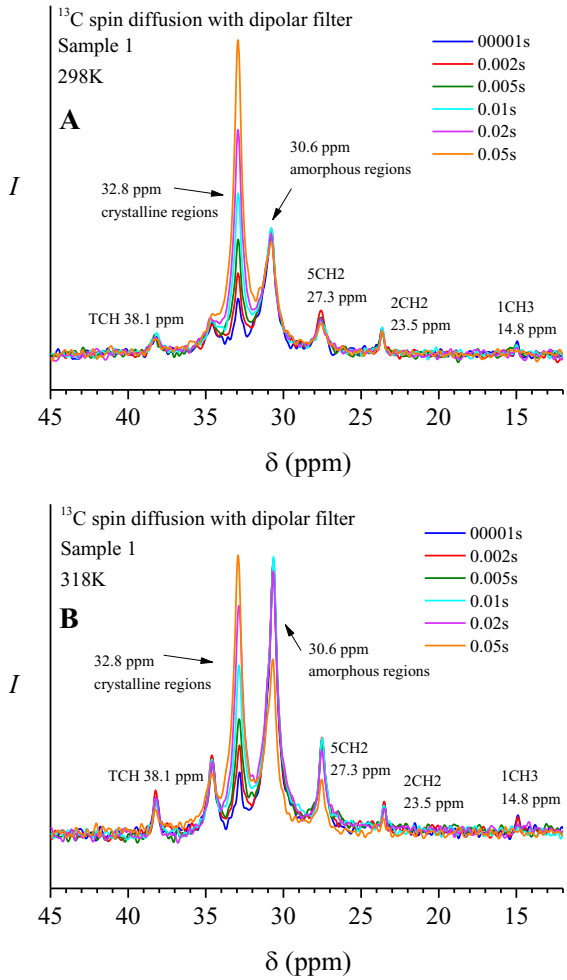

Figure 8: Series of ^{13}C NMR spectra of Sample 1 recorded at 298K (A) and 318K (B) as a function of the indicated values of the spin diffusion time, adopting a filtering scheme that minimizes (at the shortest spin diffusion time) the crystalline signal at 32.8 ppm.

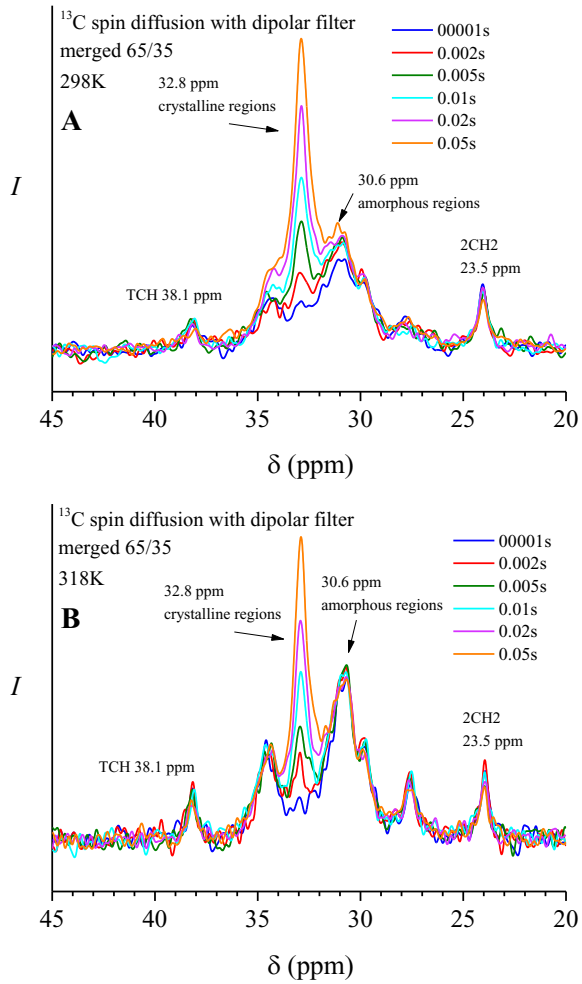

Figure 9: Series of ^{13}C NMR spectra of the OBC merged 65/35 sample recorded at 298K (A) and 318K (B) as a function of the indicated values of the spin diffusion time, adopting a filtering scheme that minimizes (at the shortest spin diffusion time) the crystalline signal at 32.8 ppm

Observation of Figures 8 and 9 allows to determine that the polarization goes directly from the backbone nuclei located in the amorphous phase to the backbone nuclei located in the crystalline phase because the only peaks involved in the polarization transfers are the peaks at 32.7 ppm and 30.6 ppm, while all the other peaks assigned to the hexyl branches stay mostly unaltered.

As a matter of fact, it is possible to observe an increase in the intensity of the crystalline peak at 32.7 ppm simultaneous to a decrease in the intensity of the amorphous phase peak at 30.6 ppm. The decrease in intensity for the signal due to the bulk amorphous chains at 30.6 ppm is not proportional to the consequent increase in intensity for the crystalline regions peak at 32.7 ppm because the polarization transfer is different for amorphous and crystalline components due to different cross polarization efficiency. Therefore, transfer of polarization is from the backbone amorphous nuclei to the backbone crystalline nuclei and, most importantly, the branches are separated and not in contact with crystalline regions. It is worth noting that a little increase in the bulk amorphous peaks at 30.6 ppm occurs during the spin diffusion at different values of spin diffusion times (Figure 8 and 9). This is due to the presence of a rigid amorphous interface between soft amorphous and crystalline regions, whose dynamics is different from dynamics of the mobile bulk amorphous. In this interface stronger dipolar couplings are present so the polarization is retained in this interfacial regions and the filter strength is reduced.

It is also apparent that there are no truly structural differences between the spectra recorded at 298K and 318K. Nonetheless, at 318K (Figures 8B and 9B), melting of the crystals with smaller lamellar thickness occurs, producing an increase in the amount of mobile components. Indeed, an increase in the intensity of the signals assigned to the amorphous fractions is visible. Furthermore, given that the increase in the amount of amorphous fraction involves both the mobile components that are directly in contact to the crystalline phase, which is the mobile components transferring the polarization, and the mobile components that are separated from the crystalline regions, the overall polarization transfer efficiency is diminished. This means that the growth in the intensity of the crystalline regions peaks is less marked

at 318K with respect to what happens at 298K. Lastly, considering the experiment at 318K for Sample 1 in Figure 8B, for the longest adopted value of delay times (0.05 s), spin diffusion time is comparable with T_1 relaxation time of mobile fractions. As a matter of fact, the signal at ≈ 30.5 ppm shows a decrease in intensity, indicating that for long spin diffusion times relaxation and spin diffusion phenomena cannot be separated and polarization, retained in the more rigid parts, can travel back to the more mobile components. It is worth noting that for delay time of 0.05 s, also the intensity of the signals related to the side chains (CH at ≈38 ppm, $6CH_2$ at ≈34.5 ppm, $5CH_2$ at ≈27.5 ppm, $2CH_2$ at ≈ 25.5 ppm, and $1CH_3$ at ≈14.8 ppm) decreases, indicating that in all mobile fractions, namely backbone amorphous segments and side chains, both spin diffusion and T_1 relaxations processes are active.

5.4. Conclusions

Solid-state NMR experiments allowed to shed light on the mobility of hard and soft blocks, in particular by identifying the groups located in the two predominant phases characterizing these systems, namely a crystalline rigid region and a mobile bulk amorphous region, through the combination of ^{13}C NMR single pulse, INEPT-MAS, CP MAS, and 2D ^{13}C-^{1}H NMR WISE techniques and relaxation experiments. In summary, the semicrystalline rigid phase is populated by both orthorhombic and monoclinic crystals due to long ethylene sequences, whereas the more mobile soft amorphous phase includes very short ethylene sequences, methine units and adjacent methylene groups, and hexyl branches. Investigating on the spatial proximity between rigid crystalline and mobile non-crystalline regions through spin diffusion experiments in association with dipolar filters of suitable strength, it was

assessed that the polarization travels form the backbone amorphous nuclei to the backbone crystalline nuclei, suggesting no involvement of the side branches and, hence, suggesting a spatial separation of the hexyl branches from the crystalline regions. In addition, it was also evidenced the presence of a rigid amorphous interface between soft amorphous and crystalline regions, whose dynamics is different from that of the mobile bulk amorphous.

Considering how the polarization is transferred from more mobile components to more rigid fractions, it is possible to support the model of complete exclusion of soft blocks from the interlamellar amorphous phase that was taken into account in Chapters 4 and 5 to explain the SAXS behavior of the commercial and home-made OBCs. According to this model, the only blocks capable of crystallizing are the hard ones; therefore, the hard blocks are responsible for the formation of the lamellar crystals and of the interlamellar amorphous phase, whereas the soft blocks are segregated in extra-lamellar domains and do not contribute to the interlamellar amorphous phase. Since the spin diffusion experiments reveal that the side branches are not in close contact with the crystalline regions, this could confirm the exclusion of the soft bulk amorphous, that contains the branches, from the lamellar stack and its segregation outside the crystalline domains. This exclusion could also be corroborated by the existence of the rigid amorphous interface in-between the bulk amorphous and the rigid crystalline domains. However, this speculations should be further validated in the future by a quantitative analysis of ^{1}H spin diffusion.

6. Conclusions

Ethylene/1-alkene multiblock copolymers synthetized through the Chain Shuttling Polymerization (CSP) process are an intriguing class of high-performance thermoplastic elastomeric materials, combining apparently conflicting properties, such as high mechanical resistance elastic behavior, high melting temperature, low glass transition temperature, and low density. They feature alternating crystallizable hard blocks (H) constituted by polyethylene (HDPE) and amorphous soft blocks (S) constituted by random ethylene/α-olefin copolymers. Furthermore, given that in the CSP growing-chain transfers occur between active metal centers, mediated by a chain shuttling agent, a reactor blend of non-uniform chains is obtained, with every chain having a statistical distribution in the molecular mass of hard and soft blocks and in the number of blocks. In spite of the features of the synthetic process, the polydispersity in molecular mass is low, being the polydispersity index Đ value equal to ≈ 2. In addition to the intrinsic polydispersity of these systems, it should also be considered that the presence of both hard crystallizable blocks and soft amorphous blocks results in a complex interplay between microphase separation and crystallization, leading to fascinating solid-state morphologies.

To properly address the complexity of the olefin-based multiblock systems, the work presented in this Ph.D. thesis has been divided into two parts with the aim to set up characterization tools and workflows. First, the microstructure and morphology of a set of five commercial ethylene/1-octene multiblock copolymers (Samples 1-5) was extensively studied through solvent and thermal fractionation techniques, melt rheology, and transmission electron

microscopy, in order to gather information on the inter- and intrachain non-uniformity and on the distributions of both block molecular mass and number.

Through solvent sequential fractionation, four fractions with increasing crystallinity, hard block content, and ethylene content were obtained, namely a fraction soluble in diethyl ether (sEE), a fraction insoluble in diethyl ether/soluble in *n*-hexane (iEE-sC6), a fraction insoluble in *n*-hexane/soluble in cyclohexane (iC6-sCC6), and a fraction insoluble in cyclohexane (iCC6). The results of aCEF, ^{13}C NMR, DSC, and X-ray diffraction analysis suggest that the sEE fractions are constituted by soft blocks or, at most, by soft blocks attached to very short hard blocks. The iEE-sC6 fractions contain an amorphous fraction along with low-crystallinity components, which means that they are constituted by soft segments linked to short hard blocks still able to crystallize. The iC6-sCC6 and the iCC6 fractions both include hard segments able to crystallize and form PE-like crystals. In particular, the high temperature peak with two maxima in the aCEF profiles of the sC6-iCC6 and iCC6 fractions suggest the existence of two population of chains. These results help to better understand the behavior of the unfractionated samples: the low-temperature elution peak at sub-zero temperature is due to the presence of the soft sEE fraction, the broad elution peak in the range 0-80°C is due to the low-crystallinity components of the iEE-sC6 fraction, whereas the high-temperature elution peaks correspond to the most crystalline components of the iC6-sCC6 and iCC6 fractions. Although these results allow to clarify the interchain distribution of the building segments, they do not justify why the iC6-sCC6 and the iCC6 fractions show a double-peaked peak at high temperatures in the aCEF profiles (around 100°C), with maxima occurring in the same position as the unfractionated samples. A non-uniform intrachain distribution of the molecular mass and number of blocks/chain has to be taken

into account suggesting that the solubility in boiling solvents, such as *n*-hexane and cyclohexane, is not only function of the length of the hard blocks, but also of the length of the attached soft blocks. Chains including a high fraction of long hard blocks linked to very long soft blocks are more soluble in *n*-hexane than chains including long hard blocks but linked to shorter soft blocks. Based on the position of the elution peak at highest temperature, an empirical method has been set up allowing to calculate a lower bound for the values of the mass of hard (M_H) and soft (M_S) blocks in a HS building unit. The calculated values are equal to 1-2 kDa and 3-4 kDa, respectively.[58]

Quantitative information on the block length has been obtained resorting to SAXS data analysis. In particular, the SAXS analysis of the sEE and iEE-sC6 fractions confirm that these fractions consist of isolated tiny lamellar crystals and/or disordered lamellar sheaves with possible inclusion of soft segments in the interlamellar regions within the stack. For the unfractionated samples and the most crystalline iC6-sCC6 and iCC6 fractions, instead, the SAXS data and the calculation of the interface distribution function (IDF) indicate molecular segregation upon crystallization, ascribable to the tendency of the hard blocks of different length to crystallize in separated domains, with little or no inclusion of the soft blocks in the interlamellar layers. At least two populations of lamellar stacks have been identified, accordingly, having similar thickness of the lamellar crystals but different average correlation distances (long spacing), and hence also different thickness of the amorphous layers. Values of the molecular mass of the hard M_H and soft M_S blocks in a HS building unit have been estimated based on an empirical approach and corresponding to 4-16 and 12-44 kDa, respectively.[78] However, it has been shown that the IDF analysis is not sufficient to fully address the intrachain complexity of these systems, because it overlooks a population of lamellar

stacks formed by hard blocks of lower molecular mass, characterized by smaller lamellar periodicity but similar lamellar thickness. The contribution to the SAXS intensity of these population is gets completely overlapped by the dominant SAXS peaks, due to the lamellar stacks with higher periodicity. Information on the third population of building blocks can be derived, in addition to the aCEF analysis, from the calculation of the mono-dimensional self-correlation function of electron density fluctuations (correlation function, CF). The molecular masses of the hard M_H and soft M_S blocks in a HS building unit calculated for this third population of lamellar stacks are in good agreement with those deduced from aCEF analysis (2-3 kDa and 6-8kDa from the CF-based analysis *vs*. 1-2 kDa and 3-4 kDa from aCEF-based analysis, respectively).

Successively, the solid-state morphology of the unfractionated commercial samples and of the corresponding fractions was investigated through transmission electron microscopy (TEM) analysis. The TEM analysis shows phase separated morphologies for the commercial grades Samples 1, 2, and 5 and for their corresponding iC6-sCC6 and iCC6 fractions, whereas more uniform morphologies for the Samples 3 and for and corresponding fractions. The phase separated morphology of the Samples 1, 2, and 5 and corresponding fractions clearly showed the tendency of the hard blocks to form tightly stacks lamellar crystals confined in roundish domains, with little or no inclusion of the soft blocks in the interlamellar amorphous regions, embedded in a matrix highly populated by the soft blocks. However, the weak segregation strength between the hard and soft block blocks leads the lamellar crystals to grow outside the roundish domains and to cross the surrounding matrix, according to the pass-through morphology. Therefore, TEM analysis allowed to confirm the existence of a non-negligible fraction of HS building units of high

molecular mass responsible for the stabilization of phase segregated morphology in the Samples 1, 2, and 5 and in their superior iC6-sCC6 and iCC6 fractions. This fraction of high molecular mass HS units is also present in the Samples 3 and 4 and in their corresponding superior fractions, although the relative amount of these building units is too low with respect to the fraction of low molecular mass HS unit. The high amount of the fractions with short HS building segments present in these samples, indeed, acts as diluent, preventing an efficient long-range segregation of the hard blocks into separated domains with well-separated boundaries, giving rise to more uniform morphologies.

To determine whether the observed mesophase separation occurred already in the melt or it was driven by the tendency of the hard blocks to crystallize in separate domains, rheological analysis was performed, since crystallization is controlled by the state of the melt. As a matter of fact, it should be expected that mesophase separation occurs already in the melt for the Samples 1, 2, and 5, and does not occur at all for the Samples 3 and 4, even though the possible occurrence of mesophase separation in the melt is in contrast with the low segregation strength of the analyzed samples. The heterogeneities arising from phase separation, order-disorder transitions, and compositional fluctuations in a melt were detected with the help of linear rheology, since the presence of heterogeneities in the melt cause a failure of the time-temperature superposition principle (TTS) at low frequencies. The TTS principle is valid over the entire frequency range, thus showing that no phase separation occurs in the melt, when the solid-state morphology is homogeneous. On the contrary, in the case of heterogeneous solid-state morphology, the viscoelastic modulus measured at different temperatures

deviate from a single master curve in the low frequency tail, clearly indicating mesophase separation already in the melt.

These results indicates that for phase segregated samples in the solid-state, the role of the chains with long blocks in stabilizing mesophase separation prevails, whereas concentration of long building units lower that a threshold coupled with a massive presence of short HS units acting as diluent attenuates the effect of concentration fluctuations, with consequent destabilization of mesophase separation, both in the melt and solid state, for more homogeneous samples.

The last step in the characterization of the commercial ethylene/1-octene grades was a thermal fractionation through a Successive Self-nucleation ad Annealing (SSA) protocols, aimed at obtaining a quantitative approximation of the real hard block length distribution. Thanks to the molecular segregation occurring during the cycles of the SSA procedure, distinct thermal fractions are obtained with well separated melting peaks. The distribution of melting peaks reflects the distribution of the thicknesses of crystals formed during the SSA, that in turn, should reflect the distribution of branching points along the hard block backbone and the distribution of the hard block length. Based on this consideration, calculation of relative and cumulative methylene sequence length distribution (MSL) was performed. It is apparent that in all cases the MSL values are lower than 150 units, suggesting that the MSL values extracted from SSA experiments correspond to the number of CH_2 units in a stem, included in unfolded lamellar crystals, and therefore they mimic with a good approximation the real values of the hard block length.

In addition, the segmental mobility of the hard and soft blocks of these ethylene-based multiblock copolymers in the crystalline and amorphous regions was determined with solid-state NMR techniques, in relation to their

complex chain microstructure. In particular, through spin diffusion experiments coupled with proper dipolar filters, it was determined that transfer of polarization is from the backbone amorphous nuclei to the backbone crystalline nuclei and that the branches are separated and not in contact with the crystalline regions. It was also revealed the presence of a rigid amorphous interface between soft amorphous and crystalline regions, whose dynamics is different from dynamics of the mobile bulk amorphous.

Regarding the second stage of this Ph.D. work, the effect of the different operating parameters in the chain shuttling copolymerization on the microstructure, on phase separation, and on the final properties was investigated, through the setting up of characterization protocols in high-throughput regime. Different series of olefin block copolymers (OBCs) were synthetized ad hoc in a parallel pressure reactor (PPR) and thoroughly characterized, assessing the role of different w_s/w_h values, that is the ratio between the weight fraction of hard and soft blocks, different comonomers (1-hexene, 1-octene, 4-methyl-1-pentene, 1-hexadecene), different values of the difference of comonomer concentration between hard and soft blocks (Δcom), different values of segregation strength (χN values), and differences in the distribution of block size.

In particular, it was first demonstrated that PPR replicas have similar microstructure and that the small difference in chain constitution, due to the fluctuations in the operating conditions during the synthesis in the different PPR miniaturized cells, do not affect significantly their physical and mechanical properties. Furthermore, the PPR approach was also validated in well reproducing the structural, thermal, mechanical, and morphological features of the commercial grades selected as benchmark, in the case of OBCs featuring $\Delta hex \approx 20$ mol% and w_s/w_h ratio of $\approx 80/20$.

At a later stage, the effect of a different w_s/w_h ratio, namely ≈ 50/50, was assessed on the solid-state morphology of the OBCs. As a matter of fact, the speckled patterns with hard-block-rich roundish domains embedded in the soft matrix, that were observed for the OBCs with w_s/w_h ≈ 80/20, were not present, indicating the low tendency of the samples with w_s/w_h ≈ 50/50 to generate well-defined phase separated morphologies upon crystallization. This behavior is at odd with theoretical predictions, being expected that polydisperse samples with symmetric (AB) base units should present a stabilization of the mesophase separation (higher T_{ODT} values). Hence, the observed morphology of the samples with w_s/w_h ≈ 50/50 was explained assuming a prevalence of the breakout crystallization mode on the mesophase separated morphology of the melt.

With the aim to increase the segregation strength and investigate its effect on the physical and morphological properties, OBCs with higher values of Δ*com*, that is the difference of comonomer content between the hard and soft blocks, and more hindered comonomers than 1-hexene or 1-octene, such as 4-methyl-1-pentene and 1-hexadecene, were synthetized and characterized. Regarding the higher values of Δ*com*, series of ethylene-1-hexene OBCs with Δ*hex* ≈ 30 mol% and decreasing values of w_s, namely samples with w_s/w_h ratio ≈ 80/20, 70/30, 65/35, and 50/50, were analyzed. In particular, it was observed that the mechanical resistance, the Young's modulus, and the strain hardening behavior of these samples increased with the increasing of the hard block content w_h and of the degree of crystallinity, whereas the values of the deformation at break ε_b decreased. Furthermore, the phase separated morphology shown in the solid-state by the samples indicated the tendency of the hard blocks to form roundish domains for the sample with w_s/w_h ≈ 80/20, worm-like entities for the samples with w_s/w_h ≈ 70/30 and ≈ 65/35, domains of

less defined shape for the sample with $w_s/w_h \approx 50/50$. In addition, in the resultant morphologies, the interface boundaries are sharp for the samples with $w_s/w_h \approx 80/20$ and 70/30 and less defined for the samples with $w_s/w_h \approx 65/35$ and 50/50. These characteristics are apparently in contrast with theoretical predictions. However, the occurrence of pass-through events decreased with the decreasing of the soft block content w_s, being sporadic for the sample with w_s/w_h ratio ≈ 80/20, more sporadic for the samples with $w_s/w_h \approx 70/30$ and 65/35, and almost null for the sample with $w_s/w_h \approx 50/50$. All in all, it appears that the increase in the difference of comonomer content between the hard and soft blocks Δ*hex* induces a neat increase in segregation strength, and hence an increased tendency of the hard blocks to crystallize in confined domains regardless of the w_s/w_h ratio.

As far as the effect of a more hindered comonomer is concerned, ethylene/4-methyl-1-pentene (E/4M1P) and ethylene/1-hexadecene (E/C16) OBCs were synthetized, with the aim to explore the occurrence of phase separation in the solid state in samples featuring a higher segregation strength between the comonomer rich (soft) and the comonomer poor (hard) blocks. For the E/4M1P OBC with $\Delta 4M1P \approx 20$ mol% and w_s/w_h ratio ≈ 80/20, the observed solid-state morphology showed the tendency of the hard blocks to form well-separated roundish domains, densely populated by PE lamellar crystals, embedded in a soft-block-rich matrix. Although the resultant morphology was similar to the "classical" phase separated morphology of the ethylene/1-hexene and ethylene/1-octene OBCs with Δ*com* ≈ 20 mol% and w_s/w_h ratio ≈ 80/20, the less pronounced pass-through morphology exhibited by the E/4M1P sample was in agreement with the high segregation strength induced by such a hindered comonomer.

In the case of the E/C16 samples, a series of OBCs with $\Delta C16 \approx 20$ mol% and values of the w_s/w_h ratio ≈ 80/20, 65/35, and 50/50 were analyzed. The TEM analysis revealed well-defined phase separated morphologies showing boundaries at the interface between the different domains that were well pronounced for the sample with w_s/w_h ratio ≈ 80/20 and less pronounced for the sample with w_s/w_h ratio ≈ 65/35. Furthermore, the E/C16 OBC with w_s/w_h ratio ≈ 50/50 showed a much more segregated solid-state morphology in comparison with the morphology of the samples with higher w_s values, featuring hard-block-rich worm-like domains, in agreement with the fact that a symmetric base unit should give rise to a higher segregation strength.

For the E/C16 samples, the possible crystallization of the long side chains at low temperatures was also investigated. In particular, by effect of the crystallization of the side chain at subzero temperatures, additional crystallinity and increased mechanical strength at low temperatures were observed, along with an immediate recovery of the initial size upon heating to room temperature. Thanks to their temperature-driven mechanical sensing properties, this novel class of OBCs could be employed in temperature sensitive food and/or drug tags.

The results emerging from the present Ph.D. work are relevant in at least two ways:

- Qualitative and quantitative aspects concerning the chain microstructure of the OBCs synthetized through chain shuttling polymerization have been elucidated.

  In particular, for the first time, multiple characterization techniques, such as aCEF, SAXS, TEM, and SSA, were combined together attempting to develop experimental and semi-empirical methods aimed at assessing the average molecular mass and number of blocks,

and the distribution of methylene sequence length (which is directly linked to the real distribution of hard block lengths). Furthermore, the application of these characterization pathways and tools on the as-polymerized samples and on fractions obtained through a solvent fractionation procedure allowed to better understand the role of each fraction and of the inter- and intrachain heterogeneity on the behavior of the pristine samples.

- The potential of the chain shuttling polymerization in producing olefin-based multiblock copolymers with tailored properties has been assessed.

  An in-depth investigation of the role of certain parameters such as the difference of comonomer incorporation between the blocks, the ratio between the fractions of hard and soft blocks, the segregation strength, and the kind of comonomer allowed to follow the evolution of the phase-separation and its competition with the concurrent crystallization in these complex systems, as shown in Figure 1. Furthermore, attention has been devoted to the study of potentially relevant industrial properties, such as the mechanical properties, demonstrating that is possible to tune the stiffness and the elastomeric properties of these materials by altering the ratio between the fraction of hard and soft blocks, introducing more hindered comonomers, or simply by changing the temperature of operation for OBCs including properly selected comonomer units such as 1-hexadecene, able to crystallize/melt below/above room temperature.

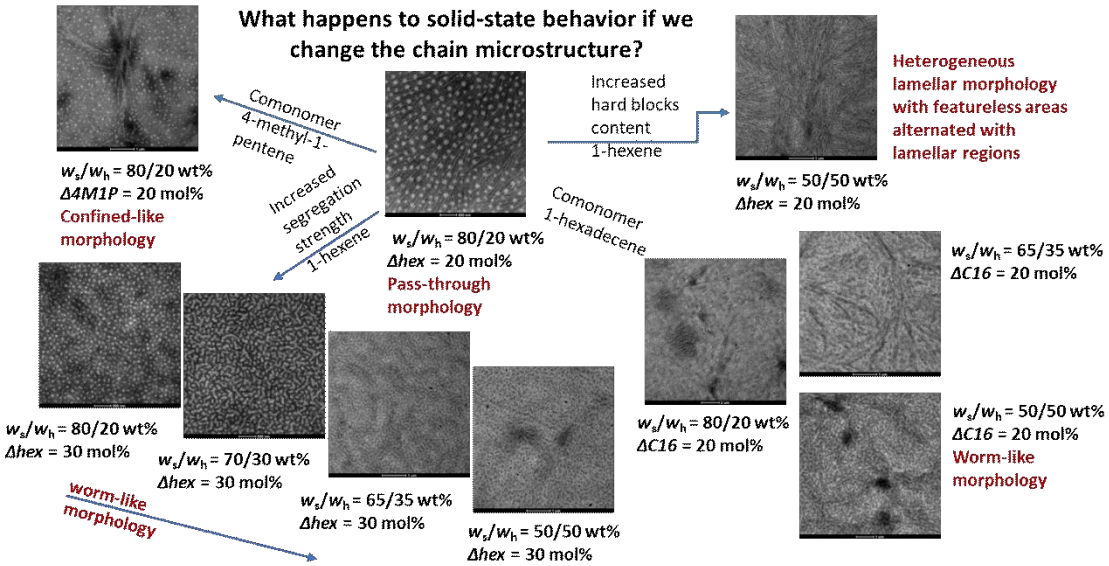

Figure 1. Schematic representation of the changes in phase-behavior of the OBCs investigated in this Ph.D. work.

> Such a wide set of variables could not have been explored without the implementation of a high-throughput workflow from synthesis to characterization, thus demonstrating that when facing complex systems, an inter-, multidisciplinary, holistic effort is needed. The chain-of-knowledge created in the Project DPI#817, which this Ph.D. thesis forms part of, has pretty well addressed the complexity and the high potential in applications of the polymeric materials that can be produced through the Chain Shuttling Technology.

Concluding, the bottleneck of chain shuttling polymerization consisting in the scarce knowledge of the compositional heterogeneity of the OBCs at inter- and intrachain level achieved so far has been tackled, taking the task of the elucidation of the structure-properties relationship of these intriguing systems and the possibility to design and synthesize materials with unprecedented, tailored properties in a short time a step ahead.

Bibliography

(1) Bates, F. S.; Fredrickson, G. H. Block Copolymer Thermodynamics: Theory and Experiment. *Annual Review of Physical Chemistry* **1990**, *41* (1), 525–557. https://doi.org/10.1146/ANNUREV.PC.41.100190.002521.

(2) Fasolka, M. J.; Mayes, A. M. Block Copolymer Thin Films: Physics and Applications. *Annual Review of Materials Research* **2001**, *31*, 323–355. https://doi.org/10.1146/ANNUREV.MATSCI.31.1.323.

(3) Hamley, I. W. The Physics of Block Copolymers. *Oxford University Press* **1998**.

(4) Hamley, I. W. Developments in Block Copolymer Science and Technology. *John Wiley & Sons, Ltd* **2004**. https://doi.org/10.1002/0470093943.

(5) Leibler, L. Theory of Microphase Separation in Block Copolymers. *Macromolecules* **2002**, *13* (6), 1602–1617. https://doi.org/10.1021/MA60078A047.

(6) Burger, C.; Ruland, W.; Semenov, A. N. Polydispersity Effects on the Microphase-Separation Transition in Block Copolymers. *Macromolecules* **1990**, *23* (13), 3339–3346. https://doi.org/10.1021/MA00215A021.

(7) Hashimoto, T.; Yamasaki, K.; Koizumi, S.; Hasegawa, H. Ordered Structure in Blends of Block Copolymers. 1. Miscibility Criterion for Lamellar Block Copolymers. *Macromolecules* **1992**, *26* (11), 2895–2904. https://doi.org/10.1021/MA00063A039.

(8) Spontak, R. J. Self-Consistent Field Theory of Ordered Block Copolymer Blends. 1. (AB).Alpha./(AB).Beta. Blends. *Macromolecules* **1994**, *27* (22), 6363–6370. https://doi.org/10.1021/MA00100A020.

(9) Court, F.; Hashimoto, T. Morphological Studies of Binary Mixtures of Block Copolymers. 1. Cosurfactant Effects and Composition Dependence of Morphology. *Macromolecules* **2001**, *34* (8), 2536–2545. https://doi.org/10.1021/ma001314

(10) Court, F.; Hashimoto, T. Morphological Studies of Binary Mixtures of Block Copolymers. 2. Chain Organization of Long and Short Blocks in Lamellar

Microdomains and Its Effect on Domain Size and Stability. *Macromolecules* **2002**, *35* (7), 2566–2575. https://doi.org/10.1021/MA011588C.

(11) Matsushita, Y.; Noro, A.; Iinuma, M.; Suzuki, J.; Ohtani, H.; Takano, A. Effect of Composition Distribution on Microphase-Separated Structure from Diblock Copolymers. *Macromolecules* **2003**, *36* (21), 8074–8077. https://doi.org/10.1021/MA0301496.

(12) Noro, A.; Iinuma, M.; Suzuki, J.; Takano, A.; Matsushita, Y. Effect of Composition Distribution on Microphase-Separated Structure from BAB Triblock Copolymers. *Macromolecules* **2004**, *37* (10), 3804–3808. https://doi.org/10.1021/MA035784Q.

(13) Lynd, N. A.; Meuler, A. J.; Hillmyer, M. A. Polydispersity and Block Copolymer Self-Assembly. *Progress in Polymer Science* **2008**, *33* (9), 875–893. https://doi.org/10.1016/J.PROGPOLYMSCI.2008.07.003.

(14) Lynd, N. A.; Hillmyer, M. A. Influence of Polydispersity on the Self-Assembly of Diblock Copolymers. *Macromolecules* **2005**, *38* (21), 8803–8810. https://doi.org/10.1021/MA051025R.

(15) Lynd, N. A.; Hillmyer, M. A. Effects of Polydispersity on the Order−Disorder Transition in Block Copolymer Melts. *Macromolecules* **2007**, *40* (22), 8050–8055. https://doi.org/10.1021/MA070962R.

(16) Lynd, N. A.; Hamilton, B. D.; Hillmyer, M. A. The Role of Polydispersity in the Lamellar Mesophase of Model Diblock Copolymers. *Journal of Polymer Science Part B: Polymer Physics* **2007**, *45* (24), 3386–3393. https://doi.org/10.1002/POLB.21321.

(17) Li, Y.; Qian, H.-J.; Lu, Z.-Y. The Influence of One Block Polydispersity on Phase Separation of Diblock Copolymers: The Molecular Mechanism for Domain Spacing Expansion. *Polymer* **2013**, *54* (14), 3716–3722. https://doi.org/10.1016/J.POLYMER.2013.04.064.

(18) Kim, I.; Li, S. Recent Progress on Polydispersity Effects on Block Copolymer Phase Behavior. *Polymer Reviews* **2019**, *59* (3), 561–587. https://doi.org/10.1080/15583724.2019.1579227.

(19) Cooke, D. M.; Shi, A.-C. Effects of Polydispersity on Phase Behavior of Diblock Copolymers. *Macromolecules* **2006**, *39* (19), 6661–6671. https://doi.org/10.1021/MA060717S.

(20) Matsen, M. W. Effect of Large Degrees of Polydispersity on Strongly Segregated Block Copolymers. *The European Physical Journal E* **2006**, *21* (3), 199–207. https://doi.org/10.1140/EPJE/I2006-10060-X.

(21) Sides, S. W.; Fredrickson, G. H. Continuous Polydispersity in a Self-Consistent Field Theory for Diblock Copolymers. *The Journal of Chemical Physics* **2004**, *121* (10), 4974. https://doi.org/10.1063/1.1776557.

(22) Jiang, Y.; Chen, T.; Ye, F.; Liang, H.; Shi, A.-C. Effect of Polydispersity on the Formation of Vesicles from Amphiphilic Diblock Copolymers. *Macromolecules* **2005**, *38* (15), 6710–6717. https://doi.org/10.1021/MA050424J.

(23) Hustad, P. D.; Kuhlman, R. L.; Arriola, D. J.; Carnahan, E. M.; Wenzel, T. T. Continuous Production of Ethylene-Based Diblock Copolymers Using Coordinative Chain Transfer Polymerization. *Macromolecules* **2007**, *40* (20), 7061–7064. https://doi.org/10.1021/MA0717791.

(24) Hustad, P. D.; Marchand, G. R.; Garcia-Meitin, E. I.; Roberts, P. L.; Weinhold, J. D. Photonic Polyethylene from Self-Assembled Mesophases of Polydisperse Olefin Block Copolymers. *Macromolecules* **2009**, *42* (11), 3788–3794. https://doi.org/10.1021/MA9002819.

(25) Li, S.; Register, R. A.; Landes, B. G.; Hustad, P. D.; Weinhold, J. D. Crystallization in Ordered Polydisperse Polyolefin Diblock Copolymers. *Macromolecules* **2010**, *43* (10), 4761–4770. https://doi.org/10.1021/MA100609K.

(26) Li, S.; Register, R. A.; Weinhold, J. D.; Landes, B. G. Melt and Solid-State Structures of Polydisperse Polyolefin Multiblock Copolymers. *Macromolecules* **2012**, *45* (14), 5773–5781. https://doi.org/10.1021/MA300910M.

(27) Widin, J. M.; Schmitt, A. K.; Im, K.; Schmitt, A. L.; Mahanthappa, M. K. Polydispersity-Induced Stabilization of a Disordered Bicontinuous Morphology in

ABA Triblock Copolymers. *Macromolecules* **2010**, *43* (19), 7913–7915. https://doi.org/10.1021/MA101140M.

(28) Widin, J. M.; Schmitt, A. K.; Schmitt, A. L.; Im, K.; Mahanthappa, M. K. Unexpected Consequences of Block Polydispersity on the Self-Assembly of ABA Triblock Copolymers. *Journal of the American Chemical Society* **2012**, *134* (8), 3834–3844. https://doi.org/10.1021/JA210548E.

(29) Schmitt, A. L.; Mahanthappa, M. K. Polydispersity-Driven Shift in the Lamellar Mesophase Composition Window of PEO-PB-PEO Triblock Copolymers. *Soft Matter* **2012**, *8* (7), 2294–2303. https://doi.org/10.1039/C2SM07041C.

(30) Schmitt, A. K.; Mahanthappa, M. K. Characteristics of Lamellar Mesophases in Strongly Segregated Broad Dispersity ABA Triblock Copolymers. *Macromolecules* **2014**, *47* (13), 4346–4356. https://doi.org/10.1021/MA5006233.

(31) Schmitt, A. K.; Mahanthappa, M. K. Order and Disorder in High χ/Low N, Broad Dispersity ABA Triblock Polymers. *Macromolecules* **2017**, *50* (17), 6779–6787. https://doi.org/10.1021/ACS.MACROMOL.7B01452.

(32) Matsen, M. W. Polydispersity-Induced Macrophase Separation in Diblock Copolymer Melts. *Physical Review Letters* **2007**, *99* (14), 148304. https://doi.org/10.1103/PhysRevLett.99.148304.

(33) Beardsley, T. M.; Matsen, M. W. Monte Carlo Phase Diagram for a Polydisperse Diblock Copolymer Melt. *Macromolecules* **2011**, *44* (15), 6209–6219. https://doi.org/10.1021/MA200966A.

(34) Jiao, G.-S.; Li, Y.; Qian, H.-J.; Lu, Z.-Y. Computer Simulation Study of Polydispersity Effect on the Phase Behavior of Short Diblock Copolymers. *Polymer* **2016**, *96*, 6–12. https://doi.org/10.1016/J.POLYMER.2016.04.065.

(35) Nojima, S.; Kato, K.; Yamamoto, S.; Ashida, T. Crystallization of Block Copolymers. 1. Small-Angle x-Ray Scattering Study of a Epsilon-Caprolactone-Butadiene Diblock Copolymer. *Macromolecules* **1992**, *25* (8), 2237–2242. https://doi.org/10.1021/MA00034A027.

(36) Nojima, S.; Nakano, H.; Ashida, T. Crystallization Behaviour of a Microphase-Separated Diblock Copolymer. *Polymer* **1993**, *34* (19), 4168–4170. https://doi.org/10.1016/0032-3861(93)90685-4.

(37) Nojima, S.; Nakano, H.; Takahashi, Y.; Ashida, T. Crystallization of Block Copolymers: 3. Crystallization Behaviour of an ε-Caprolactone-Butadiene Diblock Copolymer. *Polymer* **1994**, *35* (16), 3479–3486. https://doi.org/10.1016/0032-3861(94)90912-1.

(38) Rangarajan, P.; Register, R. A.; Adamson, D. H.; Fetters, L. J.; Bras, W.; Naylor, S.; Ryan, A. J. Dynamics of Structure Formation in Crystallizable Block Copolymers. *Macromolecules* **2002**, *28* (5), 1422–1428. https://doi.org/10.1021/MA00109A013.

(39) Lee, L.-B. W.; Register, R. A. Equilibrium Control of Crystal Thickness and Melting Point through Block Copolymerization. *Macromolecules* **2004**, *37* (19), 7278–7284. https://doi.org/10.1021/MA049143M.

(40) Rangarajan, P.; Register, R. A.; Fetters, L. J.; Bras, W.; Naylor, S.; Ryan, A. J. Crystallization of a Weakly Segregated Polyolefin Diblock Copolymer. *Macromolecules* **1995**, *28* (14), 4932. https://doi.org/10.1021/MA00118A022.

(41) Floudas, G.; Tsitsilianis, C. Crystallization Kinetics of Poly(Ethylene Oxide) in Poly(Ethylene Oxide)−Polystyrene−Poly(Ethylene Oxide) Triblock Copolymers. *Macromolecules* **1997**, *30* (15), 4381–4390. https://doi.org/10.1021/MA9616118.

(42) Richardson, P. H.; Richards, R. W.; Blundell, D. J.; MacDonald, W. A.; Mills, P. Differential Scanning Calorimetry and Optical Microscopy Investigations of the Isothermal Crystallization of a Poly(Ethylene Oxide)-Poly(Methyl Methacrylate) Block Copolymer. *Polymer* **1995**, *36* (16), 3059–3069. https://doi.org/10.1016/0032-3861(95)97866-E.

(43) Loo, Y.-L.; Register, R. A.; Ryan, A. J. Modes of Crystallization in Block Copolymer Microdomains: Breakout, Templated, and Confined. *Macromolecules* **2002**, *35* (6), 2365–2374. https://doi.org/10.1021/MA011824J.

(44) Valente, A.; Mortreux, A.; Visseaux, M.; Zinck, P. Coordinative Chain Transfer Polymerization. *Chemical Reviews* **2013**, *113* (5), 3836–3857. https://doi.org/10.1021/CR300289Z.

(45) Natta, G. Properties of Isotactic, Atactic, and Stereoblock Homopolymers, Random and Block Copolymers of α-Olefins. *Journal of Polymer Science* **1959**, *34* (127), 531–549. https://doi.org/10.1002/POL.1959.1203412738.

(46) Chien, J. C. W.; Iwamoto, Y.; Rausch, M. D.; Wedler, W.; Winter, H. H. Homogeneous Binary Zirconocenium Catalyst Systems for Propylene Polymerization. 1. Isotactic/Atactic Interfacial Compatibilized Polymers Having Thermoplastic Elastomeric Properties. *Macromolecules* **1997**, *30* (12), 3447–3458. https://doi.org/10.1021/MA961726B.

(47) Przybyla, C.; Fink, G. Two Different, on the Same Silica Supported Metallocene Catalysts, Activated by Various Trialkylaluminums-a Kinetic and Morphological Study as Well as an Experimental Investigation for Building Stereoblock Polymers. https://doi.org/10.1002/(SICI)1521-4044(19990201)50:2/3.

(48) Lieber, S.; Brintzinger, H.-H. Propene Polymerization with Catalyst Mixtures Containing Different Ansa-Zirconocenes: Chain Transfer to Alkylaluminum Cocatalysts and Formation of Stereoblock Polymers. *Macromolecules* **2000**, *33* (25), 9192–9199. https://doi.org/10.1021/MA000691J.

(49) Hazlitt, L. G.; Moldovan, D. G. . *US Patent* **1989**, *4, 798, 081*, 081.

(50) Hazlitt, L. G. . *Journal of Applied Polymer Science: Applied Polymer Symposium* **1990**, *45*, 25–37.

(51) Kukral, J.; Lehmus, P.; Klinga, M.; Leskelä, M.; Rieger, B. Oxygen-Containing, Asymmetric "'Dual-Side'" Zirconocenes: Investigations on a Reversible Chain Transfer to Aluminum. https://doi.org/10.1002/1099-0682(200206)2002:6.

(52) Hild, S.; Cobzaru, C.; Troll, C.; Rieger, B. Elastomeric Poly(Propylene) from "Dual-Side" Metallocenes: Reversible Chain Transfer and Its Influence on Polymer Microstructure. *Macromolecular Chemistry and Physics* **2006**, *207* (7), 665–683. https://doi.org/10.1002/MACP.200500505.

(53) Bruaseth, I.; Erling, R. Dual Site Ethene/1-Hexene Copolymerization with MAO Activated (1,2,4-Me3Cp)2ZrCl2 and (Me5Cp)2ZrCl2 Catalysts. Possible Transfer of Polymer Chains between the Sites. *Macromolecules* **2003**, *36* (9), 3026–3034. https://doi.org/10.1021/MA025832R.

(54) Bruaseth, I.; Soares, J. B. P.; Rytter, E. Crystallization Analysis Fractionation of Ethene/1-Hexene Copolymers Made with the MAO-Activated Dual-Site (1,2,4-Me3Cp)2ZrCl2 and (Me5Cp)2ZrCl2 System. *Polymer* **2004**, *45* (23), 7853–7861. https://doi.org/10.1016/J.POLYMER.2004.09.038.

(55) Alfano, F.; Boone, H. W.; Busico, V.; Cipullo, R.; Stevens, J. C. Polypropylene "Chain Shuttling" at Enantiomorphous and Enantiopure Catalytic Species: Direct and Quantitative Evidence from Polymer Microstructure. *Macromolecules* **2007**, *40* (22), 7736–7738. https://doi.org/10.1021/MA7020024.

(56) Arriola, D. J.; Carnahan, E. M.; Hustad, P. D.; Kuhlman, R. L.; Wenzel, T. T. Catalytic Production of Olefin Block Copolymers via Chain Shuttling Polymerization. *Science* **2006**, *312* (5774), 714–719. https://doi.org/10.1126/SCIENCE.1125268.

(57) Wenzel, T. T.; Arriola, D. J.; Carnahan, E. M.; Hustad, P. D.; Kuhlman, R. L. Chain Shuttling Catalysis and Olefin Block Copolymers (OBCs). *Topics in Organometallic Chemistry* **2009**, *26*, 65–104. https://doi.org/10.1007/978-3-540-87751-6_3.

(58) Vittoria, A.; Busico, V.; Cannavacciuolo, F. D.; Cipullo, R. Molecular Kinetic Study of "Chain Shuttling" Olefin Copolymerization. *ACS Catalysis* **2018**, *8* (6), 5051–5061. https://doi.org/10.1021/ACSCATAL.8B00841.

(59) Kempe, R. How to Polymerize Ethylene in a Highly Controlled Fashion? *Chemistry – A European Journal* **2007**, *13* (10), 2764–2773. https://doi.org/10.1002/CHEM.200601842.

(60) Hue, R. J.; Cibuzar, M. P.; Tonks, I. A. Analysis of Polymeryl Chain Transfer Between Group 10 Metals and Main Group Alkyls during Ethylene Polymerization. *ACS Catalysis* **2014**, *4* (11), 4223–4231. https://doi.org/10.1021/CS501447D.

(61) Kuhlman, R. L.; Klosin, J. Tuning Block Compositions of Polyethylene Multi-Block Copolymers by Catalyst Selection. *Macromolecules* **2010**, *43* (19), 7903–7904. https://doi.org/10.1021/MA101544N.

(62) Tongtummachat, T.; Anantawaraskul, S.; Soares, J. B. P. Understanding the Formation of Linear Olefin Block Copolymers with Dynamic Monte Carlo Simulation. *Macromolecular Reaction Engineering* **2016**, *10* (6), 535–550. https://doi.org/10.1002/MREN.201600002.

(63) Zhang, M.; Carnahan, E. M.; Karjala, T. W.; Jain, P. Theoretical Analysis of the Copolymer Composition Equation in Chain Shuttling Copolymerization. *Macromolecules* **2009**, *42* (21), 8013–8016. https://doi.org/10.1021/MA9018685.

(64) Shan, C. L. P.; Hazlitt, L. G. Block Index for Characterizing Olefin Block Copolymers. *Macromolecular Symposia* **2007**, *257* (1), 80–93. https://doi.org/10.1002/MASY.200751107.

(65) Wang, H. P.; Khariwala, D. U.; Cheung, W.; Chum, S. P.; Hiltner, A.; Baer, E. Characterization of Some New Olefinic Block Copolymers. *Macromolecules* **2007**, *40* (8), 2852–2862. https://doi.org/10.1021/MA061680E.

(66) Khariwala, D. U.; Taha, A.; Chum, S. P.; Hiltner, A.; Baer, E. Crystallization Kinetics of Some New Olefinic Block Copolymers. *Polymer* **2008**, *49* (5), 1365–1375. https://doi.org/10.1016/J.POLYMER.2007.12.046.

(67) Wang, H. P.; Chum, S. P.; Hiltner, A.; Baer, E. Deformation of Elastomeric Polyolefin Spherulites. *Journal of Polymer Science Part B: Polymer Physics* **2009**, *47* (13), 1313–1330. https://doi.org/10.1002/POLB.21735.

(68) Wang, H. P.; Chum, S. P.; Hiltner, A.; Baer, E. Comparing Elastomeric Behavior of Block and Random Ethylene–Octene Copolymers. *Journal of Applied Polymer Science* **2009**, *113* (5), 3236–3244. https://doi.org/10.1002/APP.30070.

(69) Tong, Z.-Z.; Zhou, B.; Huang, J.; Xu, J.-T.; Fan, Z.-Q. Regulation of Crystallization Kinetics, Morphology, and Mechanical Properties of Olefinic Blocky Copolymers. *Macromolecules* **2014**, *47* (1), 333–346. https://doi.org/10.1021/MA4023263.

(70) Jin, J.; Du, J.; Xia, Q.; Liang, Y.; Han, C. C. Effect of Mesophase Separation on the Crystallization Behavior of Olefin Block Copolymers. *Macromolecules* **2010**, *43* (24), 10554–10559. https://doi.org/10.1021/MA102075C.

(71) Liu, G.; Guan, Y.; Wen, T.; Wang, X.; Zhang, X.; Wang, D.; Li, X.; Loos, J.; Chen, H.; Walton, K.; Marchand, G. Effect of Mesophase Separation and Crystallization on the Elastomeric Behavior of Olefin Multi-Block Copolymers. *Polymer* **2011**, *52* (22), 5221–5230. https://doi.org/10.1016/J.POLYMER.2011.09.009.

(72) Wen, T.; Liu, G.; Zhou, Y.; Zhang, X.; Wang, F.; Chen, H.; Loos, J.; Wang, D. Epitaxy-Induced Crystallization of Olefin Block Copolymers. *Macromolecules* **2012**, *45* (15), 5979–5985. https://doi.org/10.1021/MA300619F.

(73) Park, H. E.; Dealy, J. M.; Marchand, G. R.; Wang, J.; Li, S.; Register, R. A. Rheology and Structure of Molten, Olefin Multiblock Copolymers. *Macromolecules* **2010**, *43* (16), 6789–6799. https://doi.org/10.1021/MA1012122.

(74) He, P.; Shen, W.; Yu, W.; Zhou, C. Mesophase Separation and Rheology of Olefin Multiblock Copolymers. *Macromolecules* **2014**, *47* (2), 807–820. https://doi.org/10.1021/MA402330A.

(75) Auriemma, F.; di Girolamo, R.; Urciuoli, G.; Caputo, M. R.; de Rosa, C.; Scoti, M.; Malafronte, A.; Cipullo, R.; Busico, V.; Grizzuti, N.; Vanzanella, V.; Costanzo, S. Transmission Electron Microscopy Analysis of Multiblock Ethylene/1-Octene Copolymers. *Polymer* **2020**, *193*, 122347. https://doi.org/10.1016/J.POLYMER.2020.122347.

(76) Bates, F. S. Block Copolymers near the Microphase Separation Transition. 2. Linear Dynamic Mechanical Properties. *Macromolecules* **2002**, *17* (12), 2607–2613. https://doi.org/10.1021/MA00142A025.

(77) Rosedale, J. H.; Bates, F. S.; Almdal, K.; Mortensen, K.; Wignall, G. D. Order and Disorder in Symmetric Diblock Copolymer Melts. *Macromolecules* **2002**, *28* (5), 1429–1443. https://doi.org/10.1021/MA00109A014.

(78) Auriemma, F.; de Rosa, C.; Scoti, M.; di Girolamo, R.; Malafronte, A.; Talarico, G.; Carnahan, E. Unveiling the Molecular Structure of Ethylene/1-Octene Multi-Block

Copolymers from Chain Shuttling Technology. *Polymer* **2018**, *154*, 298–304. https://doi.org/10.1016/J.POLYMER.2018.09.011.

(79) Auriemma, F.; Rosa, C. de; Scoti, M.; Girolamo, R. di; Malafronte, A.; Galotto, N. G. Structural Investigation at Nanometric Length Scale of Ethylene/1-Octene Multiblock Copolymers from Chain-Shuttling Technology. *Macromolecules* **2018**, *51* (23), 9613–9625. https://doi.org/10.1021/ACS.MACROMOL.8B01947.

(80) Auriemma, F.; Rosa, C. de; Scoti, M.; Girolamo, R. di; Malafronte, A.; D'Alterio, M. C.; Boggioni, L.; Losio, S.; Boccia, A. C.; Tritto, I. Structure and Mechanical Properties of Ethylene/1-Octene Multiblock Copolymers from Chain Shuttling Technology. *Macromolecules* **2019**, *52* (7), 2669–2680. https://doi.org/10.1021/ACS.MACROMOL.8B02470.

(81) Busico, V.; Cipullo, R.; Mingione, A.; Rongo, L. Accelerating the Research Approach to Ziegler–Natta Catalysts. *Industrial and Engineering Chemistry Research* **2016**, *55* (10), 2686–2695. https://doi.org/10.1021/ACS.IECR.6B00092.

(82) Randall, J. C. A Review of High Resolution Liquid 13Carbon Nuclear Magnetic Resonance Characterizations of Ethylene-Based Polymers. *Journal of Macromolecular Science, Part C* **1989**, *29* (2–3), 201–317. https://doi.org/10.1080/07366578908055172.

(83) Liu, W.; Rinaldi, P. L.; McIntosh, L. H.; Quirk, R. P. Poly(Ethylene-Co-1-Octene) Characterization by High-Temperature Multidimensional NMR at 750 MHz. *Macromolecules* **2001**, *34* (14), 4757–4767. https://doi.org/10.1021/MA001792K.

(84) Vacatello, M. . University of Naples "Federico II" (Italy).

(85) Brandrup, J.; Immergut, E. H.; Grulke, E. A. Polymer Handbook, 4th ed. *John Wiley & Sons, Inc*. **1999**.

(86) Fillon, B.; Wittmann, J. C.; Lotz, B.; Thierry, A. Self-Nucleation and Recrystallization of Isotactic Polypropylene (α Phase) Investigated by Differential Scanning Calorimetry. *Journal of Polymer Science Part B: Polymer Physics* **1993**, *31* (10), 1383–1393. https://doi.org/10.1002/POLB.1993.090311013.

(87) Müller, A. J.; Hernández, Z. H.; Arnal, M. L.; Sánchez, J. J. Successive Self-Nucleation/Annealing (SSA): A Novel Technique to Study Molecular Segregation during Crystallization. *Polymer Bulletin* **1997**, *39* (4), 465–472. https://doi.org/10.1007/S002890050174.

(88) Crist, B. Yet Another Visit to the Melting of Polyethylene Crystals. *Journal of Polymer Science Part B: Polymer Physics* **2007**, *45* (24), 3231–3236. https://doi.org/10.1002/POLB.21326.

(89) Ballard, D. G. H.; Cheshire, P.; Longman, G. W.; Schelten, J. Small-Angle Neutron Scattering Studies of Isotropic Polypropylene. *Polymer* **1978**, *19* (4), 379–385. https://doi.org/10.1016/0032-3861(78)90241-0.

(90) Allen, G.; Tanaka, T. A Small-Angle Neutron Scattering Study on Poly(Ethylene Oxide) Crystals. *Polymer* **1978**, *19* (3), 271–276. https://doi.org/10.1016/0032-3861(78)90220-3.

(91) Stamm, M.; Fischer, E. W.; Dettenmaier, M.; Convert, P. Chain Conformation in the Crystalline State by Means of Neutron Scattering Methods. *Faraday Discussions of the Chemical Society* **1979**, *68* (0), 263–278. https://doi.org/10.1039/DC9796800263.

(92) Allegra, G.; Famulari, A. Chain Statistics in Polyethylene Crystallization. *Polymer* **2009**, *50* (8), 1819–1829. https://doi.org/10.1016/J.POLYMER.2009.01.063.

(93) Stack, G. M.; Mandelkern, L.; Voigt-Martin, I. G. Crystallization, Melting, and Morphology of Low Molecular Weight Polyethylene Fractions. *Macromolecules* **2002**, *17* (3), 321–331. https://doi.org/10.1021/MA00133A011.

(94) Voigt-Martin, I. G.; Fischer, E. W.; Mandelkern, L. Morphology of Melt-Crystallized Linear Polyethylene Fractions and Its Dependence on Molecular Weight and Crystallization Temperature. *Journal of Polymer Science: Polymer Physics Edition* **1980**, *18* (12), 2347–2367. https://doi.org/10.1002/POL.1980.180181204.

(95) Robelin-Souffache, E.; Rault, J. Origin of the Long Period and Crystallinity in Quenched Semicrystalline Polymers. 1. *Macromolecules* **2002**, *22* (9), 3581–3594. https://doi.org/10.1021/MA00199A015.

(96) Ruland, W. The Evaluation of the Small-Angle Scattering of Lamellar Two-Phase Systems by Means of Interface Distribution Functions. *Colloid and Polymer Science* **1977**, *255* (5), 417–427. https://doi.org/10.1007/BF01536457.

(97) Lee, I.; Bates, F. S. Synthesis, Structure, and Properties of Alternating and Random Poly(Styrene-b-Butadiene) Multiblock Copolymers. *Macromolecules* **2013**, *46* (11), 4529–4539. https://doi.org/10.1021/MA400479B.

(98) Lee, I.; Panthani, T. R.; Bates, F. S. Sustainable Poly(Lactide-b-Butadiene) Multiblock Copolymers with Enhanced Mechanical Properties. *Macromolecules* **2013**, *46* (18), 7387–7398. https://doi.org/10.1021/MA401508B.

(99) Fredrickson, G. H.; Milner, S. T.; Leibler, L. Multicritical Phenomena and Microphase Ordering in Random Block Copolymers Melts. *Macromolecules* **2002**, *25* (23), 6341–6354. https://doi.org/10.1021/MA00049A034.

(100) Dobrynin, A. v.; Leibler, L. Theory of Polydisperse Multiblock Copolymers. *Macromolecules* **1997**, *30* (16), 4756–4765. https://doi.org/10.1021/MA960540.

(101) Matsen, M. W.; Schick, M. Stable and Unstable Phases of a Linear Multiblock Copolymer Melt. *Macromolecules* **2002**, *27* (24), 7157–7163. https://doi.org/10.1021/MA00102A025.

(102) Benoit, H.; Hadziioannou, G. Scattering Theory and Properties of Block Copolymers with Various Architectures in the Homogeneous Bulk State. *Macromolecules* **2002**, *21* (5), 1449–1464. https://doi.org/10.1021/MA00183A040.

(103) Kavassalis, T. A.; Whitmore, M. D. On the Theory of Linear Multiblock Copolymers. *Macromolecules* **1991**, *24*, 5340–5345. https://doi.org/10.1021/ma00019a020

(104) Wu, L.; Cochran, E. W.; Lodge, T. P.; Bates, F. S. Consequences of Block Number on the Order−Disorder Transition and Viscoelastic Properties of Linear (AB)n Multiblock Copolymers. *Macromolecules* **2004**, *37* (9), 3360–3368. https://doi.org/10.1021/MA035583M.

(105) Koo, C. M.; Hillmyer, M. A.; Bates, F. S. Structure and Properties of Semicrystalline−Rubbery Multiblock Copolymers. *Macromolecules* **2005**, *39* (2), 667–677. https://doi.org/10.1021/MA051098A.

(106) Pandav, G.; Ganesan, V. Fluctuation Effects on the Order-Disorder Transition in Polydisperse Copolymer Melts. *The Journal of Chemical Physics* **2013**, *139* (21), 214905. https://doi.org/10.1063/1.4833137.

(107) Beardsley, T. M.; Matsen, M. W. Effects of Polydispersity on the Order-Disorder Transition of Diblock Copolymer Melts. *The European Physical Journal E* **2008**, *27*, 323–333. https://doi.org/10.1140/epje/i2008-10383-6.

(108) Zuo, F.; Burger, C.; Chen, X.; Mao, Y.; Hsiao, B. S.; Chen, H.; Marchand, G. R.; Lai, S.-Y.; Chiu, D. An in Situ X-Ray Structural Study of Olefin Block and Random Copolymers under Uniaxial Deformation. *Macromolecules* **2010**, *43* (4), 1922–1929. https://doi.org/10.1021/MA902105V.

(109) Kossuth, M. B.; Morse, D. C.; Bates, F. S. Viscoelastic Behavior of Cubic Phases in Block Copolymer Melts. *Journal of Rheology* **1998**, *43* (1), 167. https://doi.org/10.1122/1.550981.

(110) Mirabella, F. M. Correlation of the Melting Behavior and Copolymer Composition Distribution of Ziegler–Natta-Catalyst and Single-Site-Catalyst Polyethylene Copolymers. *Journal of Polymer Science Part B: Polymer Physics* **2001**, *39* (22), 2800–2818. https://doi.org/10.1002/POLB.10040.

(111) Mandelkern, L.; Stack, G. M. Equilibrium Melting Temperature of Long-Chain Molecules. *Macromolecules* **1984**, *17* (4), 871–878. https://doi.org/10.1021/MA00134A057.

(112) Bonner, J. G.; Frye, C. J.; Capaccio, G. A Novel Calibration for the Characterization of Polyethylene Copolymers by Temperature Rising Elution Fractionation. *Polymer* **1993**, *34* (16), 3532–3534. https://doi.org/10.1016/0032-3861(93)90488-V.

(113) Ungar, G.; Keller, A. Inversion of the Temperature Dependence of Crystallization Rates Due to Onset of Chain Folding. *Polymer* **1987**, *28* (11), 1899–1907. https://doi.org/10.1016/0032-3861(87)90298-9.

(114) Stack, G. M.; Mandelkern, L. On the Crystallization of High Molecular Weight Normal Hydrocarbons. *Macromolecules* **1988**, *21* (2), 510–514. https://doi.org/10.1021/MA00180A038.

(115) Zhang, M.; Wanke, S. E. Quantitative Determination of Short-Chain Branching Content and Distribution in Commercial Polyethylenes by Thermally Fractionated Differential Scanning Calorimetry. *Polymer Engineering & Science* **2003**, *43* (12), 1878–1888. https://doi.org/10.1002/PEN.10159.

(116) Keating, M.; Lee, I. H.; Wong, C. S. Thermal Fractionation of Ethylene Polymers in Packaging Applications. *Thermochimica Acta* **1996**, *284* (1), 47–56. https://doi.org/10.1016/0040-6031(96)02891-2.

(117) Zhang, M.; Lynch, D. T.; Wanke, S. E. Effect of Molecular Structure Distribution on Melting and Crystallization Behavior of 1-Butene/Ethylene Copolymers. *Polymer* **2001**, *42* (7), 3067–3075. https://doi.org/10.1016/S0032-3861(00)00667-4.

(118) Fredrickson, G. H.; Helfand, E. Fluctuation Effects in the Theory of Microphase Separation in Block Copolymers. *The Journal of Chemical Physics* **1998**, *87* (1), 697. https://doi.org/10.1063/1.453566.

(119) Zhang, K.; Liu, P.; Wang, W.-J.; Li, B.-G.; Liu, W.; Zhu, S. Preparation of Comb-Shaped Polyolefin Elastomers Having Ethylene/1-Octene Copolymer Backbone and Long Chain Polyethylene Branches via a Tandem Metallocene Catalyst System. *Macromolecules* **2018**, *51* (21), 8790–8799. https://doi.org/10.1021/ACS.MACROMOL.8B01711.

(120) Galeski, A.; Bartczak, Z.; Kazmierczak, T.; Slouf, M. Morphology of Undeformed and Deformed Polyethylene Lamellar Crystals. *Polymer* **2010**, *51* (24), 5780–5787. https://doi.org/10.1016/J.POLYMER.2010.10.004.

(121) Litvinov, V. M.; Mathot, V. B. F. Partitioning of Main and Side-Chain Units between Different Phases: A Solid-State 13C NMR Inversion-Recovery Cross-Polarization Study on a Homogeneous, Metallocene-Based, Ethylene-1-Octene Copolymer. *Solid State Nuclear Magnetic Resonance* **2002**, *22* (2–3), 218–234. https://doi.org/10.1006/SNMR.2002.0078.

(122) Zhai, Y.; Zhang, R.; Yang, W.; Yang, M. Effects of Interphase on the Dispersion of MWCNTs in Ethylene-α-Octene Copolymers Revealed by Solid-State NMR Spectroscopy. *Polymer* **2017**, *114*, 44–53. https://doi.org/10.1016/J.POLYMER.2017.02.076.

(123) Hu, W.; Sirota, E. B. Monoclinic Crystallites in Ethylene Copolymers Detected by Solid-State NMR and X-Ray Diffraction. *Macromolecules* **2003**, *36* (14), 5144–5149. https://doi.org/10.1021/MA030132N.

(124) Young, R. J.; Bowden, P. B. Twinning and Martensitic Transformations in Oriented High-Density Polyethylene. *The Philosophical Magazine: A Journal of Theoretical Experimental and Applied Physics* **1974**, *29* (5), 1061–1073. https://doi.org/10.1080/14786437408226591.

(125) Torchia, D. A. The Measurement of Proton-Enhanced Carbon-13 T1 Values by a Method Which Suppresses Artifacts. *Journal of Magnetic Resonance* **1978**, *30* (3), 613–616. https://doi.org/10.1016/0022-2364(78)90288-3.

(126) Frye, J. S. Comparison of Inversion-Recovery Methods for Measuring Longitudinal Relaxation Rates. *Concepts in Magnetic Resonance* **1989**, *1* (1), 27–33. https://doi.org/10.1002/CMR.1820010107.

(127) Goldman, M.; Shen, L. Spin-Spin Relaxation in LaF3 Class. *Physical Review* **1966**, *144* (1), 321. https://doi.org/10.1103/PhysRev.144.321.

(128) Schmidt-Rohr, K.; Clauss, J.; Blümich, B.; Spiess, H. W. Miscibility of Polymer Blends Investigated by 1H Spin Diffusion and 13C NMR Detection. *Magnetic Resonance in Chemistry* **1990**, *28* (13), S3–S9. https://doi.org/10.1002/MRC.1260281304.

Appendix A1

Interface Distribution Function and Self-correlation Function Calculations

Calculation of the interphase distribution function of a biphasic multilayered system (IDF)

In order to extract the values of the lamellar parameters characterizing the lamellar stacks in the OBC samples, the SAXS intensity data $I(q)$ are elaborated to calculate the interface distribution function IDF, through the following equation:[A1]

$$IDF(z) = K\int_0^\infty [K_P - q^4(I(q) - I_{bk})]\exp(-\sigma^2 q^2)cos(qz)\,dq \quad (1)$$

where z is the distance along the normal to the lamellar crystals between the interphases defined at the boundaries between the amorphous and crystalline layers in the stacks, K_P is the Porod constant evaluated from the interpolation of SAXS data in the tail region (i.e. for q > 1.5-2 nm^{-1}) with the Porod law ($I(q\rightarrow\text{tail}) = I_{bk} + K_P\, q^{-4}$), I_{bk} is the contribution to the SAXS intensity by a flat background and K is an arbitrary constant setting the area underlying the IDF equal to one. Finally, the exponential term in Equation 1 represents a damping function having the role to reduce the noise of the SAXS signal ($I(q)q^4$) at high q, originating from thermal fluctuations of the electron density. In the calculation of the IDF, the value of the parameter σ is set equal to 0.8 – 0.9 nm.

In the direct space, the distribution function of the distances between the interfaces in a layered biphasic system including more than a single (non

interphering) lamellar stacks with lamellar parameters L_i, l_{ai} and l_{ci} is defined by the Equation:[A1]

$$IDF(z) = K'\Delta\rho^2 \sum_i f_i(h_{ai}(z) + h_{ci}(z) - 2h_{aci}(z) + h_{acai}(z) + h_{caci}(z) \ldots) \quad (2)$$

In Equation 2, the summation is extended over all the population of lamellar stacks, *K'* is an arbitrary constant proportional to the specific inner surface *S*/*V* of the layered structure, $\Delta\rho^2$ is the contrast defined by the square of electron density difference between amorphous and crystalline layers, f_i is the volume fraction of the i-th population of lamellar stacks, whereas the symbol $h_{xi}(z)$ indicate the distribution functions of the interfaces occurring along the normal to the lamellar crystals (z) in the stack i-th, centered at l_{ai} and l_{ci}, ($h_{ai}(z)$ and $h_{ci}(z)$, respectively), $L_i=l_{ai} + l_{ci}$ ($h_{aci}(z)$), $l_{ai} + l_{ci} + l_{ai}$ ($h_{acai}(z)$), $l_{ci} + l_{ai} + l_{ci}$ ($h_{acci}(z)$) etc. For each stack, the most important contributions are the first three terms, which show up in the shape of maxima centered at l_{ai} and l_{ci} and a minimum centered at $L_i=l_{ai} + l_{ci}$. In general, since the distribution of the interface distances is often broad, the maxima and minima of the IDF curves show a strong overlap, the overlap of maxima and minima being amplified for systems including more than a single population of lamellar stacks.

Calculation of the mono-dimensional self-correlation function of electron density fluctuations (Correlation Function, CF)

In the hypothesis that the SAXS intensity of the unfractionated samples and the iCC6 and iC6-sCC6 fractions probes the additive contributions from different populations of lamellar stacks, resulting from crystallization of the hard blocks characterized by different molecular mass in separated domains, (molecular fractionation during the crystallization),[A2] a further population of

lamellar stacks characterized by hard blocks with M_H lower than 10 kDa may be identified, through the calculation of the self-correlation function of electron density fluctuations.

In practice, the contribution to the SAXS desmeared data $I(q)$ in the low region (<0.55-0.60 nm^{-1}) is neglected, whereas the intensity in the q region higher than 0.55 nm^{-1} is extrapolated at low q using the Debye−Bueche equation, and at high q (>1.8 nm^{-1}) using the Porod law.[A3-A5]

Focusing only on the contribution to the SAXS intensity at high q, the correlation function for a lamellar morphology is calculated by:[A3]

$$\gamma(z) = \frac{\int_0^\infty cos(qz)\, I_{tot}(q) q^2 dq}{\int_0^\infty I_{tot}(q) q^2 dq} \quad (3)$$

The most important part of the correlation function $\gamma(z)$ corresponds to the "self-correlation triangle" located at the origin. For a lamellar morphology with long period L, thickness of amorphous layers and crystalline lamellae l_a and l_c (= L-l_a), respectively, and linear crystallinity $\varphi_c = l_c\, L^{-1}$ >0.5, $\gamma(z)$ has a maximum at q = 0, decreases with slope $s = [\ \varphi_c(1-\varphi_c)\ L]^{-1}$ up to become negative, with a minimum at $\gamma(z_{min}) = (1-\varphi_c)/\varphi_c$. The secondary maximum corresponds to the average periodicity L of the layered structure whereas the minimum layer thickness in the stacks, in our case l_a, corresponds to the length of the base cathetus of the main self-correlation triangle. We have checked that the values of linear crystallinity φ_c calculated independently as $\varphi_c = l_c\, L^{-1}$, from the slope s and from the absolute minimum of $\gamma(z)$ are identical within the experimental error.

(A1) Ruland, W. The Evaluation of the Small-Angle Scattering of Lamellar Two-Phase Systems by Means of Interface Distribution Functions. *Colloid and Polymer Science* **1977**, *255* (5), 417–427. https://doi.org/10.1007/BF01536457.

(A2) Mehta, A.; Wunderlich, B. A Study of Molecular Fractionation during the Crystallization of Polymers. *Colloid and Polymer Science* **1975**, *253* (3), 193–205. https://doi.org/10.1007/BF01470229.

(A3) Roe, R.-J. Methods of X-Ray and Neutron Scattering in Polymer Science. *Oxford University Press: New York* **2000**.

(A4) Stribeck, N. X-Ray Scattering of Soft Matter. *Springer-Verlag: Berlin Heidelberg* **2007**.

(A5) Debye, P.; Bueche, A. M. Scattering by an Inhomogeneous Solid. *Journal of Applied Physics* **2004**, *20* (6), 525. https://doi.org/10.1063/1.1698419.

Appendix A2

X-ray powder diffraction profiles and Differential Scanning Calorimeter (DSC) curves for the commercial grades

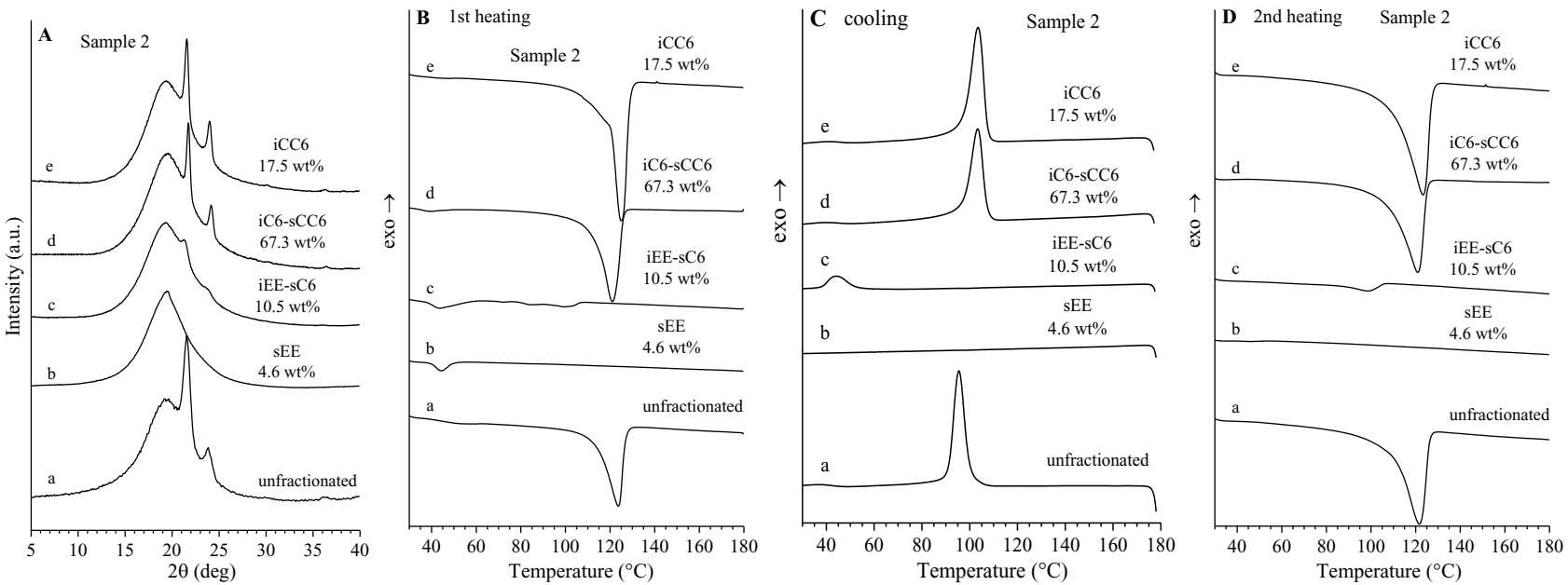

Figure A2-1. X-ray powder diffraction profiles (A) and DSC curves recorded during 1st heating (B), cooling (C), and 2nd heating (D) of the unfractionated Sample 2 (a) and of the corresponding sEE (b), iEE-sC6 (c), iC6-sCC6 (d), and iCC6 (e) fractions.

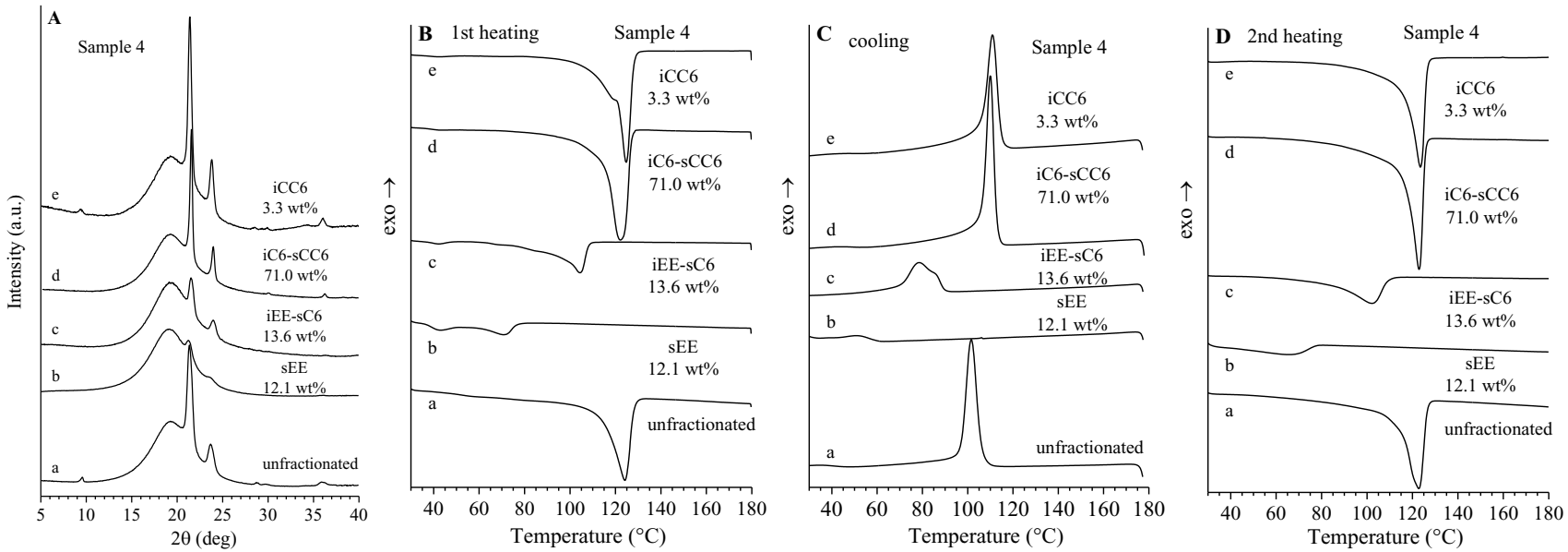

Figure A2-2. X-ray powder diffraction profiles (A) and DSC curves recorded during 1st heating (B), cooling (C), and 2nd heating (D) of the unfractionated Sample 4 (a) and of the corresponding sEE (b), iEE-sC6 (c), iC6-sCC6 (d), and iCC6 (e) fractions.

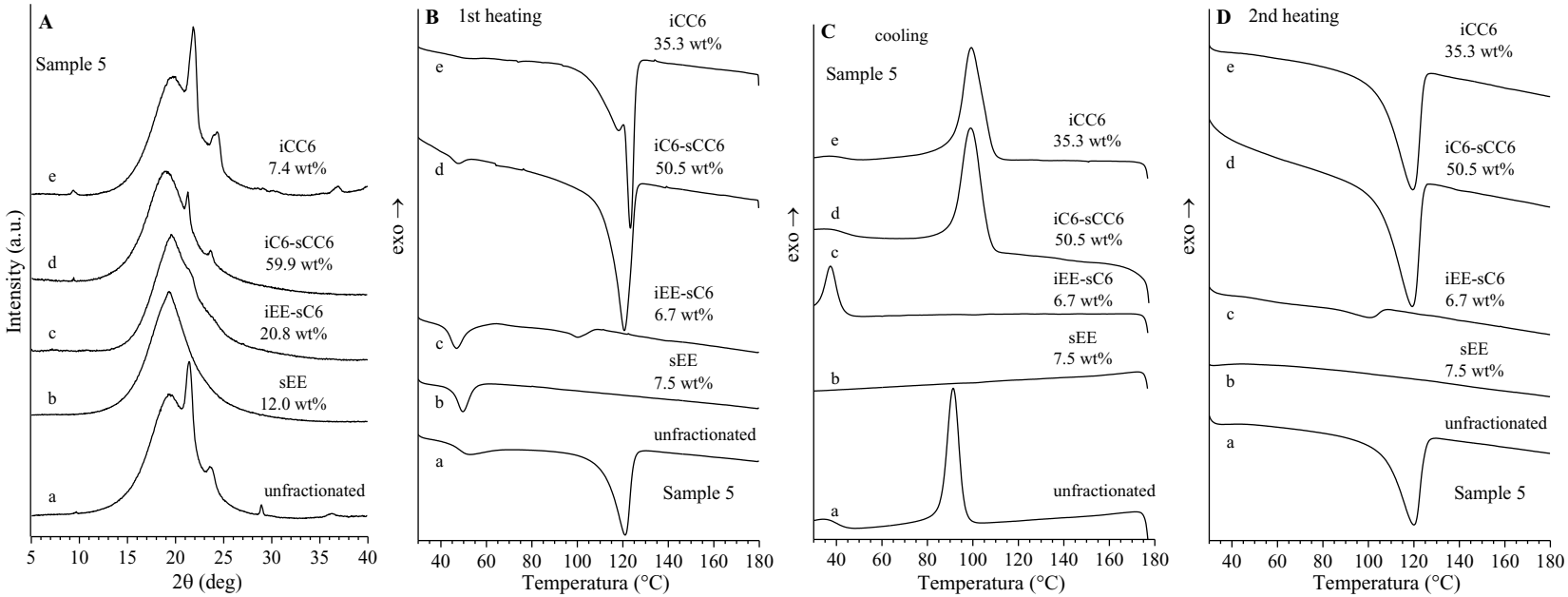

Figure A2-3. X-ray powder diffraction profiles (A) and DSC curves recorded during 1st heating (B), cooling (C), and 2nd heating (D) of the unfractionated Sample 5 (a) and of the corresponding sEE (b), iEE-sC6 (c), iC6-sCC6 (d), and iCC6 (e) fractions.

Structural and thermal data extracted from X-ray powder diffraction profiles and DCS curves

Table A2-1. First (T_{mI}) and second melting temperatures (T_{mII}), crystallization temperatures (T_c) and corresponding enthalpies (ΔH_{mI}, ΔH_{mII}, and ΔH_c), average crystallinity indexes x_c(WAXS) and x_c(DSC) extracted from data of Figures A2-1, 2, and 3, and crystallinity index relative to the sole hard blocks x_c(WAXS)/w_h for the Samples 2, 4, and 5 and of the corresponding fractions.

Sample	T_{mI} (°C)	ΔH_{mI} (J/g)	T_{mII} (°C)	ΔH_{mII} (J/g)	T_c (°C)	ΔH_c (J/g)	x_c(WAXS) (%)	x_c(WAXS)/w_h (%)	x_c(DSC) (%)
2-unfractionated	123.7	32.9	121.7	40.7	95.5	40.7	12	43.6	13.9
2-sEE	44.2	2.5	/	/	/	/	/	/	/
2-iEE-sC6	43.6/98.9	4.5, 3.7	98.4	2.4	44.2	6.5	4.3	75.4	0.8
2-iC6-sCC6	121.0	44.9	120.9	39.6	103.3	36.1	13.2	51.1	13.5
2-iCC6	124.9	57.2	123.3	47.9	103.5	44.2	18	57.3	16.3
4-unfractionated	124.3	40.5	122.8	43.5	101.6	40.6	18	76.6	14.8
4-sEE	42.4, 71.1	2.2, 4.2	65.6	9.1	51.4	2.45	3	/	3.1
4-iEE-sC6	42.3, 104.4	1.1, 21.4	102.1	20.7	78.4	20.7	6.5	92.8	7.1
4-iC6-sCC6	122.2	55.7	122.8	52.5	110.1	48.6	18.1	68.8	18.0
4-iCC6	124.7	48.5	123.4	45.0	110.8	43.0	28.5	83.3	15.4
5-unfractionated	51.6, 121.0	0.84, 15.85	120.0	17.4	36.1, 91.3	0.72, 17.4	3	19.4	6.0
5-sEE	49.8	3.6	/	/	/	/	/	/	/
5-iEE-sC6	46.9, 100.3	4.4, 1.5	100.4	1.8	37.4	5.4	4.5	86.5	0.6
5-iC6-sCC6	47.1, 120.7	1.72, 29.5	119.2	26.8	38.7, 99.1	0.4, 23.1	6.9	37.2	9.1
5-iCC6	123.4	25.5	119.4	23.9	99.4	21.7	18.5	89.8	8.2

Appendix A3

Self-Nucleation and Annealing (SNA)

All the Self-Nucleation and Annealing (SNA) DSC curves for the ethylene/1-octene random copolymer chosen as reference sample and for the commercial grades Samples 1, 2, 3, 4, and 5 and their corresponding iCC6 and iC6-sCC6 fractions at the selected self-seeding temperatures T_s are reported in Figures A3 1-48. In particular, for each sample the heating curves from 25°C up to the selected T_s values, the crystallization curves obtained by cooling from T_s to 25°C, and the subsequent heating curves up to 180°C are reported. The crystallization temperatures T_c are reported in Figure A3-49 as a function of the seeding temperature T_s, along with the ideal self-seeding temperature $T_{s\ ideal}$, the corresponding crystallization temperature T_c, the standard DSC curve recorded at 10°C/min, and the melting temperature T_m.

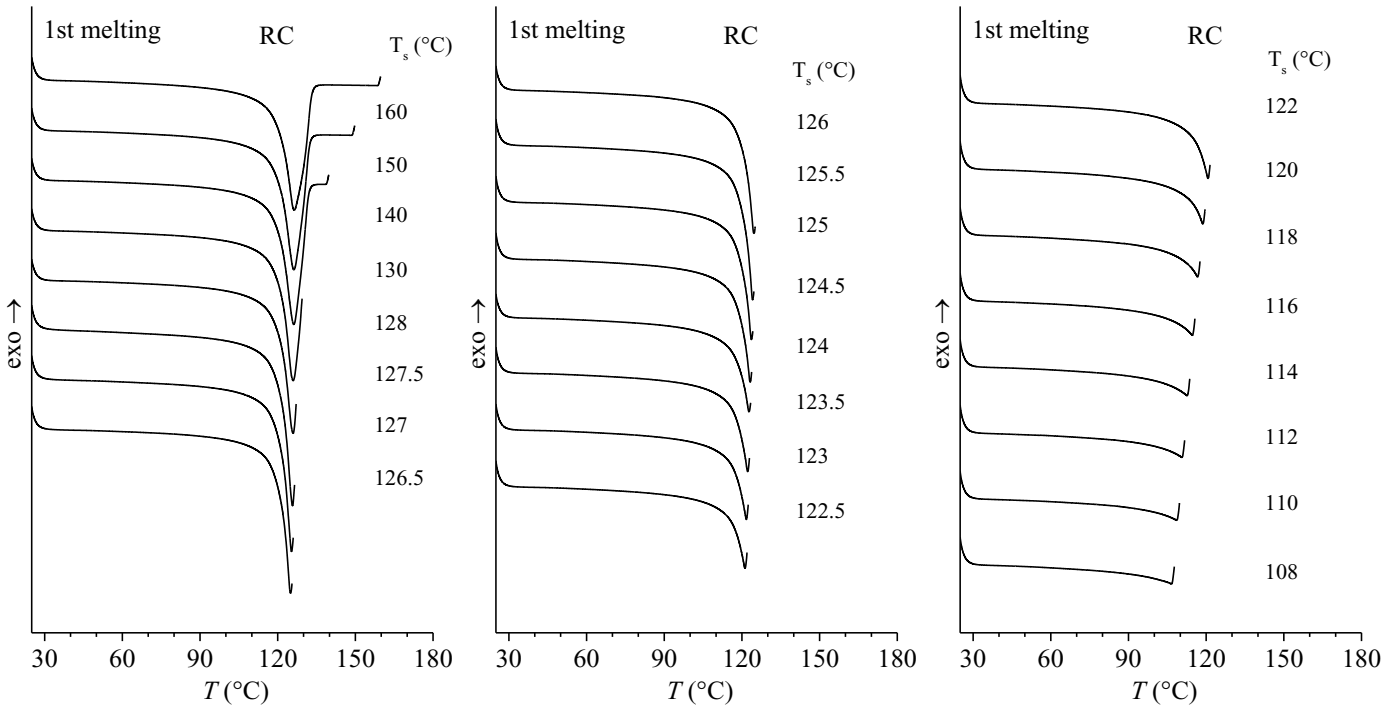

Figure A3-1. SNA DSC heating curves up to the selected T_s recorded for the ethylene/1-octene random copolymer RC taken as reference.

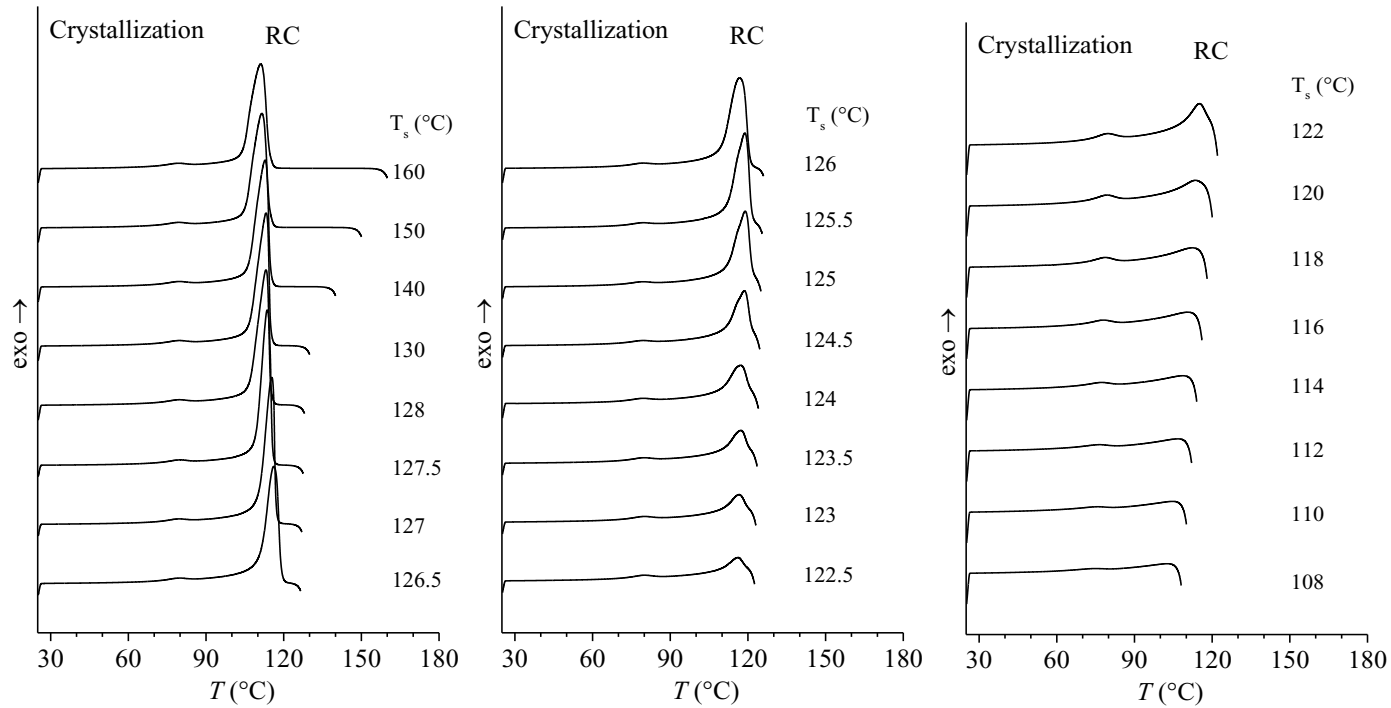

Figure A3-2. SNA DSC cooling curves from the selected T_s recorded for the ethylene/1-octene random copolymer RC taken as reference.

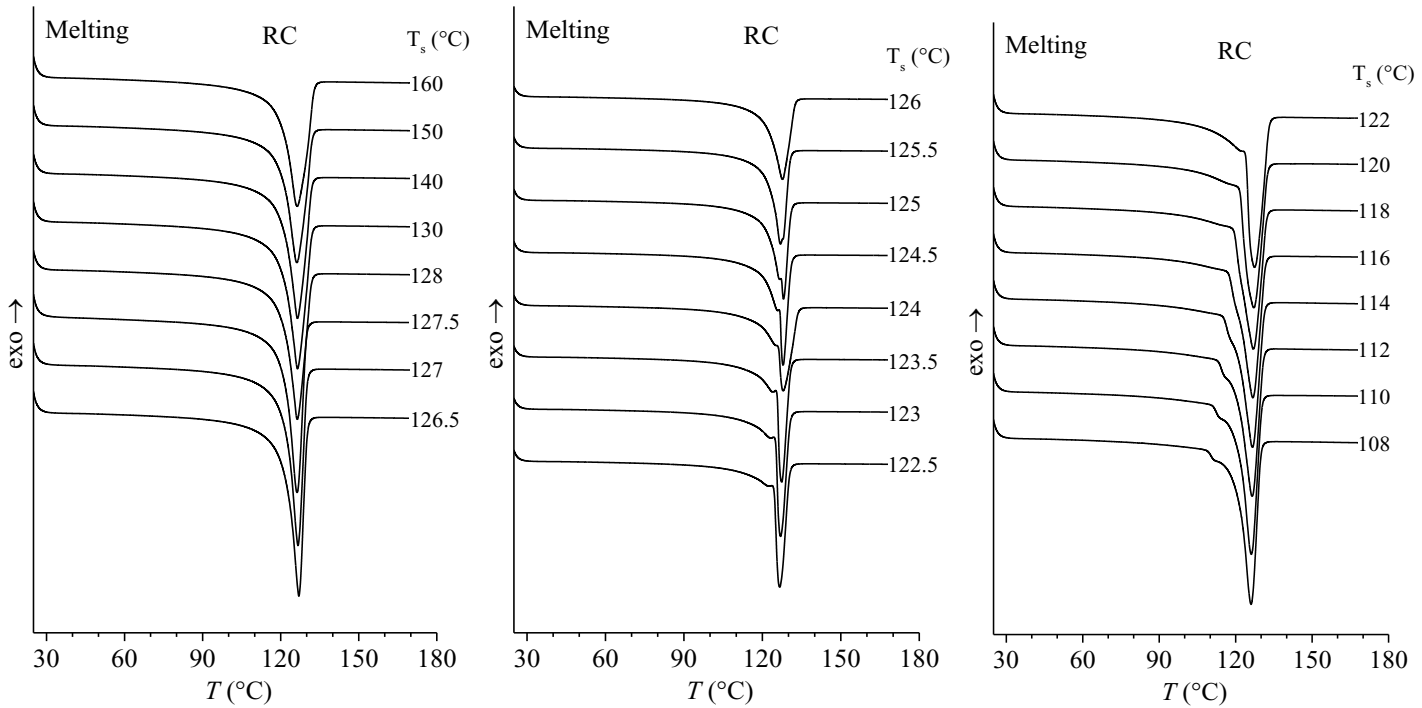

Figure A3-3. SNA DSC subsequent heating curves for the selected T_s recorded for the ethylene/1-octene random copolymer RC taken as reference.

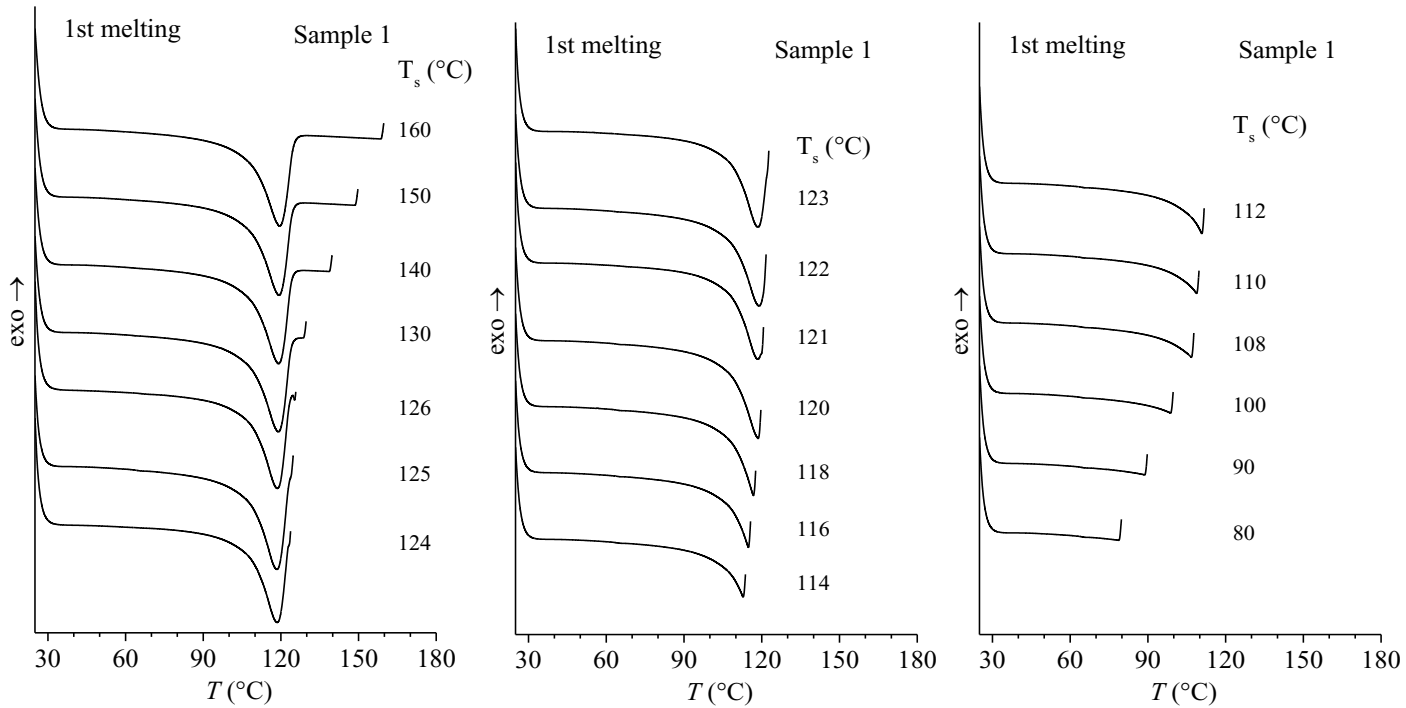

Figure A3-4. SNA DSC heating curves up to the selected T_s recorded for the commercial grade Sample 1.

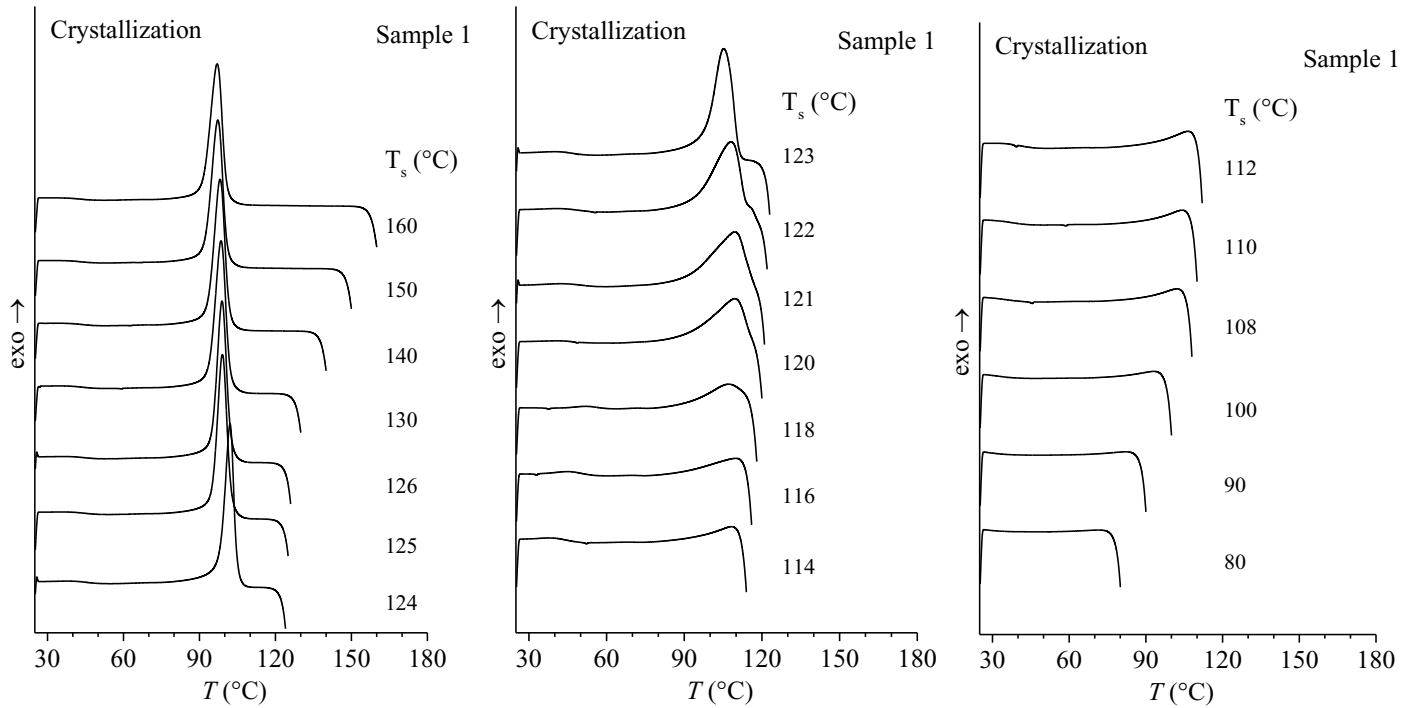

Figure A3-5. SNA DSC cooling curves from the selected T_s recorded for the commercial grade Sample 1.

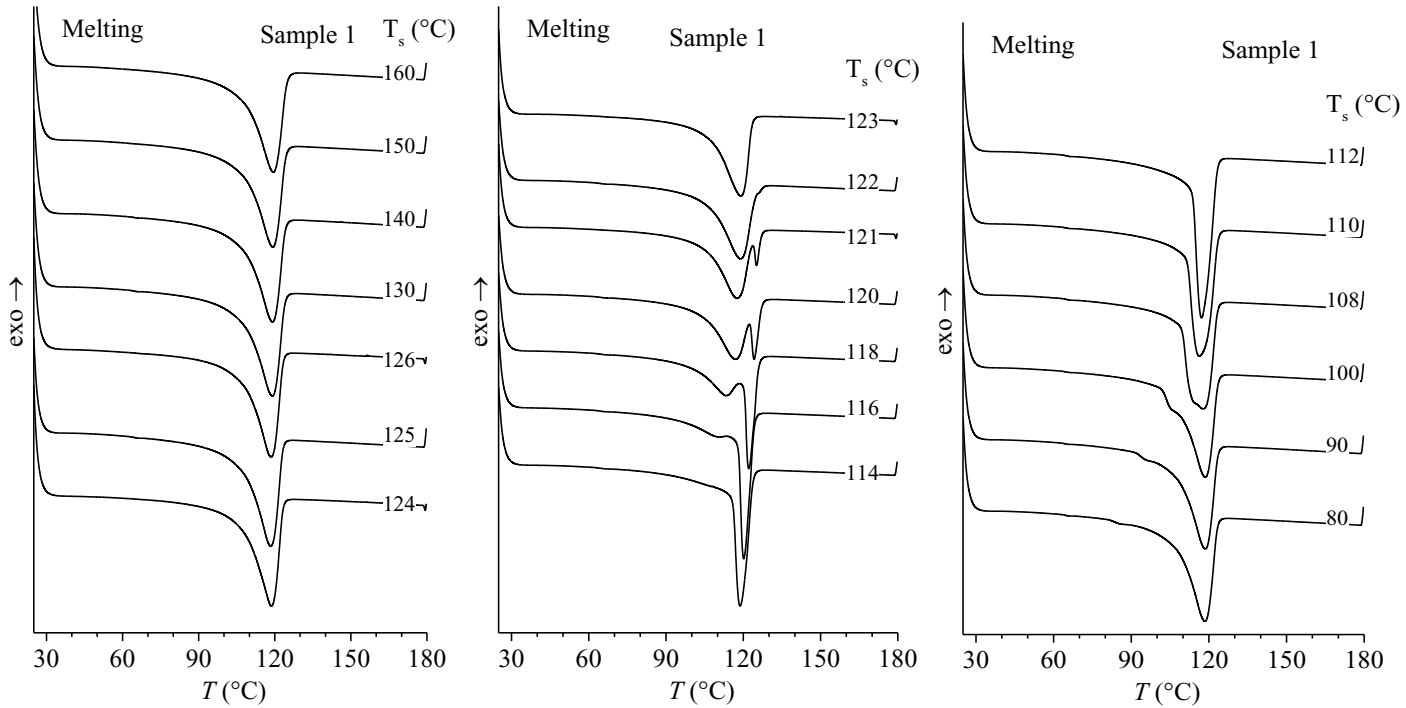

Figure A3-6. SNA DSC subsequent heating curves for the selected T_s recorded for the commercial grade Sample 1.

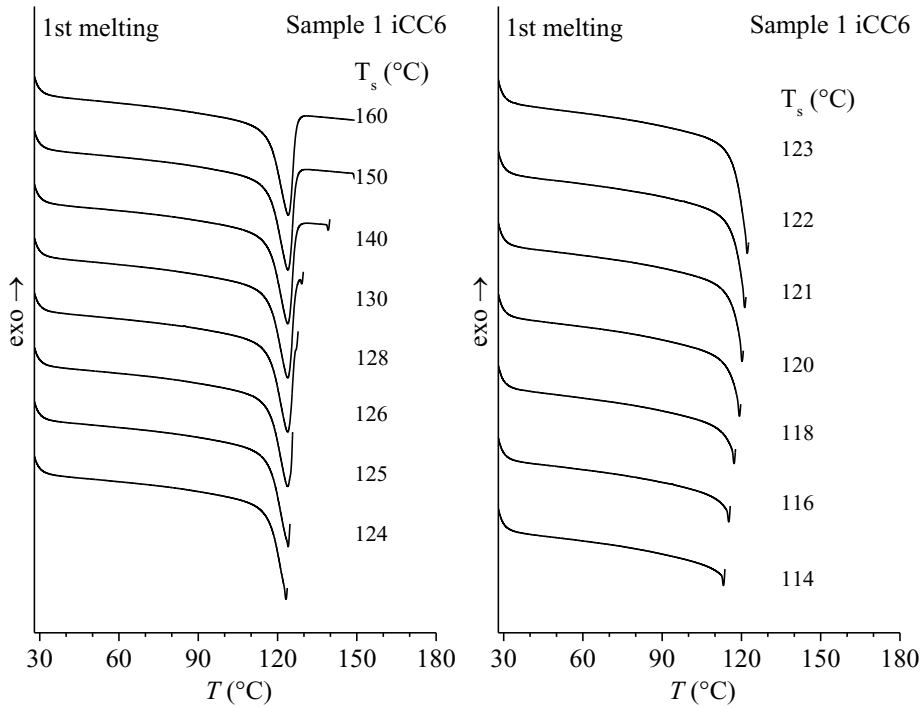

Figure A3-7. SNA DSC heating curves up to the selected T_s recorded for the iCC6 fraction of the commercial grade Sample 1.

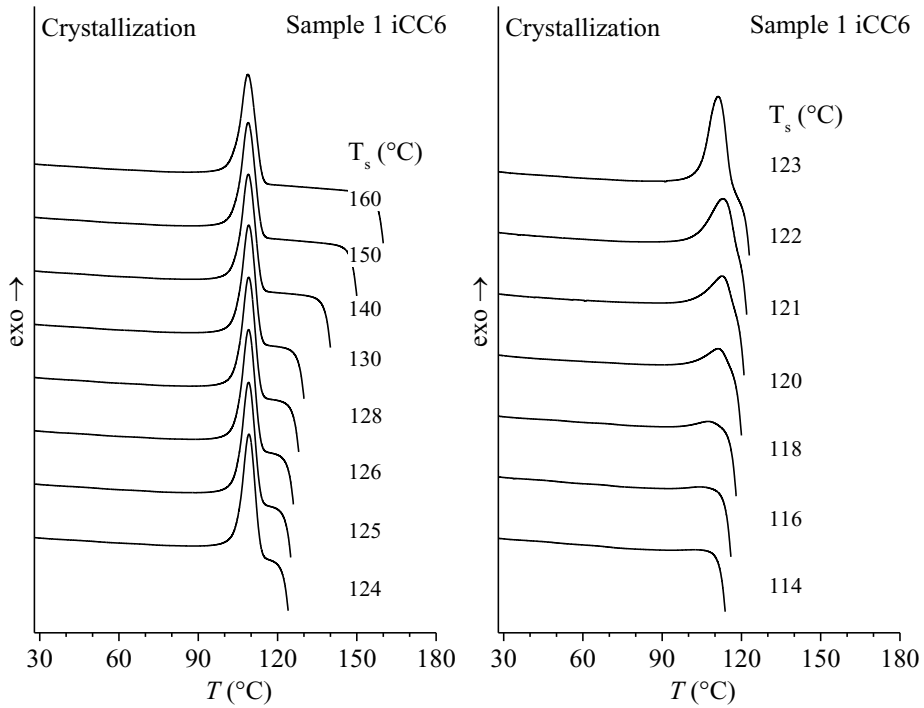

Figure A3-8. SNA DSC cooling curves from the selected T_s recorded for the iCC6 fraction of the commercial grade Sample 1.

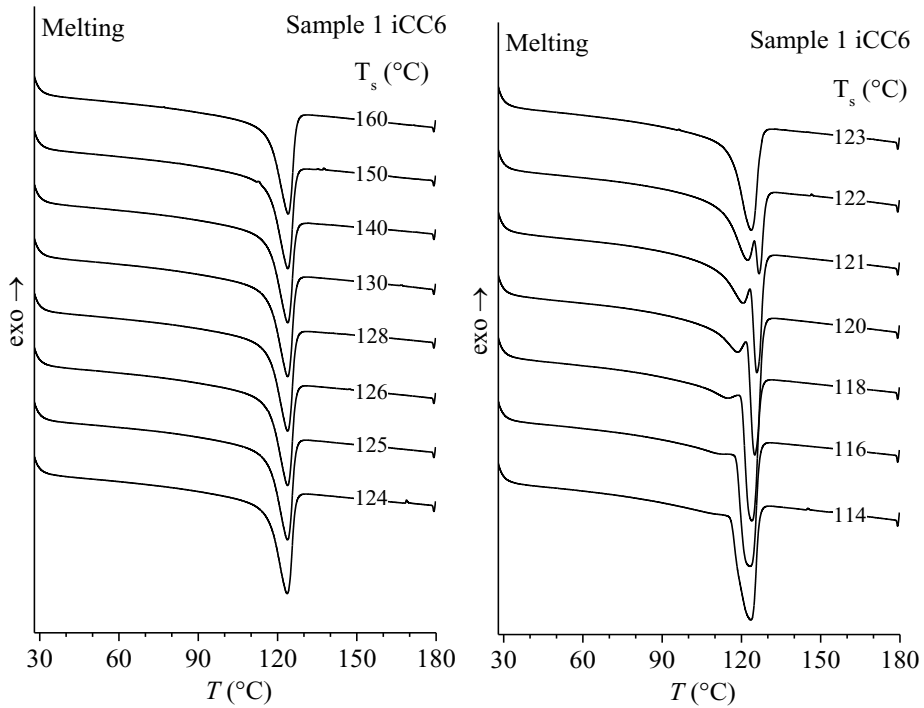

Figure A3-9. SNA DSC subsequent heating curves for the selected T_s recorded for the iCC6 fraction of the commercial grade Sample 1.

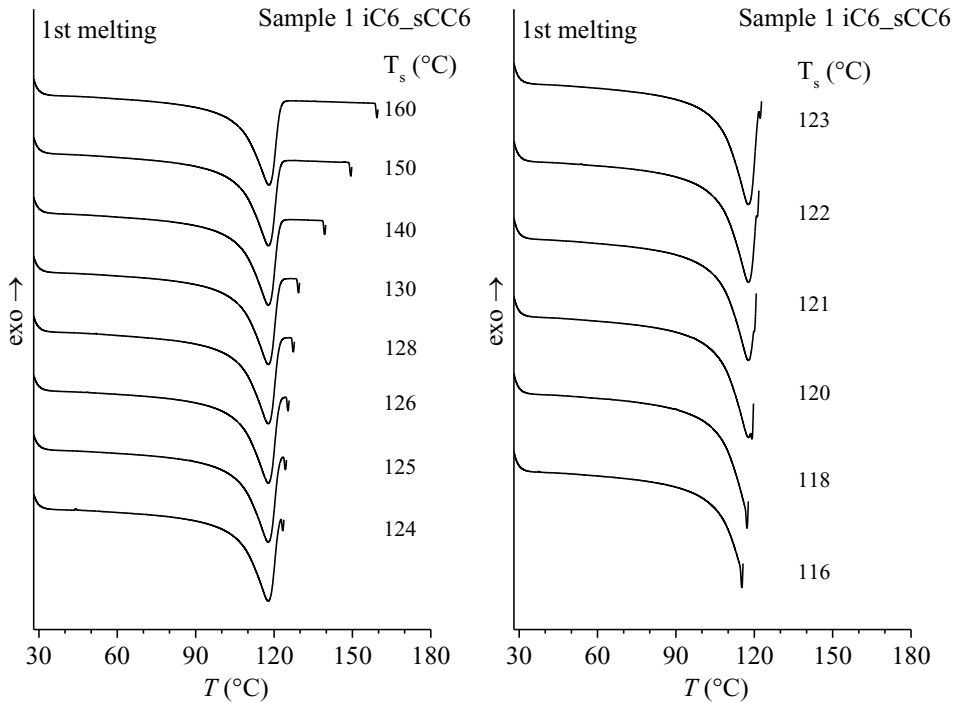

Figure A3-10. SNA DSC heating curves up to the selected T_s recorded for the iC6-sCC6 fraction of the commercial grade Sample 1.

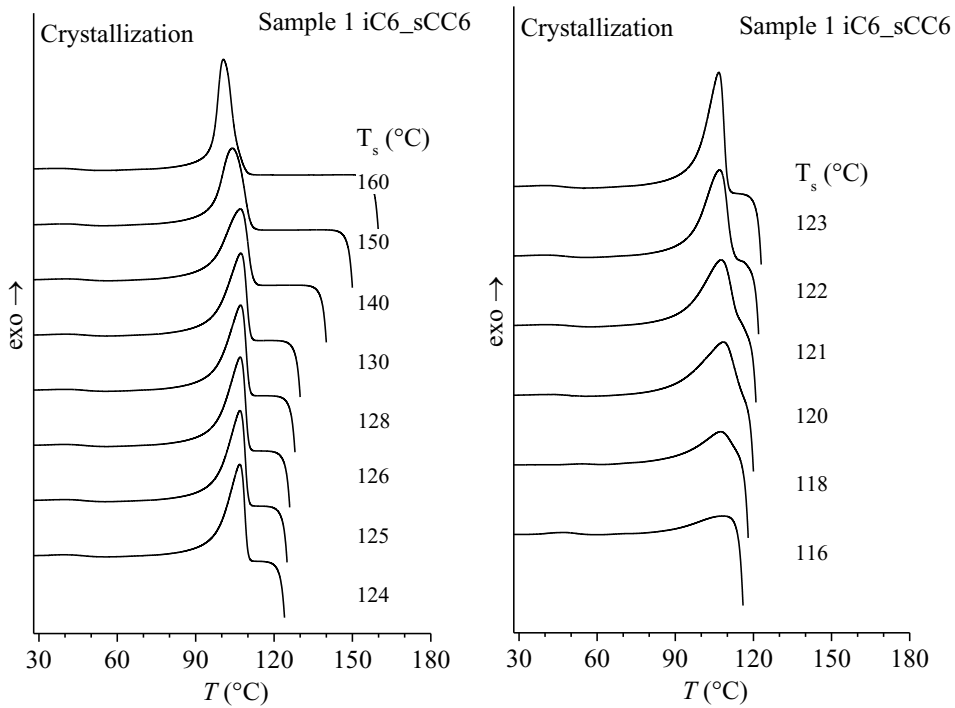

Figure A3-11. SNA DSC cooling curves from the selected T_s recorded for the iC6-sCC6 fraction of the commercial grade Sample 1.

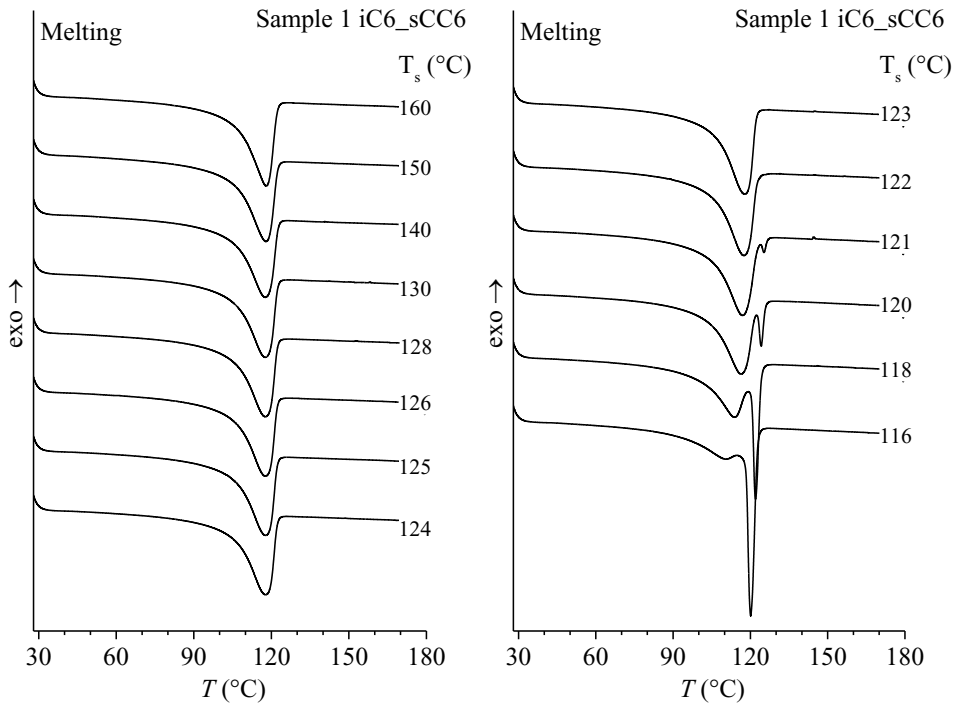

Figure A3-12. SNA DSC subsequent heating curves for the selected T_s recorded for the iC6-sCC6 fraction of the commercial grade Sample 1.

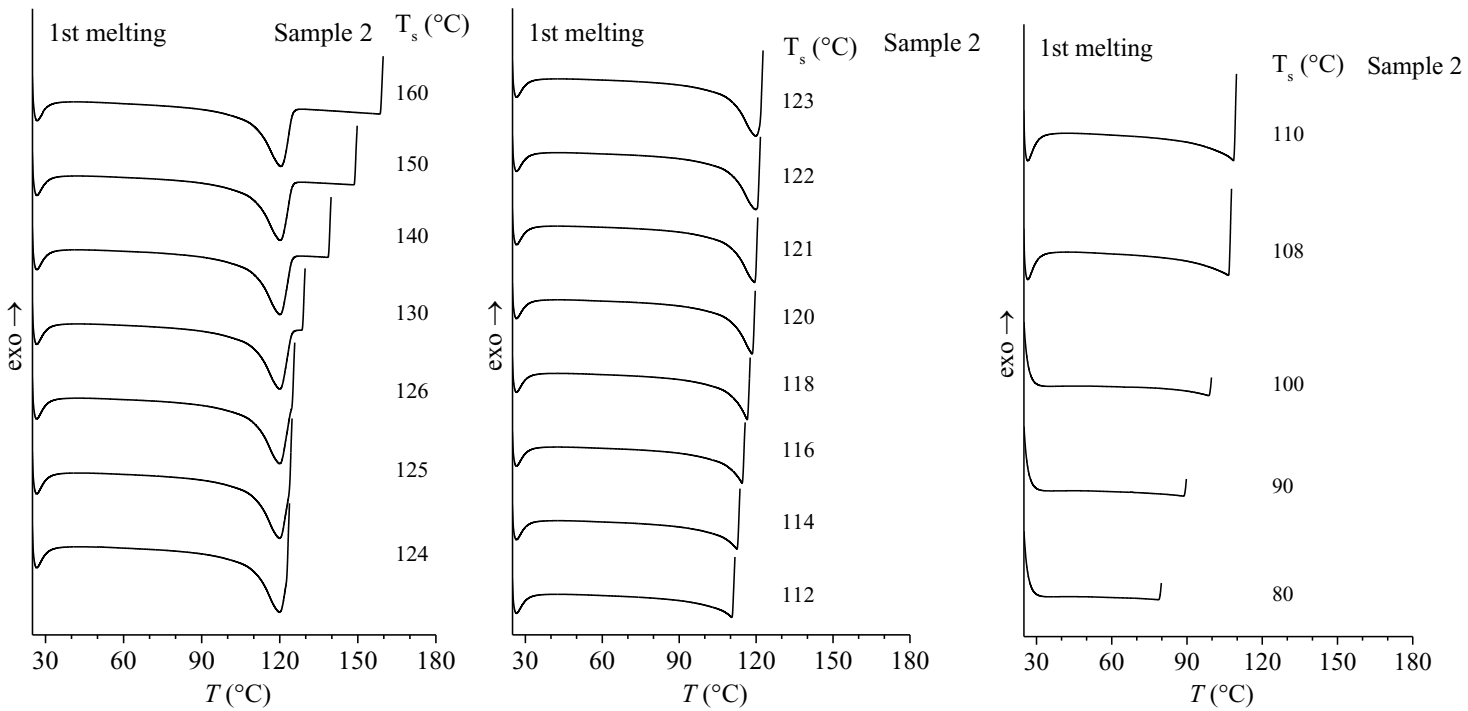

Figure A3-13. SNA DSC heating curves up to the selected T_s recorded for the commercial grade Sample 2.

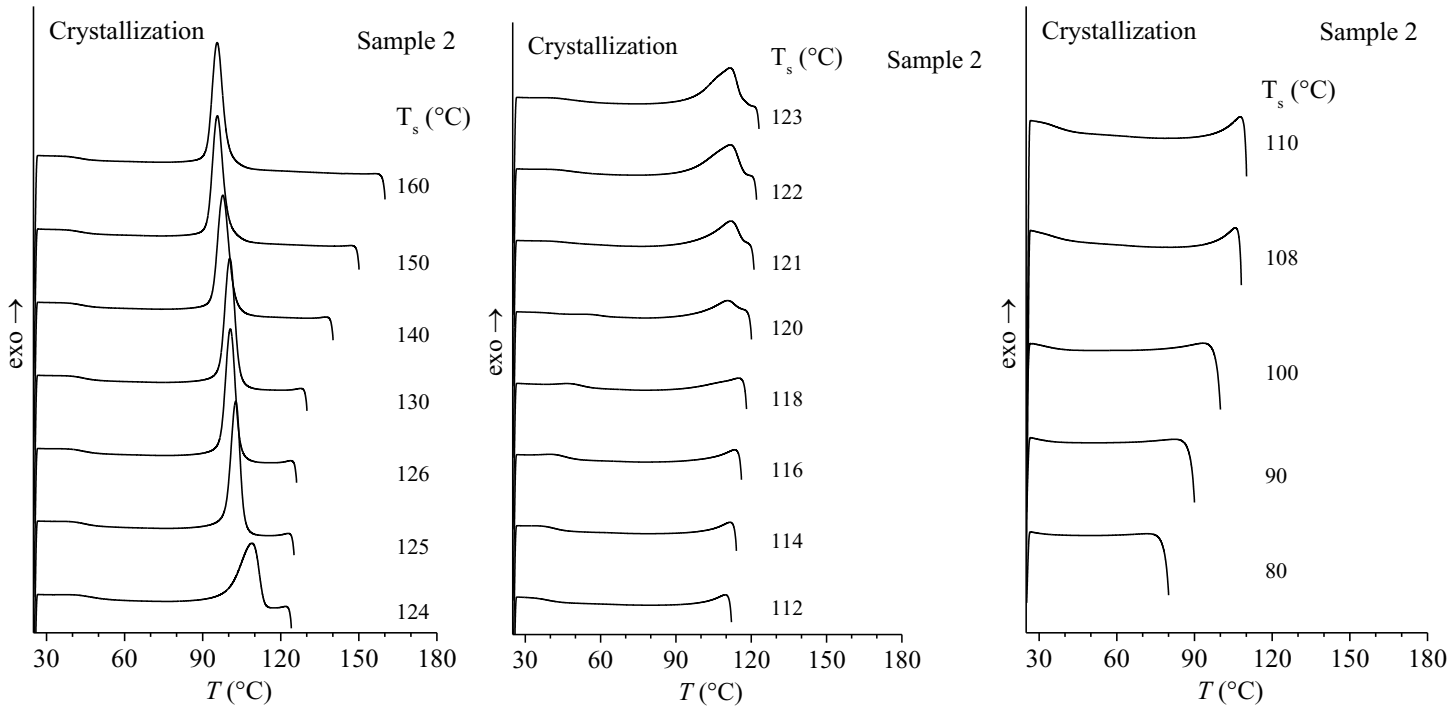

Figure A3-14. SNA DSC cooling curves from the selected T_s recorded for the commercial grade Sample 2.

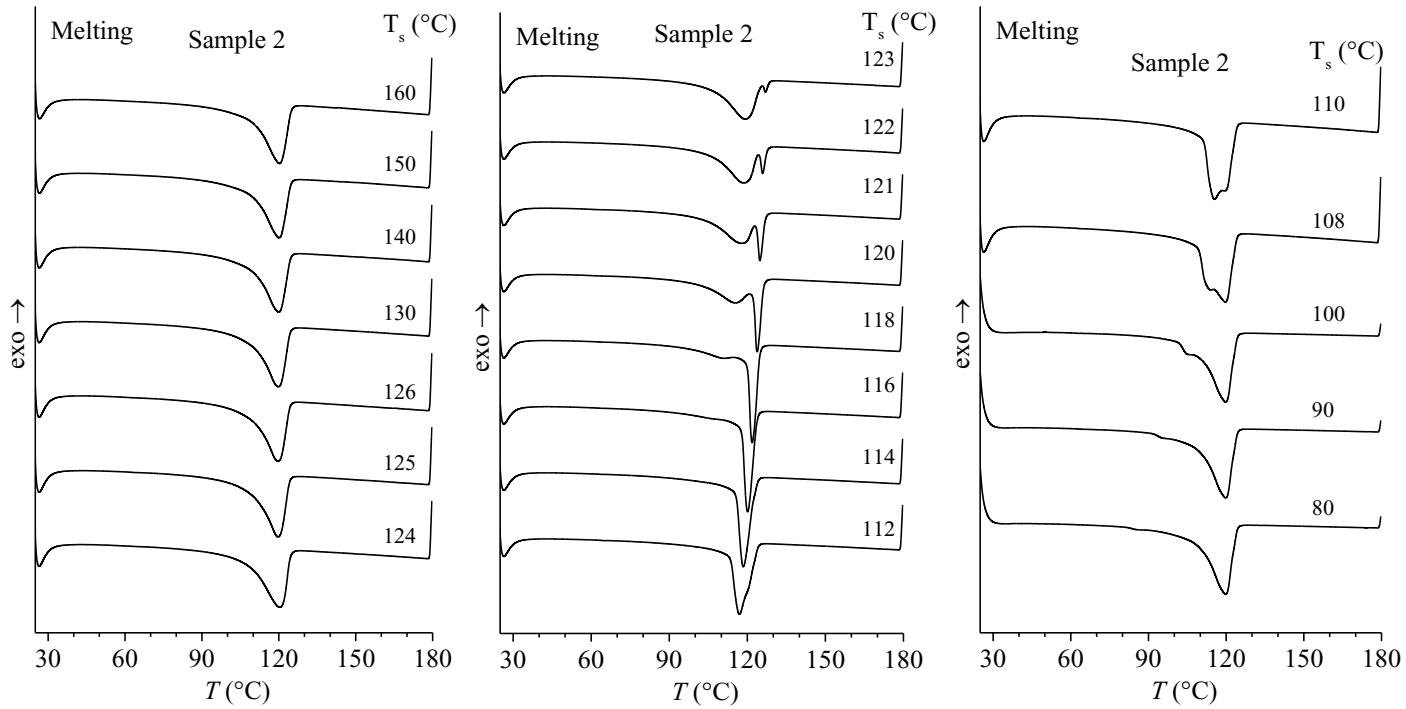

Figure A3-15. SNA DSC subsequent heating curves for the selected T_s recorded for the commercial grade Sample 2.

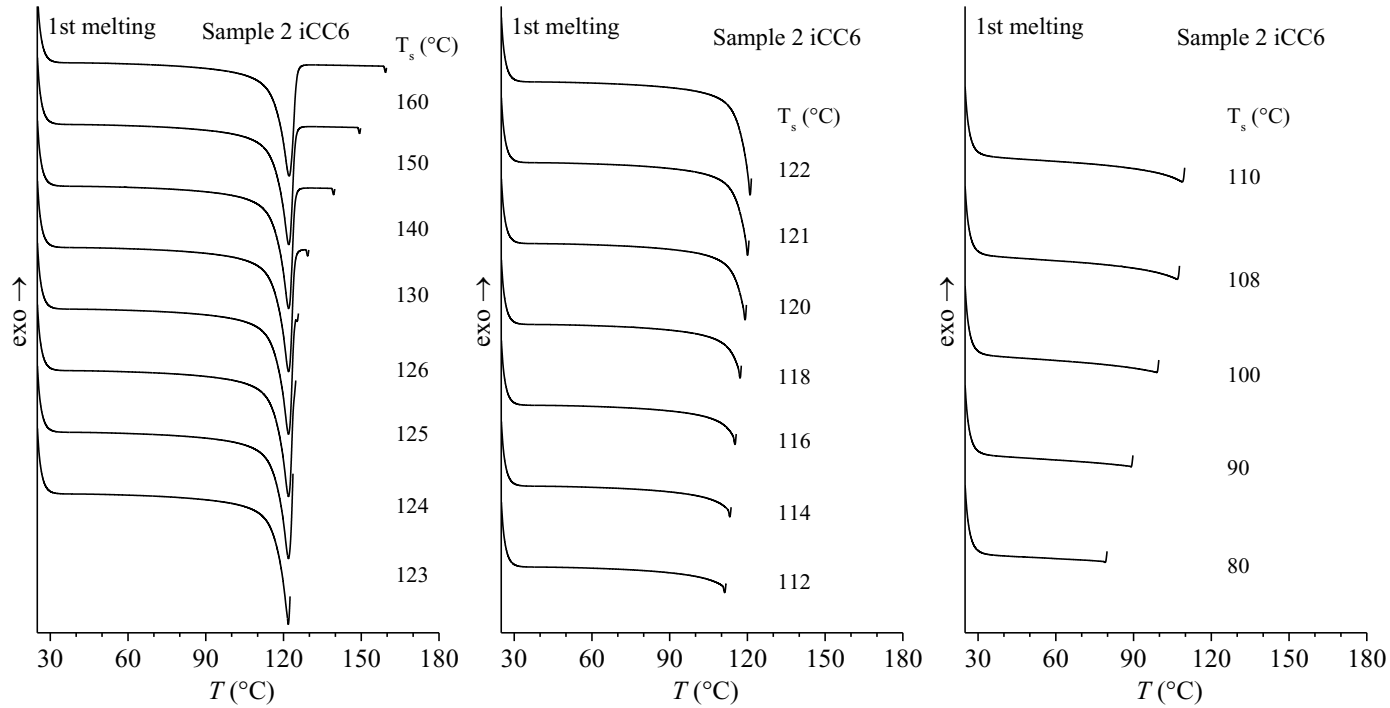

Figure A3-16. SNA DSC heating curves up to the selected T_s recorded for the iCC6 fraction of the commercial grade Sample 2.

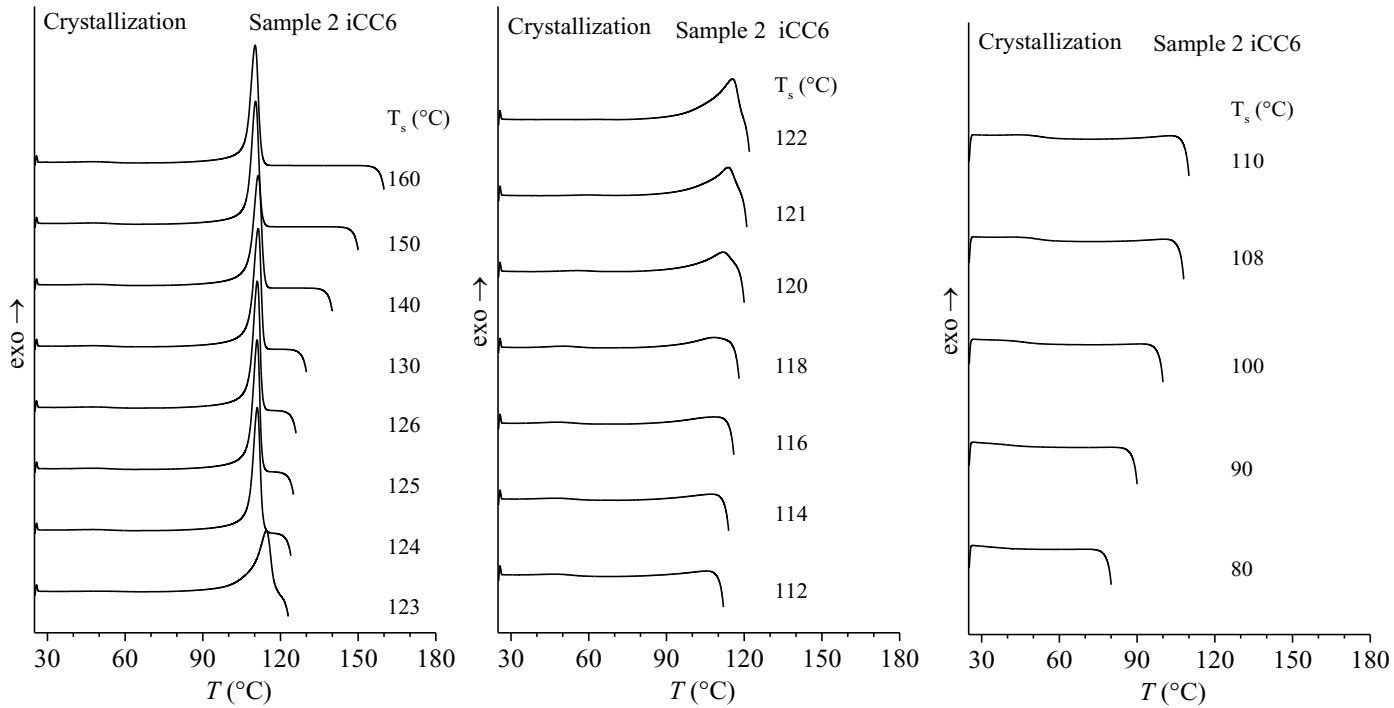

Figure A3-17. SNA DSC cooling curves from the selected T_s recorded for the iCC6 fraction of the commercial grade Sample 2.

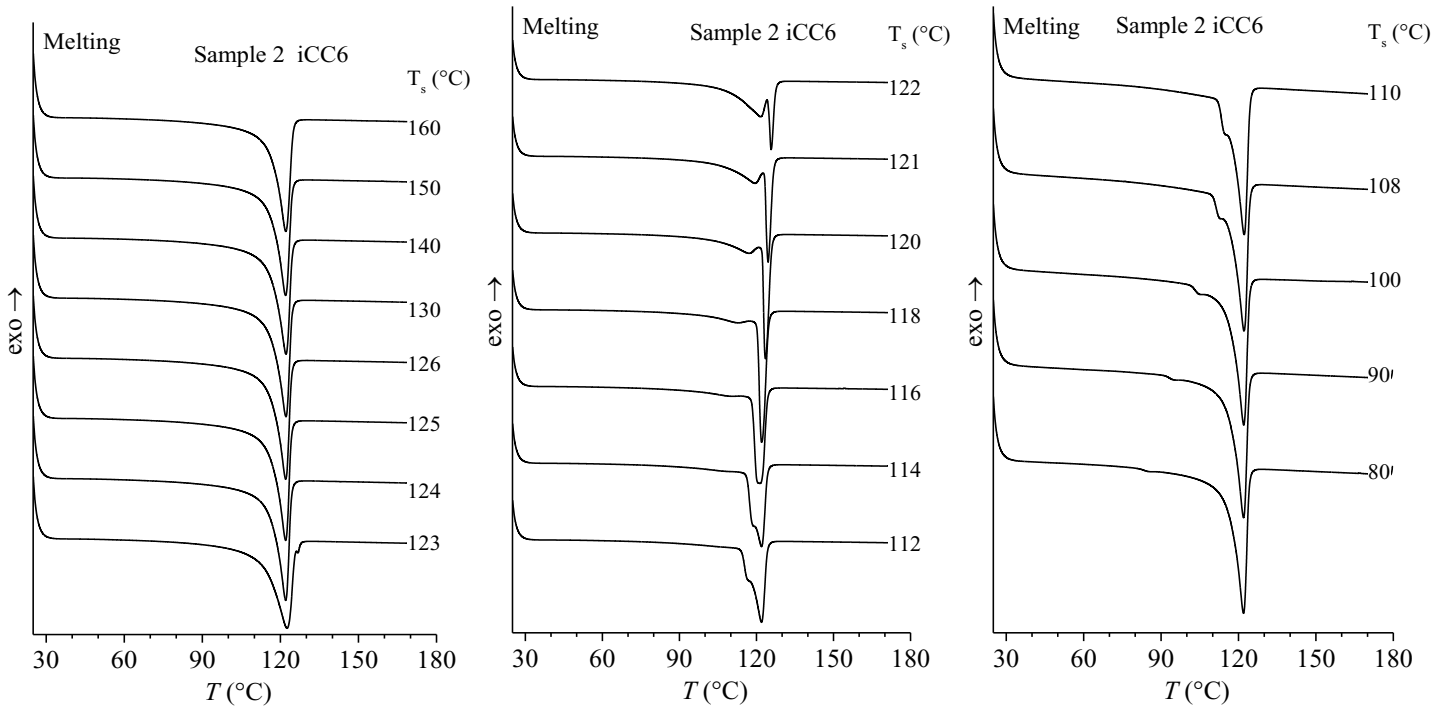

Figure A3-18. SNA DSC subsequent heating curves for the selected T_s recorded for the iCC6 fraction of the commercial grade Sample 2.

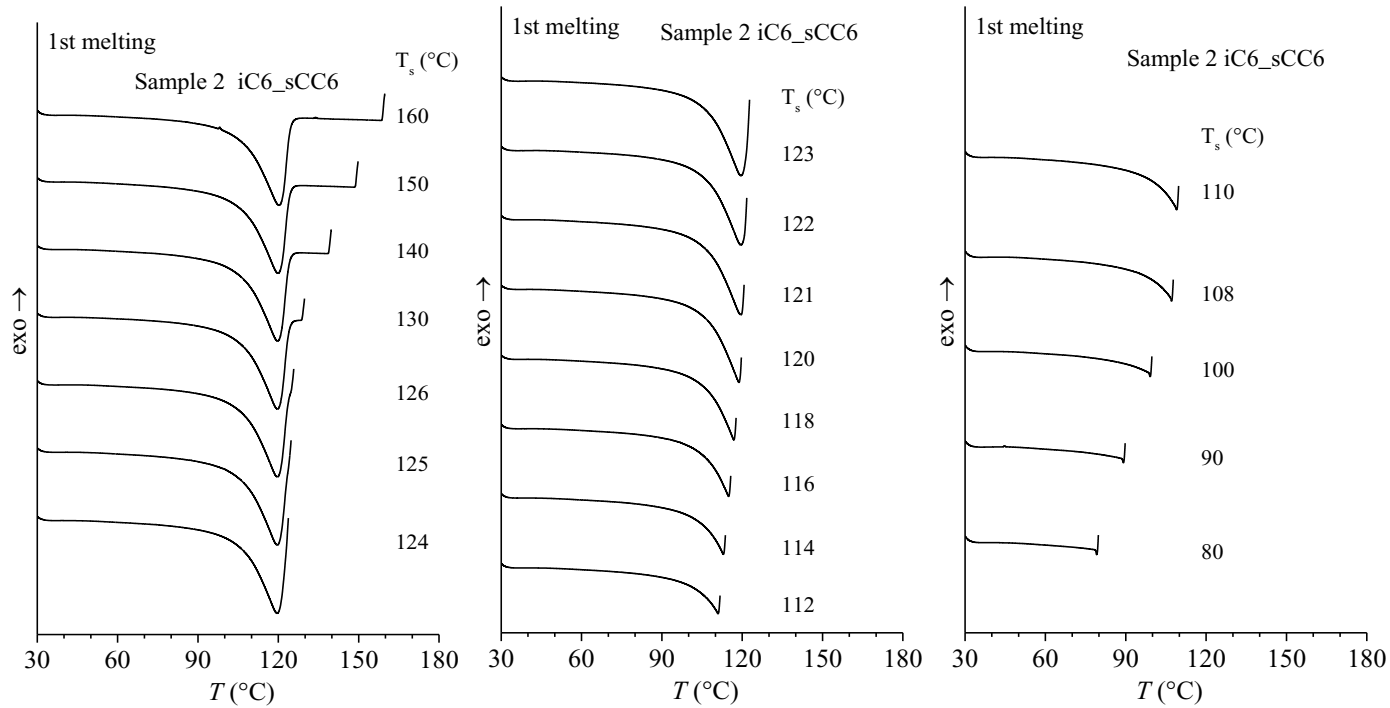

Figure A3-19. SNA DSC heating curves up to the selected T_s recorded for the iC6-sCC6 fraction of the commercial grade Sample 2.

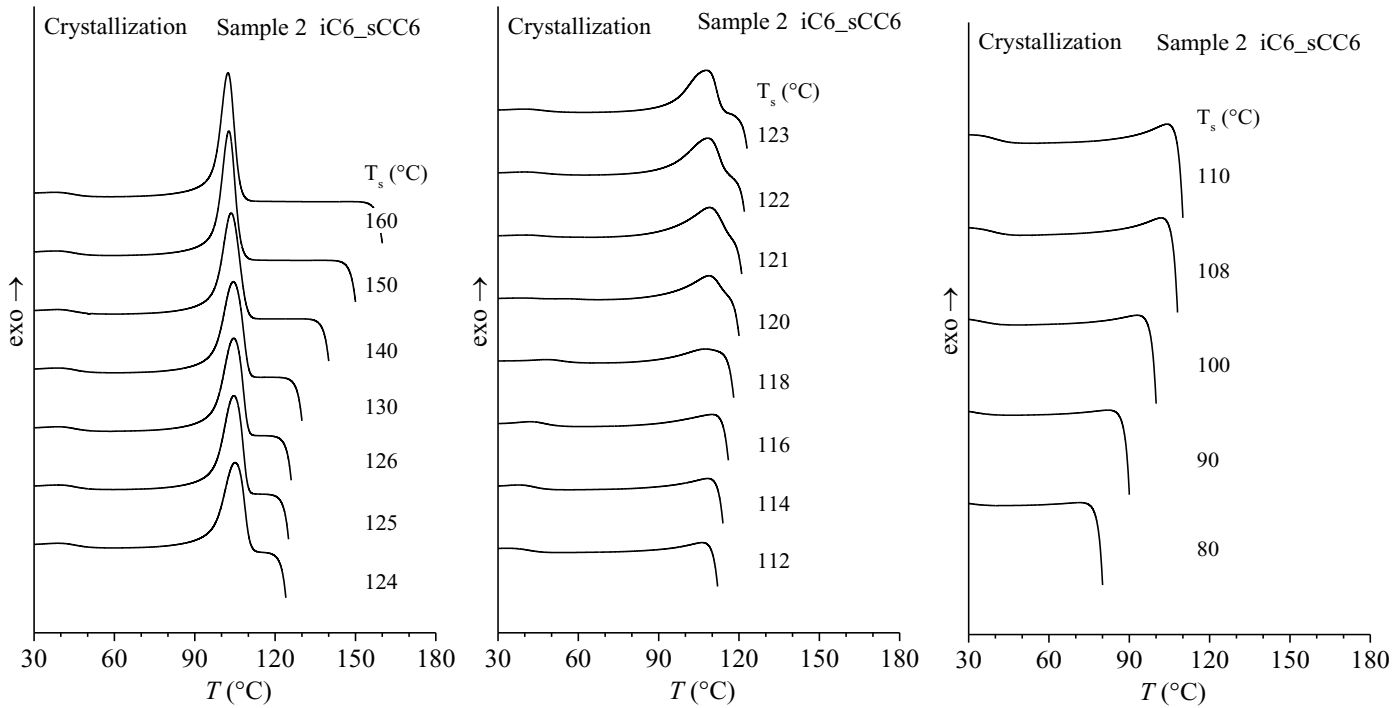

Figure A3-20. SNA DSC cooling curves from the selected T_s recorded for the iC6-sCC6 fraction of the commercial grade Sample 2.

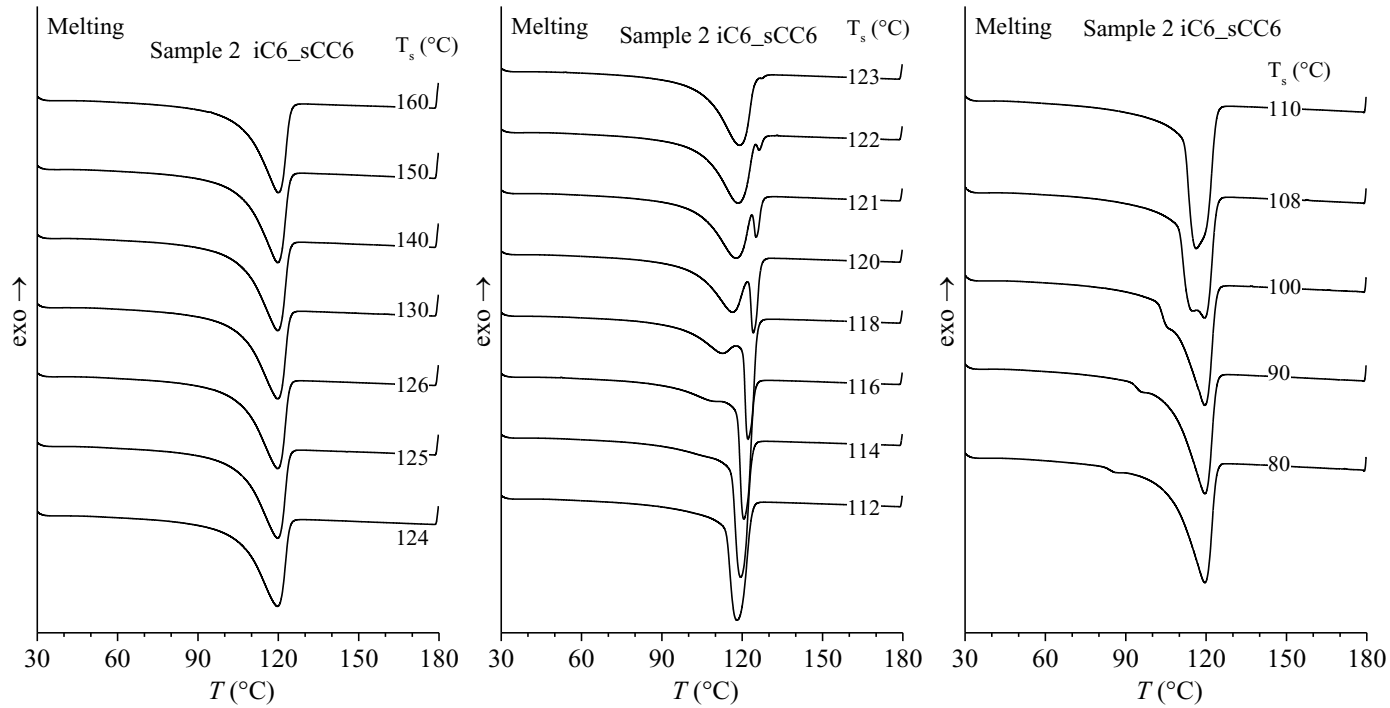

Figure A3-21. SNA DSC subsequent heating curves for the selected T_s recorded for the iC6-sCC6 fraction of the commercial grade Sample 2.

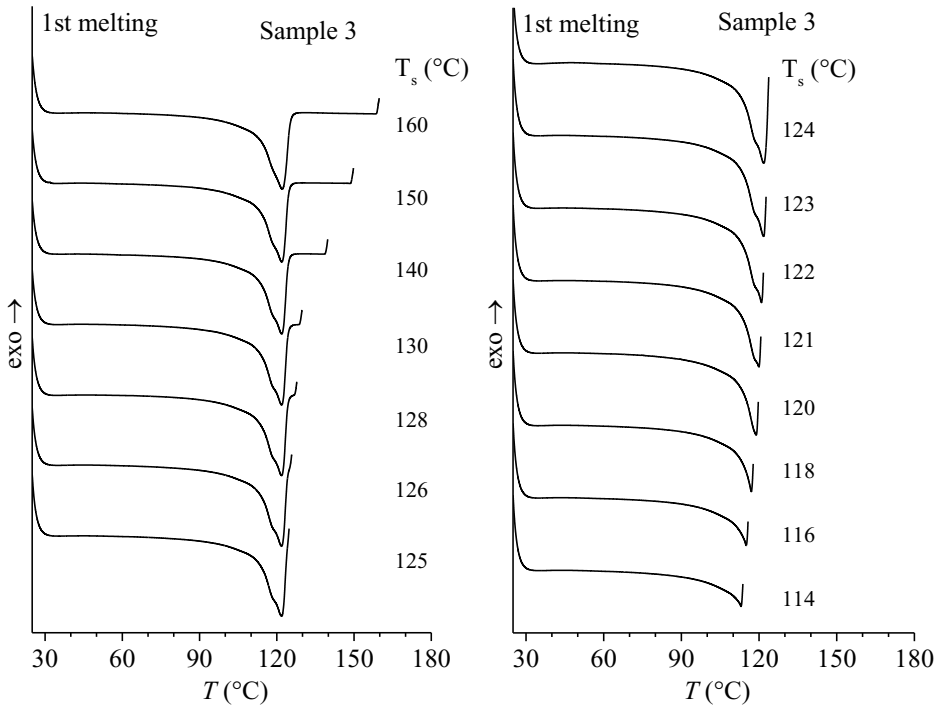

Figure A3-22. SNA DSC heating curves up to the selected T_s recorded for the commercial grade Sample 3.

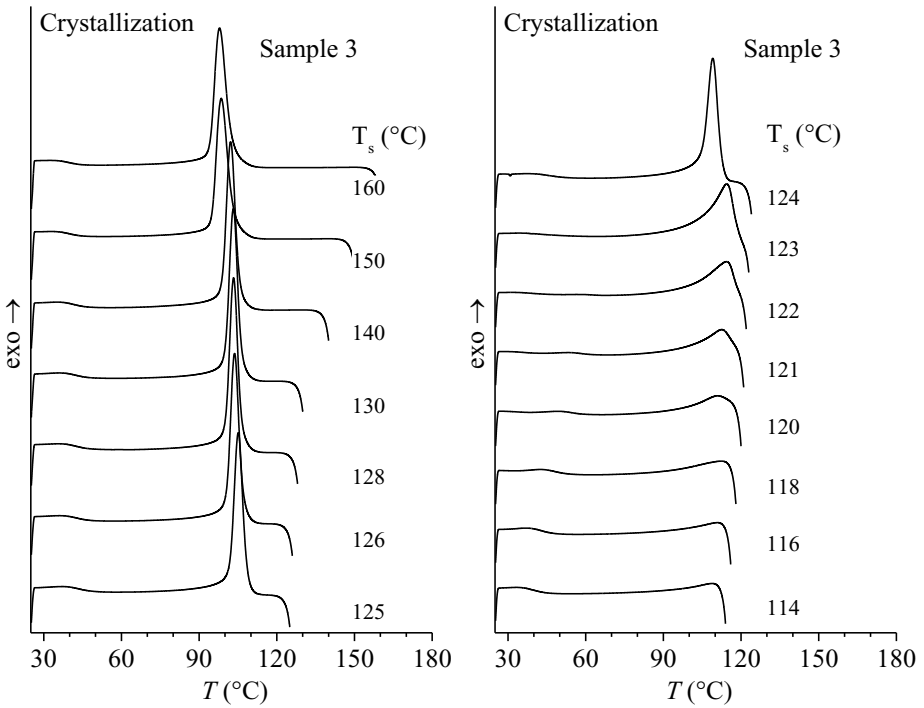

Figure A3-23. SNA DSC cooling curves from the selected T_s recorded for the commercial grade Sample 3.

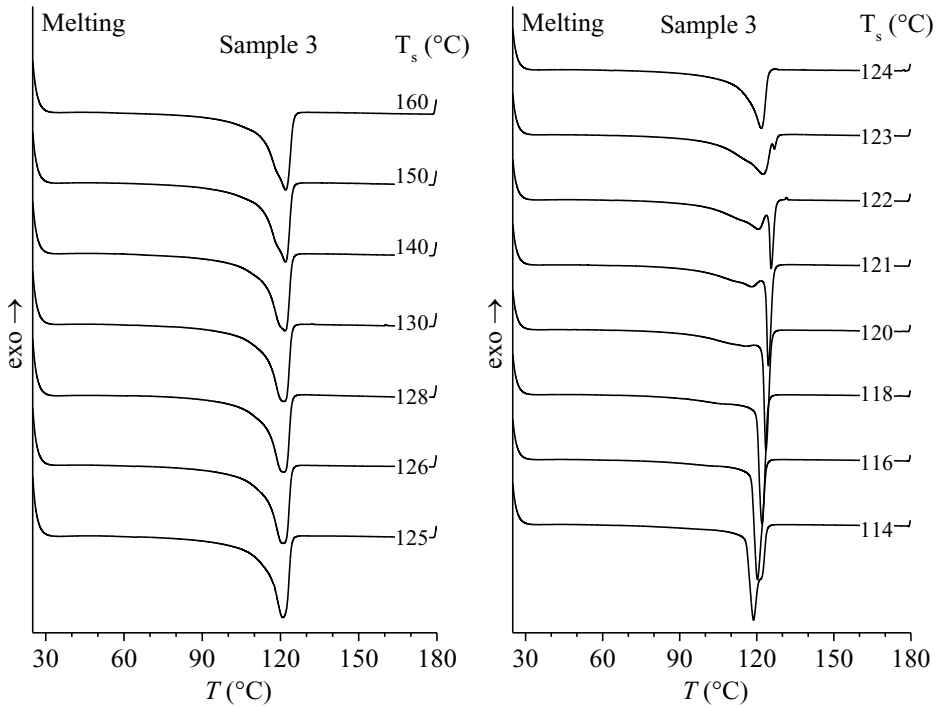

Figure A3-24. SNA DSC subsequent heating curves for the selected T_s recorded for the commercial grade Sample 3.

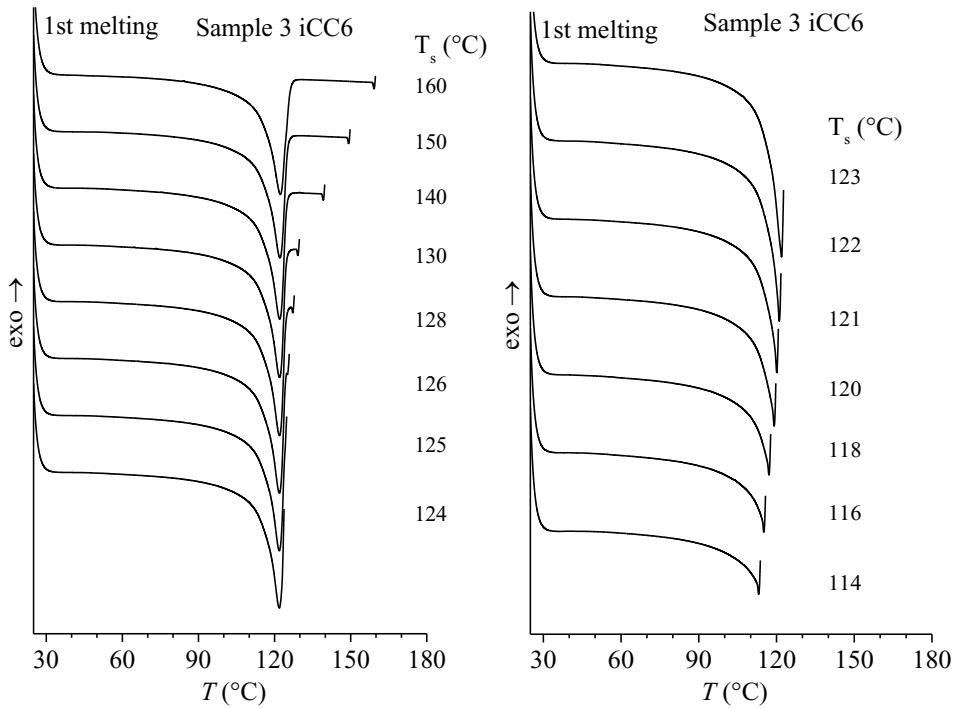

Figure A3-25. SNA DSC heating curves up to the selected T_s recorded for the iCC6 fraction of the commercial grade Sample 3.

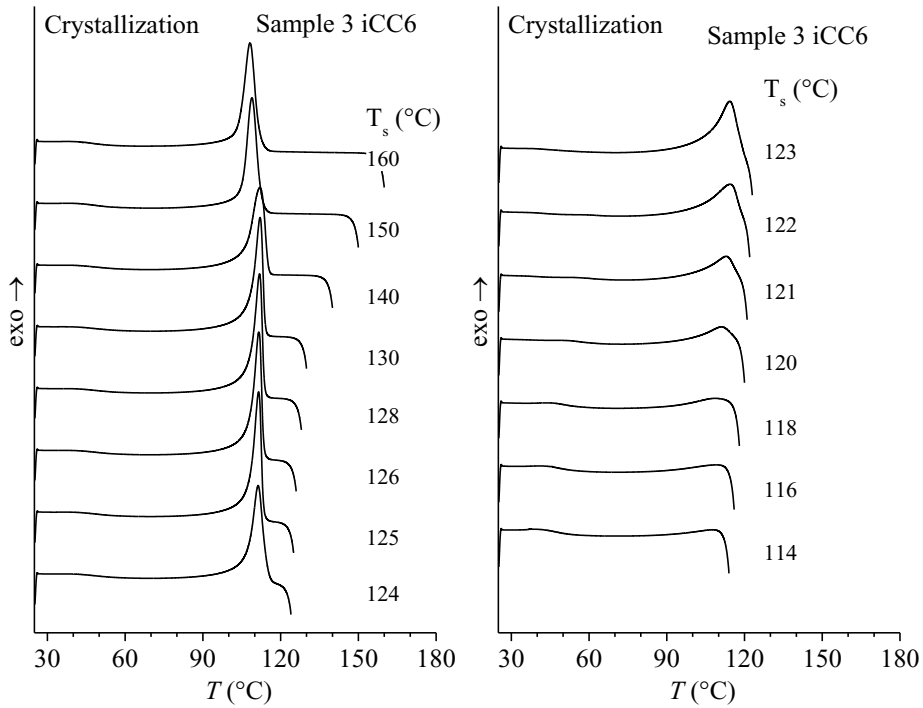

Figure A3-26. SNA DSC cooling curves from the selected T_s recorded for the iCC6 fraction of the commercial grade Sample 3.

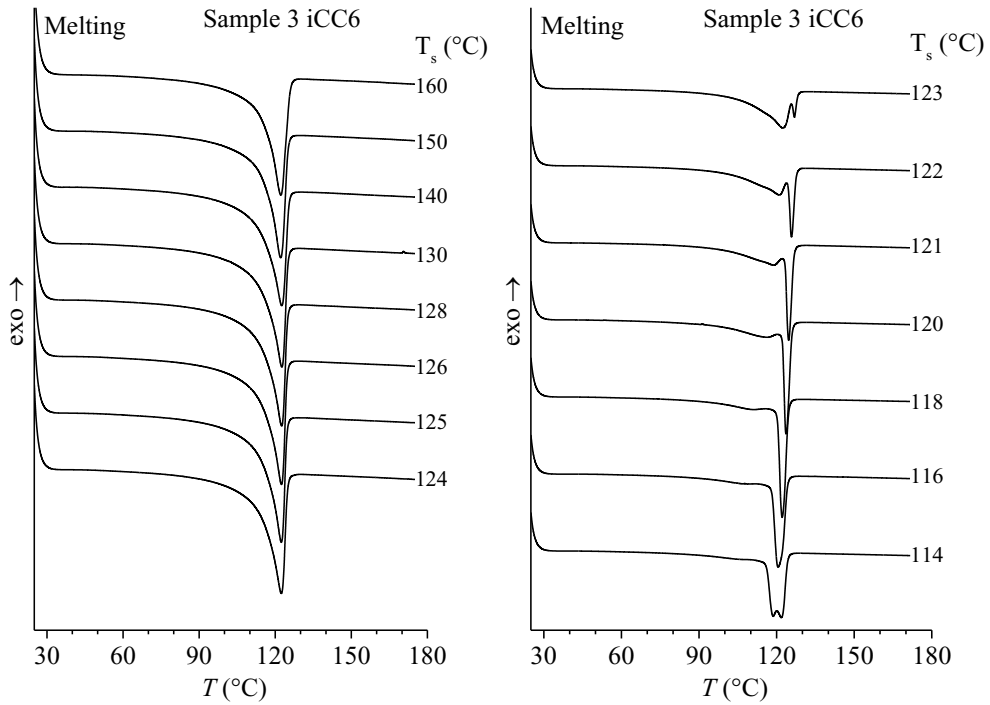

Figure A3-27. SNA DSC subsequent heating curves for the selected T_s recorded for the iCC6 fraction of the commercial grade Sample 3.

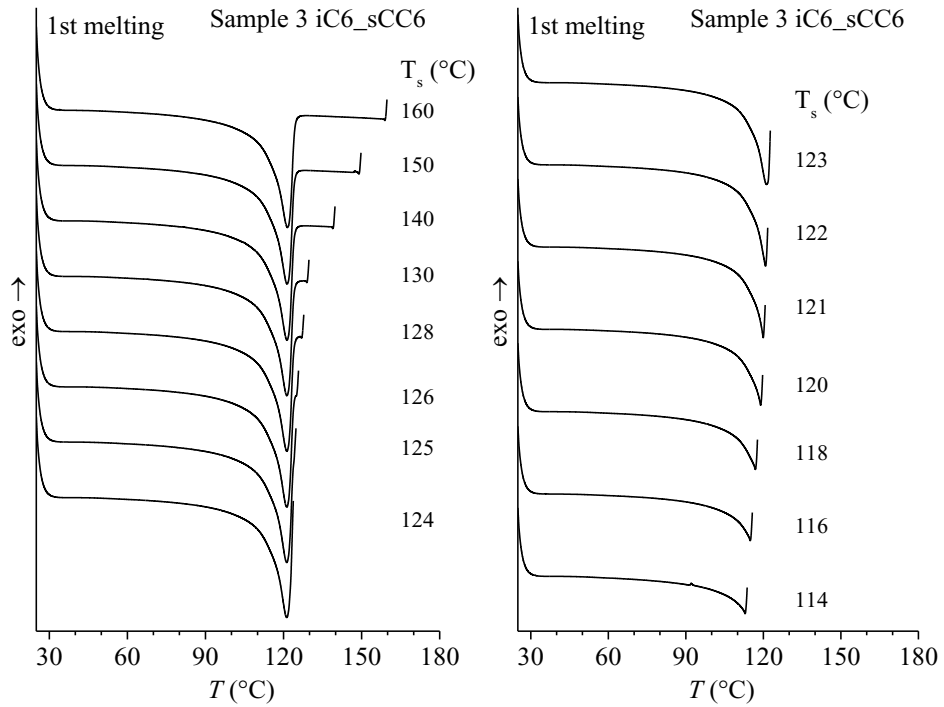

Figure A3-28. SNA DSC heating curves up to the selected T_s recorded for the iC6-sCC6 fraction of the commercial grade Sample 3.

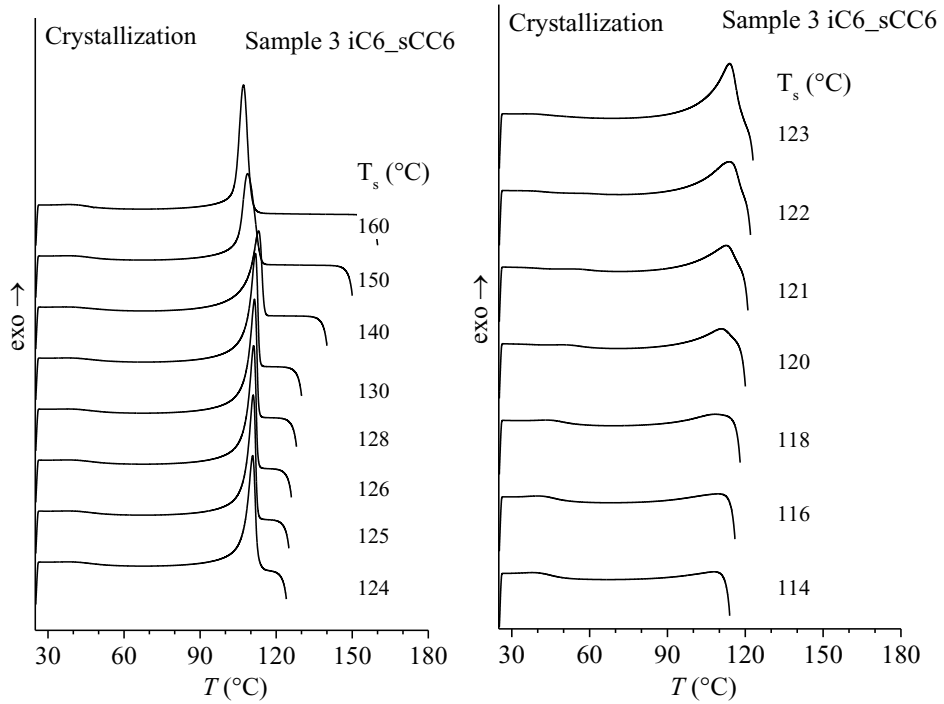

Figure A3-29. SNA DSC cooling curves from the selected T_s recorded for the iC6-sCC6 fraction of the commercial grade Sample 3.

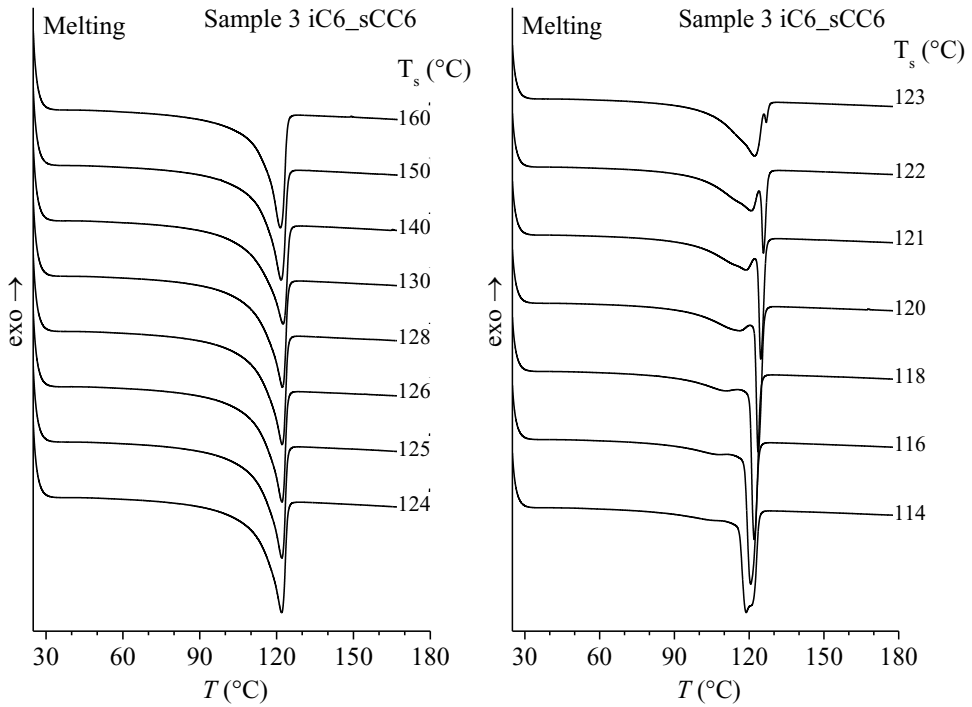

Figure A3-30. SNA DSC subsequent heating curves for the selected T_s recorded for the iC6-sCC6 fraction of the commercial grade Sample 3.

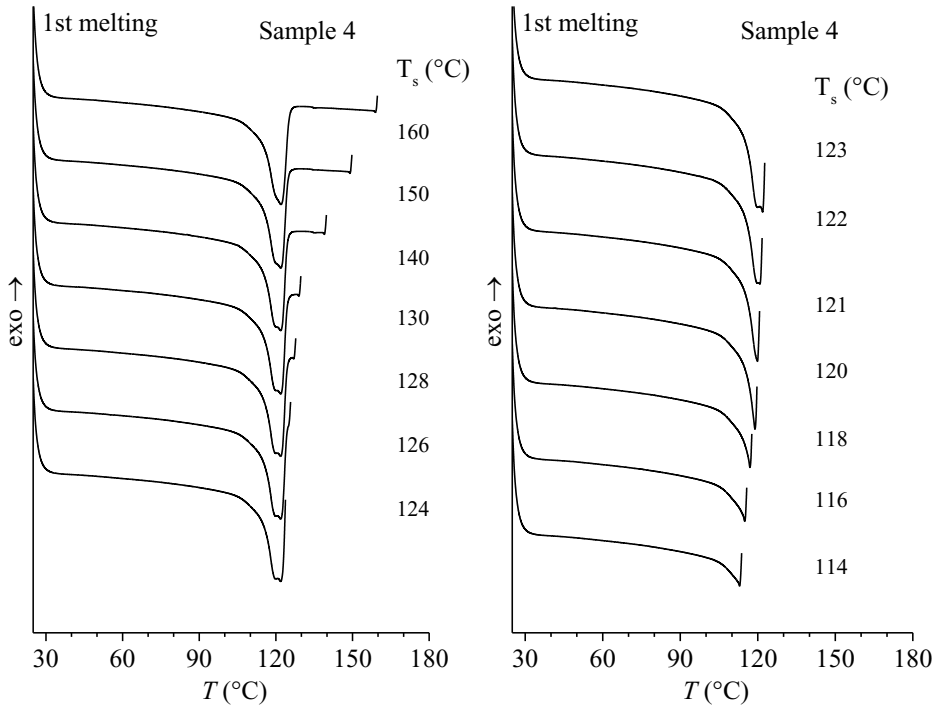

Figure A3-31. SNA DSC heating curves up to the selected T_s recorded for the commercial grade Sample 4.

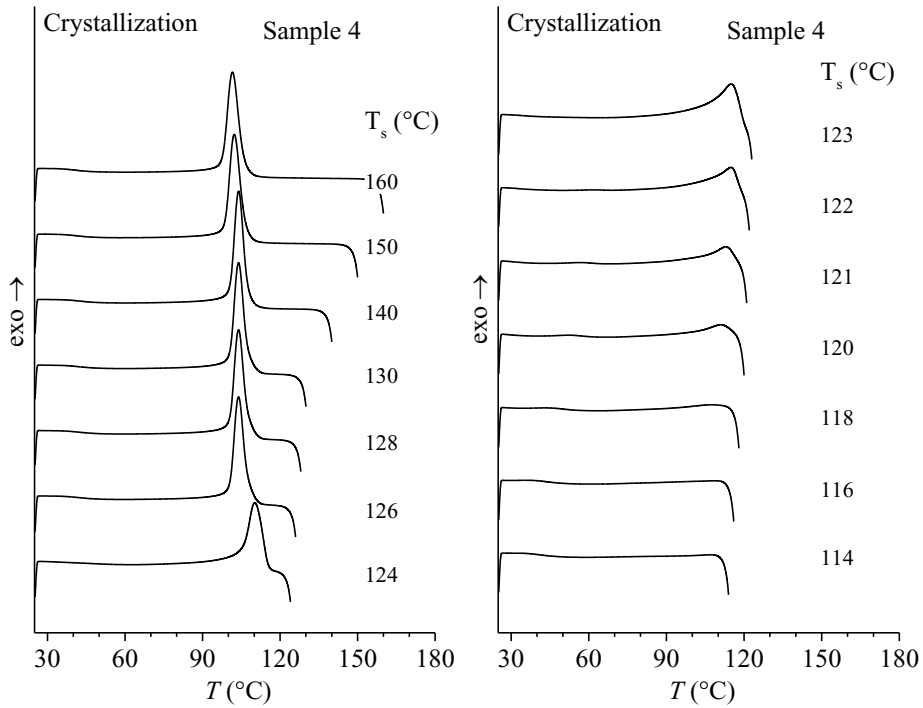

Figure A3-32. SNA DSC cooling curves from the selected T_s recorded for the commercial grade Sample 4.

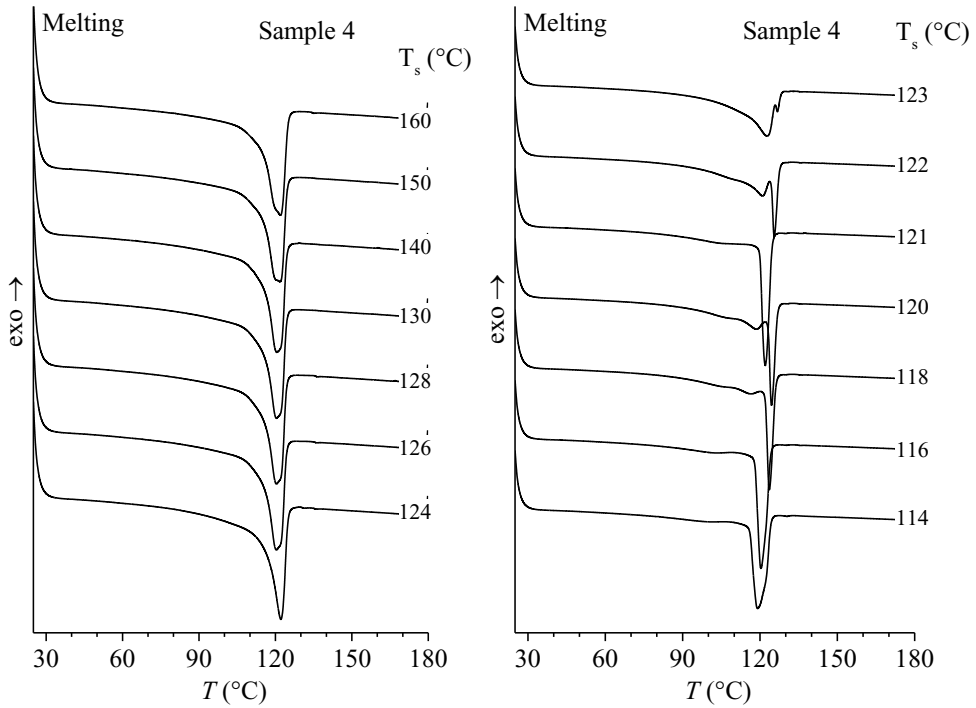

Figure A3-33. SNA DSC subsequent heating curves for the selected T_s recorded for the commercial grade Sample 4.

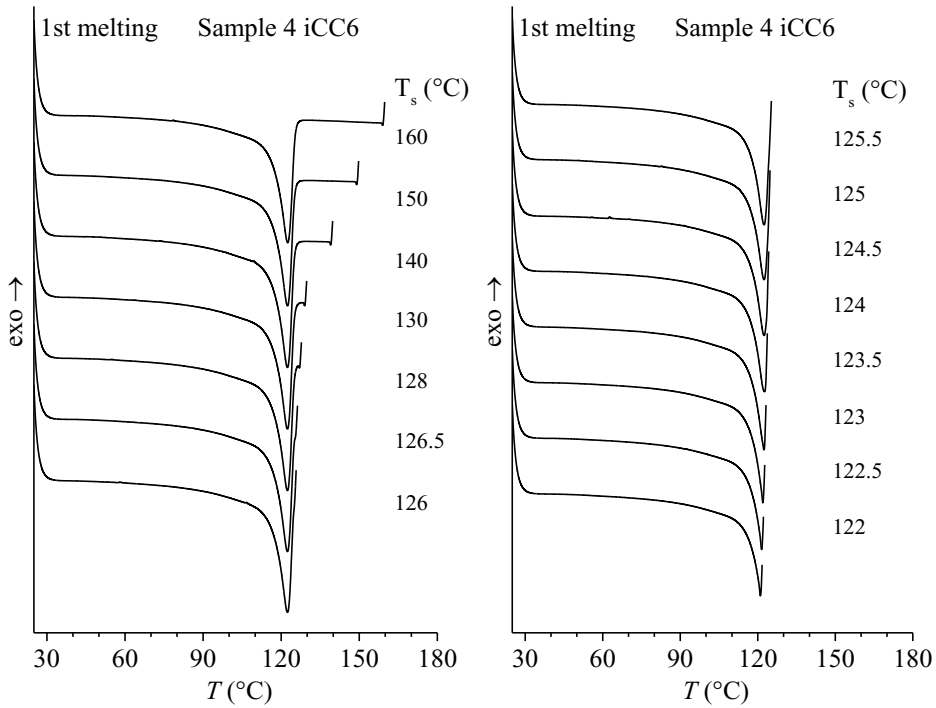

Figure A3-34. SNA DSC heating curves up to the selected T_s recorded for the iCC6 fraction of the commercial grade Sample 4.

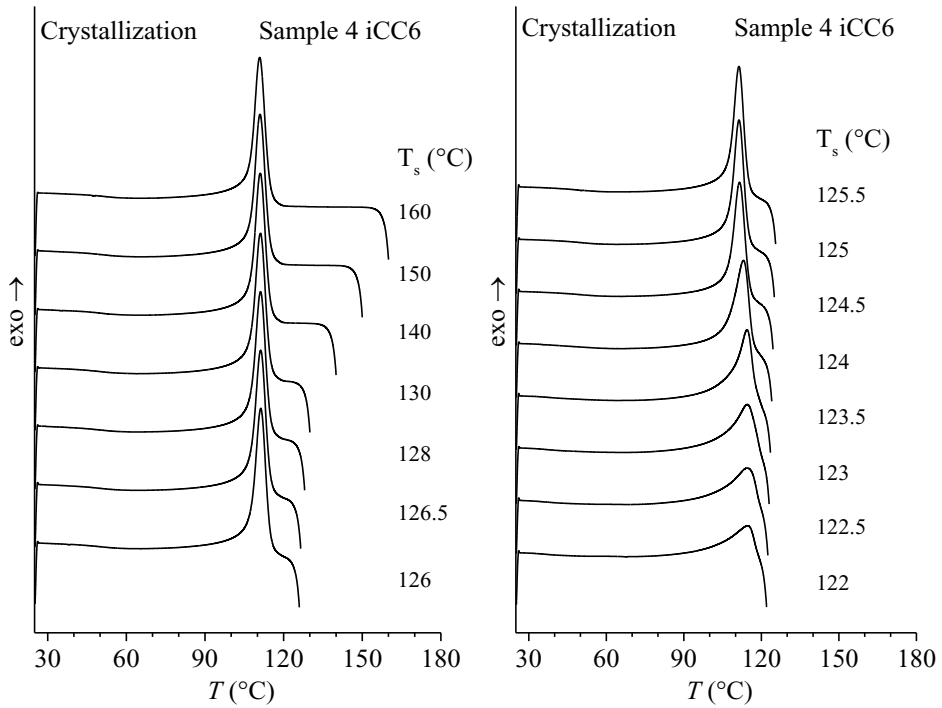

Figure A3-35. SNA DSC cooling curves from the selected T_s recorded for the iCC6 fraction of the commercial grade Sample 4.

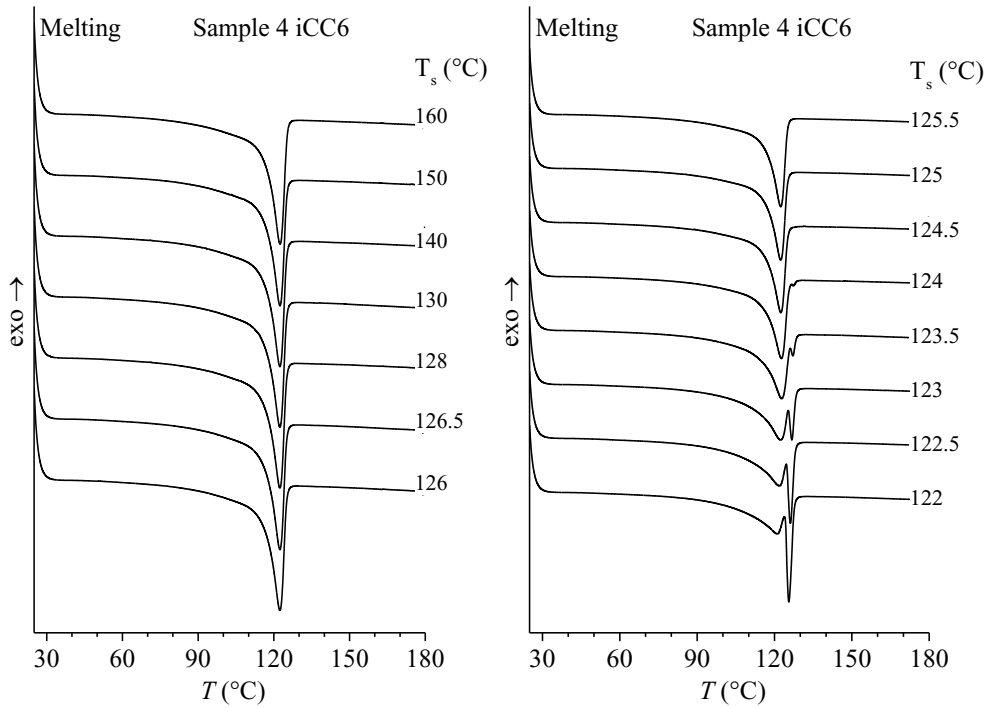

Figure A3-36. SNA DSC subsequent heating curves for the selected T_s recorded for the iCC6 fraction of the commercial grade Sample 4.

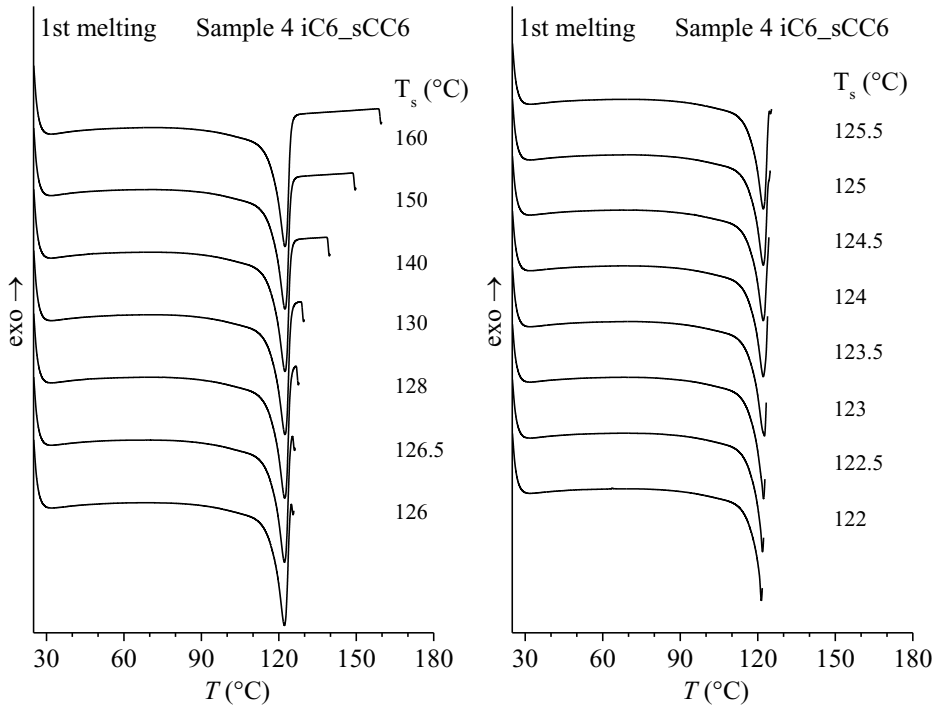

Figure A3-37. SNA DSC heating curves up to the selected T_s recorded for the iC6-sCC6 fraction of the commercial grade Sample 4.

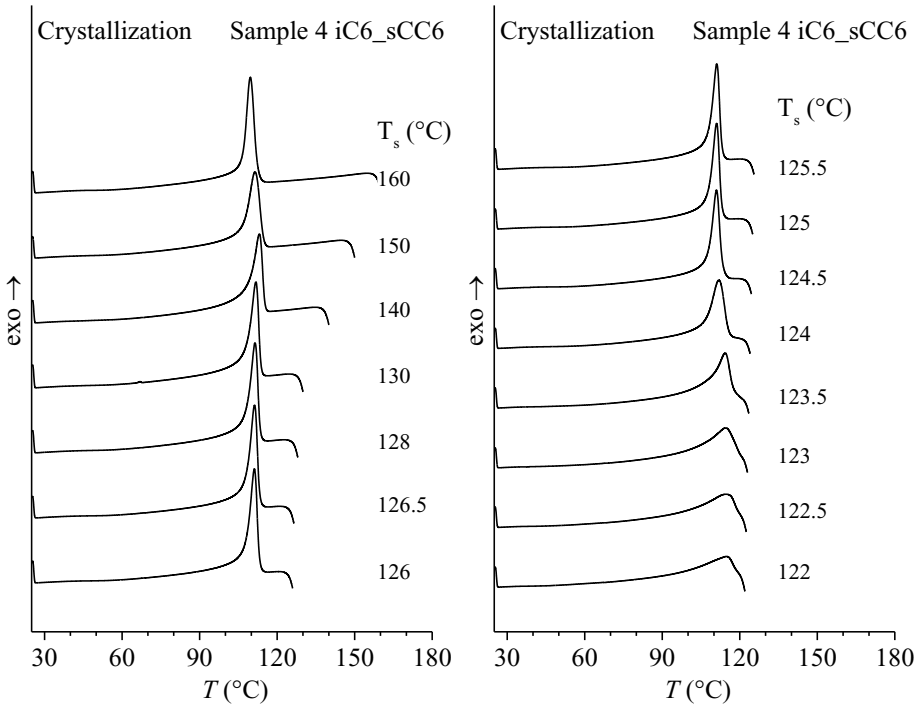

Figure A3-38. SNA DSC cooling curves from the selected T_s recorded for the iC6-sCC6 fraction of the commercial grade Sample 4.

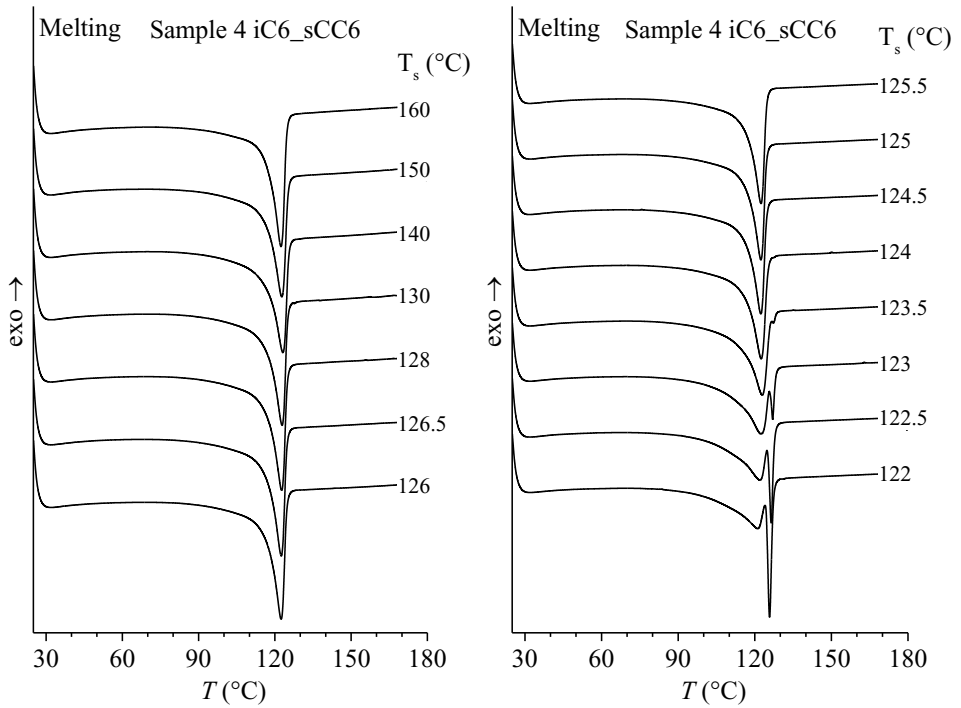

Figure A3-39. SNA DSC subsequent heating curves for the selected T_s recorded for the iC6-sCC6 fraction of the commercial grade Sample 4.

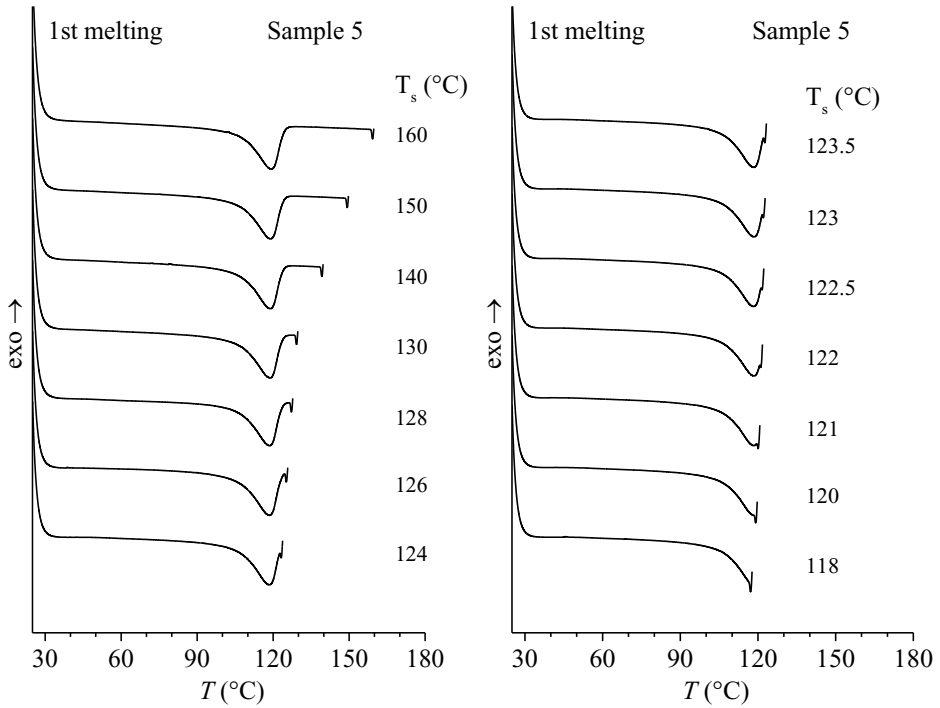

Figure A3-40. SNA DSC heating curves up to the selected T_s recorded for the commercial grade Sample 5.

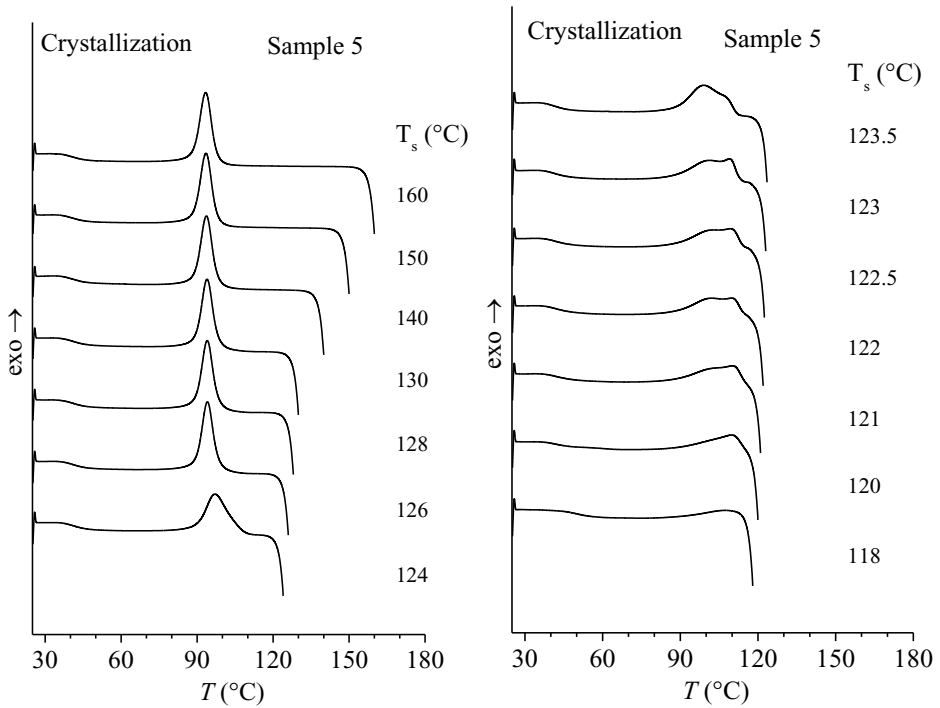

Figure A3-41. SNA DSC cooling curves from the selected T_s recorded for the commercial grade Sample 5.

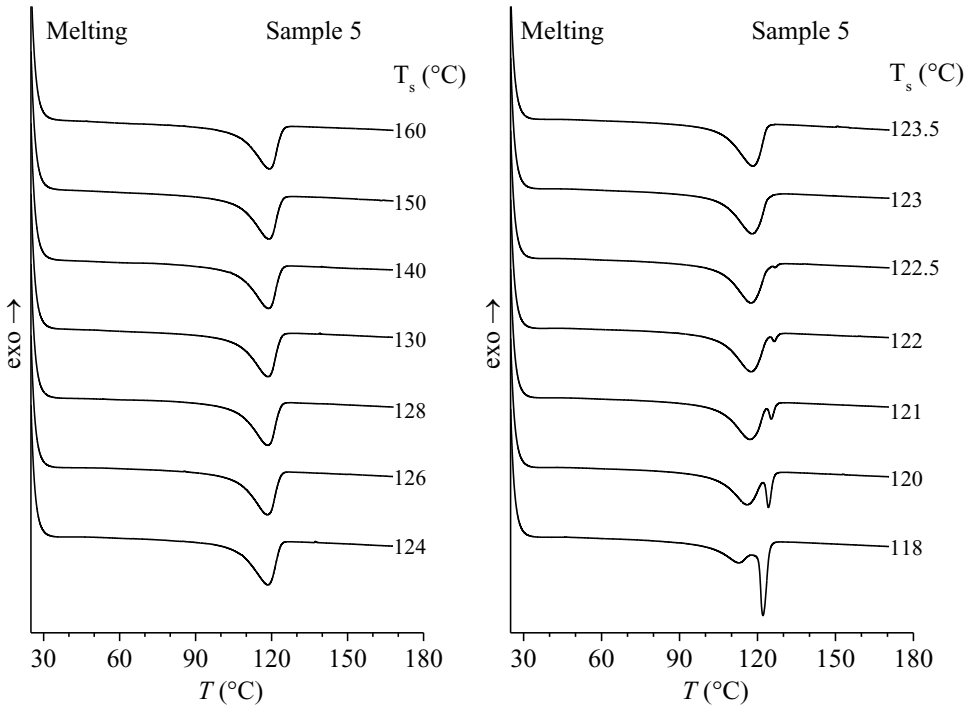

Figure A3-42. SNA DSC subsequent heating curves for the selected T_s recorded for the commercial grade Sample 5.

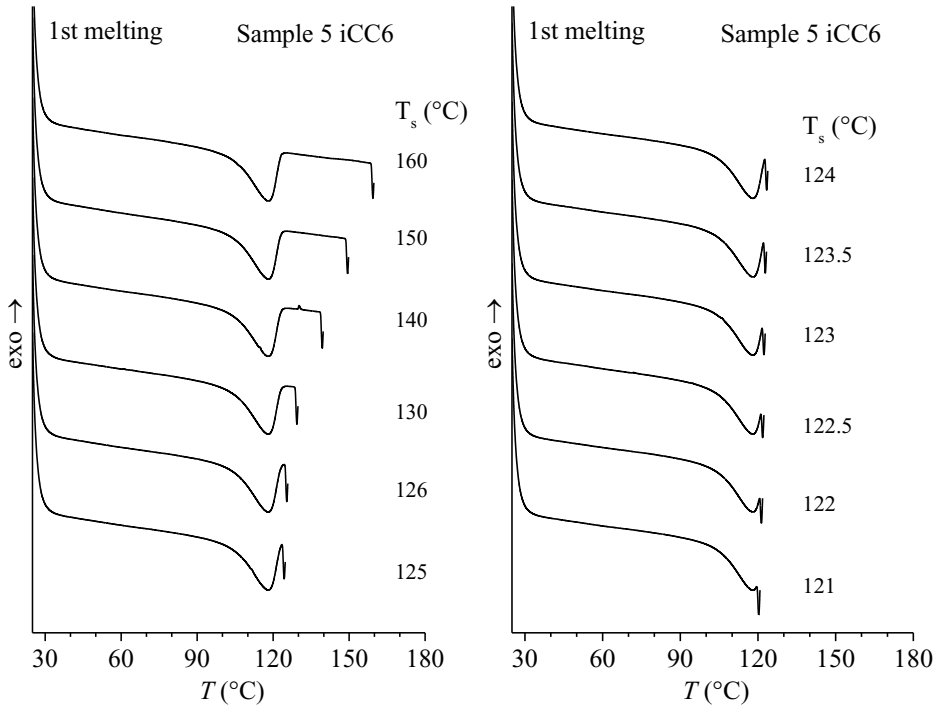

Figure A3-43. SNA DSC heating curves up to the selected T_s recorded for the iCC6 fraction of the commercial grade Sample 5.

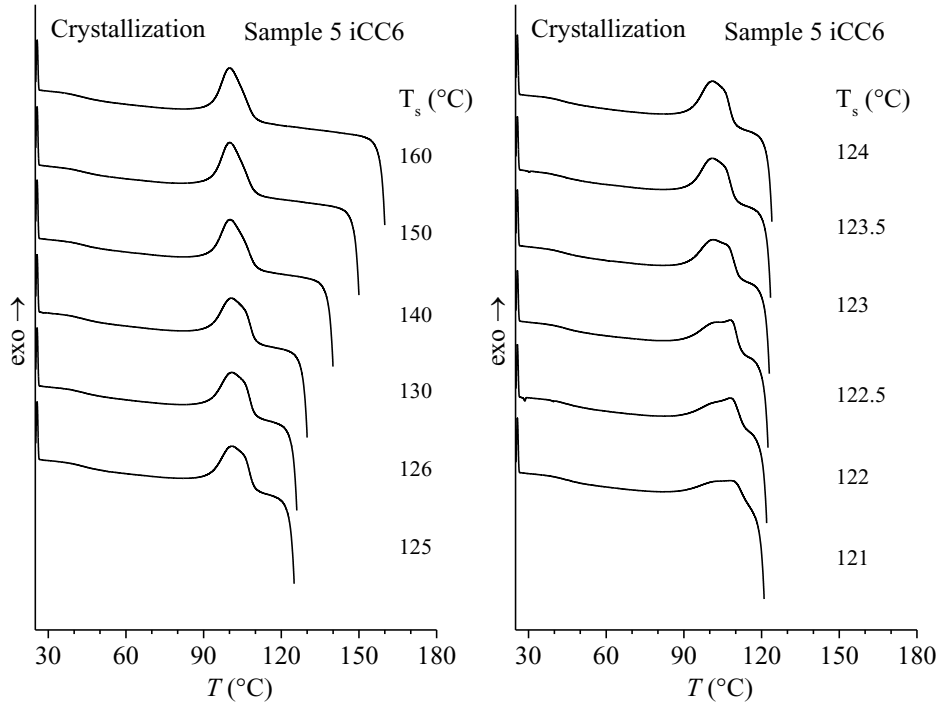

Figure A3-44. SNA DSC cooling curves from the selected T_s recorded for the iCC6 fraction of the commercial grade Sample 5.

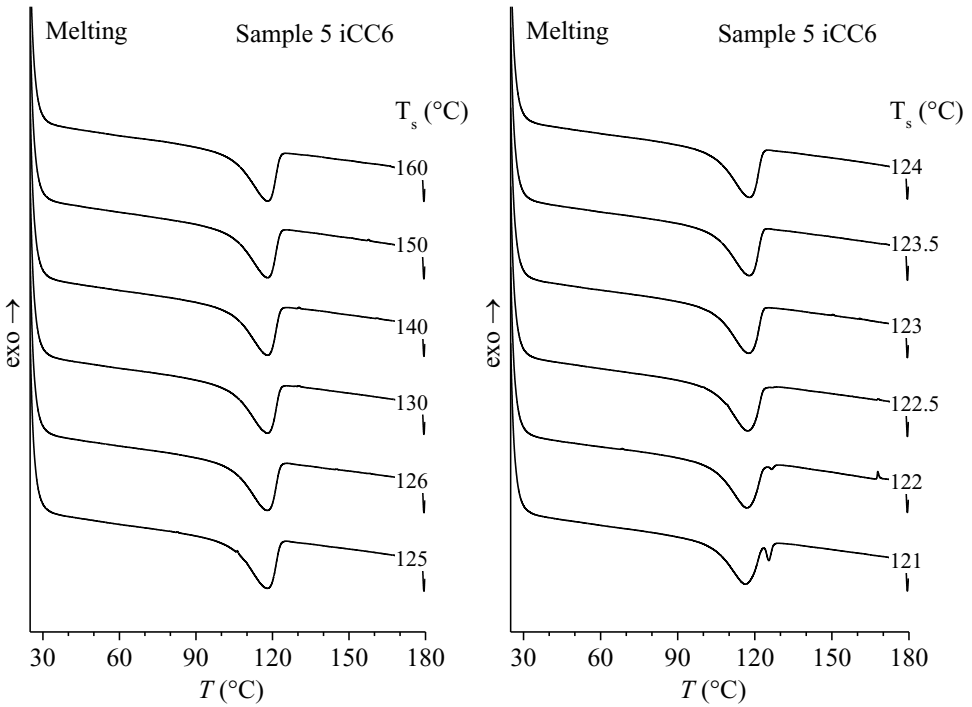

Figure A3-45. SNA DSC subsequent heating curves for the selected T_s recorded for the iCC6 fraction of the commercial grade Sample 5.

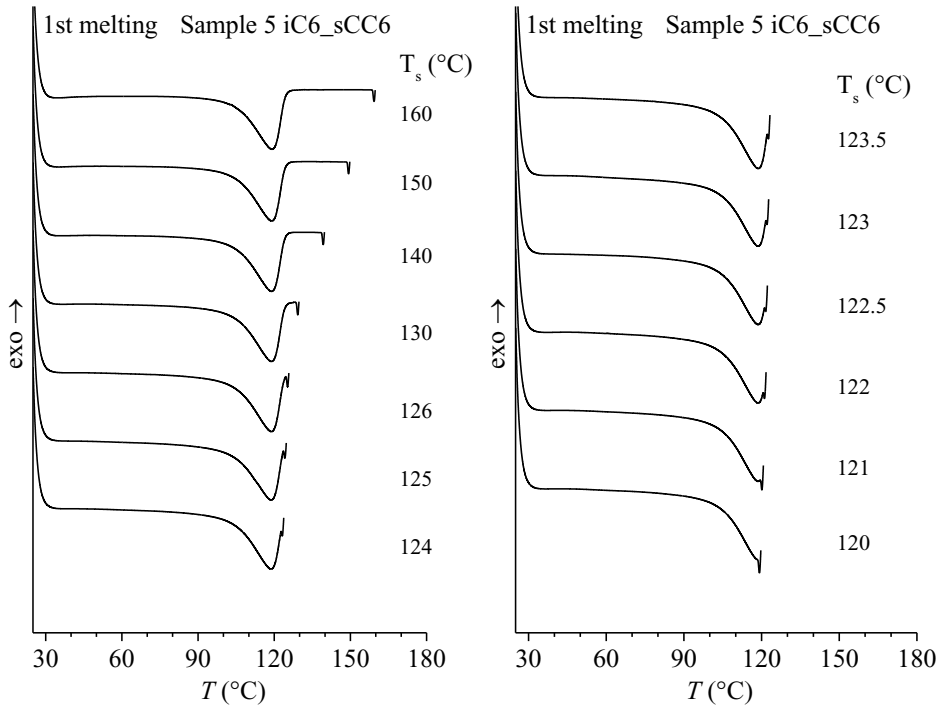

Figure A3-46. SNA DSC heating curves up to the selected T_s recorded for the iC6-sCC6 fraction of the commercial grade Sample 5.

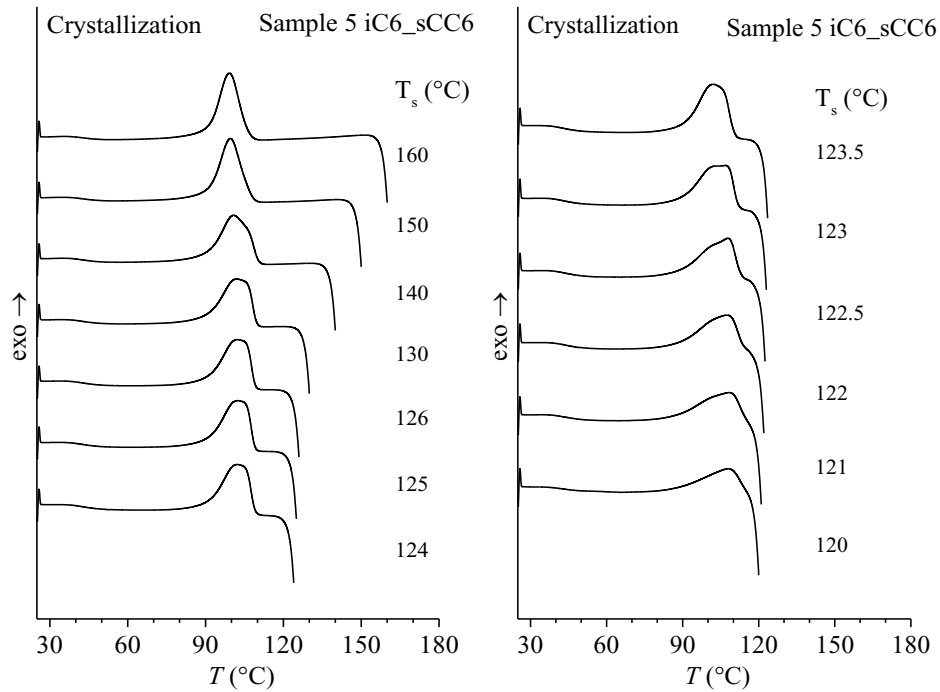

Figure A3-47. SNA DSC cooling curves from the selected T_s recorded for the iC6-sCC6 fraction of the commercial grade Sample 5.

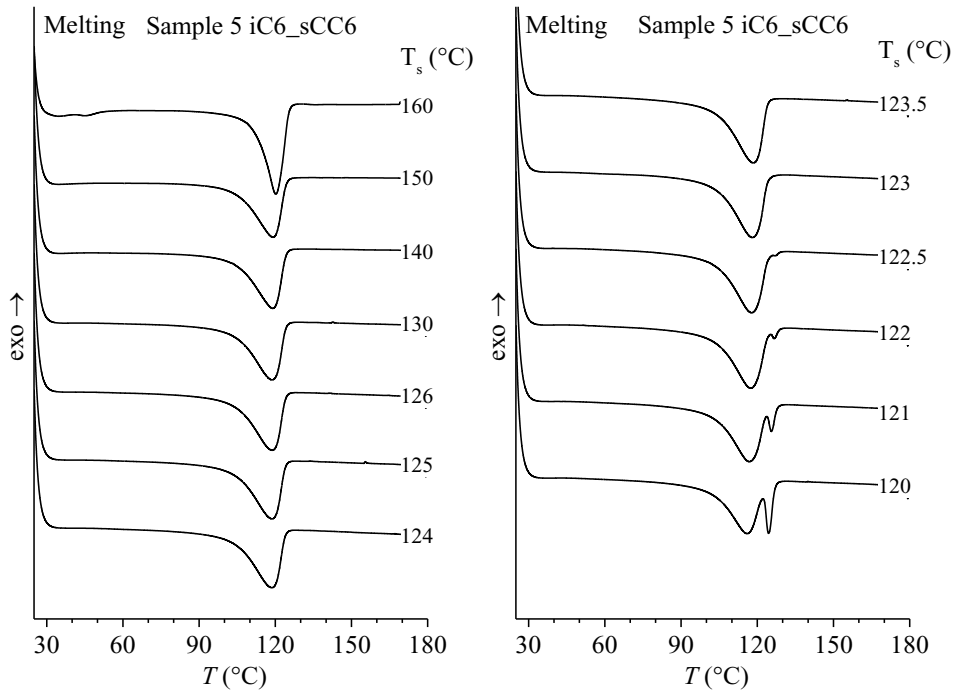

Figure A3-48. SNA DSC subsequent heating curves for the selected T_s recorded for the iC6-sCC6 fraction of the commercial grade Sample 5.

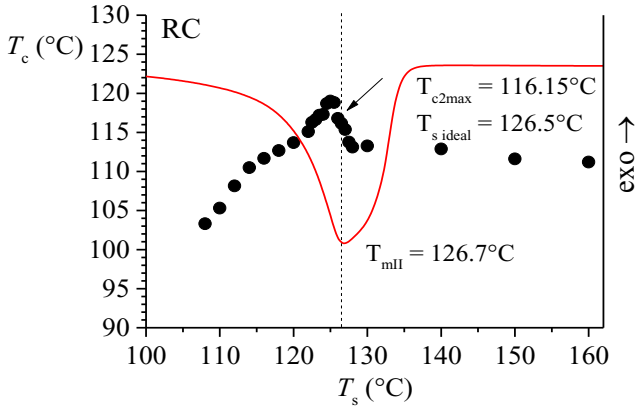
RC
T_c (°C)
T_s (°C)
T_{c2max} = 116.15°C
$T_{s\ ideal}$ = 126.5°C
T_{mII} = 126.7°C
exo

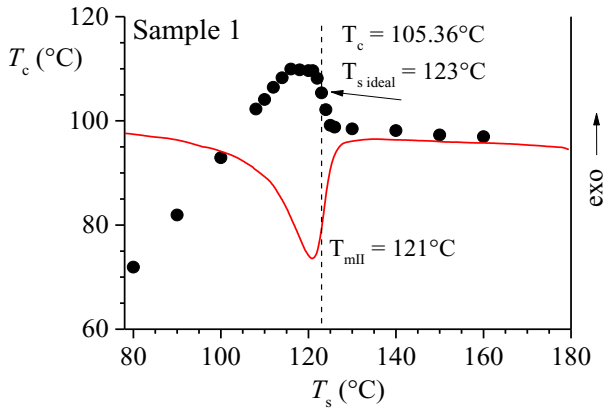
Sample 1
T_c (°C)
T_s (°C)
T_c = 105.36°C
$T_{s\ ideal}$ = 123°C
T_{mII} = 121°C
exo

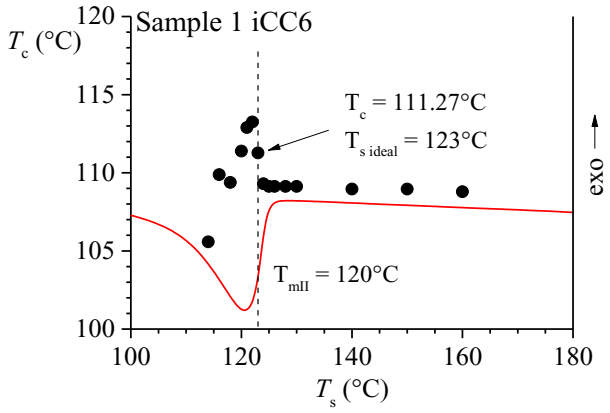
Sample 1 iCC6
T_c (°C)
T_s (°C)
T_c = 111.27°C
$T_{s\ ideal}$ = 123°C
T_{mII} = 120°C
exo

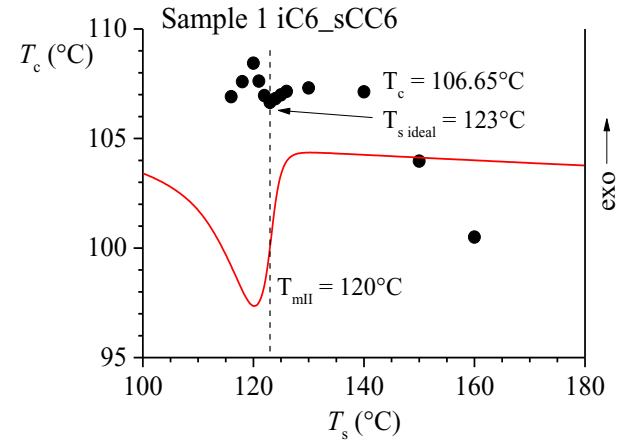
Sample 1 iC6_sCC6
T_c (°C)
T_s (°C)
T_c = 106.65°C
$T_{s\ ideal}$ = 123°C
T_{mII} = 120°C
exo
110
105
100
95
100
120
140
160
180

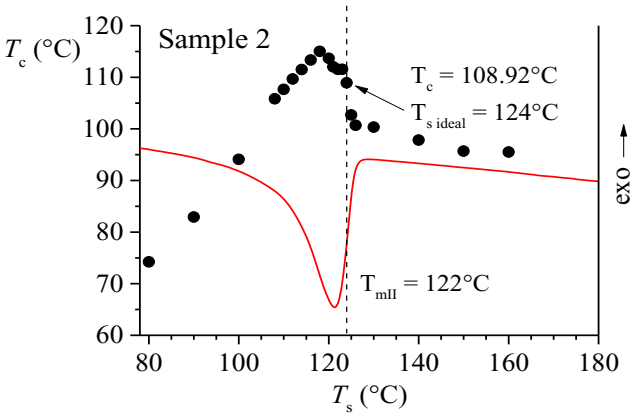
Sample 2
T_c (°C)
T_s (°C)
T_c = 108.92°C
$T_{s\ ideal}$ = 124°C
T_{mII} = 122°C
exo
120
110
100
90
80
70
60
80
100
120
140
160
180

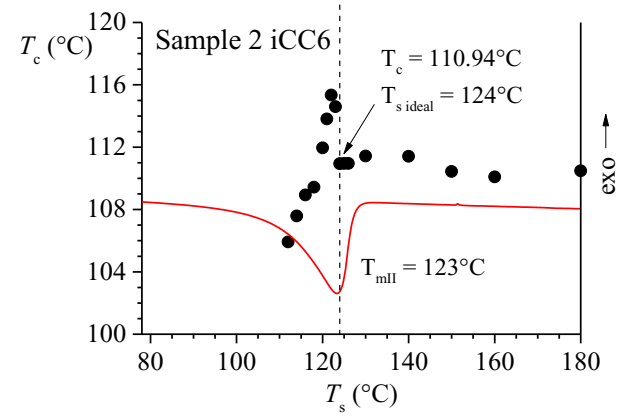
Sample 2 iCC6
T_c (°C)
T_s (°C)
T_c = 110.94°C
$T_{s\ ideal}$ = 124°C
T_{mII} = 123°C
exo
120
116
112
108
104
100
80
100
120
140
160
180

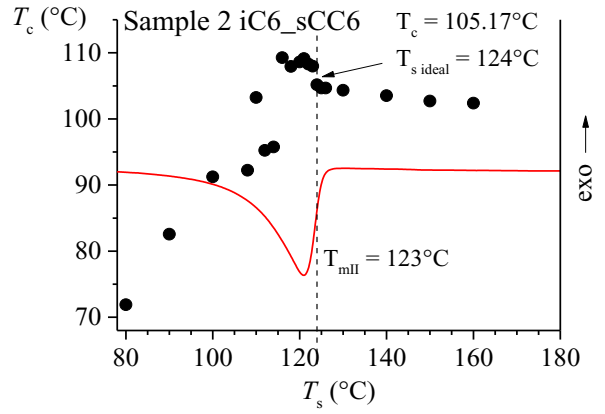
Sample 2 iC6_sCC6
T_c (°C)
T_s (°C)
T_c = 105.17°C
$T_{s\ ideal}$ = 124°C
T_{mII} = 123°C
exo

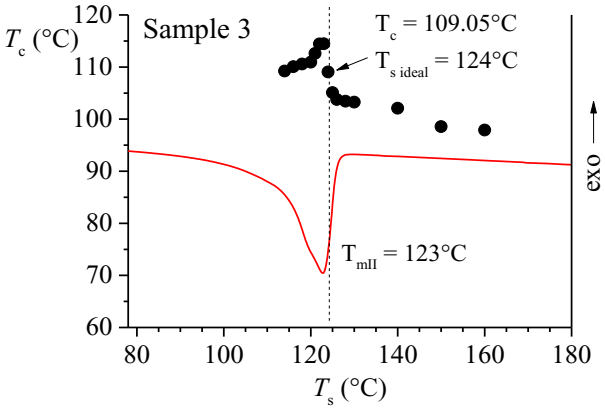
Sample 3
T_c (°C)
T_s (°C)
T_c = 109.05°C
$T_{s\ ideal}$ = 124°C
T_{mII} = 123°C
exo

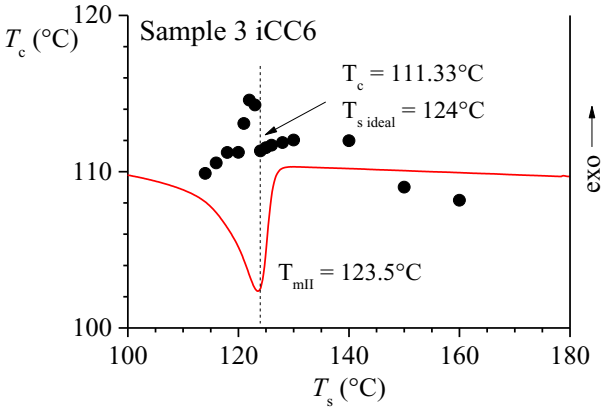
Sample 3 iCC6
T_c (°C)
T_s (°C)
T_c = 111.33°C
$T_{s\ ideal}$ = 124°C
T_{mII} = 123.5°C
exo

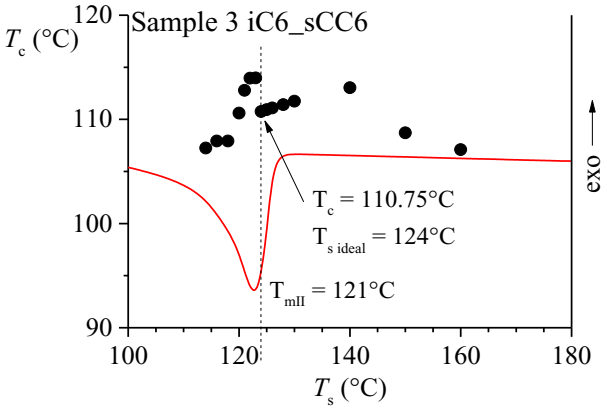
Sample 3 iC6_sCC6
T_c (°C)
T_s (°C)
T_c = 110.75°C
$T_{s\ ideal}$ = 124°C
T_{mII} = 121°C
exo
120
110
100
90
100
120
140
160
180

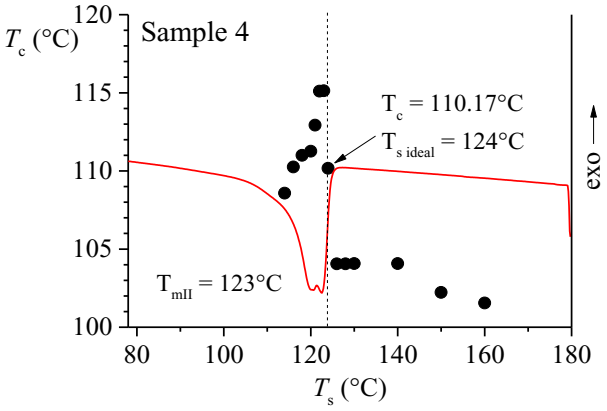
Sample 4
T_c (°C)
T_s (°C)
T_c = 110.17°C
$T_{s\ ideal}$ = 124°C
T_{mII} = 123°C
exo
120
115
110
105
100
80
100
120
140
160
180

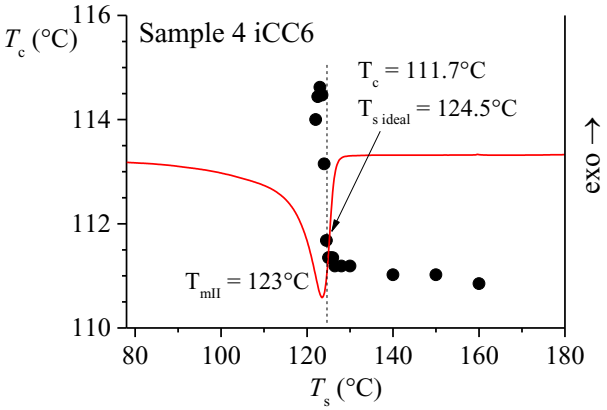
Sample 4 iCC6
T_c (°C)
T_s (°C)
T_c = 111.7°C
$T_{s\ ideal}$ = 124.5°C
T_{mII} = 123°C
exo
116
114
112
110
80
100
120
140
160
180

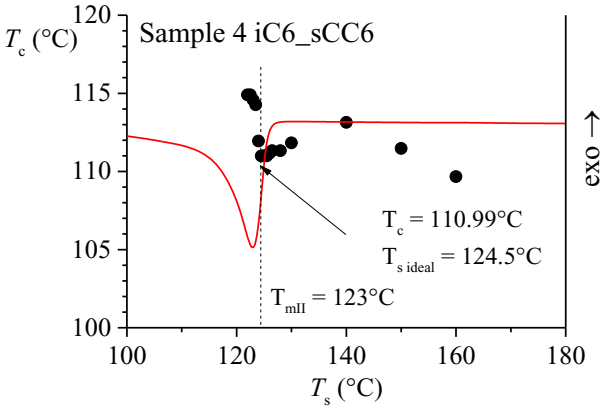
Sample 4 iC6_sCC6
T_c (°C)
T_s (°C)
120
115
110
105
100
100
120
140
160
180
T_c = 110.99°C
$T_{s\ ideal}$ = 124.5°C
T_{mII} = 123°C
← exo

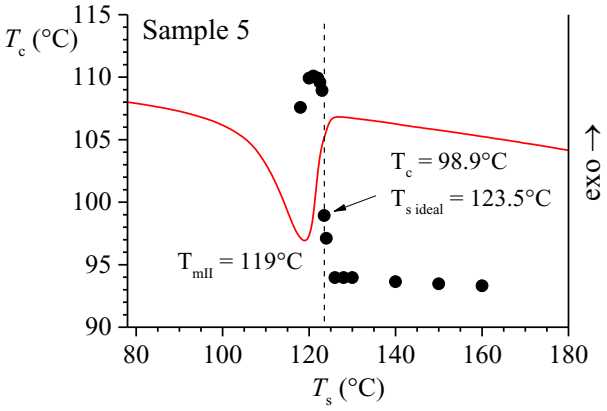
Sample 5
T_c (°C)
T_s (°C)
115
110
105
100
95
90
80
100
120
140
160
180
T_c = 98.9°C
$T_{s\ ideal}$ = 123.5°C
T_{mII} = 119°C
← exo

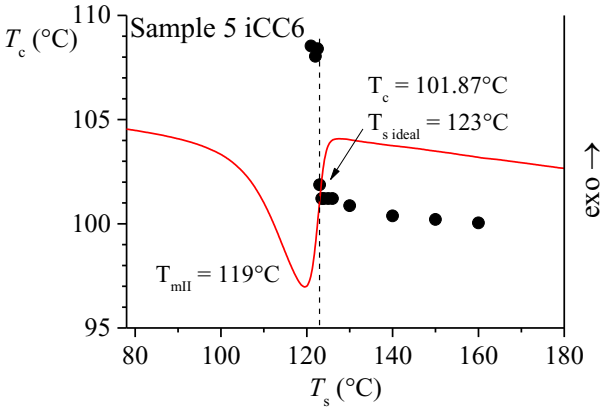
Sample 5 iCC6
T_c (°C)
T_s (°C)
110
105
100
95
80
100
120
140
160
180
T_c = 101.87°C
$T_{s\ ideal}$ = 123°C
T_{mII} = 119°C
← exo

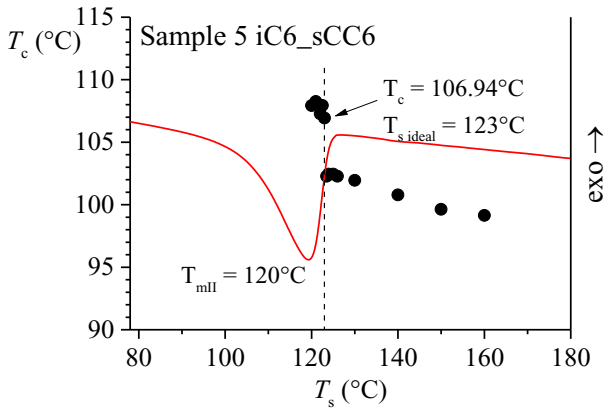

Figure A3-49. Crystallization temperatures T_c as a function of the seeding temperature T_s for the ethylene/1-octene random copolymer RC taken as reference and for the commercial grades Samples 1, 2, 3, 4, and 5 and their corresponding iCC6 and iC6-sCC6 fractions. Ideal self-seeding temperatures $T_{s\ ideal}$ and corresponding crystallization temperatures T_c are also reported; in addition, the standard DSC melting curve recorded at 10°C/min is reported as red trace, along with the melting temperature T_m.

Appendix A4

Successive Self-Nucleation and Annealing (SSA)

The DSC thermograms recorded during the SSA protocol for the Samples 1-5, their corresponding superior iC6-sCC6 and iCC6 fractions, and the random copolymer RC are reported in Figures A4 1-16. In particular, for each sample, the heating and cooling scans to create the standard crystalline state, the curves recorded heating from 25°C up to the ideal self-seeding temperature $T_{s\ ideal}$ and the subsequent cooling scans down to room temperature are reported, along with the curves recorded heating to increasingly lower T_s and the subsequent cooling curves. The heating and cooling scan rate is 10°C/min.

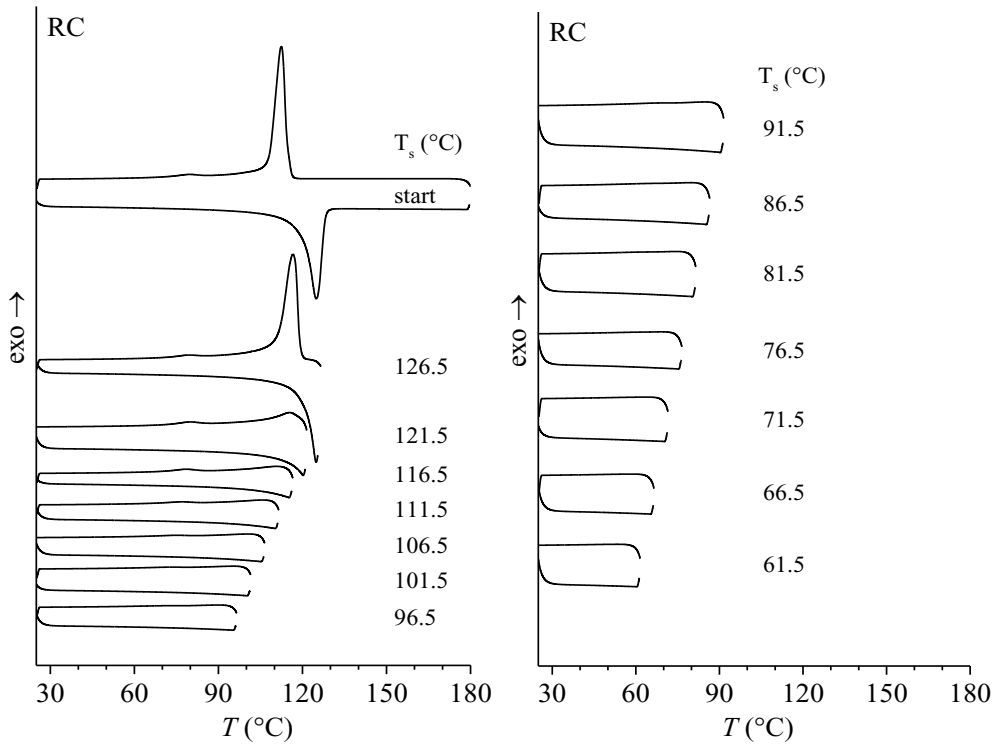

Figure A4-1. DSC thermograms recorded during the SSA protocol at the different self-seeding temperatures T_s for the random copolymer RC selected as benchmark.

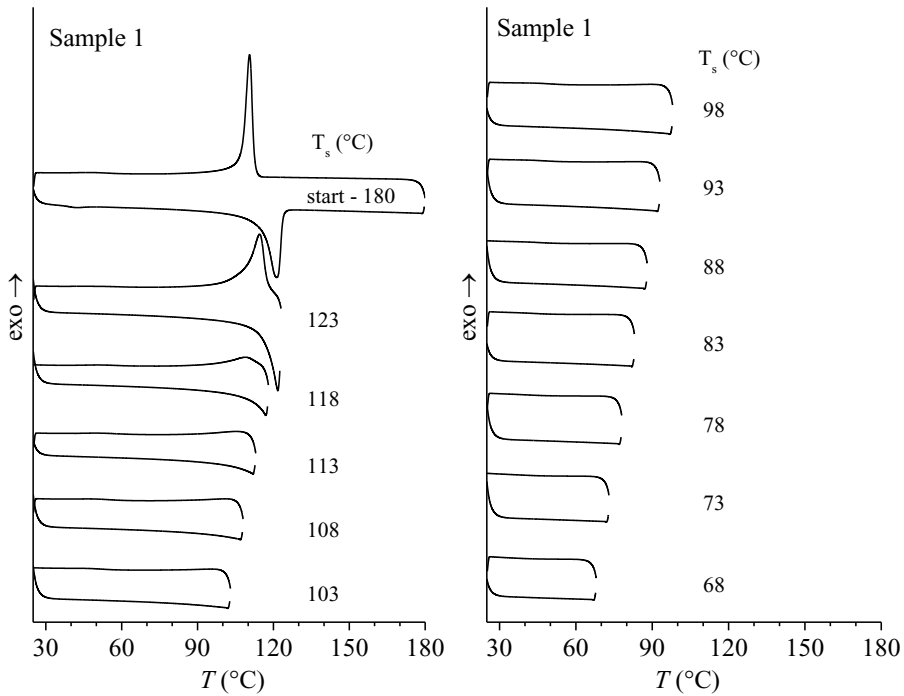

Figure A4-2. DSC thermograms recorded during the SSA protocol at the different self-seeding temperatures T_s for the commercial grade Sample 1.

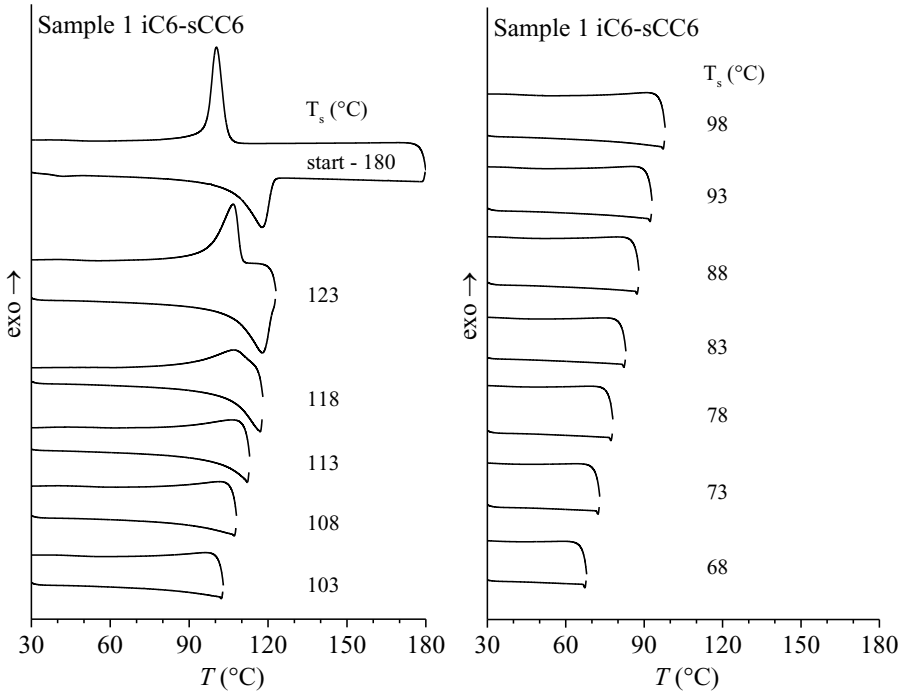

Figure A4-3. DSC thermograms recorded during the SSA protocol at the different self-seeding temperatures T_s for the iC6-sCC6 fraction of the commercial grade Sample 1.

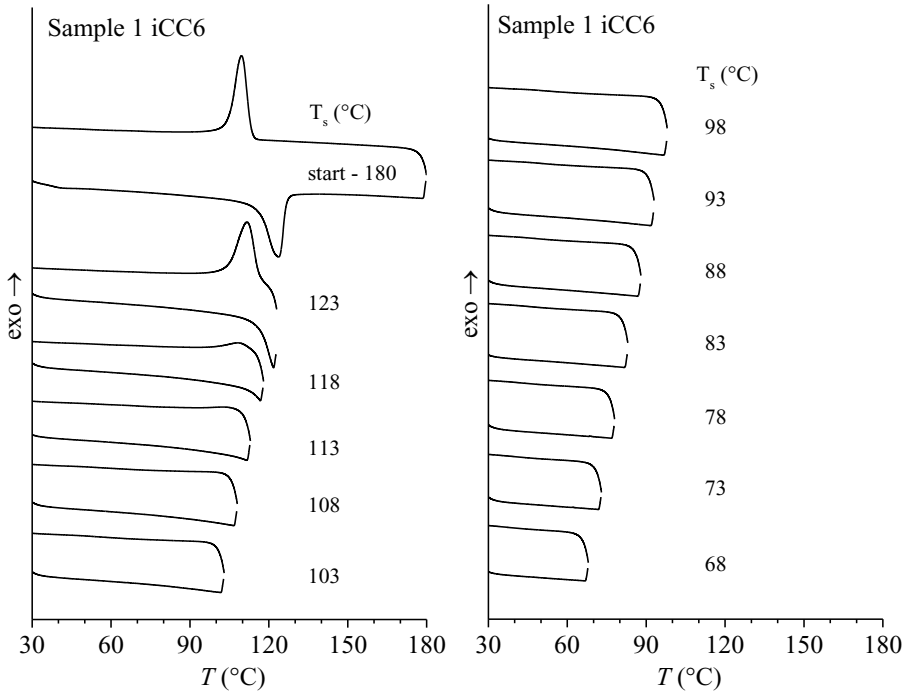

Figure A4-4. DSC thermograms recorded during the SSA protocol at the different self-seeding temperatures T_s for the iCC6 fraction of the commercial grade Sample 1.

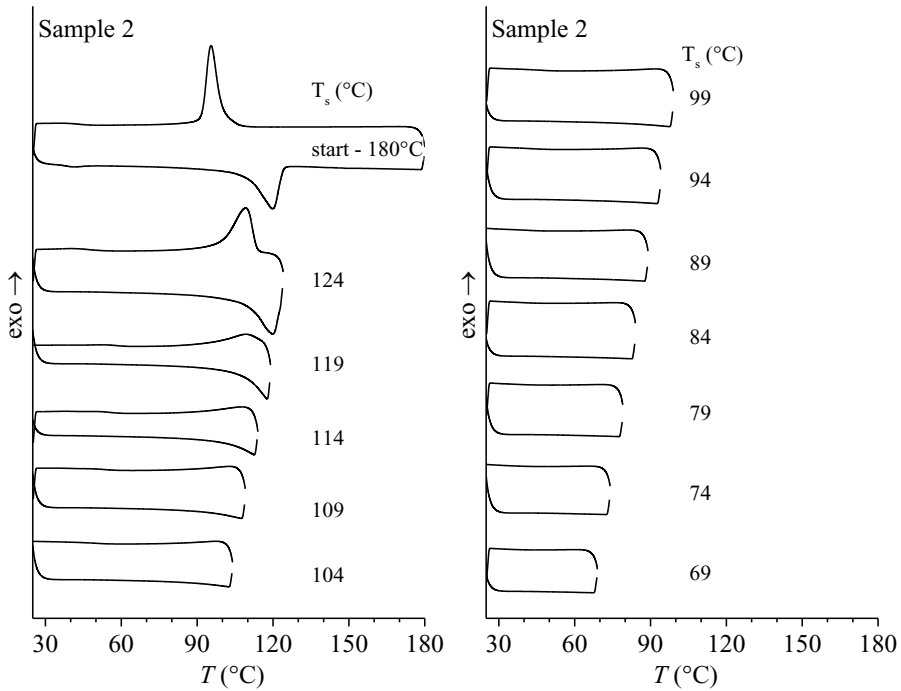

Figure A4-5. DSC thermograms recorded during the SSA protocol at the different self-seeding temperatures T_s for the commercial grade Sample 2.

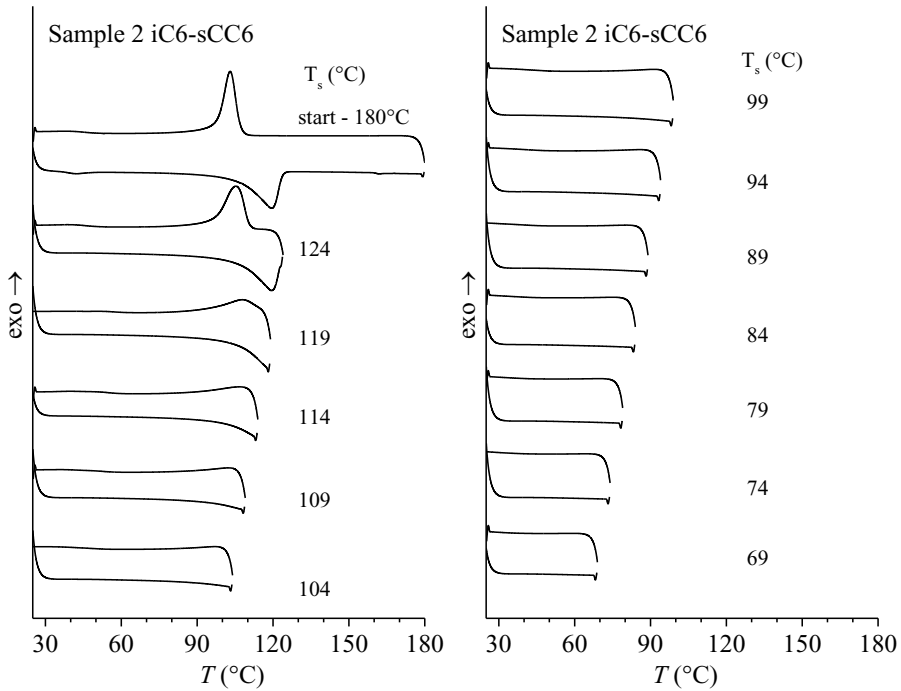

Figure A4-6. DSC thermograms recorded during the SSA protocol at the different self-seeding temperatures T_s for the iC6-sCC6 fraction of the commercial grade Sample 2.

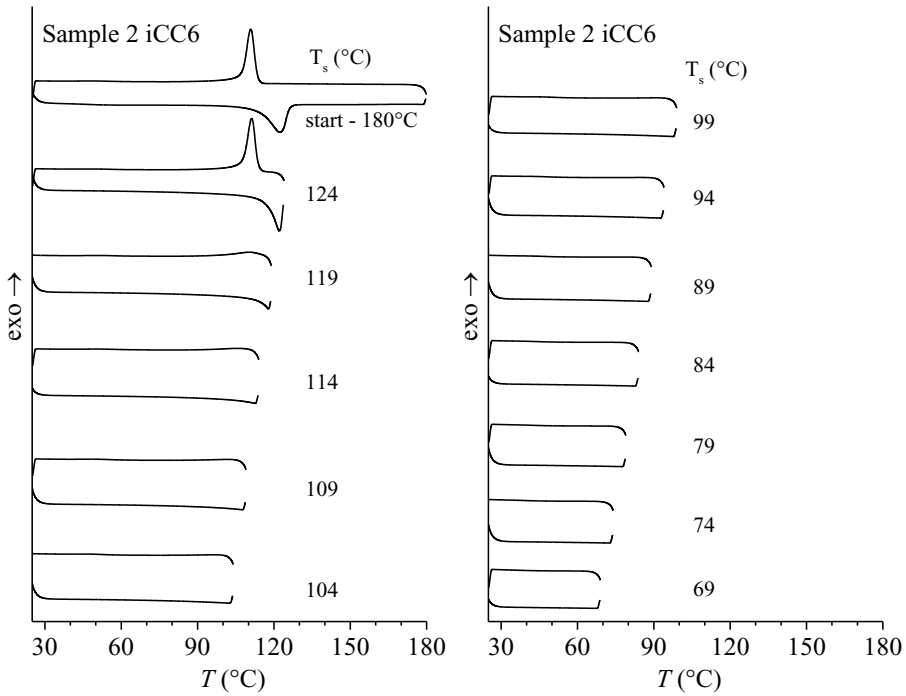

Figure A4-7. DSC thermograms recorded during the SSA protocol at the different self-seeding temperatures T_s for the iCC6 fraction of the commercial grade Sample 2.

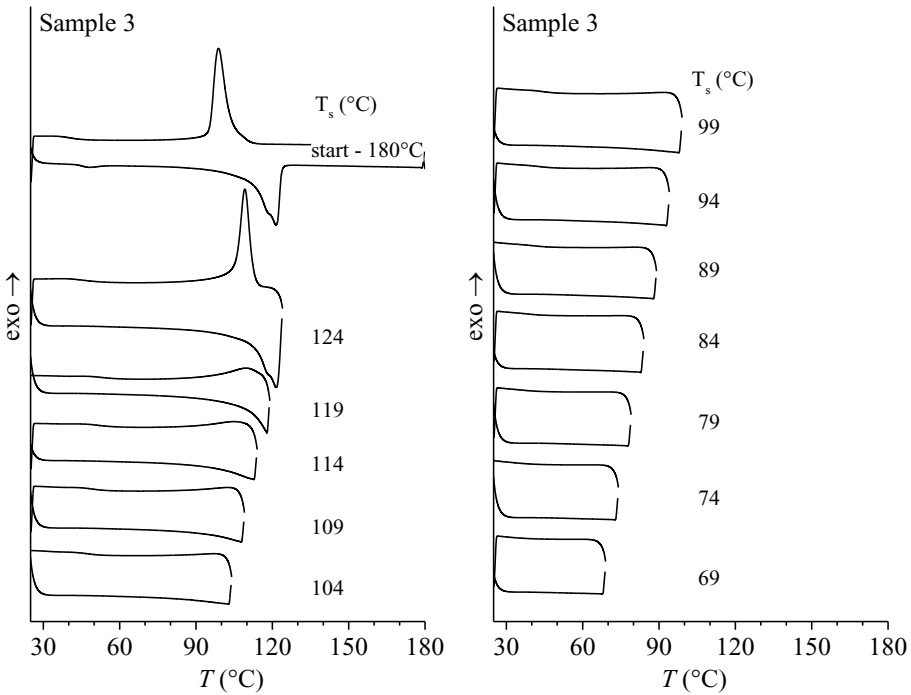

Figure A4-8. DSC thermograms recorded during the SSA protocol at the different self-seeding temperatures T_s for the commercial grade Sample 3.

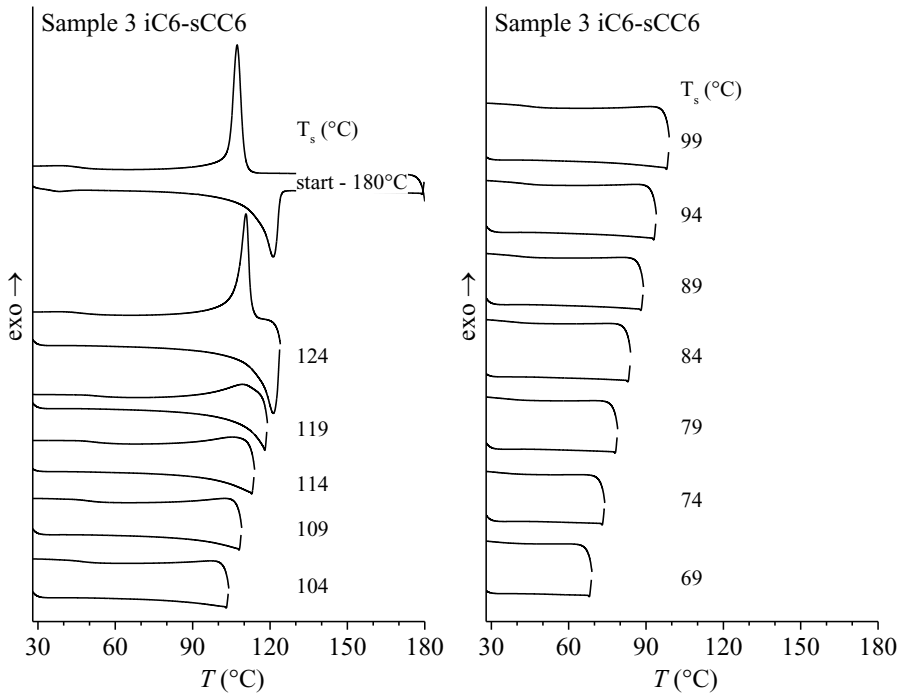

Figure A4-9. DSC thermograms recorded during the SSA protocol at the different self-seeding temperatures T_s for the iC6-sCC6 fraction of the commercial grade Sample 3.

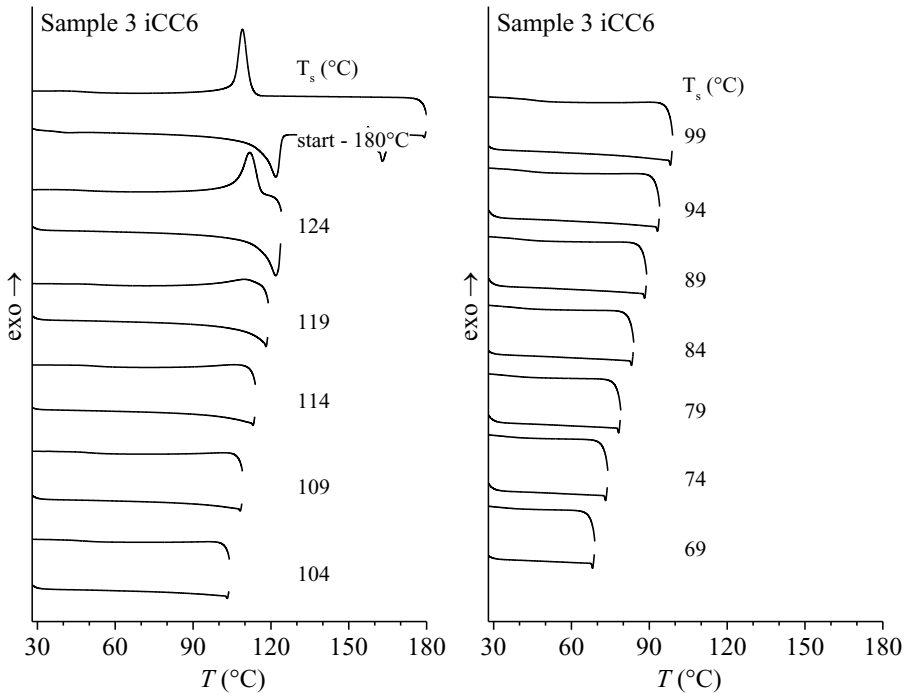

Figure A4-10. DSC thermograms recorded during the SSA protocol at the different self-seeding temperatures T_s for the iCC6 fraction of the commercial grade Sample 3.

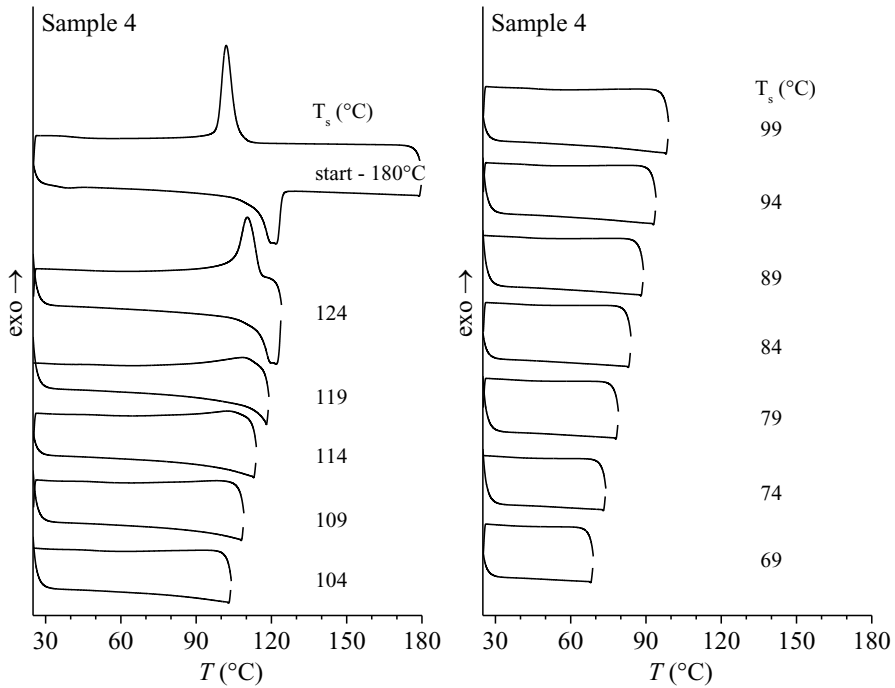

Figure A4-11. DSC thermograms recorded during the SSA protocol at the different self-seeding temperatures T_s for the commercial grade Sample 4.

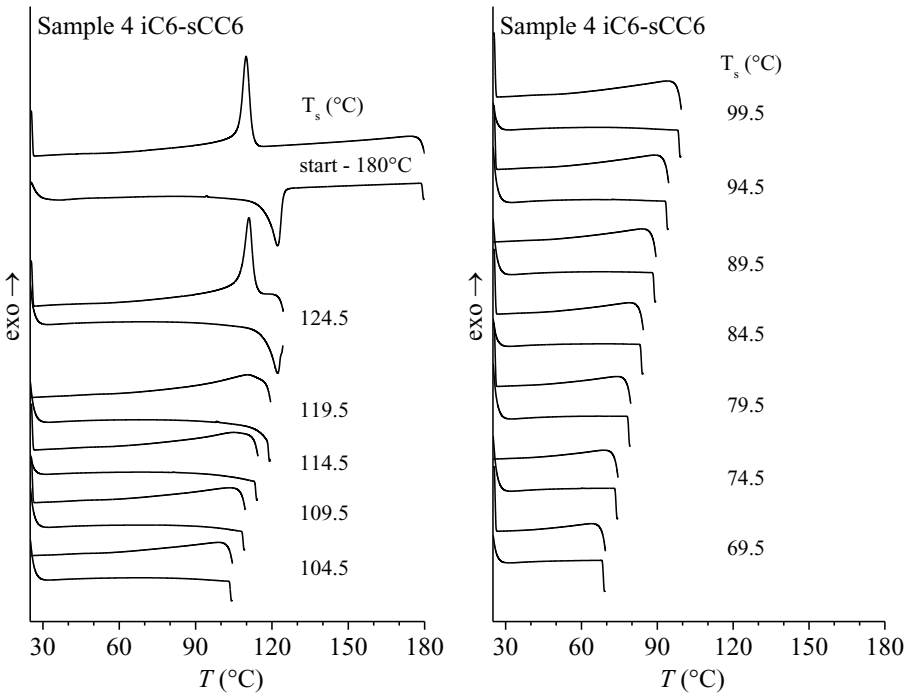

Figure A4-12. DSC thermograms recorded during the SSA protocol at the different self-seeding temperatures T_s for the iC6-sCC6 fraction of the commercial grade Sample 4.

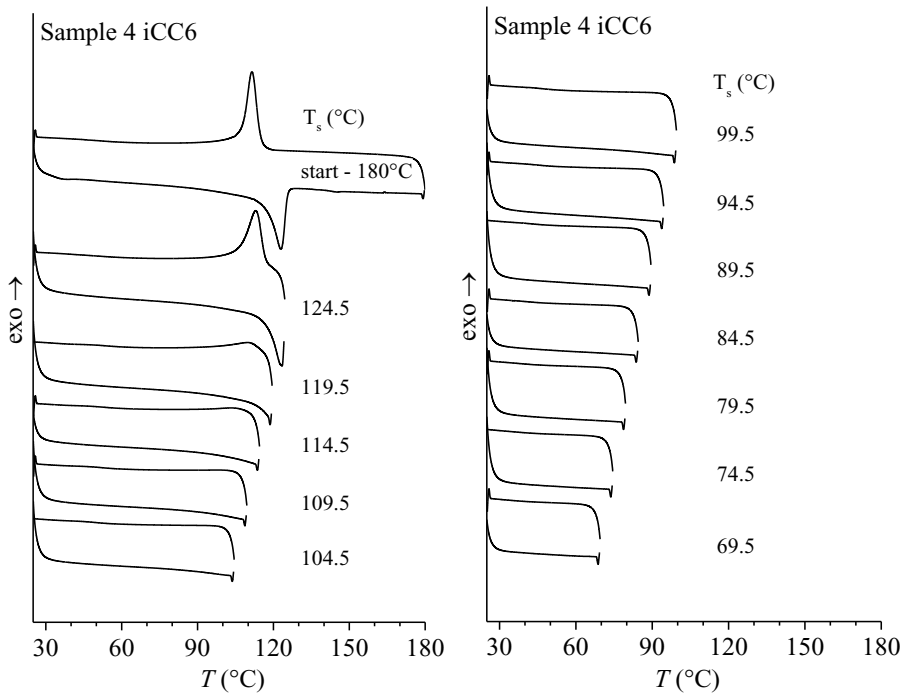

Figure A4-13. DSC thermograms recorded during the SSA protocol at the different self-seeding temperatures T_s for the iCC6 fraction of the commercial grade Sample 4.

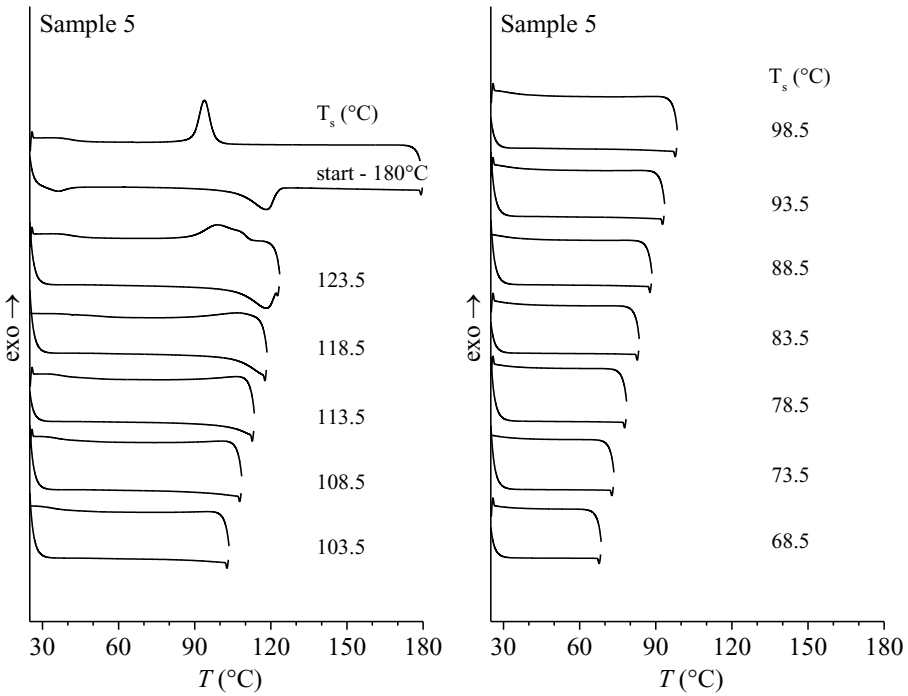

Figure A4-14. DSC thermograms recorded during the SSA protocol at the different self-seeding temperatures T_s for the commercial grade Sample 5.

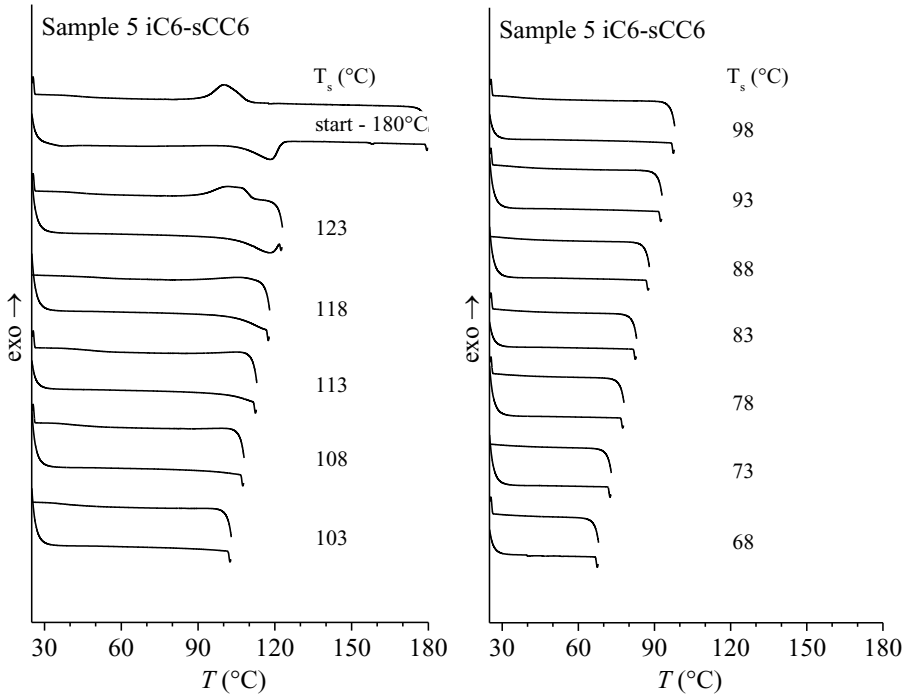

Figure A4-15. DSC thermograms recorded during the SSA protocol at the different self-seeding temperatures T_s for the iC6-sCC6 fraction of the commercial grade Sample 5.

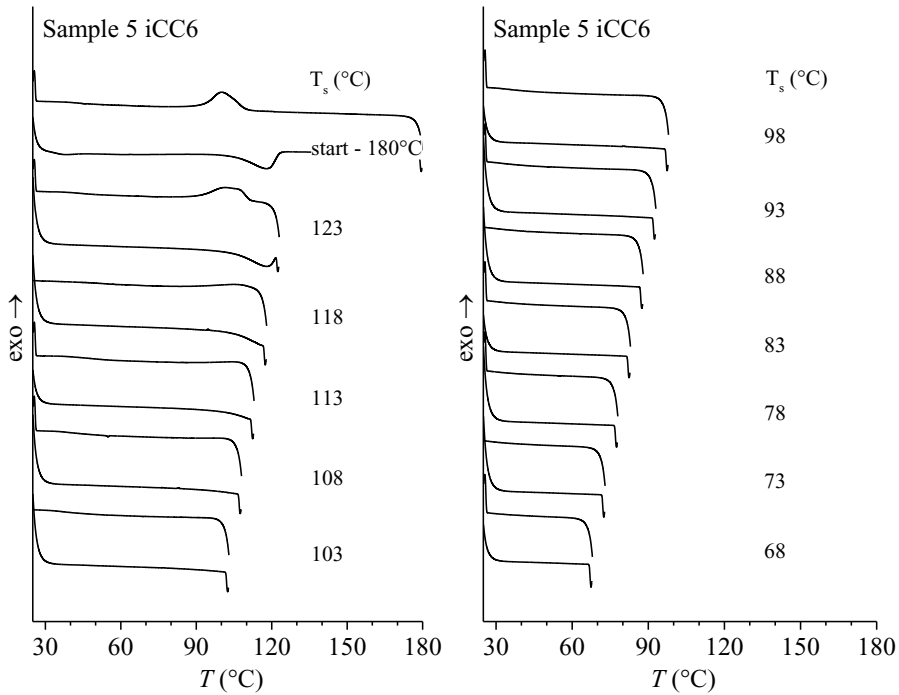

Figure A4-16. DSC thermograms recorded during the SSA protocol at the different self-seeding temperatures T_s for the iCC6 fraction of the commercial grade Sample 5.

Appendix A5

Solution ^{13}C NMR and GPC analysis for the OBCs synthetized in the PPR

Ethylene/1-hexene OBCs at Δhex ≈ 20 mol% and w_s/w_h ≈ 80/20

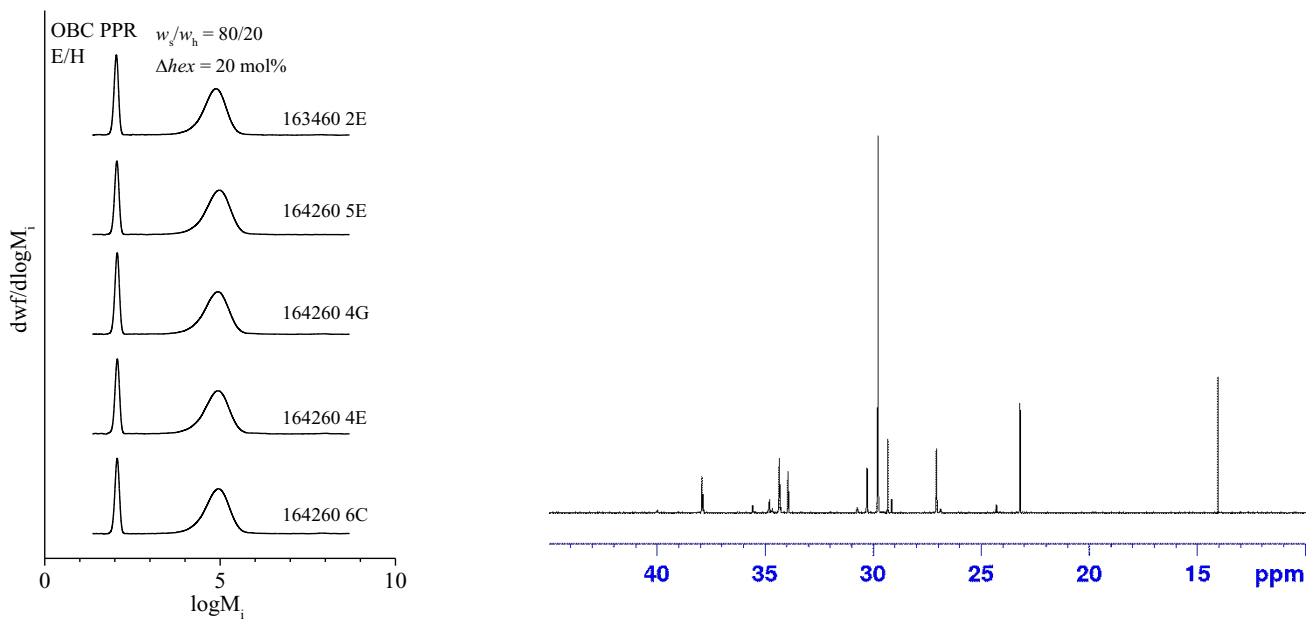

Figure A5-1. GPC traces and ^{13}C solution NMR spectra for the ethylene/1-hexene OBCs with Δ*hex* ≈ 20 mol% and w_s/w_h ≈ 80/20. The NMR spectrum is shown only for a representative sample.

Ethylene/1-hexene OBCs at Δhex ≈ 20 mol% and w_s/w_h ≈ 50/50

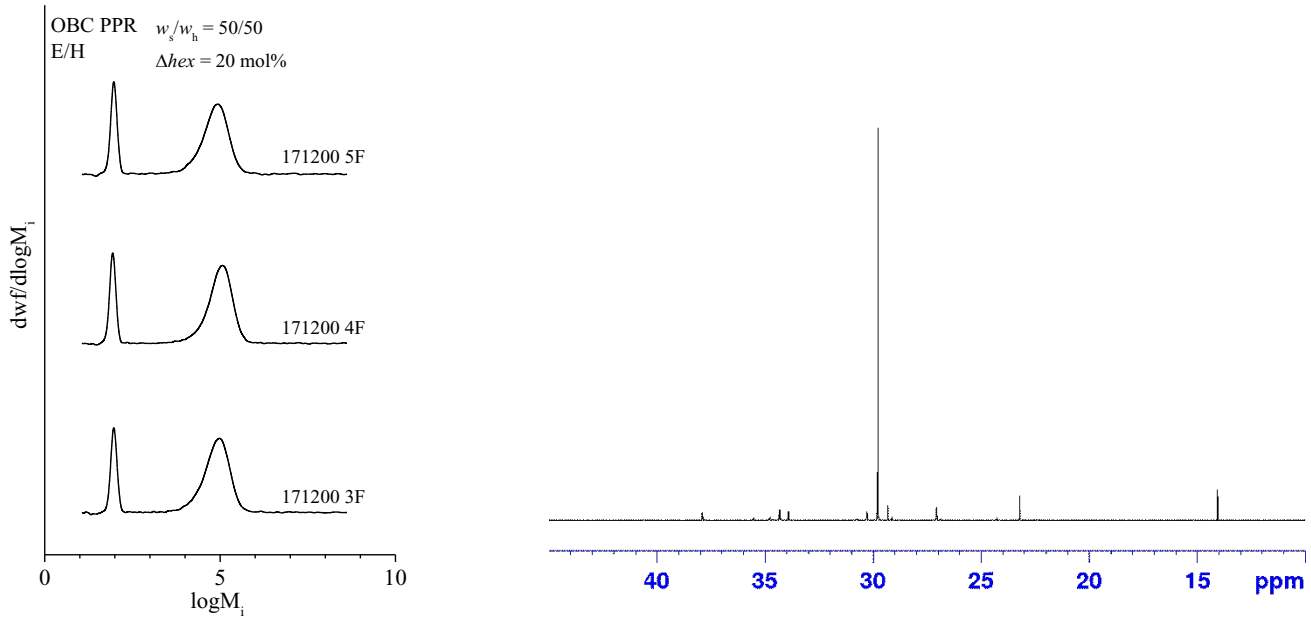

Figure A5-2. GPC traces and ^{13}C solution NMR spectra for the ethylene/1-hexene OBCs with Δ*hex* ≈ 20 mol% and w_s/w_h ≈ 50/50. The NMR spectrum is shown only for a representative sample.

Ethylene/1-hexene OBCs at Δhex ≈ 30 mol% and varying w_s/w_h

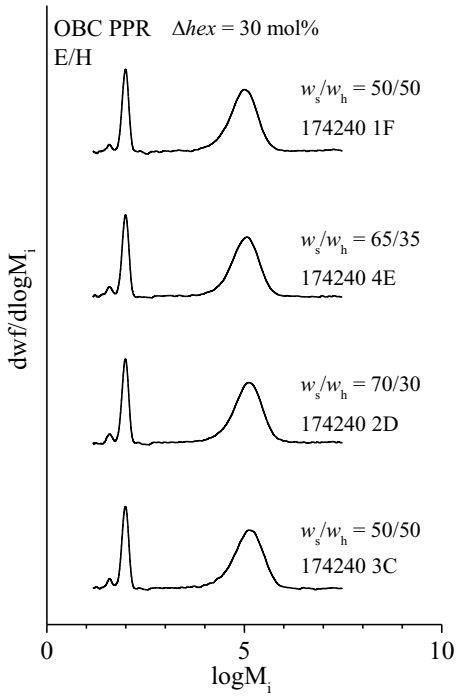

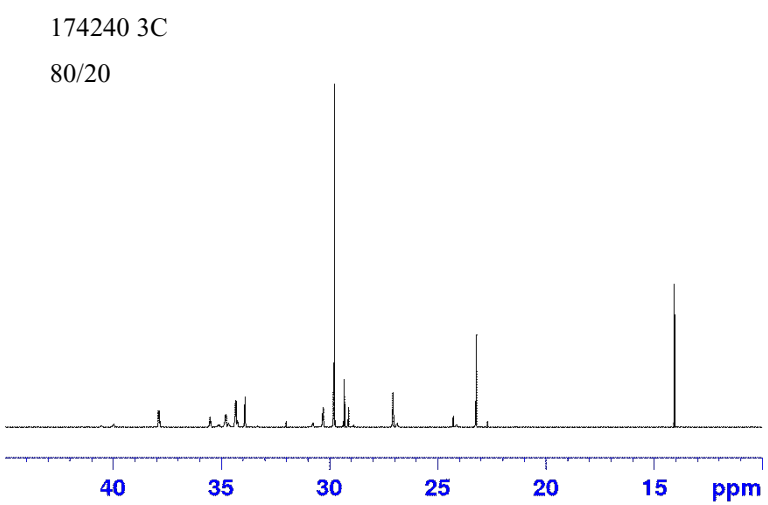

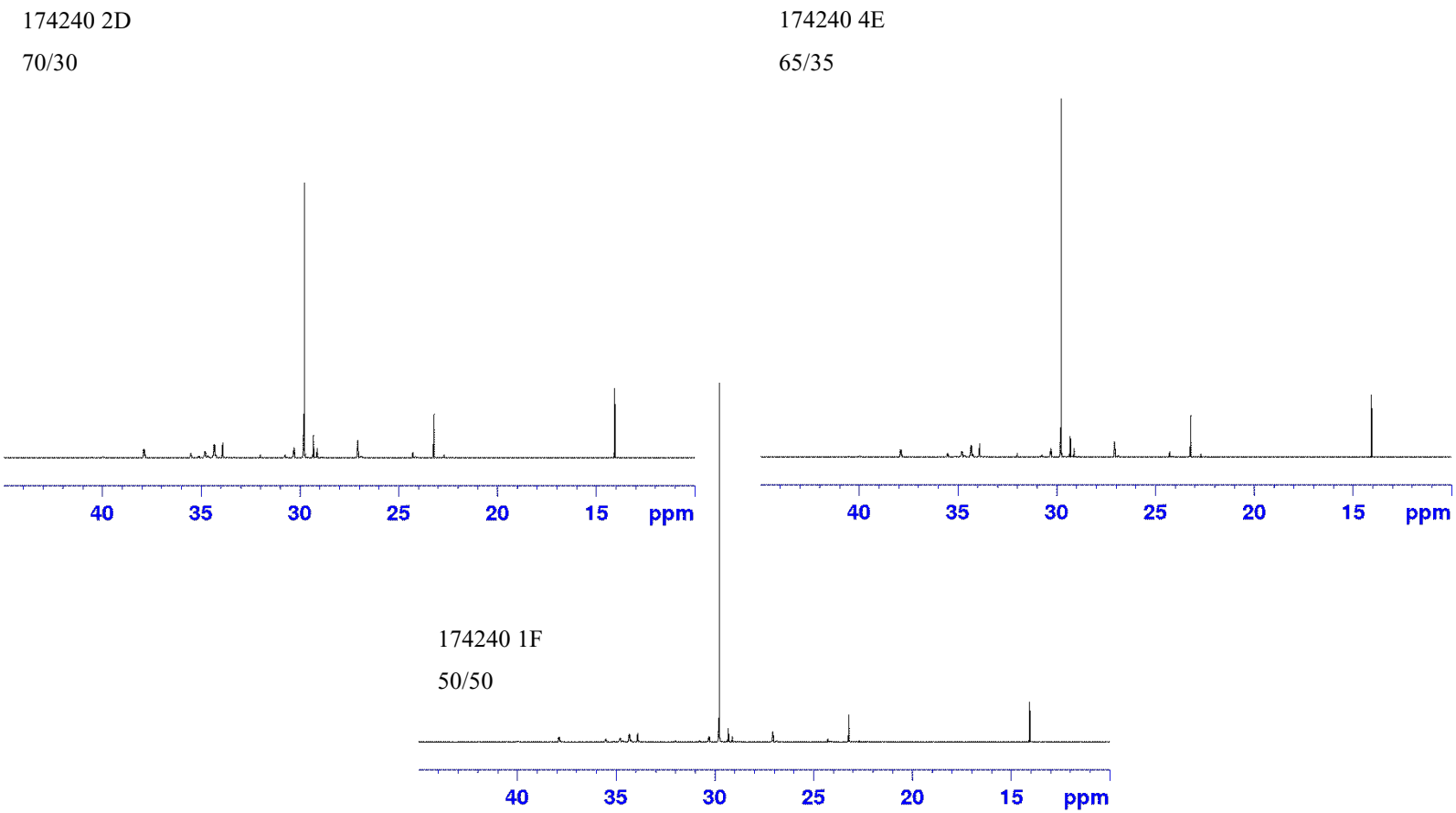

Figure A5-3. GPC traces and ^{13}C solution NMR spectra for the ethylene/1-hexene OBCs with $\Delta hex \approx 30$ mol% and $w_s/w_h \approx 80/20$, 70/30, 65/35, and 50/50.

Ethylene/4-methyl-1-pentene OBCs

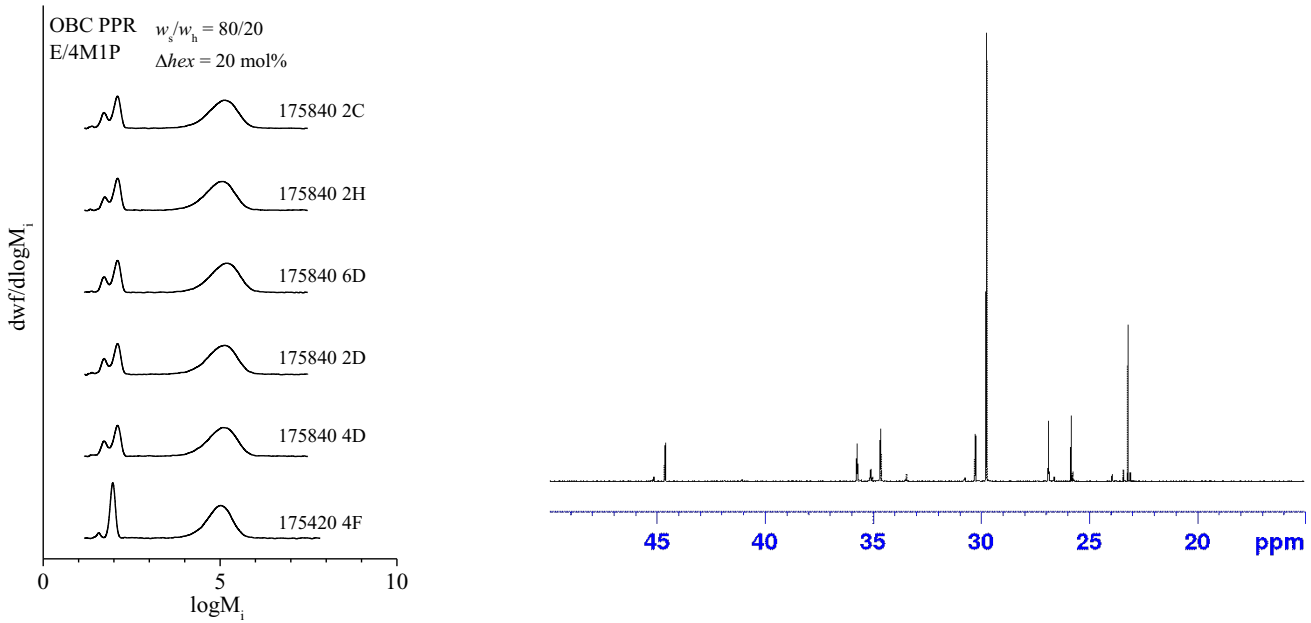

Figure A5-4. GPC traces and ^{13}C solution NMR spectra for the ethylene/4-methyl-1-pentene OBCs with Δ*hex* ≈ 20 mol% and w_s/w_h ≈ 80/20. The NMR spectrum is shown only for a representative sample.

Ethylene/1-hexadecene OBCs

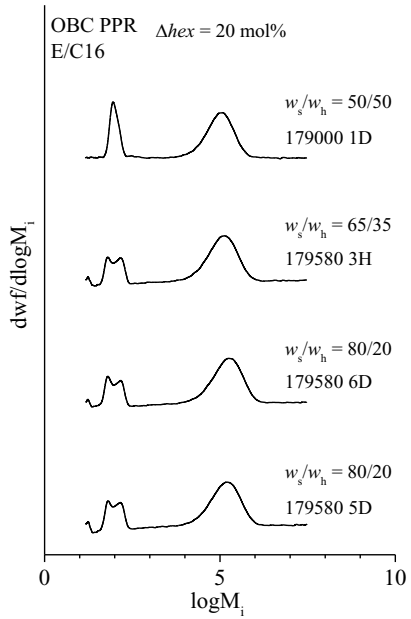

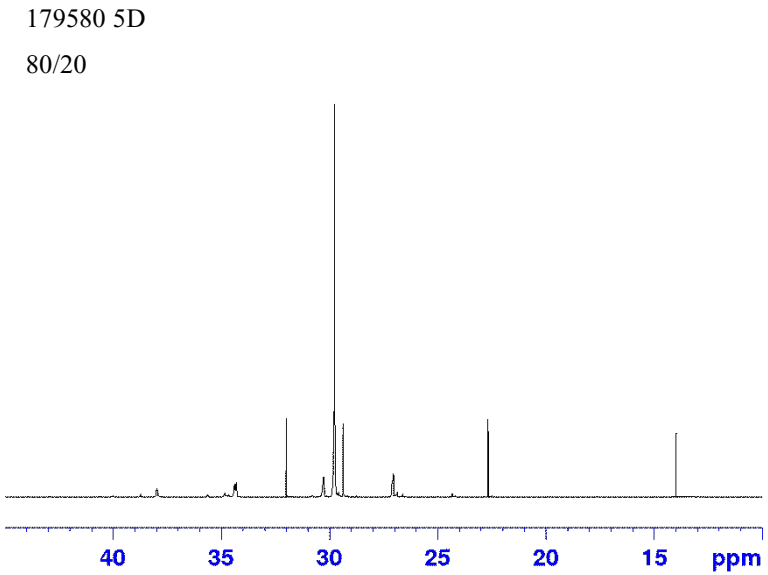

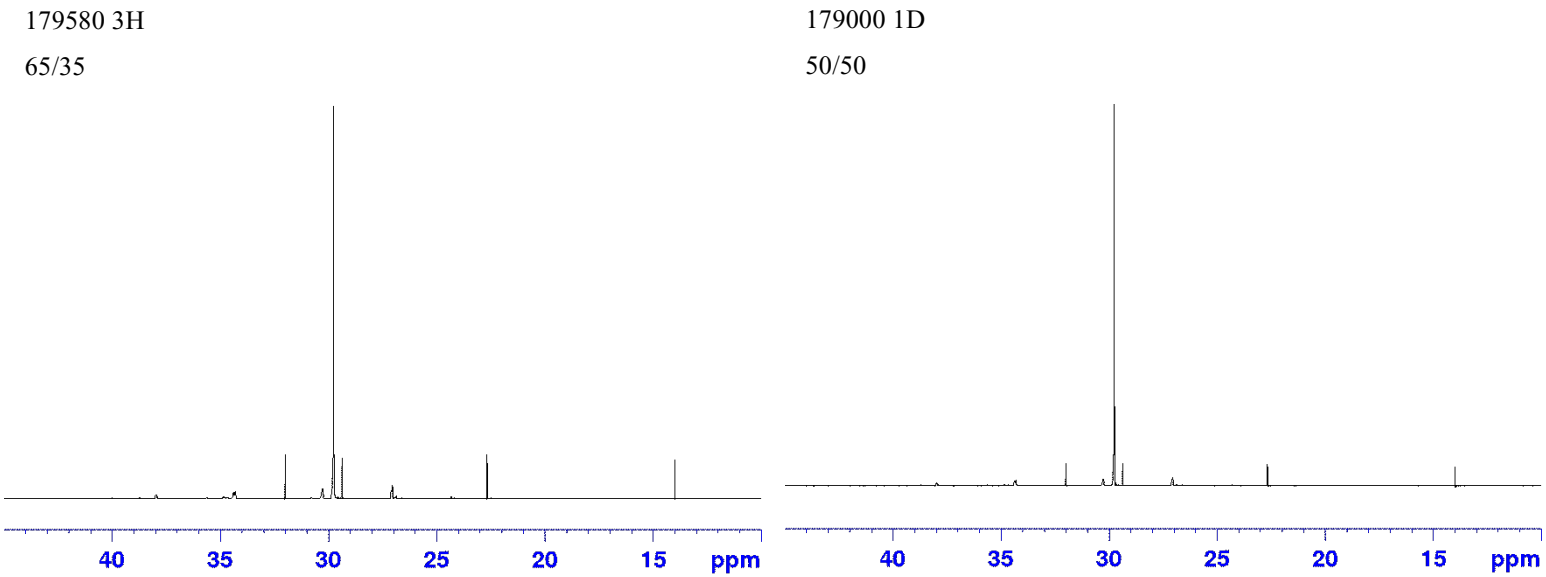

Figure A5-5. GPC traces and ^{13}C solution NMR spectra for the ethylene/1-hexadecene OBCs with $\Delta hex \approx 20$ mol% and $w_s/w_h \approx 80/20$, 65/35, and 50/50.

Appendix A6

Self-correlation Function for the OBCs synthetized in the PPR

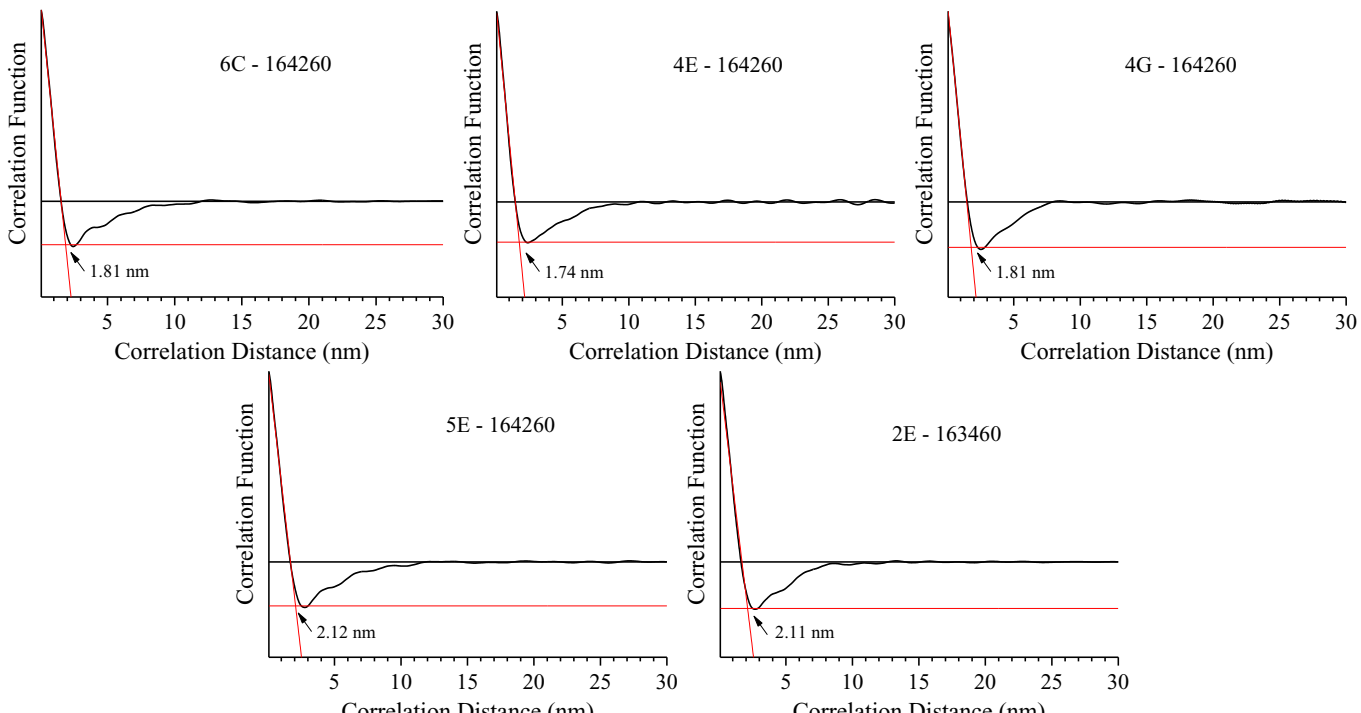

Figure A6-1. Self -correlation functions for the ethylene/1-hexene OBCs with $\Delta hex \approx 20$ mol% and $w_s/w_h \approx 80/20$.

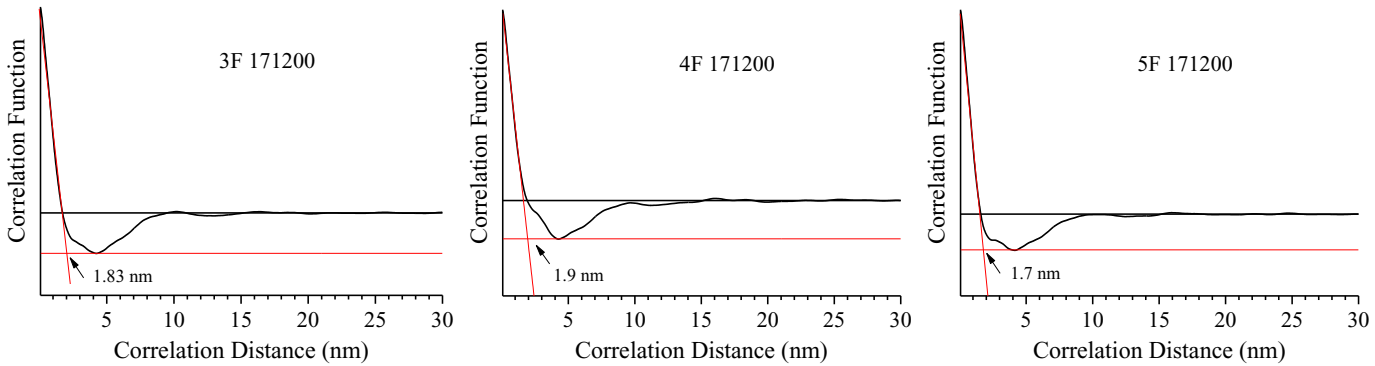

Figure A6-2. Self -correlation functions for the ethylene/1-hexene OBCs with $\Delta hex \approx 20$ mol% and $w_s/w_h \approx 50/50$.

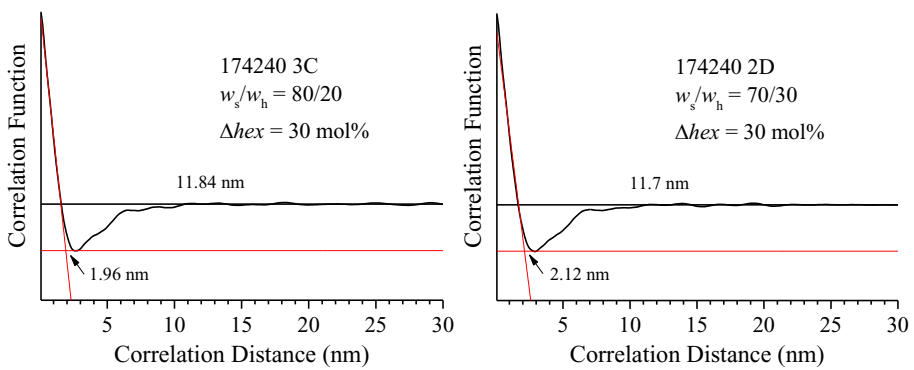

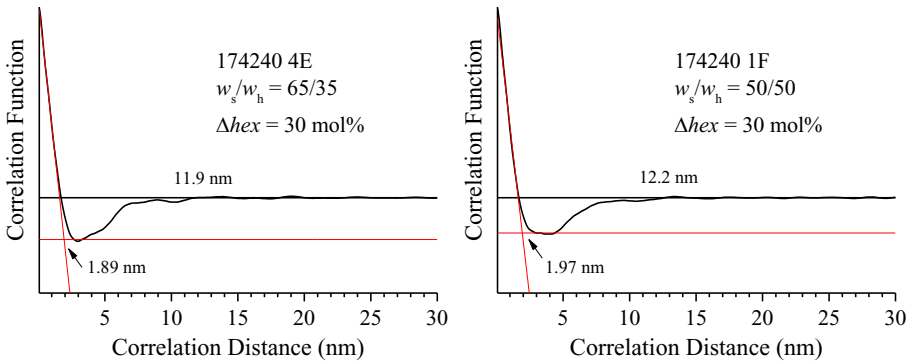

Figure A6-3. Self -correlation functions for the ethylene/1-hexene OBCs with Δ*hex* ≈ 30 mol% and w_s/w_h ≈ 80/20, 70/30, 65/35, and 50/50.